Non-destructive electromagnetic sensing technique to determine the level of chloride ions in reinforced concrete structures

By

GORAN SDIQ OMER

**A thesis submitted in partial fulfilment of the requirements of Liverpool John Moores University
for the degree of Doctor of Philosophy**

May 2021

DECLARATION

The research reported in this thesis was conducted at Liverpool John Moores University, Built Environment Department between Jun 2016-March 2021. I declare that the work is my own and has not been submitted for a degree at another university.

Goran Sdiq Omer

Liverpool John Moores University

May 2021

Abstract

Corrosion of the reinforcing steel arising from contamination by chloride ions from de-icing salt is the primary cause of deterioration of concrete bridges in the UK and many parts of the world. Those elements of structures exposed to cyclic wetting and drying have already proven the most vulnerable to corrosion damage. Chloride ions penetrate the concrete, resulting in deterioration (cracking, spalling due to reinforcement corrosion).

Currently, the existing methods such as Ion-Selective Electrode (ISE), Electrical Resistivity, and Optical Fibre Sensor to detect the chloride level in marine concrete structures are destructive, time-consuming, and unable to analyse large structures. This investigation aims to use a non-destructive electromagnetic (EM) wave technique to determine the chloride level in maritime concrete structures early to prevent the corrosion of the reinforcement developing.

An experimental programme was conducted to understand better the effect of different saltwater concentrations in concrete samples. The described Electromagnetic (EM) wave sensor operates at the frequency range between 2-13 GHz and a power of 0dBm using a Rohde Schwarz ZVL13 Vector Network Analyser (VNA). The sensor was positioned in front of the concrete specimens to determine chloride ions in the substantial sample. Finally, the graphical interface package LabVIEW was used to control the sensor's frequency sweep and capture the data from the sensor.

The experimental data obtained was analysed by the WEKA workbench tool to classify the most critical frequency point to detect the level of chloride ions in concrete. The input parameter was S_{21} measurements of one single frequency that has been selected by the classification algorithm decision tree (J48). After selecting the most critical frequency point, the Artificial Neural Network (ANN) models were trained by electromagnetic (EM) waves and chloride profile experiments. The outcome results demonstrated that electromagnetic waves have a response to saltwater concentrations. Therefore, the validation model was developed using the ANN method, which exhibited an excellent capability of the microwave sensors to validate the percentage of chloride ions per weight of cement with R^2v (Validation) =0.986709 and root mean square error of validation (RMSEV)=0.000120.

Acknowledgements

I would like to express my true gratitude and appreciation to my supervisory team that includes the Director of studies (DoS)- Prof.Michael Riley, Dr. Patryk Kot, Dr. Bill Atherton and Prof. Andy Shaw, for their support and help in the overall enhancement of this project by their review process and constant guidance and encouragement throughout the completion of my Ph.D.

Also, I would like to thank the entire RF and Microwave research group and members of the Built Environment and Sustainable Technologies (BEST) Research Institute, Especially Dr. Steve Wylie, Dr. Magomed Muradov, Dr. Jeff Cullen and Dr. Alex Teng for providing me with technical assistance to help with the project within the laboratory as required.

I would like to extend thanks to the technical staff of the Civil Engineering Department especially Malcolm Feegan, who provided great assistance and expertise for the experimental program of work. I would like to thank Dr. Mawada Abdellatif and Dr. Ahmed Zia Japeri for sharing their knowledge and experience with me during my data analysis.

I wish to express my extreme love and appreciation to my beloved family, particularly my brother Gaffor Omer, for his continuous encouragement and motivation during my study. Last but not least, I would like to express my thanks to my lovely wife Mrs. Hazha Bushir Mohammed and my lovely daughter Hava, as without their understanding, patience and continued encouragement it would have been very hard for me to successfully finish my Ph.D thesis.

Table of Contents

List of Figures

Figure 4.1: Electromagnetic waves with their full frequencies and wavelengths [160] 61
Figure 4.2: Microwave resonance curves, resonance curves in the air (solid line), resonance curve in wet material (dash line) [220]. 66
Figure 4.3: Microwave sensor technique. 66
Figure 4.4: Electromagnetic waves components [222] 67
Figure 4.5: Microwave penetration and reflection are demonstrated using a schematic design 72
Figure 4.6: Pyramidal horn antenna [LJMU Lab sensor] 74

List of Tables

List of Abbreviations

Letters	**Names**
ASCE	American Society of Civil Engineers
ANNs	Artificial Neural Network Analyse
ASR	Alkali-Silica Reaction
ARFF	Attribute Relation File Format
AI	Artificial intelligence
b	bias
BEST	Built Environment and Sustainable Technologies
BP	Back Propagation
CD	Coefficient of determination
$Ca(OH)_2$	Calcium Hydroxide
$CaCO_3$	Calcium Carbonate
C_{crit}	Critical Chloride Content
CL	Chloride Ion
CI	Computational Intelligence
CO_2	Carbon dioxide
DAQ	Data Acquisition
EM	Electromagnetic Waves
ER	Electrical Resistivity
E	Photon energy
Fe	Ion
f	Frequency
$Fe(OH)_2$	Hydrated ferric oxide (rust)
FHWA	Federal Highway Administration
GPR	Ground-penetrating radar
GNI	General Public License
GUI	Graphical User Interface
H2O	Water
HPC	High-performance concrete
HCFA	High Calcium Fly Ash
IVs	Independent variables
ISAT	Initial Surface Absorption Test
ISE	Ion-Selective Electrodes
IG	Info Gain Attribute Eval
KNN	K-Nearest Neighbour
LJMU	Liverpool John Moors University
LM	Levenberg-Marquardt
MAE	Mean Absolute Error
MLP	Multilayer Perceptron
MRI	Magnetic Resonance Imaging
MSE	Mean Square Error
MUT	Material under test
ML	Machine Learning
ɳ	Impedance
NaCl	Sodium Chloride
NAE	Normalised Absolute Error

NDT	Non-destructive test method
NI	National Instrument
OFS	Optical Fibre Sensors
OPC	Ordinary Portland Cement
PEs	Processing elements
R^2	Correlation Coefficient
RBF	Radial-Basis Function
RC	Reinforced Concrete
RMSE	Root Mean Square Error
RF	Radio Frequency
SWR	Standing Wave Ratio
TF	Transfer function
TM	Transverse magnetic
TE	Transverse electric
TPT	Torrent permeability tester
UPV	Ultrasonic Pulse Velocity
US	Ultrasound
VNA	Vector Network Analyser
VSWR	Voltage Standing Wave Ratio
W/C	Water Cement Ratio
WW2	Second World War
XO	No risk of attack or corrosion;
XC	Corrosion risk induced by carbonation
XD	Corrosion risk induced by chloride(s) (other than by seawater);
XS	Corrosion risk induced by chloride(s) (seawater).
XF	Risk of attack from freezing and thawing
XA	Chemical attack

List of Symbols

Symbols	**Name**
A	The surface through which the current pass
α	Momentum
C	Speed of light
E_i	Expected value
hi	Hidden neuron output
I	Electrical current
I_J	Node activation
J^TJ	Hessian matrix
J	Jacobian matrix
K_T	Permeability coefficient
O_i	Observation
R	Electrical resistance
R^2	Correlation Coefficients
S_{11}	Reflected Coefficient
S_{21}	Transmitted Coefficient
Tanδ	Loss Tangent
wij	Weight
Wn	Weights
xn	Input values
x^2	Chi-square
y	Output values
σ	Conductivity
ρ	Density of the volume charge
ε^*	Complex permittivity
ε'	The real part of the complex permittivity
ε''	The imaginary part of the complex permittivity
ε_0	Permittivity of the free space
ε_r'	Relative permittivity known as dielectric constant
ε_r''	Imaginary part of the relative permittivity (loss factor)
μ_o	Air permeability
v	Velocity
λ	Wavelength
φ	Activation function
ɳ	Impedance
θ_j	Bias on hidden neuron
δk	Error back-propagation
$\sum$	Sum
Γ	Reflection coefficient
δ	Skin depth
x	Distance from the surface
α	Attenuation
ω	Angular frequency

Chapter One: Introduction

1.1 Research background

Reinforced concrete (RC) is the main element within infrastructure worldwide due to its high compressive and tensile strength and cost-effectiveness [1]. Its relative cheapness is because of raw material availability; its versatility allows a broad range of applications and forms, and with proper design and execution, its durability can be impressive. However, RC can be used to construct docks, bridges, piers, floating platforms, and has many other kinds of marine applications, both offshore and along coastlines. The primary cause of deterioration in structures constructed of reinforced concrete is when the embedded steel corrodes due to exposure to marine-type environments or salts used for de-icing; this is because of the actions of chloride. The reinforcement steel provides the tensile strength; however, this may weaken due to corrosion over time. Deteriorating strength occurs in a more pronounced way in structures that are in industrial or marine environments [2]. As well as the reinforcement corrosion, other kinds of deterioration mechanisms can occur in RC structures such as, for example, freezing and thawing, acid attack, erosion/abrasion, mechanical loading, and alkali-silica reaction (ASR) [3].

However, the principal, most common deterioration mechanism is reinforcement steel corrosion [4]. Steel corrosion in concrete has two main causes, i.e., carbonation and chloride attack. There is a reduction in the pH level of concrete due to carbon dioxide and chloride penetration and the effects of moisture and oxygen. Tuutti's (1982) classic model notes that it can identify two periods of reinforced concrete service life, i.e., the initiation and propagation. The initiation period is defined as that phase before the detection of steel depassivation. For proper design in this phase, there is a need for information about the rate of chloride ingress and critical depassivation condition. The period known as the propagation phase calls for knowledge concerning the corrosion rate to make predictions regarding structural integrity [5].

1.1.1 Problems and processes in chloride-induced corrosion

Problems associated with corrosion that chlorides have induced within the steel reinforcement within bridges are not just an issue in the UK, but it is a phenomenon worldwide that has serious implications for both safety and economies. In 2002, a report was presented to Congress in the United States on the costs of corrosion and strategies for prevention. According to the report by the Federal Highway Administration (FHWA), highway bridge corrosion has a cost to the US economy of approximately £8.3 billion every year. In addition, there was an outlay estimated for the following ten years of £3.8 billion for the replacement of structurally deficient bridges, and £2 billion for maintenance and capital costs for superstructures (minus decks) and substructures, as well as £0.5 billion for costs of painting to maintain steel bridges [6]. It was stated by the American Society of Civil Engineers (ASCE) in 2009 that there was a need for investment of £2.2trillion over five years to enhance structures in America to conditions that were appropriate [7]. In Europe, more recently, a lot of the infrastructure related to transport within the Atlantic area has an age of greater than fifty years. Many of the structures are in severe deterioration as marine environments can be highly aggressive [8]. In Denmark, for example, the costs of damage, down to programs for maintenance and delays in traffic, can reach a level of between 15% and 40% of construction costs [9].

In the latter half of the twentieth century, since chloride could cause significant corrosion of the steel in RC structures, a great deal of research effort began to occur. In fact, over the last 50 years, many papers have been published that presented critical chloride content (C_{crit}) values within reinforced concrete [10-17]. The process of penetration of chloride and carbonation is shown in Figure 1.1[18]. There are chlorides present in potable water; as such, one should never use potable water with significant chloride content within the mixing of concrete. However, chlorides may build up within the lifespan of a structure due to environmental factors. If, for instance, there is the exposure of a building to salty seawater or de-icing salts, there can be a much quicker accumulation of the chlorides experienced. With the reaching of a threshold chloride concentration value for the steel bars, there can be chloride-induced corrosion, which destroys thin passive layers in construction products. If there is high concrete alkalinity during the construction phase, the steel bars can be corrosion protection. However, carbonation can occur when the carbon dioxide within the environment is involved in a reaction with the alkaline constituents, which results in pH reduction around the steel. The corrosion rate for reinforcement steel is raised significantly through both carbonation and chloride attacks [19].

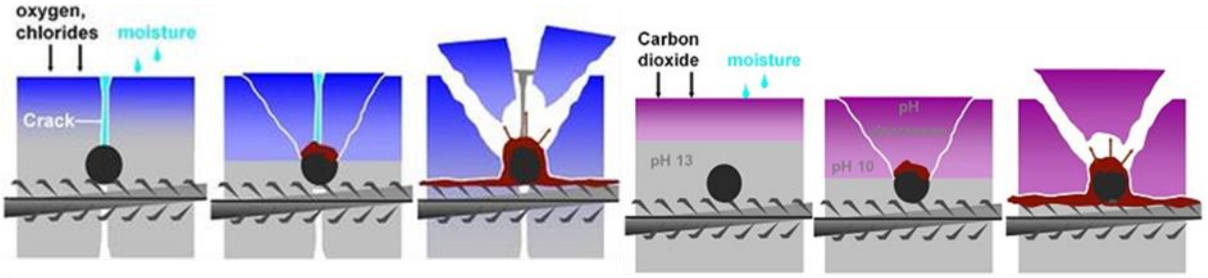

Figure 1.1: Process of penetration of chloride and carbonation within concrete [18]

Reinforced concrete durability is mainly affected by aggressive substances penetrating the concrete and degrading the concrete and the reinforcement. The environmental load that is most critical for structures within a marine environment is chlorides since they cause serious damage through corrosion [20].

1.1.2 Different exposure conditions for maritime-related concrete structures

To investigate practices for addressing corrosion-related deterioration as well as bridge maintenance and repair, it has been noted that the construction of pier columns, being in a coastal area, leads to them experiencing a constantly changing climate [18]. Chloride attack is a preliminary problem for bridges because it leads to concrete reinforcement corrosion in parts of RC structures. Since columns are load-carrying elements in bridges, they are essential. However, columns are frequently exposed to chloride ions due to salt utilised in removing ice or splashing of water or marine waters [21]. There can normally be the categorisation of material strength and quality by considering the ratio of water to cement (w/c) and the associated porosity ratio. The smallest degree of pore porosity is an indication of less contact. As regards the association of the permeability with the porous structure, moisture loss increases along with porosity. A high level of porosity results in the transfer of water inside the concrete more easily and faster [22]. Furthermore, in the context of melted ice and snow due to salts for de-icing, as along roadways, the presence of chloride ions can lead to concrete becoming contaminated. A corrosive deterioration process can be persistent because of the presence of such chloride ions along with the availability of moisture, carbon dioxide, and oxygen [23]. The exposure conditions in marine environments are highly aggressive for reinforced concrete structures, and reinforcement corrosion is the most significant deterioration mechanism. Corrosion of reinforcement causes the concrete cover to crack and delaminate, resulting in a reduction in the cross-section of the reinforcement [24]. When that happens, the load-bearing capacity within the structural elements can be reduced very significantly. The corrosion starts as a result of the penetration of chloride at the reinforcement level or through the carbonation of the concrete cover [25].

The majority of structures made using RC are designed in such a way that their performance is good enough during their construction life due to their careful fabrication. However, RC can, as in the case of steel, be severely impacted through environmental attack; corrosion of steel reinforcement is considered the main reason for RC structure deterioration in marine environments. Carbonation occurs because of the entry of air-based CO_2 into the concrete and the consequent reaction with the hydroxides present, such as, for instance, calcium hydroxide, which leads to carbonate formation. Calcium carbonate production occurs when there is a reaction with the carbon dioxide as shown in the equation [24]:-

$$Ca(OH)_2 + CO_2 \rightarrow CaCO_3 + H_2O \qquad \text{Eq [1]}$$

In response to the reaction, the pH of the concrete decreases to perhaps 8.5, and, consequently, there is a lack of steadiness in the passive film on the steel. With carbonation of good quality steel, the process mentioned above is somewhat slower, with a rate of carbonation proceeding at maybe 1mm per year penetrated in concrete. Concrete carbonation may be affected significantly by low content of cement, low strength of concrete, and high water to cement ratio. Salt and moisture ingress into concrete can all be permitted if there are quality control problems such as any construction defects, e.g. an inadequate cover depth, or issues of structure age, or high permeability of the concrete. When salt and moisture concentrations are high, there can be an acceleration of the reinforcing steel corrosion and major deterioration of the concrete structure. The category of exposure is very apparent for concrete structures in marine environments, an example being those bridge elements that are part of the substructure [26]. There are three distinct areas of concrete structure concerning corrosion that can be identified in marine environments, i.e.

1. The submerged zone (parts always lying beneath the seawater surface).
2. Tidal movement and splashing (parts that are wet and dry intermittently).
3. The atmospheric zone (those parts well above the mean of the high tide that are only infrequently wetted) [27].

There is the most rapid deterioration in the splash zone because both moisture and oxygen are available. Corrosion rates are also high in the tidal zone at rates higher than those for the atmospheric or submerged zones; those zones are often critical in the construction of concrete. Generally, the corrosion rate is lower in fully immersed zones with less oxygen availability [27]. Corrosion zones related to steel piles are shown below in Figure 1.2 [28].

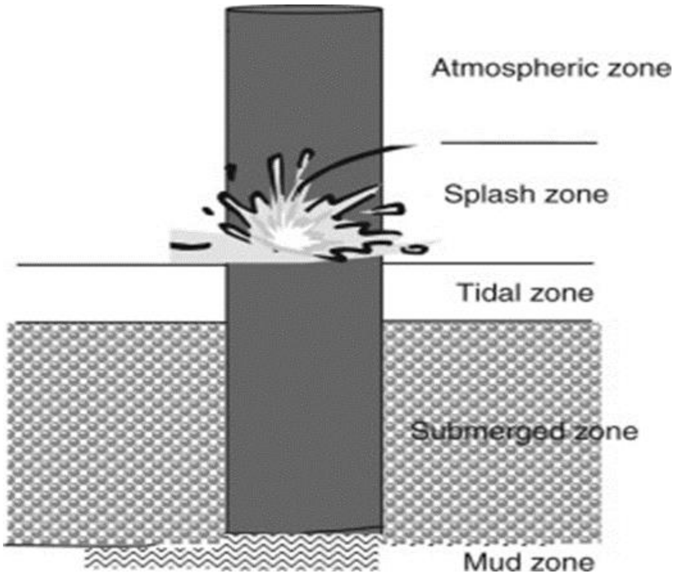

Figure 1.2: Corrosion zones in steel Piles [28]

1.1.3 Electromagnetic (EM) waves compared with different methods to determine the chloride level in concrete structures.

Many existing methods have been employed as non-destructive and destructive techniques in detecting free chloride ions within concrete structures. Conventional methods for determining chloride ion levels within concrete have included, for example, the test for rapid chloride permeability. Nowadays, destructive techniques are applied worldwide to detect chloride levels. However, there is broad recognition that they time-consuming procedures and it would improve assessment methodologies appreciably if a non-destructive technique could provide the information during testing [29].

Non-destructive techniques have also been employed in the investigation of levels of chloride ion penetration within concrete. There has been classification of non-destructive methods into three primary groups [30] ion-selective electrodes (ISE) [31, 32], electrical resistivity (ER) [33, 34], and optical fibre sensors (OFS) [35, 36]. Each technique has its particular advantages and disadvantages; all the techniques are described in further detail within the review of the literature in Chapter 2. Imaging through magnetic resonance is an appropriate technique for profiling the distribution of chloride and sodium within cement-based materials [37]. Nevertheless, nuclear magnetic resonance (NMR) can determine the presence and concentrations of chloride in principle. For NMR, the low sensitivity of detection of chloride makes its discovery tough, therefore, demanding the use of MRI systems with high-field superconducting magnets to increase signal intensity. This restricts the use of MRI in studying cement-based materials because these kinds of MRI systems are costly and not widely available [38]. Currently, there has been a focus of study upon applying the method of ultrasound (US) for assessing concrete deterioration and strength. Also, the use of radar that is ground penetrating is a non-destructive method for investigation of chloride ions' presence and their ingress within concrete structures [39-42]. Since existing techniques for measuring chloride ions have their limitations, further investigations are undertaken within this research. As such, positive study results can provide the industry with a less time-consuming technique, with lower cost, and non-destructive nature for determining the level of chloride ions within the highway and marine concrete structures. Generally, electromagnetic (EM) sensors are employed in various industrial processes, especially those working at microwave or radio frequencies such as in chemical processing [43], in medicine [44], and within the analysis of civil engineering materials [45]. The potential of using microwave sensors for the detection of moisture content within concrete structures was demonstrated by researchers based in the institute of Built Environment and Sustainable Technologies (BEST) within Liverpool John Moores University (LJMU) [46].

The purpose of this project is to determine the level of chloride ions in industrial concrete structures. Therefore, this research has investigated whether electromagnetic waves can detect the amount of chloride in different saltwater concentrations at various depths through the use of a set horn antenna. However, in principle, the EM sensor can detect the level of chloride based upon the operating frequency; this will be shown in chapter 6. Combining the EM waves technique and artificial neural network (ANN) analysis contributes to new knowledge since it experimentally demonstrates the use of microwave sensors at a frequency range of 2-12 GHz for monitoring and determining the level of chloride ions within the concrete. The advantages of using Electromagnetic (EM) waves are a high penetration depth and relatively lower cost, allowing for a flexible sensor design and providing non-destructive measurement in a real-time manner.

1.2 Aim

This research aims to investigate and validate to use of Electromagnetic (EM) waves as a non-destructive technique to determine the chloride level in reinforced concrete structures.

1.3 Objectives

The specific objectives of the research are as follows:

- To investigate the effect of chloride attack and problems associated with chloride presence in steel-reinforced concrete structures.
- To evaluate the current state-of-the-art techniques for the determination of the level of chloride ions content and moisture content of concrete structures.
- To determine the chloride ions level in concrete samples under various saltwater concentrations at different concrete depths using other techniques.
- To apply the artificial neural network ANN technique to evaluate the performance of the proposed EM technique in comparison to the chlorimeter tool, commonly used as a gold standard in the industry.

1.4 Novelty

For the first time, this thesis demonstrated the combination of an electromagnetic wave as a non-destructive technique with an application of an artificial neural network ANN to determine chloride concentration in concrete. The detected level is below the currently used gold standard techniques and, therefore, can transform the early detection of deterioration in steel-reinforced concrete structures. ANN was used to analyse the microwave wave signal to validate the level of chloride ions in the concrete samples.

1.5 Overview of the Thesis

The thesis is divided into seven chapters to achieve the goal and objectives of this research project. Chapter 1 has discussed the industry's major issues in relation to chloride-exposed reinforced concrete. Chloride attack is a preliminary problem for bridges because it leads to concrete reinforcement corrosion in parts of RC structures. However, due to salt used in removing ice or splashing water or in maritime conditions, columns are regularly exposed to chloride ions.

Chapter 2 will start a literature review by focusing on the impact of the chloride ion attack mechanism and evaluate the current commercially available techniques to measure the level of chloride ions in the concrete structures used in the field. Moreover, it covers the recent research carried out to develop non-destructive techniques to detect the level of chloride ions at the early stages before reaching the rebars and corrosion commencing. This will focus on the need to investigate electromagnetic wave sensors to develop a non-destructive method for determining the level of chloride ions in concrete structures.

Chapter 3 reviews literature on the ANN concept and the proposed use of the Levenberg-Marquardt (LM) training algorithm. Additionally, a literature review on the machine learning algorithm concept such as classification will be discussed. In Chapter 4, the theory of electromagnetic waves will introduce the microwave sensing technique as a proposed system to detect moisture content and saltwater concentration in the concrete samples. Different types of horn antennas and their advantages will describe and compare their features to select the most suitable sensors for this project and the associated investigation. In addition, this chapter will represent the skin depth of the electromagnetic waves to penetrate the concrete sample according to civil engineering requirements in detail. Chapter 5 discusses the research methodology and experimental techniques followed in the study. The chapter provides a flow chart indicative of the research methodology. The final section in this chapter will define the data processing and the development of the validation models. Chapter 6 covers the results and discussion of the microwave horn antenna used to determine the level of chloride ions in the samples. Also, the superiority of the LM algorithm and WEKA workbench classification has been demonstrated in this chapter by validation of results using an unseen data set with targeted values obtained by the chlorimeter tool currently used as a gold standard method.

Chapter 7 includes the concluding summary of the current study. Research limitations and recommendations for further investigation are also provided in this final chapter.

Chapter Two: Literature Review

In this chapter, the literature review will focus on chloride attacks and the problems associated with chloride present in concrete structures. Then follows a critical review of current measurement instruments for the detection of chloride levels. Lastly, there is a provision of a summary of the main findings within this review of the literature and a discussion over the need for a new approach in determining chloride concentrations.

2.1 Factors affecting reinforced concrete durability

The primary factors having a bearing on reinforced concrete (RC) structures, whilst experiencing exposure to aggressive and corrosive environments, are i) practices in design and construction and ii) factors that are environmentally related.

2.1.1 Design and construction practices

The construction practice and the design choice significantly affect the durability of reinforced concrete structures exposed to a very aggressive environment, such as that with chloride contamination. The selection of nominal concrete cover thickness, appropriate values for water to cement ratio (w/c), and compressive strength of concrete during the design combined with efficiency during construction, such as casting and proper curing, is paramount to ensure durability for reinforced concrete (RC) structures [47, 48]. For example, three days of concrete curing period with a 0.4 w/c ratio used and a 30 mm cover thickness of the concrete sample reduced chloride ingress more effectively than with a 0.5 w/c ratio and one day of curing period with the same cover thickness [49]. Concerning design considerations, the time needed for corrosion of a steel bar to begin increases with greater cover. However, higher concrete strength, by lower w/c ratio and the addition of certain admixtures, also reduce the ingress of chloride, moisture, and oxygen rates of diffusion within concrete. However, a lower w/c proportion in concrete allows for the formation of honeycombs and flaws in the surface, allowing aggressive agents like O2, Cl−, CO_2, and H_2O to penetrate more easily [50]. Construction practices define important concrete properties such as porosity, permeability, etc., that dictate durability. For example, an unsuitable curing process increases the permeability, which describes the physical characteristics of the concrete matrix against chloride ingress. [51]. Furthermore, the circumstances at the surface of reinforcing steel have a significant impact on behaviour with respect to the initiation of corrosion [52]. Some studies have looked into the possibility of finding points of higher activity on rough steel surfaces (as opposed to smooth ones); processes of corrosion may be quicker on rough steel surfaces. Also, with rebars with mill scales, corrosion is much faster than with polished treatment [53]. Finally, because of the casting direction, the corrosion process was increased by the presence of gaps inside the concrete-steel interface [53].

On the whole, planning for durable structures of RC may be progressed through consistency for the conditions presented, i.e., cement substance, the proportion of w/c, admixture utilisation, increased cover thickness, and so on. From the viewpoint of preparation for construction, there can be a reduction in chloride ingress and harm from corrosion by undertaking specific activities such as ensuring appropriate curing, control of chlorides within the water, total washing of aggregate, etc. Finally, other factors such as structural member complexity and execution quality influence the feasible cover thickness by extending or shortening the corrosion initiation stage. Figure 2.1 below shows the impact of chloride ingress and processes of corrosion within structures of reinforced concrete.

For the reinforced concrete design, a few key points need to be brought to the reader’s attention while the reinforcement is embedded in the concrete up to a particular distance from the member’s face [54] [55]:

- Protects corrosion enhancement.
- To provide reinforcement resistance against fire.
- To provide adequate embedded depth to develop the required stress by the reinforcement.

This distance is measured differently and is known by several names:

- The nominal cover: It is the distance between the surface of the reinforcement and the exposed concrete surface (which can be the main bar, longitudinal bar or stirrups). But the nominal cover should not be less than the diameter of the bar.
- Clear cover: It is the distance from the member’s face to the reinforcement outermost side, including the shear or torsion Stirrups.
- Effective Cover: is the distance between the exposed concrete surface to the centroid of the main reinforcement.

However, the skin depth is a measure of how closely electromagnetic waves can penetrate along the material's surface. The skin depth depends on current /signal frequency and material resistivity. It is inversely proportional to the frequency and directly related to resistivity.

Enhancing the permeability and conductivity of a given material can significantly increase the absorption of EM [56] [57].

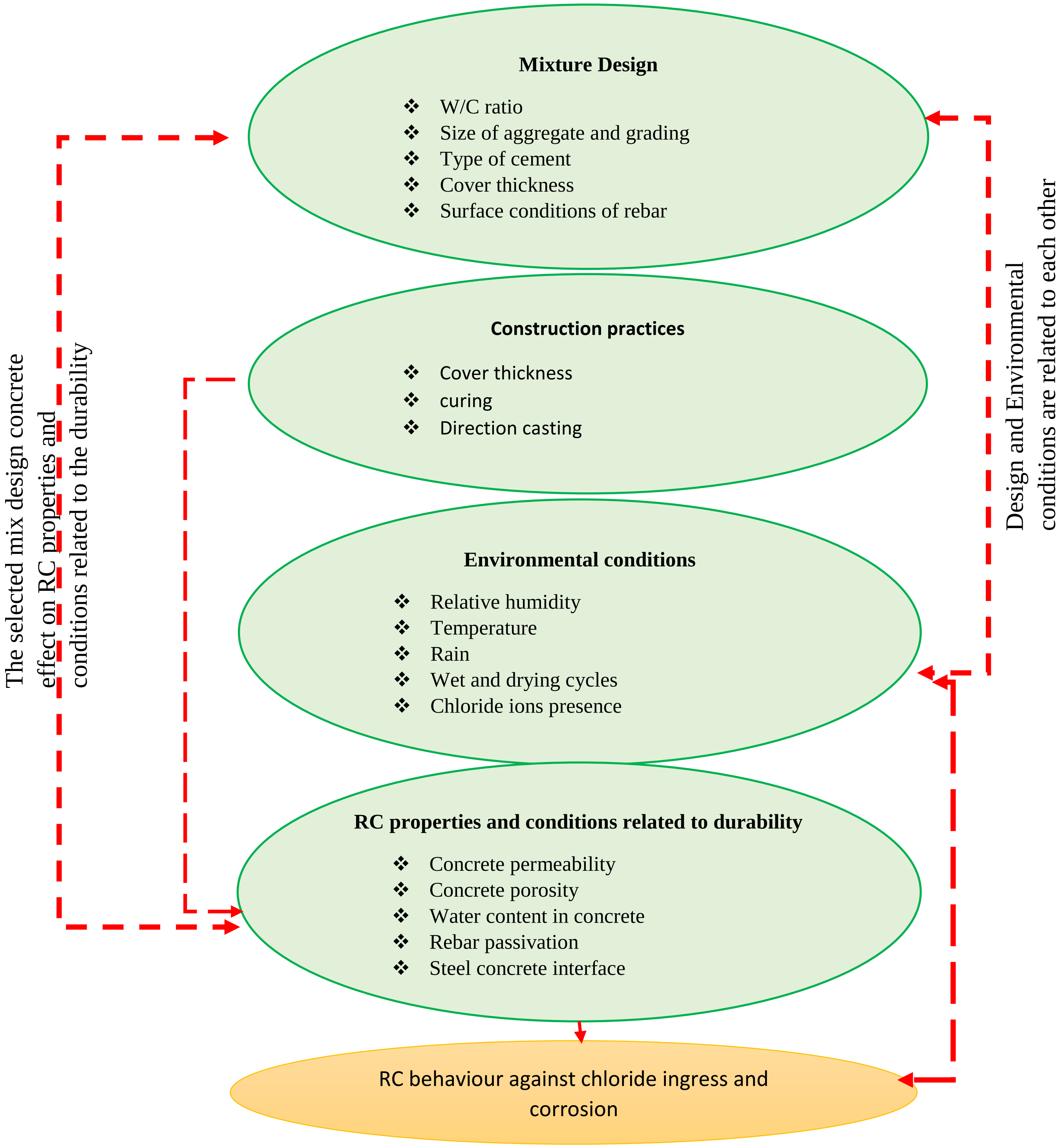

Figure 2.1: Factors influencing chloride ingress and the process of corrosion in reinforced concrete structures

2.1.2 Environmental factors

The corrosion rate of reinforced concrete is also affected by the standard test conditions. For chloride ingress, there is a dependence on surface chloride concentration and upon other conditions such as temperature and relative humidity [58]. As such, higher temperatures and relative humidity that is ideal lead to an acceleration of the processes of chloride penetration and propagation of corrosion according to the BS 8500-2:2006+A1:2012 [59]. Corrosion processes are significantly influenced by the presence of water, such as through seawater exposure and cycles of drying and wetting that increase the entry of chloride and corrosion volumes [60]. As a consequence, procedures of deterioration will vary in their kinematics depending on the micro-environment (atmospheric, splash, tidal, or submerged conditions within marine environments) or macro-environment (environmental conditions specific to a particular place) [61].

Further significant environmental factors are the presence of gaseous contaminants that are acidic such as nitrogen oxides, carbon dioxide and sulphur dioxide [62, 63]. Such acidic compounds, produced through urban activity and industrial processes, can transfer to concrete matrices through wet or dry deposition. Entrance is usually from the concrete surface and mainly depends upon the concrete structure's penetrability. It has been noted that sulphates, when present, may improve the conditions of concrete resistance against chloride ingress during early exposure. However, it can also increase the penetration of chloride during exposure at later stages. Also, whilst there is a presence of water within the concrete and once polluting sulphates have managed to reach reinforcement, the consequent reduction in pH leads to an acceleration of the corrosion processes [64].

2.2 Infrastructure in aggressive environments

Environmental exposure conditions for concrete structures are separated into five areas, with severity levels ranging from mild to moderate through severe, very severe, and extreme. However, where structures are constructed in different conditions and experience other effects, measures need to be taken to protect the structures, particularly those under severe to extreme conditions. The different environmental exposure conditions and their impact on structures are shown in the following Table 2.1.

According to the European Standard EN206-1, published in 2005, exposure classes are categorised based on different degradation mechanisms. The details of the European

exposure classes demonstrated in Table 2.2 are divided into the following six major categories [59, 65]:

XO - No risk of attack or corrosion;

XC - Corrosion risk induced by carbonation;

XD - Corrosion risk induced by chloride(s) (other than by seawater);

XS - Corrosion risk induced by chloride(s) (seawater).

XF- Risk of attack from freezing and thawing;

XA- Chemical attack;

These categories are further sub-divided into sub-classes, totalling about 18. Table 2.2 includes typical examples explaining different sub-classes.

Table 2.1: Severity of environmental exposure conditions [66]

Environment Factors	Exposure conditions
Mild	Concrete surfaces are protected against aggressive conditions or weather, except those situated in coastal areas.
Moderate	Concrete surfaces sheltered from freezing and severe rain whilst wet, concrete exposed to condensation and rain, concrete continuously underwater; concrete in contact with, or buried under, non-aggressive soil/groundwater; concrete surfaces sheltered from saturated salt air in the coastal area.
Severe	Concrete surfaces exposed to severe rain, other wetting and drying or occasional freezing whilst wet or severe condensation, concrete completely immersed in seawater; concrete exposed to the coastal environment.
Very Severe	Wet concrete surfaces exposed to seawater spray, corrosive exhausts, or extreme freezing conditions, concrete in touch with soil, or concrete submerged beneath aggressive subsoil and groundwater
Extreme	Members in the tidal zone's surface, as well as members in direct touch with liquid and solid harsh chemicals.

Table 2.2: Exposure classes [59, 65, 66]

Class designation	Description of the environment	Informative examples applicable in the United Kingdom
a) No risk of corrosion or attack		

X0	For the concrete without reinforcement or any embedded metal: all exposures except where it is freeze-thaw, abrasion or chemical attack For concrete with reinforcement or embedded metal: very dry	This is for concrete inside the building with very low air humidity.
b) Corrosion made by carbonation		
XC1	Dry or permanently wet	Concrete inside buildings with low air humidity Concrete permanently submerged in water
XC2	Wet, rarely dry	Concrete surfaces subject to long term water contact Many foundations
XC3	Moderate humidity	Concrete inside buildings with moderate or high air humidity External concrete sheltered from rain
XC4	Cyclic wet and dry	Concrete surfaces subjected to water contact, not within exposure class XC2
c) Corrosion made by chlorides		
XD1	Moderate humidity	Concrete surfaces exposed to airborne chlorides
XD2	Wet and rarely dry	Swimming pools Concrete Components exposed to industrial waters containing chlorides
XD3	Dry and wet cyclic	Parts of bridges exposed to spray containing chlorides Pavements Car park slabs
d) Corrosion induced by chlorides from seawater		
XS1	Exposed to airborne salt but not direct contact with seawater	For those structures quite close to the coastal area
XS2	Permanently submerged	Parts of marine concrete structures
XS3	Tidal, Splash and Spray zone	Pars of the marine concrete structures
e) Freeze/ thaw attack with or without de-icing salts		
XF1	Moderate water saturation, without de-icing agents	Vertical concrete surfaces exposed to rain and freezing
XF2	Moderate water saturation, with de-icing agents	Vertical concrete surfaces of road structures exposed to freezing and airborne de-icing agents
XF3	High water saturation, without de-icing agents	Horizontal concrete surfaces exposed to rain and freezing

XF4	High water saturation, with de-icing agents or seawater	Road and bridge decks exposed to de-icing agents. Concrete surfaces exposed to direct spray containing de-icing agents and freezing. Splash zones of marine structures exposed to freezing
f) Chemical attack		
XA1	Slightly aggressive chemical environment according to Table 2.1	
XA2	Moderately aggressive chemical environment according to Table 2.1	
XA3	Highly aggressive environment according to Table 2.1	

The primary cause of deterioration within reinforced concrete marine structures because of chloride ion ingress is discussed below in Section 2.3.

2.3 Chloride attack

The corrosion of reinforcements in RC structures in the presence of chlorides is a crucial issue of durability that has been observed worldwide. Reinforcement corrosion affects many kinds of RC infrastructure, mainly the kinds of structures exposed to marine-type conditions [67]. Primarily, there are two kinds of corrosion of reinforcement steel, i.e. usual corrosion and pitting corrosion. Because of the presence of a layer of passivation upon the steel surface of the two kinds of corrosion, the pitting kind is the more rapid and harmful [68]. Structures such as bridges are prone to pitting corrosion if located by the sea; the most critical area in these structures is the splash zone near the air and water interface. Because there is an abundance of chloride in the water and oxygen in the surrounding air, the cell processes of electrochemical corrosion are accelerated [19]. Of the two kinds, normal corrosion is of lesser criticality as the steel is protected from more deterioration by a film of passivation. There is a breakage of the passivation film if the chloride ion number exceeds a certain threshold, leading to pitting corrosion. The deterioration noted above and shown in Figure 2.2; indicates that a significant degree of corrosion leads to detachment of the concrete cover in the splash zone area.

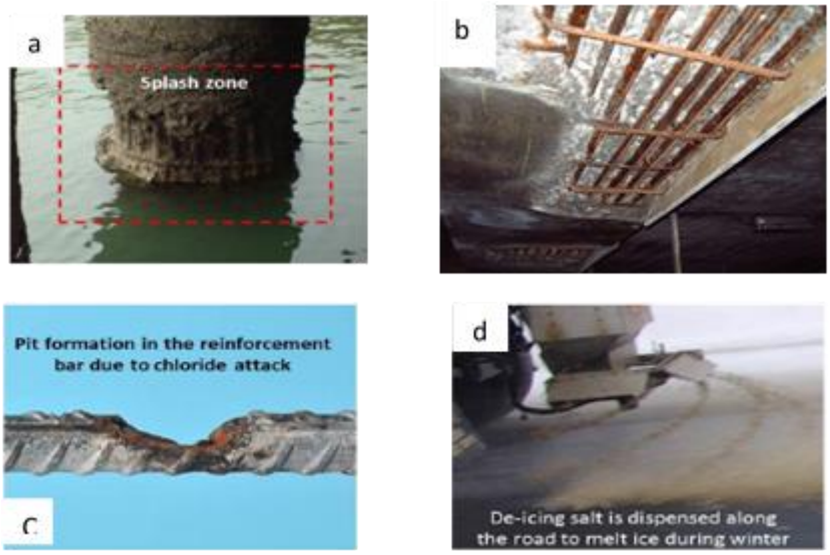

Figure 2.2: (a) The splash zone of the concrete bridge pillar [69][61]; (b) Concrete bridge cover deterioration [70], permission to reproduce this figure has been granted by John Broomfield; (c) Pitting corrosion to the reinforcing bar (16 mm), permission to reproduce this figure has been granted by Dieter Friede; (d) Salt for de-icing is dispensed along the road [71].

If such deterioration happens, structures may collapse if delays occur in providing appropriate maintenance, leading to human casualties. On the other hand, if maintenance work is unnecessary, there may be financial cost implications and other pointless CO2 emissions [72].

2.4 Chloride ingress within concrete

The presence of ions of chloride in concrete can hail from sources that are both internal and external. External sources could be salts used in de-icing roads or melting ice on bridges, and the salt within seawater that impacts structures within a marine environment; see Figure 2.3 [73]. Moreover, concrete surfaces can have chloride ions deposited upon them from the air, as a turbulent sea and a strong wind can carry them a distance and deposit them. Airborne chlorides can travel considerable distances; a distance of 2 km is recorded [74], though greater distances are possible depending on geography and wind speed. On the other hand, internal chloride ion sources come from the salts present within the aggregates and mixtures when the casting of the concrete occurs [75]. A typical profile for chloride ingress can be seen in Figure 2.3, illustrating various exposure times [76]. The chloride diffusion happens within the concrete in wet conditions. Then, upon drying, the chloride remains inside the concrete; therefore, specific content along with the depth of concrete cover is considered.

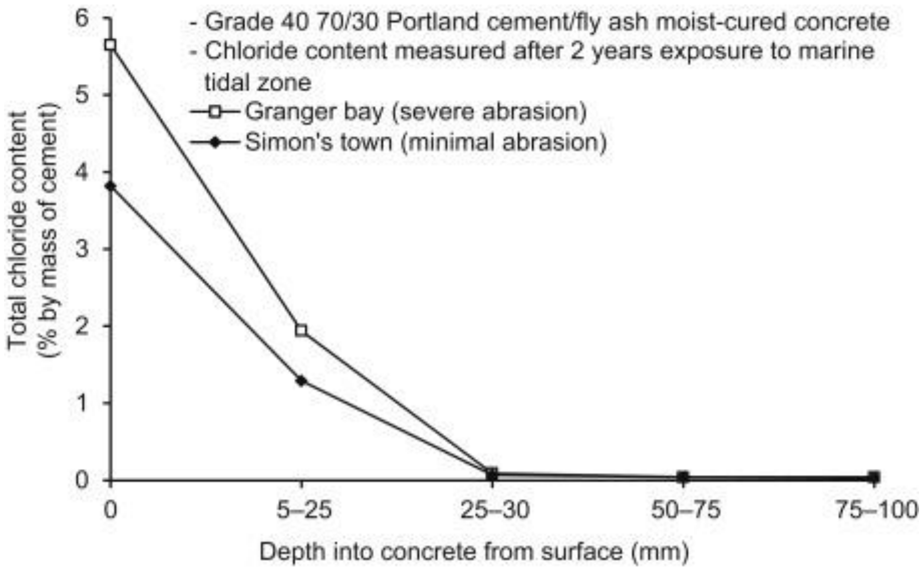

Figure 2.3: Chloride ion concentration compared to the depth of cover for different exposure times [70]

2.5 Steel corrosion within concrete

Steel reinforcement is associated with the nurturing alloy consisting of iron, a little carbon, and different trace parts. For steel corrosion within the concrete to be initiated, there need to be the following conditions:

1) Facilitation of a cathode and anode couple with some steel parts working as the anode.
2) An electrical circuit is maintained.
3) Oxygen presence
4) Moisture presence.

However, two key processes join in the corrosive attack upon the steel within concrete structures, i.e. pitting corrosion with the presence of a certain level of ions of chloride and reactions from carbonation; see Figure 2.4 for a schematic representation [77]. Many additional energies are applied to the mineral to rework steel during the manufacturing process, and corrosion involves a tendency for steel to rework into a thermodynamically stable original state [78]. Corrosion of metals is associated with nurturing chemical science method, which suggests that it happens not by direct chemical reaction of the metal with its setting, but instead through coupled chemical science half-cell reactions involving the passage of electrical charge. The chemical reactions that occur when steel is in a neutral or alkalescent solution are generally relevant [79].

The anodic reaction for iron dissolution is represented in Eq. 2.1 [79]:

$$\mathrm{Fe} \rightarrow \mathrm{Fe}^{2+} + 2\mathrm{e}^{-} \qquad \text{Eq (2.1)}$$

Chemical reactions occur between the electrode and the metal surface at a rate that is consistent across the metal surface. Eq. 2.2 shows a balanced type of response [79]:

$$2\mathrm{Fe} + \mathrm{O}_2 + \mathrm{H}_2\mathrm{O} + 4\mathrm{e}^{-} \rightarrow 2\mathrm{Fe(OH)}_2 \qquad \text{Eq (2.2)}$$

Where rust hydrated ferric oxide is the final reaction product.

With carbonation present, contamination begins at the concrete surface and moves gradually towards inner zones. Concrete alkalinity may be neutralised by CO2 in the atmosphere, with the level of pH in the concrete structure pore liquid reducing to about 9-8 where there is no more extended stability of the passive film. However, chloride ions from an aggressive environment may penetrate the concrete to the point where it reaches the reinforcement; if chloride concentration amounts at the reinforcement surface reach a critical level, then there may be local destruction of the passive film that was protecting the steel surface [19].

When the concrete has exposure to air, there is a reaction of the calcium hydroxide with the carbon dioxide within the air with water, as represented in Eq. 2.3:

$$\mathrm{Ca(OH)}_2 + \mathrm{CO}_2 \rightarrow \mathrm{CaCO}_3 + \mathrm{H}_2\mathrm{O} \qquad \text{Eq (2.3)}$$

Thus, carbonation has the effect of lowering the pH value in the concrete cover layer to less than 8.3; this pH is, therefore, sufficient to cause the reinforcement rebar passive layer to be more unstable [80]. Chlorides, on the other hand, cause localised breakdown unless they are present in significant quantities. As a result, it is possible to state that:

a. Corrosion caused by carbonation may occur at the entire reinforcement surface that is in contact with carbonated concrete.
b. Corrosion caused by chloride (pitting corrosion) is localised as the chloride penetrates and attacks specific areas surrounding uncorroded areas.

There can be the destruction of the passive film over broad reinforcement areas whilst there are very high chloride levels on the rebar surface [80].

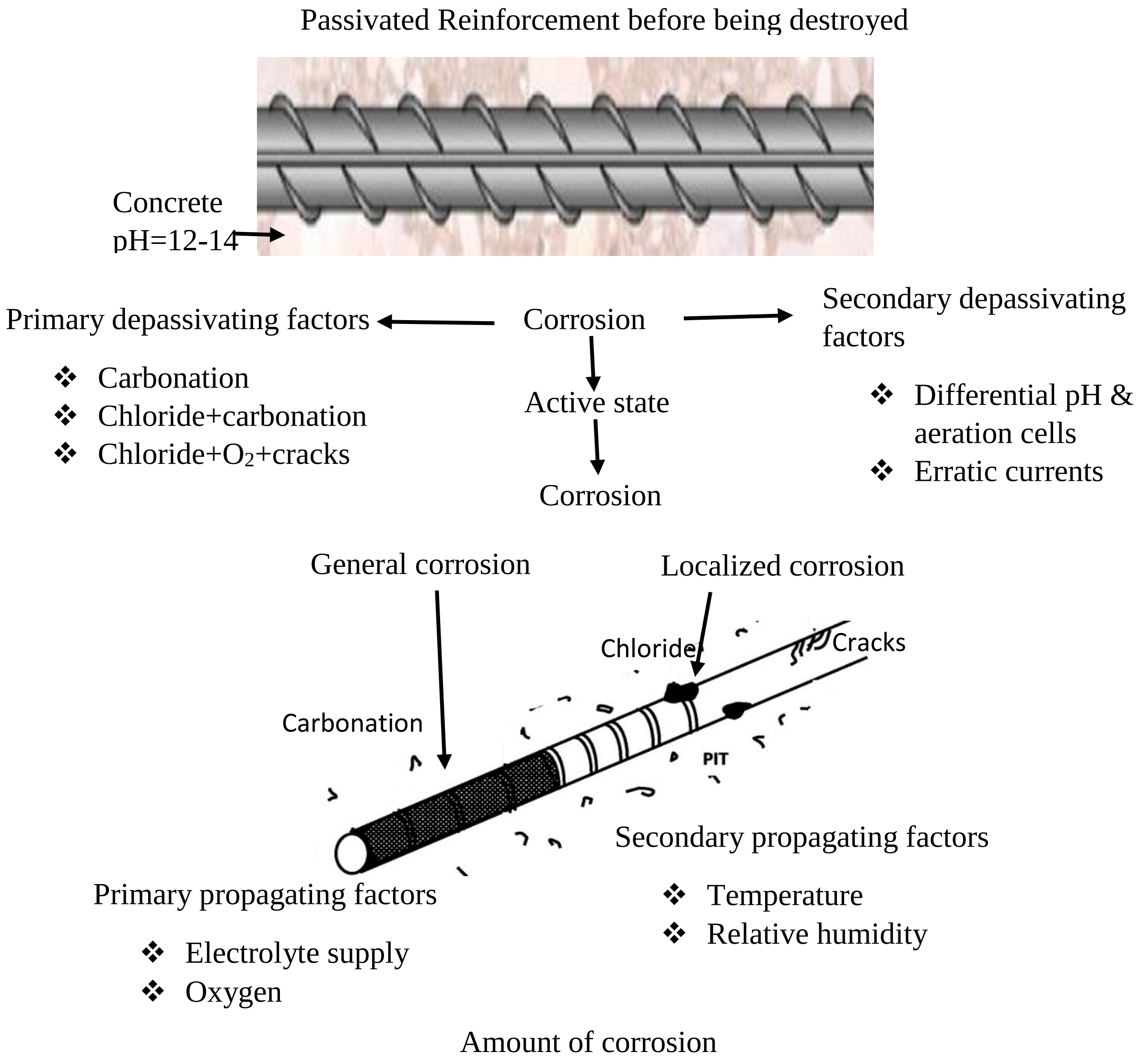

Figure 2.4: Schematic diagram showing corrosion that has been induced by carbonation and chloride [74]

2.6 Localised corrosion

Passive film flexibility for shielding the metal is known to be potentially compromised when different halides or chlorides are present [81] [82] [79]. Those aggressive ions produce a passive film breakdown area that accelerates the dissolution of the underlying steel alloy. If the attack starts upon a concave surface, it is known as corrosion; if impeded, it is known as crevice type corrosion [79] [82]. Once it has started, an attack has similar characteristics geometrically, i.e. a pit. There is no clear understanding of the mechanisms involved in a breakdown initiation in an otherwise protective kind of passive film. However, various theories have been put forward to break down the passive film and the initiation of pitting [83]. Figure 2.5 shows pit propagation for steel within the concrete in the presence of chloride ions [83].

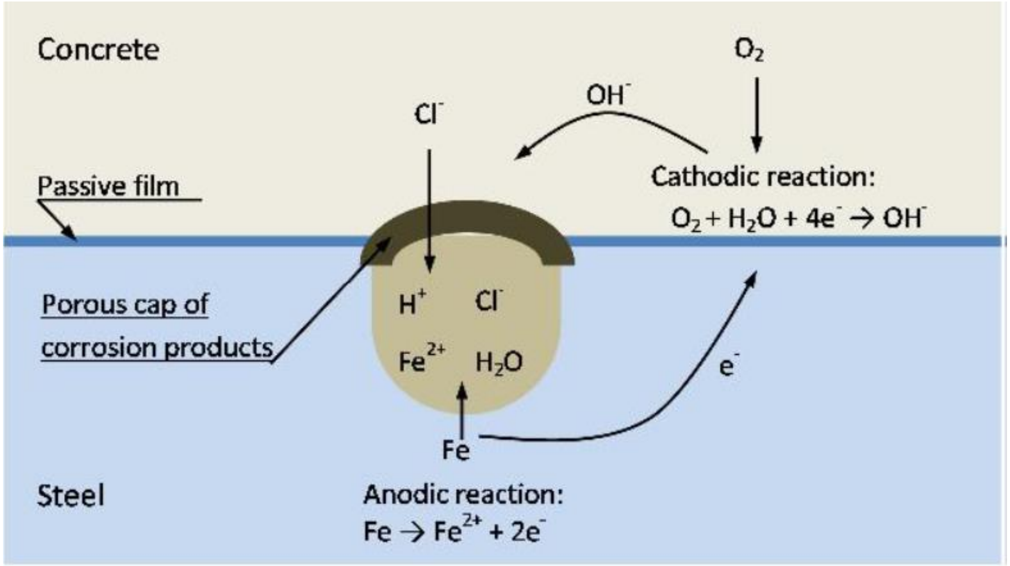

Figure 2.5: Propagation stage of the pitting of steel embedded within concrete [77]

The steel area unprotected by the passive film may start to act as forms of anodes when there has been the initiation of pitting corrosion upon steel embedding within the concrete, whilst passive areas nearby remain passive. They may begin to act as forms of the cathode, and they are sites where oxygen is reduced [84]. When chlorides are present in sufficient concentration above the critical level, the passive layer on the surface of steel bars is destroyed, causing localised deterioration on the surface of the steel. This type of deterioration is known as pitting corrosion, in which the anodic zones are concentrated in those pits [79]. The result is that the accumulated metal ions can endure the chemical reaction. There is a development of an acidic area within the pitting region that makes the surroundings very aggressive. Finally, to account for charge neutrality, there is the migration of chloride ions across to pit electrolytes from the majority of the solution. Pitting corrosion is typically seen on passive metals and alloys such as aluminium alloys, stainless steels, and stainless alloys when chemically or mechanically damaged and not immediately re-passivated by the ultra-thin passive film [79]. The standard potential is between the passive steel as a natural anode, typically with -200 to -500 mV (SCE) [85].

2.7 Concentrations of chloride

Critically for chloride ions, a particular concentration is needed for the destruction of the steel surface passive film for the steel embedded within concrete, and it is dependent mainly on the pore solution pH; a higher level of ions of OH- within concrete initiates an increase in corrosion [86]. The problem of chloride attack usually increases when the chloride ions ingress from outside. Two significant sources of chloride ions are de-icing salt and seawater in contact with concrete. A more common transport method is absorption. As a concrete surface is exposed to the environment, it will undergo wetting and drying cycles. When water, probably containing chlorides, encounters a dry surface, it will be drawn into the pore structure through capillary pressure. A researcher has shown that limits on the total chloride ion content in reinforced concrete should be 0.4% by mass of cement; see Figure 2.3 in Section 2.4 above [75]. There needs to be penetration of chloride, however, for corrosion to start. The half-cell and associated measurements are the most common method for determining steel corrosion potential within reinforced concrete without destroying the specimen structure [87]. The transport rate of chloride ions within a concrete structure is mainly defined by the concrete porosity, which depends upon void and compaction volume. The degree of moisture and the w/c ratio have significantly impacted capillaries' presence and pores' structure. As a result, a rise in the w/c ratio leads to a non-linear increase in permeability, especially for w/c values greater than 0.5 [86]. The test for initial surface absorption (ISAT) was originally developed for the measure concrete porosity [88]. The concrete cover, however, affects the rate of transportation. The ultrasonic pulse velocity (UAPV) is used on concrete as a non-destructive test to assess the integrity and homogeneity of the concrete. If there is a low velocity of ultrasonic pulse and high porosity, then the transportation rate will take place more quickly [89].

Several recent studies have investigated various modern techniques for monitoring the attack of chloride on structures built from reinforced concrete within various industries; the limitations and advantages of different approaches are discussed in detail in the section below.

2.7.1 The potentiometric sensor or ion-selective electrode

The potentiometric sensor or ion-selective electrode (ISE) can determine free chloride ions and, as such, it is possible to avoid destructive and chemical tests. When used in the field, the device has embedded sensors to detect chloride concentration amounts by the rebar in a way that does not change the surrounding environment. If chemical and practical factors are considered, there certainly are some advantages to ISE. For instance, ISE shows chemical stability in aggressive environments, and it is easy to fabricate through electrochemical processes. It is possible to adapt to other kinds of sensors to measure different parameters such as temperature and the presence of ions [90]. However, it should be noted that it may induce measurement errors;

therefore, due consideration needs to be given to temperature, alkalinity, presence of electric fields, and the previously made calibration. High temperatures may lead to shifts in measurement [90]. High pore solution alkalinity may interfere with the ISE potentiometric response, mainly with low chloride concentrations [91]. The presence of an electrical field because of corrosion, extraction of chloride, and the cathodic protection for other sensors produce shifts in the probable measurements of difference. Lastly, since RE (reference electrode) is required, it has to show stability over the long term; this cannot be done, however, except under strict experimental conditions [92]. Figure 2.6 illustrates that for the electrical potential difference to be measured, there is a need for the ISE to be complemented by a reference electrode (RE) which is usually a calomel type [93].

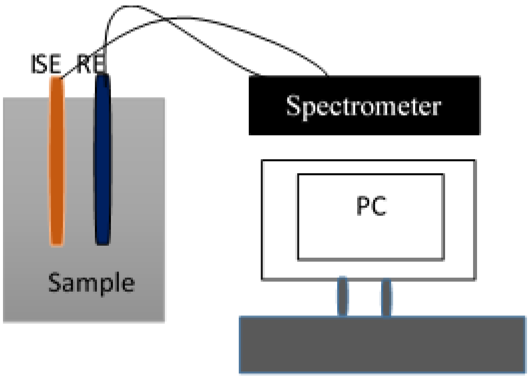

Figure 2.6: Block diagram based upon the ISE method [87]

2.7.2 Electrical resistivity

The electrical resistivity (ER) has been linked to RC corrosion and moisture and heat transfer in the concrete and, more recently, to chloride ion presence [94]. The technique of ER has a link to chloride ingress as chloride presence can increase electrical current and result in a concrete resistivity reduction [95]. So, ER may be employed in estimating the profile of chloride by determining the coefficients of chloride diffusion. The method entails applying a voltage to measure current flow, followed by determining electrical resistance using Ohm's law's proportionality for electrical resistivity, as shown in Eq [96].

$$V = IR$$

$$R = \frac{A}{l}\rho \qquad \text{Eq (2.4)}$$

were

I is the electrical current, A the surface area through which the current passes m^2, ρ Electrical resistivity, R Electrical resistance, V Potential difference, and the length m.

Electric current: is defined as the rate at which charge flows through a surface (the cross-section of a wire, for example).

Cross-section area A: is the amount of charge passing through a surface.

Electrical resistivity: is unique to every material, which is essential to understand before creating and designing electrical and electronic systems.

Resistance (R): is a property of a material used for describing the opposition provided to the flow of current. The higher the resistance provided by a material, the lower the flow of electrons or current through the material.

Potential difference: is the amount of energy that charge carriers have between two points in a circuit.

l the length; is the electrical resistance of a wire, would be expected to be greater for a longer wire, less for a wire of larger cross-sectional area, and would be expected to depend upon the material out of which the wire is made.

The unique characteristic of electrical resistivity is inherent for every material, dependent upon experimental conditions. Figure 2.7 shows two techniques for the resistivity measurement to assess the corrosion through the use of a Wenner array [96]. Due to concerns of geometrical position, electrode contact number, and the space between them and the distance to the rebar, we did not propose to utilise it for chloride measurement [97]. Another proposed device is multi-electrode resistivity, a device comprising of two probes with one mobile and the other embedded. The method is effective, as is the Wenner array technique; it does need, however, moisture to improve measurements [98]. According to the research results, the method may only be employed in the exploration of the diffusivity of chloride, and resistivity depends upon cement type and degree of hydration. For most ER techniques, concrete surfaces have to be wet as the conductivity of dry concrete is zero. Furthermore, for repeatability and accuracy to be ensured, calibration ought to be discovered for various moisture levels. Measurements also rely upon the reinforcing geometry and structure; however, the method has extreme sensitivity to moisture content within the elements of the building and is easy and quick to undertake [99].

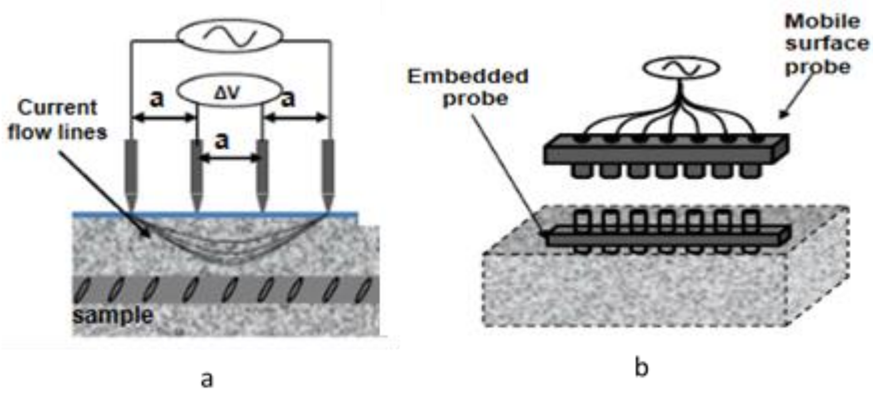

Figure 2.7: Techniques based on ER method (a) Wenner array, (b) Multi-electrode resistivity probes [91]

2.7.3 Optical fibre sensors

There are several advantages to the optical fibre sensors (OFS) method compared to some other methods. Since it has a higher degree of sensitivity to low chloride concentrations, it saves energy, and the presence of fields of electromagnetism do not influence the measurements [35]. Also, sensor sharing is more convenient in larger structural applications due to the long and thin geometry and capacity for coping with surroundings. The outcome is that, as each fibre segment may perform as a sensor, there can be the detection of slight defects for any part of the structure [100]. Figure 2.8 shows an analyser of the optical spectrum giving the spectra of transmission employed in estimating the refractive index.

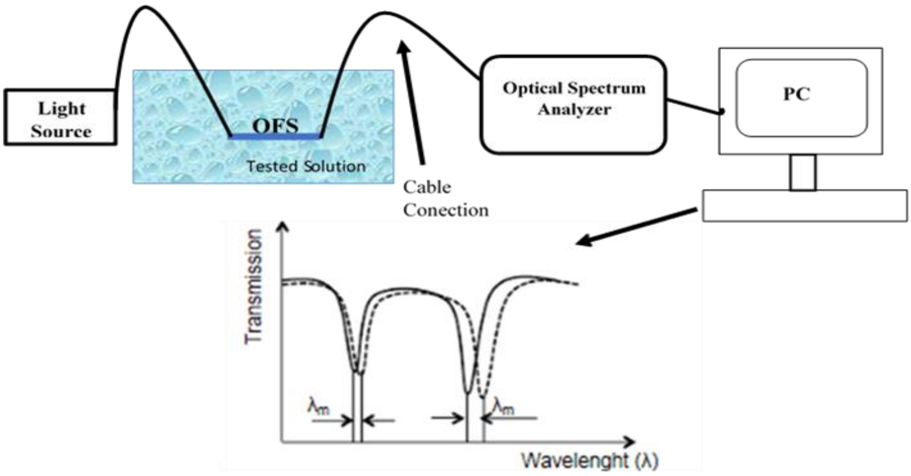

Figure 2.8: Optical fibre sensor diagram [100].

There are, however, essential considerations if seeking to make measurements that are reliable and accurate. For instance, adequate optical fibre protection needs to be done to prevent breakage during casting or service life. The protection needs to permit light transmission without obstruction or bending of optical fibre since that would lead to data being missed [101].

2.7.4 Ground-penetrating radar

Ground penetration radar GPR is a technique closer to ultrasonic pulse-echo methods and microwave spectroscopy, differing only by the kind of energy used and single frequency. In simple terms, the antenna sends short electromagnetic energy pulses of the high nominal centre frequency (0.5-2GHz) into the ground (pulse systems). Depending on the application, they may represent any medium to air, such as natural ground, concrete structures, masonry structures, pavement or bridge decks [102]. The antenna represents a transition device between a guided wave and a free space wave. The transmission line transports electromagnetic energy to or from the antenna. In the first case, it works as a transmitter and in the second as a receiver. When the dielectric properties of two consecutive layers produce enough contrast, the transmitted energy is partially reflected at the boundary surface. The remainder is transmitted and refracted at the same interface before continuing propagation through the next layer until it finds a new interface, at which point the process is repeated.

GPR has proved to be a powerful tool in investigating a wide range of applications, particularly as an NDT technique, using high-resolution antennas (> 500MHz). Radar has had varying levels of success in locating and detecting reinforced bars, metallics, and plastics, detecting moisture and voids, detecting chlorides, estimating pavement and structural thickness, and identifying building details. A maximum frequency should be proposed in GPR surveys to prevent clutter. It suggests that the wavelength should be ten times larger than the characteristic dimension for geological materials [103]. Figure 2.9 shows the possible path of the radar wave emitted from the GPR antenna. This demonstrates that some of the electromagnetic EM wave's energy passes through the asphalt and deck concrete layers. In contrast, the remaining EM waves are reflected from the boundary at different permittivity. Hence, the reflected EM wave is detected by the receiving antenna of the GPR system and stored for data analysis. Therefore, the reflected EM wave analysis detects underground cavities, layer thickness, and rebar location [104]. The method is based on the principle that deteriorated concrete with higher water content and chloride concentration would exhibit higher energy attenuation than the sound area. Many researchers have verified that the in-situ testing method is effective in assessing the condition of concrete bridge decks[105] [106] [107]. Moreover, several researchers have demonstrated the feasibility of GPR as an in-situ NDE method to evaluate the depth of chloride-induced deterioration of concrete in bridge decks [108].

However, this technique has limitations to be considered, which probably explains why radar has not had success in many applications; limitations such as it requires considerable personnel expertise to operate the equipment; interpretations of data are still in many cases comparative in nature, often necessitating visual inspection and drilling, coring excavation; frequently requires sophisticated signal processing when the data present high noise level or complex signatures [40, 109]. The signal does not always improve the results significantly and thus is not always economically justifiable. The commercial systems available are still quite expensive, restricting their availability as an NDT technique for most potential users in the civil engineering field. The radiated energy is not like a laser beam, and it diverges with angles depending on the electrical properties of the medium [110].

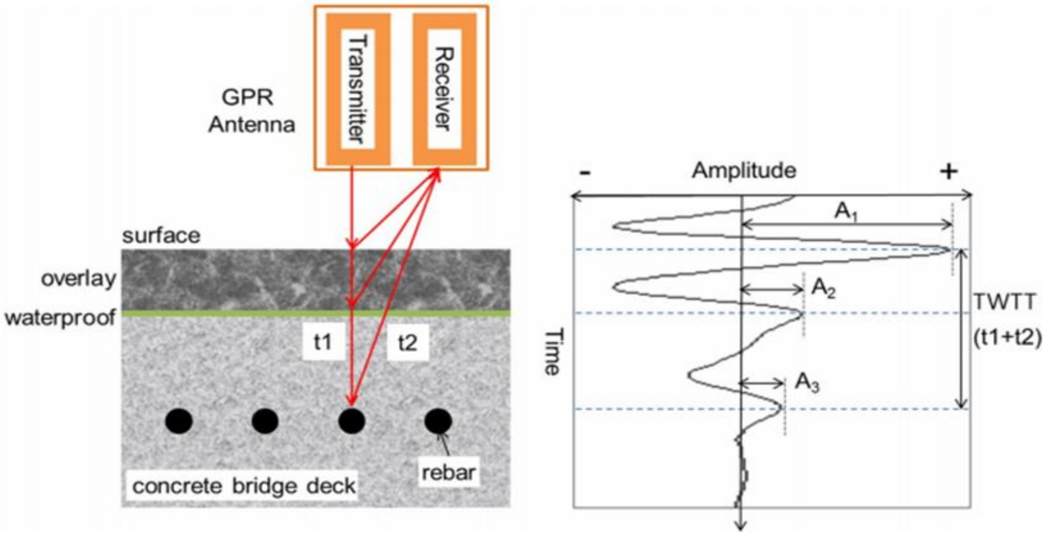

Figure 2.9: GPR scanning on a concrete bridge deck and a possible path of EM waves penetrating the concrete cover [105].

2.7.5 Chlorimeter tool

The tool known as the chlorimeter is a gold standard technique with the now-common use of model no. C-CL-3000 within the industry is a kind of destructive method for detecting chloride amounts within concrete samples. The system of chlorimeter testing offers an accurate and fast way of determining the total content of chloride within concrete. One can undertake the test to detect chloride ion presence within the concrete and the respective penetration of ions. Chlorimeter tool accuracy has a broad range per unit weight from 0.002% - 2% chloride. The device limitations are that a partially destructive drill hole is required during the testing, it is time-consuming, there is a high cost to the chloride liquid used, repair and maintenance are needed, and the main concrete quality will decrease. Figure 2.10 shows a chlorimeter kit [111].

Figure 2.10: Chlorimeter tool for the chloride field test system [106]

2.8 Corrosion potential

The following test is used to measure the corrosion potential of reinforced concrete.

2.8.1 Half-cell potential

Reinforcing steel corrosion is an electrochemical process. The behaviour of the steel can be assessed using a half-cell potential measurement, the higher the potential, the higher the danger of corrosion. Several components may affect resulting accuracy and should follow many steps and procedures to acquire correct readings. There then needs to be careful concrete cover removal over the bar in question followed by a half-cell connection with a reinforcing bar using a digital voltmeter. This is an NDT method; as preparation is needed, it can be problematic, and the testing itself can be time-consuming, and there can be a lack of accuracy in the results. The basic measurement elements are shown in Figure 2.11 [112]

.

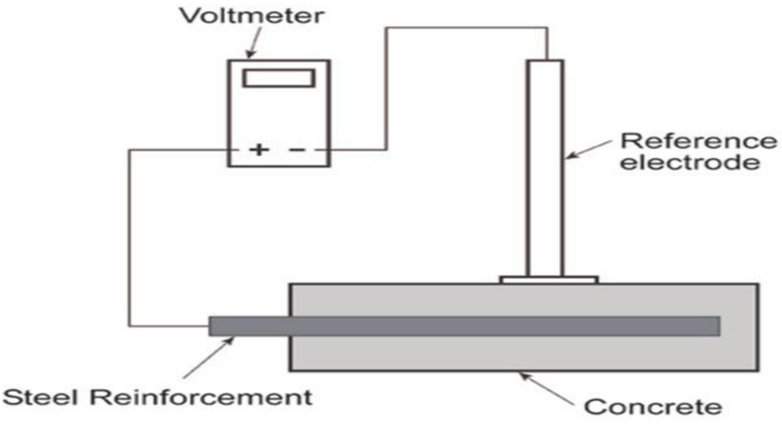

Figure 2.11: A potential technique for half-cell measurement [112]

Table 2.3: Corrosion probability under half-cell reading [112]

Half-cell potential reading, Vs.Cu/cuSo$_4$	**Corrosion activity**
Less negative than -0.200V	90% Probability of no corrosion
Between -0.200V and -0.350V	An increasing probability of corrosion
More negative than -0.350V	90% probability of corrosion

2.8.2 Ultrasonic Pulse Velocity

The ultrasonic pulse velocity (UPV) method may be employed in concrete testing to determine concrete uniformity and the voids, cracks, and cavities present. Material pulse velocity depends upon its elastic properties and density, and these are related to the compressive strength and quality of the concrete. UPV also has applicability concerning the indication of changes in concrete properties. The UPV test can also detect physical deterioration of the concrete structural capabilities. However, the method is limited in that the wave is unable to transmit through a gap [113]. A transmitting transducer is used to create ultrasonic waves, and a receiving transducer is used to receive these waves. The travel time of these waves from one point to another point is measured. The distance measured between these points plays a vital role in the case of the indirect method of transmission.

Table 2.4 shows electromagnetic (EM) waves compared to the current techniques used to detect the level of chloride in concrete structures, with the advantages and limitations of each technique briefly described

Table 2.4: EM techniques in comparison to state-of-the-art techniques to monitor chloride level

Parameter Measured	Detection Methods	Advantages	Limitation	Principle
Determined free chloride in concrete structures	Ion Selective electrode (ISE),[94]	It shows chemical stability in the aggressive environment; the fabrication is easy, through an electrochemical process, it can be adapted to other sensors for measuring other parameters (e.g., temperature, ions presence)	The accuracy of this method is dependent on various factors such as temperature, alkalinity, and electric field presence.	The device is inserted near the rebar. Therefore, this is a partially destructive method requiring drilling into the concrete sample
	Electrical Resistivity (ER) [95, 99]	This method can be used to estimate the chloride profiles by determining the chloride diffusion coefficient.	The measurements are sensitive to the moisture content, which affects the accuracy of the results.	The device is inserted near the rebar. Therefore, this is a partially destructive method requiring drilling into the concrete sample.
	Optical Fibre Sensor [101, 114]	It is energy saving. It is very sensitive to small chloride concentrations, but the measurements are not affected by the electromagnetic field. The sensor is better applicable to large structural applications.	Optical fibre needs adequate protection to prevent its breakage during casting or service life. Temperature variation can affect accuracy.	This method involves detecting the refractive index shift due to the chloride presence that changes light behaviour. This sensor is embedded into the structure for continuous monitoring.
Corrosion rate, percentage of corrosion, corrosion progress	Half-cell potential [114]	The simple, portable device, which produces chloride concentration contour mapping via the data logger.	Needs preparation, a saturation of the concrete surface required along with the electrical connection to the steel reinforcement, It is not very accurate and is time-consuming	The electric potential of the rebar is measured by half-cell and indicates the probability of corrosion.
Permeability test	Initial Surface Absorption Test (ISAT) [88]	Simple interpretation and moderate cost	The accuracy results are affected by moisture content, Concrete mix, aggregate, age of concrete, cracking, water type curing, and temperature.	The technique is based on the measurement of volume flow into a test specimen with known surface area.
Compressive strength, permeability surface hardness, adhesion	Ultrasonic Pulse Velocity (UPV) [113]	Quick, portable larger penetration depth, simple interpretation, and moderate cost.	Not very reliable, because the wave cannot transmit through the gaps and the presence of reinforcement can affect results	Ultrasonic wave velocity and its attenuation

Determine of location reinforcement, moisture content, location of chloride,	Ground penetrating radar (GPR) [40, 115]	It can be used to survey large areas rapidly for locating reinforcement, voids, and cracks. It is capable of detecting several parameters in reinforced concrete structures: location of the reinforcement, the depth of cover, the location of cracks, moisture content, and variations	Results must be correlated to test results on samples obtained. Any features screened by steel reinforcement will not be recorded. With increasing depth, low-level signals from small targets are harder to detect due to signal attenuation. It is expensive to use and uneconomical for surveying small areas.	Radiofrequency waves (0.5 to 2GHz) from the radar transmitter are directed into the material. The waves propagate through the material until a boundary of different electrical characteristics is encountered. Then part of the incident energy is reflected and the remainder travels across the boundary at a new velocity. The reflected (echo) wave is picked up by a receiver. The transducer is drawn over a surface and forms a continuous profile of the material condition below. The equipment consists of a radar console, a graphic scanning recorder, and a combined transmitting and receiving transducer.
Determine of chloride, Partial destructive	Chlorimeter device [111]	The Chlorimeter test system offers a fast and accurate determination of the total chloride content in concrete. Only a small area of the concrete can be tested	Need preparation, during the test, time-consuming, high cost of extraction chloride liquid	The device is a partially destructive method requiring drilling into the concrete sample.
Determine of chloride, Non-destructive method	Electromagnetic (EM) wave methods	Electromagnetic (EM) wave has high penetration, is a relatively low cost, it’s got a very good flexible sensor design to suit the application and <1 minute time-consuming.	Not used for detecting chloride ions in the industry yet	The device is providing a non-destructive measurement method in a real-time manner.

2.9 Summary

Within Chapter 2, a literature review has detailed studies into chloride content level within concrete structures. The choice of design and the practice in construction have a significant bearing on the level of durability for structures of reinforced concrete that have exposure to very aggressive environments such as with contamination from chlorides. Deterioration because of chloride is one of the two primary types of corrosion for reinforcement, i.e. typical corrosion and pitting corrosion. Structures such as bridges are prone to pitting corrosion when located close to exposure to seawater. If there is a splash zone close to the interface between air and water, the splash zone is, in fact, very critical for the safety of such structures. Corrosion of rebar within a concrete structure is a time-consuming chemical process. It suggests that it occurs indirectly through coupled half-cells and chemical science reactions involving the passage of electrical charge rather than directly through the metal having a chemical reaction with its surroundings.

Chloride ions initiate the corrosion process upon the steel through their localisation at a specific steel part and then depletion at the steel surface because of the concrete's aggressive environment. The problem of chloride attack usually increases when the chloride ions ingress from outside. Two critical sources of chloride ions are de-icing salt and seawater in contact with concrete. The aggressive ions produce a breakdown area in the passive film that leads to the dissolution of metal that underlies it in an accelerated way. If such an attack is impeded, it is known as crevice corrosion. The presence of chloride ions in concrete may hail from both internal and external sources. External sources may include salts used for de-icing, i.e. melting ice on roads and bridges, and salts within seawater if a structure is located in a marine environment. Several methods of NDT are currently available that can be employed in detecting chloride levels and corrosion within steel-reinforced concrete. Limitations and advantages of a number of the current techniques have been described briefly here within this chapter. Based on the limitations of existing approaches, there must be further development. This research aims to address those limitations using a novel technique of EM waves for the determination of chloride ion levels within concrete structures with different concentrations of salt water in a way that is reliable, real-time, and non-destructive.

Chapter Three: Use of Artificial Neural Networks

This chapter will begin by focusing on an Artificial Neural Network ANN method in general. Then, concentrate on the ANN model design and activation and transfer function in detail , followed by a further critical review of the use of a single-layer feed-forward network and multilayer feed-forward networks. This chapter will introduce classification techniques used such as the WEKA method in detail, followed by a further critical review of related studies of ANNs used and classifications approaches in different contexts, including the numerous geotechnical engineering specialities areas. Finally, a summary of the key findings of the literature review will be provided.

3.1 Introduction

Artificial neural networks (ANNs) are computational models, which attempt to represent the biological structures of the human brain and its nervous system. It is possible to track composite structures using damage assessment techniques, detect and localise possible imperfections in curtain wall systems, and monitor structural health through damage-induced changes with the cooperation of ANNs. They have the potential to properly implement difficult tasks, such as function approximation and classification and pattern recognition [116]. ANNs comprise interconnected processing elements (PEs). The PEs receive input indicators (Xi 1, Xi-2,…..Xi-n) (see Figure 3.1) from either external sources or perhaps adjacent PEs, then transfer these to blinkers in the next layer by the method of an activation feature (AF). A vector of IVs could represent the layer input. In an attempt to fix problems, the proposed unit should be trained. The strategies of training might generally be categorised into two types: supervised and non-supervised.

The supervised training model is based on a comparison between the selected input variables and the output model. This learning method is usually formulated when the mistake feature, such as the mean square error between the measured and the expected values, is summed over all available data. In contrast, the non-supervised type is entirely dependent on the correlations among entering data. Throughout the learning process, the i^{th} level outputs are multiplied by an optimised vector, the so-called link weight (w_{ij}). Subsequently, the newest is added in and together they have a threshold bias and are later summarised before being used as inputs to the following PE within the next i^{th} level. The PEs in hidden layers and the output layers will be identified using an activation feature, which is brought to the input and creates the valuation of the i^{th} processing aspect in the output layer. It should say that a bias doesn't include an activation function and has a specific value-driven value throughout the training process along with the importance value of the synaptic interconnection weights [117]. Both the wij and the biases are kept up to date during the learning process, reducing the overall error between the actual and predicted values. An essential fact of significant importance is that these layers' optimum setup is calculated using a range of steps. More precisely, these phases may be summarised as:

1) The variety of input model parameters.
2) The maximum number of hidden layers.
3) The number of unit outputs.
4) The number of processing elements (PEs).
5) The computing performance indicator.
6) The set of activation functions (linear or non-linear).

The type of training algorithm is one of the most important features that play a crucial role in the performance of ANNs [118]. Indeed, following the model's configuration, other essential aspects need to be specified, such as the standardisation mechanism and the data set division process, to prevent over-fitting and ensure the trained network's strong generalisation capability [119]. It is notable that Rumelhart et al. (1986) initially introduced a definition of ANN [120].

3.2 ANN model design

The framework of the ANN has been discussed by many researchers [121] [122] [123]. ANNs consist of a variety of artificial neurons known differently as processing elements nodes (PEs). In the multilayer perceptron (MLP) approach, which is the most frequently utilised ANN in the field of geotechnical engineering, usually, processing components are assembled in layers. These consist of an output layer and an input layer and one or perhaps more intermediate layers identified as hidden layers as exposed in Figure 3.1.

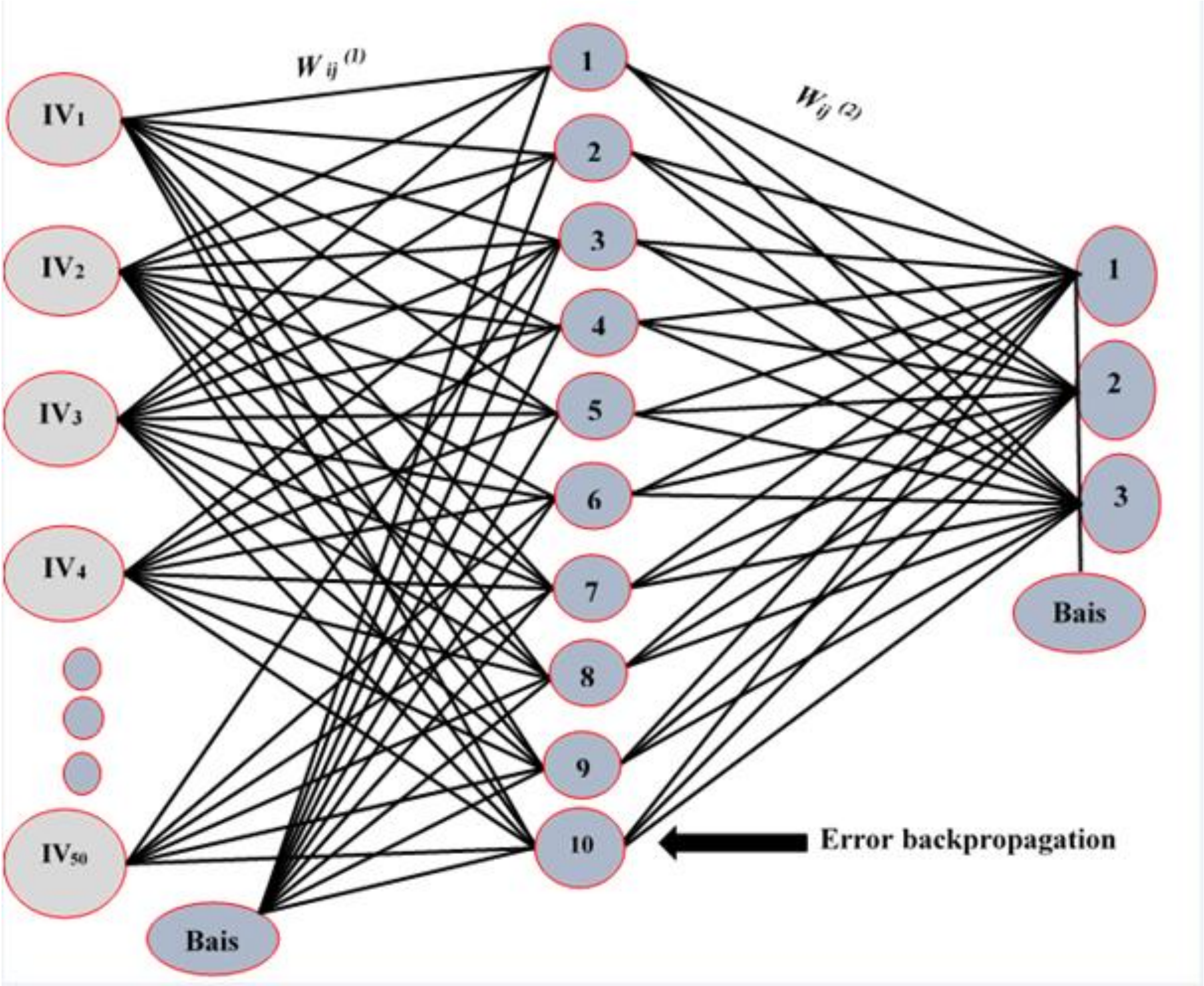

Figure 3.1: Schematic structure of ANN model inputs and output variables

The scalar weights figure out the strength of the contact between interconnected nodes [124]. An individual processing unit sums its weighted input connections and applies a bias or a threshold device. However, reducing the percentage of error between the validated value and the target values of the neural training network that the bias unit, generally provides to scale the input to a value range to improve convergence properties. The put together values of the independent variables (IVs) processed out of the very first level are then passed by way of a transfer function (TF) to create the output of the processing component. The TF maps a set of (IVs) to a finite output range. The process described is summarised in Equations 3.1 and 3.2, respectively.

$$\mathrm{I_j} = \sum_{\mathrm{i}}^{\mathrm{n}} \mathrm{w}_{\mathrm{ij}}^{(1)} \mathrm{IV_i} \pm \mathrm{b}^{(1)} \qquad \text{Eq (3.1)}$$

$$\mathrm{y} = \sum_{\mathrm{i=1}}^{\mathrm{n}} \mathrm{w}_{\mathrm{j}}^{(2)} \mathrm{I_j} \pm \mathrm{b}^{(2)} \qquad \text{Eq (3.2)}$$

Were

n is the number of independent variables, I_J the node activation level, the factors $\mathrm{b}^{(1)}$and $\mathrm{w}_{\mathrm{ij}}^{(1)}$ are the weights and biases from the input and output of the hidden layer, $\mathrm{b}^{(2)}$ and $\mathrm{w}_{\mathrm{j}}^{(2)}$ are the weight and the bias for the second layer.

3.2.1 Activation or transfer functions

Transfer functions (TFs) can have a selection of forms. The logarithmic, hyperbolic tangent sigmoid (tansig), sigmoid (logsig), bipolar sigmoid, and radial basis (radbas) transfer operators are in most cases commonly utilised transfer operators in artificial neural networks. The primary key objective would be to transfer the weighted value of all signals hitting the processing component to determine its firing intensity [125]. The log-sigmoid transfer functionality is generally utilised once the desired production values are to the caps of zero and +1. In contrast, the tan-sigmoid is usually used when the selected paper values are between -1 and +1 [126]. The hyperbolic tangent and the logistic sigmoid transfer capabilities are seen in Figure 3.2, the process described in Equations 3.3-3.5, respectively.

$$f(\mathrm{I}_j) = \frac{1}{1+e^{-(I_j)}} \qquad \text{Eq (3.3)}$$

$$f(\mathrm{I}_j) = \frac{e^{(I_j)}-e^{-(I_j)}}{e^{(I_j)}+e^{-(I_j)}} \qquad \text{Eq (3.4)}$$

$$\mathrm{y} = \sum_{\mathrm{i=1}}^{\mathrm{n}} \mathrm{w}_{\mathrm{i}}^{(\mathrm{j})} f(\mathrm{I}_j) \pm \mathrm{b}^{(\mathrm{j})} \qquad \text{Eq (3.5)}$$

Were,

$f(\mathrm{I}_j)$ transfer function, $\mathrm{b}^{(\mathrm{j})}$and $\mathrm{w}_{\mathrm{i}}^{(\mathrm{j})}$ artificial connections bias and weights between the input values and output values (hidden) layer.

A transfer function: Represents the relationship between the output signal of a control system and the input signal, for all possible input values.

Bias: Bias is used for shifting the activation function towards left or right, it can be referred to as a y-intercept in the line equation.

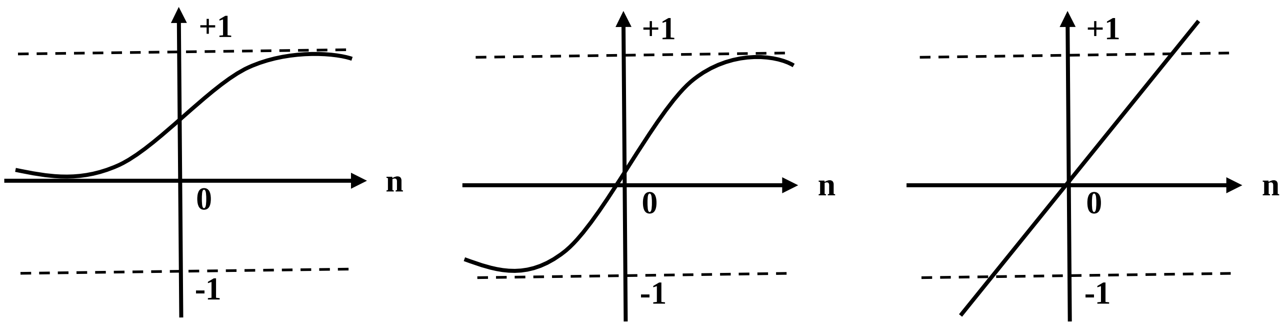

a) Log-Sigmoid b) Tan-Sigmoid c) Linear

Figure 3.2: Procedures of the commonly used ANN transfer functions

For the purposes of used ANNs, the following definitions need to be considered:

(1) Inputs: An input vector is one input to the system usually written as vector x where x_i = one element, I = (1,…..,m).

(2) Weights: w_{ij} is the weighted connection between nodes I and j. Modelled after synapses in a nervous system and arranged as matrix w.

(3) Outputs: An output vector y is the output vector y_i = one element, j = (1,….,n), formally y(x,w) since the vector is a function of x and w.

(4) Hidden layer: A hidden layer in an artificial neural network is a layer in between input layers and output layers, where artificial neurons take in a set of weighted inputs and produce an output through an activation function.

(5) Targets: A target vector t contains extra data needed for supervised learning – contains the "correct" or training data. Note that t_j = one element, j = (1,…..,n).

(6) Activation function: A mathematical function, usually given as g() for gain or conductance, describes the neuron's firing in response to the weighted inputs. Often a simple binary decision or threshold. If the sum of $w_{ij}x_i$ coming to node y_j exceeds a threshold, provide output = 1; else, output = 0. Formally, A = f(x,w).

(7) Error: Usually a function, E, computes the network's inaccuracies as a function of targets t and output y; that is, E= f(t,y).

3.3. Neurons

Neurons are the most precise units of processing within an ANN. The perceptron is an example of a model of a neuron put forward in 1958 by Rosenblatt; thought of as the model of neurons that brought about the development of ANNs [127]. The general structure for the perceptron is shown in Figure 3.3.

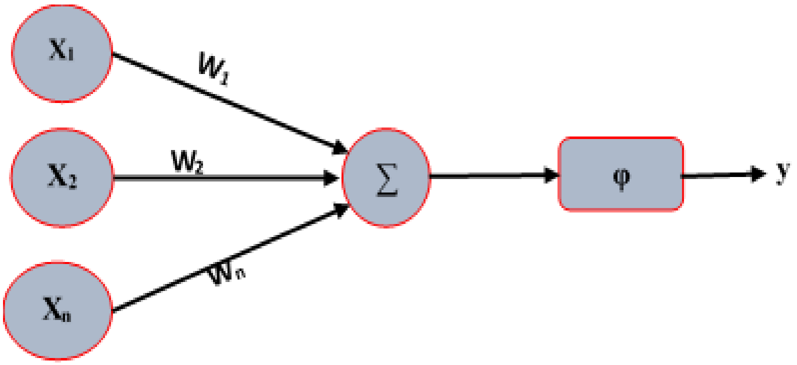

Figure 3.3: Schematic diagram of a perceptron neuron

$$y = \varphi(\textstyle\sum_{N=1}^{n} w_n . x_n + b) \qquad \text{Eq (3.6)}$$

where,

(X_n) input values, (Wn) weights and (b) bias values, (φ) the activation function, and (y) the output value.

Equation 3.6 shows the activation function or transfer for a perceptron. A perceptron initially performs a linear input value combination (X_n) and the weights and bias (∑) value. Then, the activation function (φ) is applied to the linear combination (∑) results to obtain (y) (the output value). Nonetheless, there are currently many different functions of activation put forward for the implementation of perceptrons, such as sigmoid functions, saturating functions, and linear functions [128].

3.3.1 The Single-layer feed-forward network.

In this particular type of ANN structure, a neural network encompasses just one layer of computational processing element (PE) If no feedback is received from the neurons' outputs to inputs across the network, the network is referred to as a single layer feed-forward network. A set of nodes creates an input layer that acts as a middleman between the single layer of neurons and the input layer sources in the surrounding environment to provide these PEs with their input signals. It's essential to emphasise that absolutely no computations are applied in input nodes [130]. Within this network type, there is the availability of two types of neurons as shown in Figure 3.4, a single layer fully connected feed-forward neural network is displayed. As shown in Figure 3.4, only two kinds of neurons are available in this network: input neurons that send input signals to the output layer and output neurons that use the same transfer function to compute their outputs. However, the input layer does not count because there are no computations performed in that layer. Input signals transmit via weights to the output layer, and the neurons in the output layer compute output signals [131] [132]. As such, both the transfer and input functions flow just one way; this is why this kind of application of ANN structure may strictly only be of the forward type, beginning from input nodes in the direction of the network output [133].

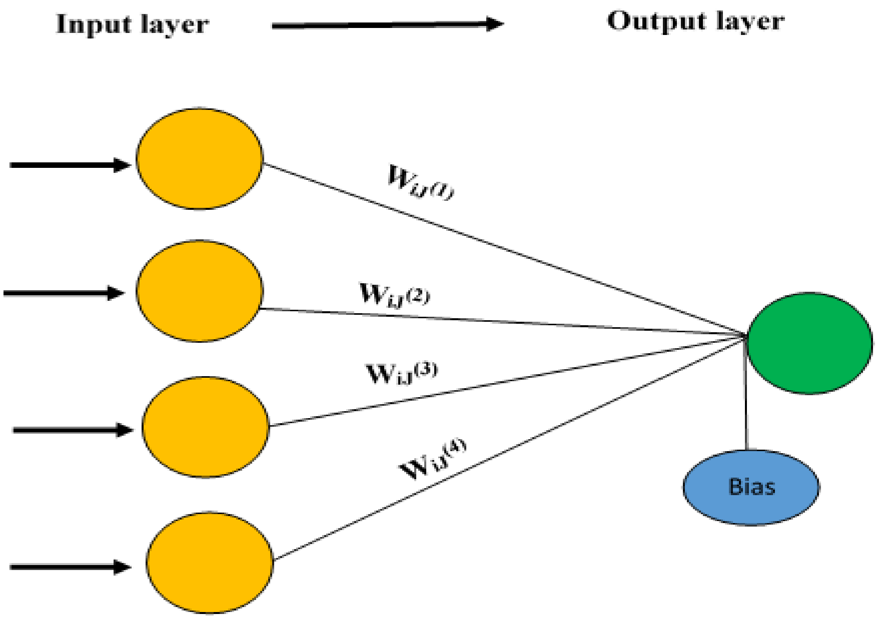

Figure 3.4: Single-layer feed-forward network design

3.3.2 The multilayer feed-forward networks

Multilayer feedforward networks are utilised to overcome computational boundaries and knowledge limitations within a single layer network [129]. The architecture of these networks is such that it is just an extension updated from the previous artificial structure for the neural network. There is an introduction of more layers between the input and output layers. Those layers are hidden, and so they are known, unsurprisingly, as hidden layers. The introduction of hidden layers leads to neural networks being superior to most algorithms of machine learning. Just one hidden layer brings a sufficiency for most problems. Usually, the same neuron number is contained in each of the hidden layers. The presence of one or more hidden layers helps the network to collect statistics of a higher order. There is only one hidden layer for the example given in Figure 3.5, and the network is referred to as a 5-10-3 network because there are five input neurons, ten hidden neurons, and three output neurons. The networks are fully connected in both Figure 3.4 and Figure 3.5 because, in the following forward layer, every neuron in each layer connects to each other's neurons.

The network would be known as partially connected if some of the synaptic connections were missing. A multilayer perceptron is a class of feedforward artificial neural networks. The term MLP or particular layer nodes is used ambiguously [134]. Generally, the function of activation is non-linear within the units of the practically hidden layer. As such, about high-level kinds of interaction between input parameter signals, the non-linearity between dependents and independents is allowed [135] [136]. In Figure 3.5, a multilayer neural feedforward network with one hidden layer is seen. There is at least one layer of hidden neurons between the input and output layers instead of a single layer network. According to Haykin (1999), the role of hidden neurons is to interfere in some useful manner between the external input and the network output [137] [132].

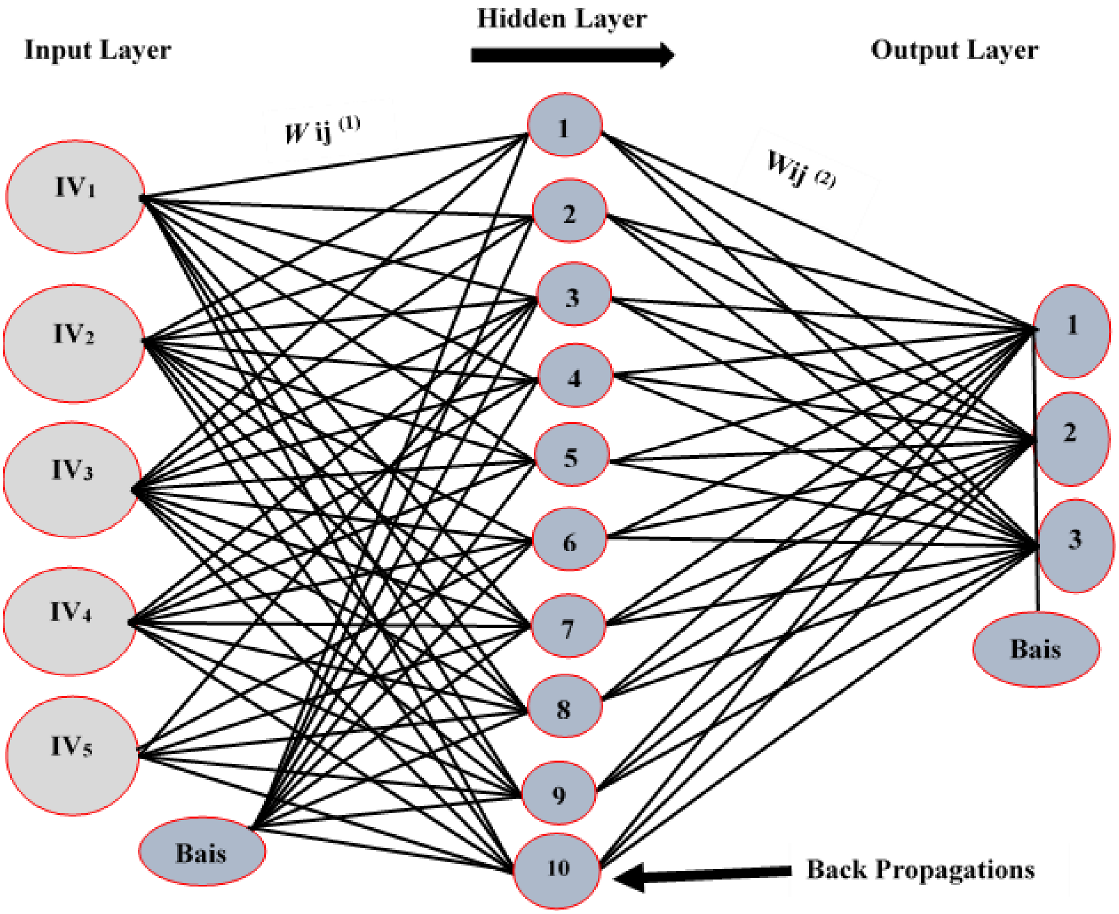

Figure 3.5: Multi-layer feed-forward network structure

3.3.3 Recurrent network

In the case of a single-layer feedforward ANN, a recurrent network usually is introduced if the output signals feedback as an input that replaces part or all of the input signals [126]. This could also be extended to include feedforward multilayer networks. Simply put, a recurrent ANN incorporates neurons feeding the output of their outputs again to function as new inputs to randomly selected neurons or maybe themselves [138]. Self-feedback can happen when the output layer of a particular node is fed back to the same node. Feedback loops improve with postponing components because of the nodes' nonlinear surroundings, resulting in a nonlinear dynamic behaviour. The inputs model as well as output signals in a recurrent ANN system are provided as x(n) and also y(n) respectively to be able to reflect the simple fact of being features of discrete period variables n [139].

3.4 The error back-propagation algorithm

The error back-propagation is one of the most popular and robust artificial neural network configurations [140] [141] [142]. The feed-forward error back-propagation technique is highly effective in modelling nonlinear relationships [135] [122]. The algorithm for back-propagation (BP) seeks the minimum error function value for weight space through a technique known as gradient descent or the delta rule. Weights that lead to the minimisation of the error function are considered then as solutions to the problem of learning. The back-propagation algorithm is a prevalent kind of ANN algorithm. It was stated by Rojas (2005) that the BP algorithm may be split into four key steps. The algorithm splits down, then, into the four steps of [143]:

a) Feed-forward type of computation.
b) BP to the output layer.
c) BP to the hidden layer
d) Updates to weight.

For forwarding propagation of the operating signal, the input signal is propagation to an output layer from an input layer via a hidden layer. The algorithm is halted when the error function value is sufficiently small. The system of error feed-forward BP has shown itself to be a tool with excellent efficiency in the modelling of relationships that are non-linear [135]. The ANN is creating; therefore, it is a technique that fully links each element processing within a precise layer to the layer next to it. As a result, every neuron in the input layer sends output to every neuron in the model output layer, and every node in the input layer sends output to every neuron in the middle layer [144]. The network's weight value and offset value are kept constant through the operating signal forward propagation. Each neuron layer status only exerts an effect upon that of the neuron's next layer.

Consequently, there cannot be the achievement of predictable output within the output layer – it may switch into the error signal back-propagation. For error signal back-propagation, the error signal can be defined as the variance between actual output and the network's expected output. Within error signal back-propagation, the error signal is propagated layer by layer from the end of output to the layer of input. Therefore, whilst the error signal back-propagation is done, the error feedback regulates the network weight value. However, continuous offset value and weight value modification are applied for the real network output to make it a lot closer to the one expected [145].

There is an assumption that all weighted Synaptics of the network are fixed whilst the forward step takes place. During the backward pass, the weighted synaptic of the network is adjusted under the updated error. During the training process, the iteration procedure repeats the error term required to change weight until a connection weight is set with the output/input mapping containing the minimum error value provided by the trained network. The ANN learning method for multilayer back-propagation consists of two processing elements that pass through the different network layers: a forward and backward pass, by measuring the gradient for each connection weight and bias using the chain rule, as seen in Figure 3.6. The synaptic network weights are fixed during the forward phase, yet they're adjusted based on an updated error. This iteration method repeats during the training cycle, which propagates the error period needed for weight adjustment until the trained network can give a collection of link weights, which has the input/output mapping that provides the minimum value for errors. Among the changes that have been made to the error back-propagation algorithm, one approach includes the use of the learning rate. The learning rate parameter (η) can be considered as the factor that initiates the step size the ANN takes in negative through the weight spaces to minimise the training error magnitude. Another factor that is considered in any training process of ANN is the term of momentum (α). Momentum may speed training up within error surface regions that are very flat as well as suppress weight oscillation within ravines or steep valleys [146].

3.4.1 The algorithm for back-propagation

The back-propagation equations provide a manner of computing the loss function gradient. Also, the following equations are used by the MATLAB algorithm to calculate the hidden neuron output, output layer through the combination of weight calculations and back-propagation during the whole training process. The values that are obtained through the sensors used as input data, and the target values collected from the alternative method will be validated through the ANN MATLAB algorithm. This can be expressed explicitly as an algorithm form by [140]:

i) Initialise the weight of the network connection between the values measured and the values predicted.

ii) Repeat the steps below until all conditions are met.

iii) Summarise weighted inputs and use the transfer function to calculate the hidden layer output.

$$h_i = f \sum_{i=1}^{n} \left(x_i \, w_{ij} \right) + \theta_j \qquad \text{Eq (3.7)}$$

Where,

(h_i) hidden neuron output, (w_{ij})*;* connection weight between input neuron *i* and hidden neuron j, (x_i) The input signal is, (θ_j) bias on a hidden neuron, (f) activation function.

iv) Summarise the output weighted by the hidden layer and apply the activation function to calculate the output layer.

$$y_k = f \sum_{i=1}^{n} \left(h_j \, w_{jk} \right) + \theta_k \qquad \text{Eq (3.8)}$$

Where,

(y_k) independent output, (w_{jk}) connection of weight between the hidden nodes j and k.

v) Back-propagation combinations

$$\delta_k = (d_k - y_k) f^{-} (\sum j h_j w_{jk} + \theta_k) \qquad \text{Eq (3.9)}$$

Where,

d_k the desired output of the neuron, (f^{-}) the activation function derivation;

vi) Weight calculation

$$\Delta w_{jk}(n) = \eta\delta_k h_j + a\Delta w_{jk}(n-1) \qquad \text{Eq (3.10)}$$

Where,

$\Delta w_{jk}(n)$ is an adjustment on connection weight between nodes j and k;(η) the rates of learning, (a) term momentum, (h_j) the actual output of the hidden neuron, (δ_k) the error back-propagation, $\Delta w_{jk}(n-1)$. The earlier weight correction.

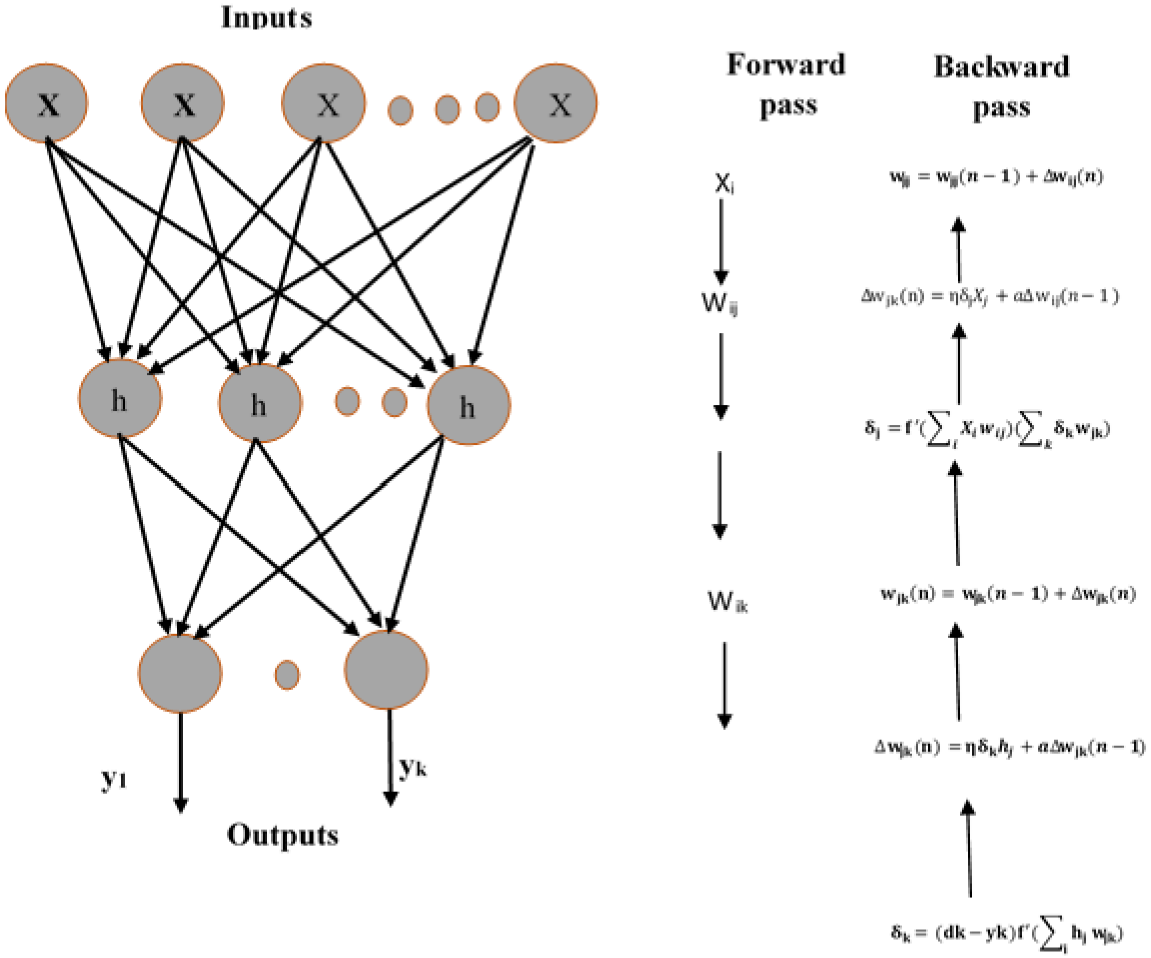

Figure 3.6: The Back-propagation algorithm error steps

3.5 The training algorithm of Levenberg-Marquardt

One aspect of the artificial intelligence (AI) principle is the Levenberg-Marquardt (LM) training algorithm. The LM approach is well known for achieving dramatically higher performance by making training 10 to 100 times more effective, quicker, safer and more frequently converging. The cycle of optimisation and training means defining the optimal parameters of the ANN model, which are the relation bias, weights, number of hidden layers, and the maximum number of hidden neurons. It should be noted that the key objective behind the LM algorithm implemented is to minimise the error value between the expected and target value by changing the connection weights most contributing to the error [147]. The error function is typically a non-linear function for multi-layer feed forwards. Therefore, it cannot force an empirical approach to minimise the error percentage to its lowest value. Alternatively, it's essential to find an algorithm that requires a search through the spaces of weight consisting of a sequence of the form steps:

$$w_{k+1} = w_k + \Delta w_k \qquad \text{Eq (3.11)}$$

Where,

w_{k+1} is the weight value at a certain iteration, w_k the value of the same weight at the previous step k, Δw_k is the increase of the weight vector.

The LM algorithm: is an iterative technique that locates the minimum of a function expressed as the sum of squares of nonlinear functions. It has become a standard technique for nonlinear least-squares problems and combines the steepest descent and the Gauss-Newton method.

The use of secondary algorithms, such as the LM algorithm, significantly increases the speed of training [147, 148]. Through a combination of the Newton and EBP algorithms, the LM algorithm ranks as a relatively efficient training algorithm for medium and small-sized patterns. Usually, the error function is a function that is non-linear for the multilayer type of feedforward networks. So, an analytical solution is impossible to implement to reduce the error percentage to the lowest value. The method of LM has been put forward for overcoming the main problems and limitations associated with conventional approaches and, in general, is often cited as being a robust and well-organised training algorithm in all aspects of engineering [149]. Different types of algorithms found in the related literature by several scholars include various techniques for calculating the increase in weight vectors [139]. ANN implements the LM technique to address the key disadvantages and weaknesses of conventional approaches and is widely cited as efficient and reliable in all aspects of the engineering training algorithm [117, 150]. The derivation of the LM algorithm will be presented in four parts. (1) Steepest descent algorithm [151] (2) Newton’s method [151] (3) Gauss-Newton’s algorithm [152] (4) LM algorithm.

However, this project focuses more on the Levenberg-Marquardt algorithm. The LM approach offers additional approximation to Hessian Matrix J^TJ to ensure that the approximated Hessian matrix J^TJ is invertible [153]:

The update of the Gauss-Newton algorithm is presented as:

$$w_{k+1} = w_k - H_k^{-1} g_k \qquad \text{Eq (3.12)}$$

$$w_{k+1} = w_k - (J_k^T J_k)^{-1} J_k e_k \qquad \text{Eq (3.13)}$$

The Gauss-Newton algorithm is a commonly used iterative method for addressing nonlinear least-squares problems. It is particularly well-suited to treat very large-scale variational data assimilation problems that arise in the atmosphere and ocean forecasting.

The advantage of the Gauss-Newton algorithm over the standard Newton's method equation (3.12) is that the former does not require calculating the second-order derivatives of the total error function by introducing Jacobian matrix J instead.

The LM scheme is an effective algorithm but a much more computationally intense model of a version of back-propagation. This process was developed to enhance the Gauss-Newton technique to remove the numerical uncertainty connected with the latter matrix inversion. This particular technique will add another approximation to the Hessian matrix, H denoted as:

$$H \approx J^T J + \mu I \qquad \text{Eq (3.14)}$$

Where,

μ always positive, which is called combination coefficient, I is the identity matrix, J is the Jacobian matrix, which could be determined using a less complicated back-propagation technique than Hessian matrix computing.

H: is Hessian matrix of partial derivatives.

I an identity matrix: It is a square matrix with 1s on the main diagonal and 0s on the rest of the diagonal.

J Jacobian matrix: The Jacobian matrix is used to examine the system's small-signal stability.

Jacobian is the matrix of all the first-order derivatives of a function $f(x_1,x_2,x_3,\ldots\ldots x_m)$ denoted by: $J(x_1,x_2,x_3,\ldots\ldots x_n)$ and is defined as:

$$J(\chi) = \begin{bmatrix} \frac{\partial f_1}{\partial x_1} & \cdots & \frac{\partial f_1}{\partial x_n} \\ \vdots & \ddots & \vdots \\ \frac{\partial f_m}{\partial x_1} & \cdots & \frac{\partial f_m}{\partial x_n} \end{bmatrix} \qquad \text{Eq (3.15)}$$

From the above equation (3.13), one may notice that the elements on the main diagonal of the approximated Hessian matrix will be larger than zero. Therefore, with this approximation equation (3.13), it can be sure that matrix H is always invertible.

We trained the LM algorithm in the current study with five input parameters and three outputs. However, by combining the equations 3.13 and 3.14, the update rule of the Levenberg-Marquardt (LM) algorithm can be presented as:

$$\mathrm{w_{k+1}} = \mathrm{w_k} - (\mathrm{J_k^T J_k} + \mu I)^{-1} \mathrm{J_k e_k} \qquad \text{Eq (3.16)}$$

The Levenberg-Marquardt algorithm, a mixture of the steepest descent algorithm and the Gauss-Newton algorithm, switches between the two algorithms during the training process. While the combination coefficient μ is minimal (nearly zero), equation 3.16 approaches equation 3.13, and the Gauss-Newton algorithm is used. When the combination coefficient μ is huge, equation 3.16 approximates to equation (3.14), and the steepest descent method is used.

A symmetric matrix containing all of a multivariate function's second derivatives is the Hessian matrix.

The following is the definition of a second partial derivative:

$$f_{xij} = \frac{\partial}{\partial_{xi}} \left(\frac{\partial f}{\partial_{xi}} \right) \qquad \text{Eq (3.17)}$$

The symmetric matrix of the Hessian matrix is as follows:

$$H(\chi) = \begin{bmatrix} f_{11} & f_{12} & \cdots & f_{1n} \\ f_{21} & f_{22} & \cdots & f_{2n} \\ \vdots & \vdots & \vdots & \vdots \\ \vdots & \vdots & \vdots & \vdots \\ f_{n1} & f_{n2} & \cdots & f_{nn} \end{bmatrix} = \begin{bmatrix} \frac{\partial}{\partial_{x1}}\left(\frac{\partial f}{\partial_{x1}}\right) & \frac{\partial}{\partial_{x1}}\left(\frac{\partial f}{\partial_{x2}}\right) & \cdots & \frac{\partial}{\partial_{x1}}\left(\frac{\partial f}{\partial_{xn}}\right) \\ \frac{\partial}{\partial_{x2}}\left(\frac{\partial f}{\partial_{x1}}\right) & \frac{\partial}{\partial_{x2}}\left(\frac{\partial f}{\partial_{x2}}\right) & \cdots & \frac{\partial}{\partial_{x2}}\left(\frac{\partial f}{\partial_{xn}}\right) \\ \vdots & \vdots & & \vdots \;\; \vdots \\ \vdots & \vdots & & \vdots \;\; \vdots \\ \frac{\partial}{\partial_{xn}}\left(\frac{\partial f}{\partial_{x1}}\right) & \frac{\partial}{\partial_{xn}}\left(\frac{\partial f}{\partial_{x2}}\right) & \cdots & \frac{\partial}{\partial_{xn}}\left(\frac{\partial f}{\partial_{xn}}\right) \end{bmatrix} \qquad \text{Eq (3.18)}$$

3.5.1 Determination of the Levenbverg- Marquardt

Determining the optimum ANN structure is one of the challenging tasks in network advancement. It involves selecting the optimal number of layers, the most effective model input parameters, the total number of hidden layers, and the total number of nodes in each layer. There is currently no coherent theory to assess an optimal ANN topology [154]. There are essentially two layers representing the input and output variables in every proposed network. The researcher has reported that one hidden layer is satisfactory and can map any continuous feature between model variables [155].

It should be remembered that adding more than one hidden layer leads to significant delays in the training cycle and raises the chances of being stuck in local minima [156]. Trial and error is the approach promoted [157], widely used to optimise hidden layers number and connectivity. It has been recommended by [158] that the maximum number of nodes in a single hidden layer might be considered as 2N+1, in which N is the number of independent variables. Another method, recommended by [154] is that the top selection of the nodes used at the hidden layer is a characteristic of mean square error (MSE) as well as correlation coefficient (R). When the MSE is the minimum value and the R numerical value at its possible upper limit, it can finalise the number of neurons.

3.6 The training process

3.6.1 The selection of model and estimation of performance

The performance of the ANN should be assessed once the successful completion of the training process has taken place. The goal of the overall performance evaluation stage is to make sure that the unit can be generalised to the overall performance analysis limits set by the program information sufficiently, as would be expected [149]. The acceptable strategy frequently implemented in the appropriate literature is testing the measuring operation of the trained network on an assessment data subset [159]. The generalised model can be considered robust if these output parameters are necessary. Many researchers have reported various measuring performance indicators, such as the correlation coefficients (Pearson's R and p), root mean square error (RMSE) and mean absolute error (MAE). The critical statistical performance is usually measured mainly to assess the efficiency of the ANN model.

The coefficient of determination (CD) value is used to determine the correlation and fitness between the measured and the predicted value [160]. The simplest and most commonly used method employed in ANN is the method of holdout cross-validation. There is a subdivision of training data with this particular technique into sets of testing and training and validation. The training set is used in the network training, whilst the validation set is utilised to evaluate the network's performance by estimating mean absolute error. There is the repetition of the process for each type of network design, and the one that is selected as the best model of ANN is the one that produces the lowest absolute error on average. The correlation coefficient, for the measurement of performance denoted by (R), is a measure of the strength of the straight line or linear relationship between two variables of 0.0 and 1.0, the index that follows was suggested [161]:

$|R| \leq 0.2$ weak correlation in existence between two variable sets.
$0.2 < |R| < 0.8$ a correlation is in existence between two variable sets.
$|R| \geq 0.8$. there is the existence of a strong correlation between two variable sets.

Equation 3.16 shows the correlation coefficient (R) to determine the relative correlation between two variable sets.

$$\mathrm{R} = \frac{\sum_{\mathrm{i}=1}^{\mathrm{n}}(\mathrm{T_i}-\mathrm{T}^-)(\mathrm{P_i}-\mathrm{P}^-)}{\sqrt{\sum_{\mathrm{i}=1}^{\mathrm{n}}(\mathrm{T_i}-\mathrm{T_i^-})}\hat{}2\sum_{\mathrm{i}=1}^{\mathrm{n}}(\mathrm{P_i}-\mathrm{P}^-)\hat{}2} \qquad \text{Eq (3.16)}$$

The most flexible criterion for measuring error between predicted and measured values is the RMSE which is beneficial because the more significant error value considers more than minor errors. However, MSE removes emphasis placed on significant errors. Therefore, it ought to be noted that both MSE and RMSE are desirable when there is a continuous result for assessed data output. The equations that follow may be applied in the calculation of MSE and RMSE:-

$$\mathrm{RMSE} = \sqrt{\frac{1}{N}\sum_{i=1}^{n}|T_i - P_i|} \qquad \text{Eq (3.17)}$$

$$\mathrm{MSE} = \sqrt{\frac{1}{N}\sum_{i=1}^{n}(T_i - T_i^-)\hat{}2} \qquad \text{Eq (3.18)}$$

Where,

N symbolises the number of data sets, Pi, and T is the computational and targeted value, and $\bar{T}$ and $\bar{P}$ are the means of the targeted and predicted values.

3.6.2 Testing process

The trained network's performance is assessed in the testing procedure by looking at the errors on the training and validation sets and the test results. When the correlation coefficient (R) is close to one, there is a significant connection between the intended and network outputs. In contrast, when it is close to zero, it means the opposite. However, the best network is training for measurement of network performance expressed in terms of R-value that, once more, uses both validation and training sets as entire data for training. There is then an assessment of its performance through the use of the testing data. A fully trained network ought to have the ability to predict quickly from this unseen data set; its evaluation is done by measurement of R-value. A flowchart presents the algorithm of ANN for the entire process mentioned above in Figure 3.7.

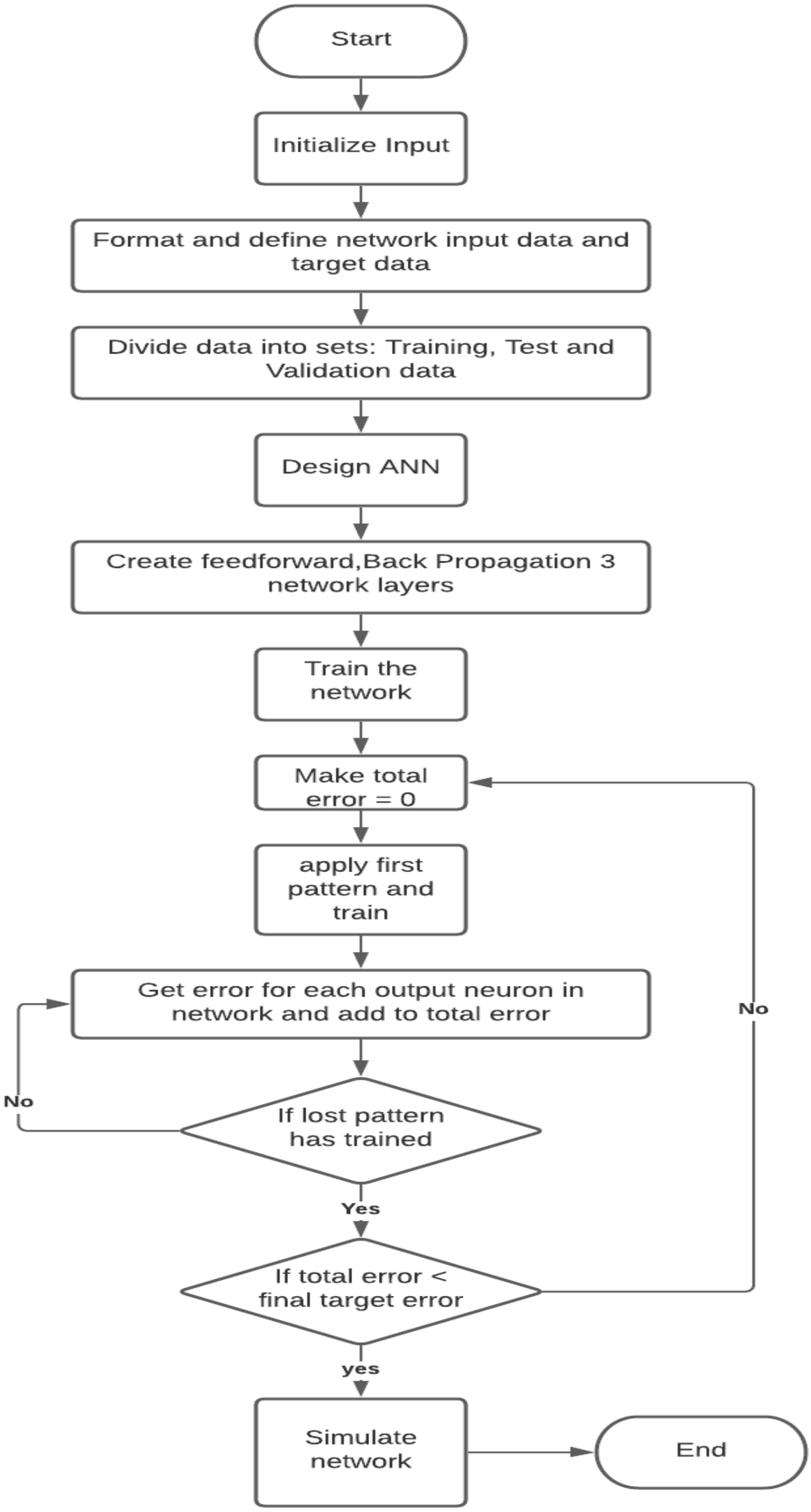

Figure 3.7: Flow chart of the ANN algorithm

3.7. Classification

Classification is the most common form of the machine learning application. The goal of the classification process is to discover a way of classifying unseen examples founded on the knowledge extracted from a pre-classified set of instances provided. Sometimes the classification is known as supervised. In a sense, a scheme operates under supervision by giving an actual outcome for each training example in the training process. This outcome is, therefore, called the example 'class'. Achievement of learning of classification may include arbitration through a trial of the learned explanation of the concept upon a set of independent test data, the proper classification of which is known though not available for the machine. The rate of success on the test data provides an objective measure dependent on how well the concept is learning.

Algorithms for machine learning discover natural patterns within data to generate insights that can help make better predictions and decisions—data used in machine learning to produce a model for the performance of a particular task. Machine learning employs two techniques: unsupervised learning, which tries intrinsic structures or hidden patterns within data input; and supervised learning, which involves training a model on known output and input data to predict future outputs. These techniques are presented in Figure 3.8.

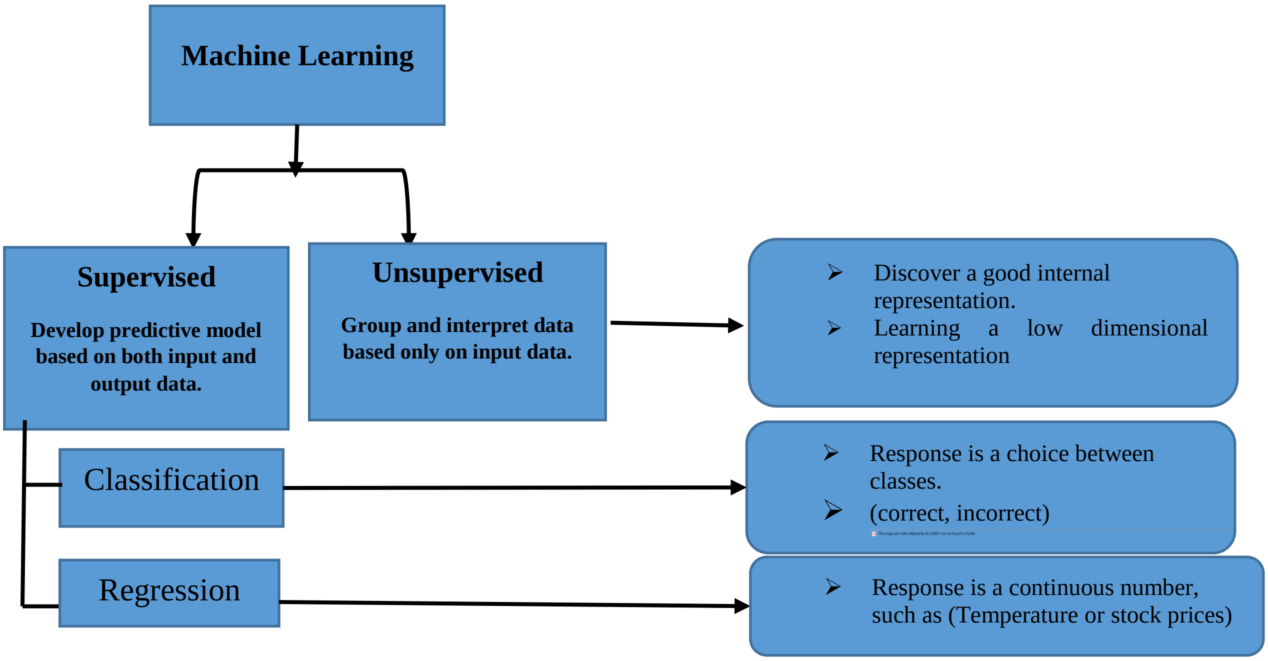

Figure 3.8: Schematic for machine learning techniques.

Supervised learning

When there is uncertainty, supervised machine learning aims to build a model for predictions based on evidence. An algorithm for supervised learning takes a known input data set and the known responses for the output data. it trains a model for the generation of reasonable predictions in response to the new data classification and regression techniques used in supervised learning to develop predictive models.

3.7.1 Classification techniques

Classification models start the classification of data into various categories. Classification is a fundamental task in data analysis that requires constructing a classifier, a function that assigns a class label to instances within the set of attributes described. However, this thesis focuses on the basic concept of the data mining technique of classification. For the classification of data collection, Meta, Misc, Rules, and Trees classifiers are used. In the current study, the WEKA tool is used to classify the database into different classes. WEKA is an abbreviation for Waikato Environment for Knowledge Analysis. The full details of the WEKA are discussed in the next section after the most significant frequency has been selected from the WEKA Workbench classification technique as discussed in the next section. The level of chloride ions in concrete structures was validated using an ANNs method in five different saltwater concentrations. Based on five experimental data sets collected within five different saltwater concentrations, the ANN model is applied to validate the level of chloride ions in the concrete structures. Data was collected using a Rohde and Schwarz ZVL Vector Network Analyzer connected to a microwave horn antenna with a frequency range of 2 to 12 GHz, with each sample measured ten times. Then, the Chlorimeter tool method was used to measure the level of chloride ions in different cover depths directly after the microwave sensor measurement was finished on each sample. The model is developed, trained, validated and tested using a multi-layer back-propagation method. The validated values compare with actual test results by applying the Chi-squared technique to calculate the percentage error.

3.7.1.1 WEKA

Waikato University academics in New Zealand created the WEKA. The first implementation of WEKA in its current form was in 1997. WEKA uses the Graphical User Interface (GNI) and General Public License (GPL). The software is written in the JavaTM language and comprises a GUI for data file interaction. There is no need for in-depth data mining knowledge to operate WEKA, making WEKA a prevalent tool for mining data. Also, WEKA provides the users with a GUI and offers many facilities. WEKA is a state-of-the-art machine learning (ML) technology and it is applied to real-world data mining issues. The data file that WEKA usually uses is in ARFF or CSV file format. ARFF stands for Attribute Relation File Format, consisting of unique tags showing distinction in the data set. WEKA implements pre-processing algorithms for data, classification, clustering, regression, and association Rules of the procedure [162].

3.7.2 Methods

This section describes the most critical classification techniques with their basic working and the advantages and disadvantages of being used in this project.

3.7.2.1 Bayesian network

This type of algorithm refers to a graphical model for possible relationships between a set of variables [163]. The advantages of this algorithm are presented in [164], including the flexible applicability; this algorithm can resolve both classification issues and regression; smoothness properties; minor changes in the Bayesian network model do not influence the system's working. Handling missing data; this algorithm again has excellent capability to fill out missing data by assimilating overall opportunities of the missing values. One of the problems with the Bayesian networks classifier is that it usually requires continuous attributes to be discretized [165].

3.7.2.2 K-Nearest neighbour

K Nearest Neighbour is a basic algorithm that maintains all available examples and classifies new data or cases based on a similarity measure (KNN). It is often used to define a data point based on how it ranks its neighbours [166]. This type of algorithm technique divides into two categories: structure-based KNN and structureless KNN. The structure-based method deals with the basic structures of the data where the system has less mechanism associated with training data samples [167]. However, the entire data is categorised into sample data points and training data in the structureless technique. The distance is calculated between sample points and all training points. The points with smaller distances are known as the nearest neighbour. [168].

Advantages:

(1) One of the KNN algorithm's most notable benefits is that it works well with huge training data sets and is unaffected by noisy data [169].
(2) No Training Period: Lazy Learner (Instance-based learning) is called KNN. In the training phase, it does not learn anything. It does not derive any unfair function from the data from the training. There is no preparation time for it, in other words. It stores and learns from the training data set only at the moment of making predictions in real-time. This makes the KNN algorithm much faster than other training algorithms, such as SVM, Regression Linear, etc.
(3) Since the KNN algorithm needs no training before making predictions, it is possible to seamlessly add new data that will not affect the algorithm's accuracy.
(4) KNN is very simple to implement. To implement KNN, only two parameters are required, i.e. the value of K and the distance function.
(5) Quick calculation time.
(6) Versatile – useful for regression and classification.

Disadvantages:

(1) It doesn't work well with large data sets: the cost of measuring the distance between the new point and each current issue is massive in large data sets, which degrades the algorithm's efficiency.
(2) With high dimensional data, the KNN algorithm does not work well because it becomes difficult to measure the distance in dimension with a large number of sizes.
(3) Accuracy depends on the quality of the data.
(4) Requires high memory-need to store all of the training data.
(5) Sensitive to noisy data input, missing values, and outliers: in the data set, KNN is noise sensitive. Therefore, there is a need to assign missing values manually and delete outliers [168].

3.7.2.3 Decision tree induction

Decision tree algorithms are the most commonly used algorithms in classification [170]. The method of decision tree selects an attribute that maximises specific values and fixes the timing. Then attribute values are divided recursively into several branches until the termination is reached [171]. The decision tree is a transparent mechanism that facilitates users to follow a tree structure making it easier to see how it is made [172]. However, the main objective of the decision tree is to create a model that evaluates the value of the required variable based on numerous input variables [173]. C4.5 (J48) is a well-known algorithm for decision tree production. C4.5 (J48) tries to delete data branches by swapping them with leaf nodes after the tree has been constructed [174]. Thus the strengths of C4.5 are dealing with training data with missing feature values and dealing with both discrete and continuous features [175, 176].

The weaknesses include that this algorithm is unsuitable for small data sets [175] and has a higher processing time than other decision trees. The decision tree is created by picking a function and dividing the supplied example set according to the values of that function in an iterative process from a set of training examples. The algorithm REPTree is a fast decision tree learner. RepTree uses the regression tree logic and creates multiple trees in different iterations. After that, RepTree selects the best one from all generated trees. Reduced Error Pruning Tree is a fast decision tree learning technique, and it builds a decision tree based on the information gain variance, using reduced error [177]. Algorithm Random Tree is a supervised Classifier; it is a band learning algorithm that produces many individual learners. A random tree is a collection of tree predictors that is called a forest [177]. The algorithm Decision Stump is a class for using and building a decision stump. This type of algorithm is always used in conjunction with a boosting algorithm. The most critical issue is which characteristics are most effective in deciding classification and should be selected first. Information gains choose the most important, intuitively deemed the feature of probably the lowest entropy or perhaps the highest information gain [178].

3.7.2.4 Info gain attribute eval

Info Gain Attribute Eval (IG) must use the Ranker search method from the Weka workbench to select attributes to reduce the dimensionality of the data [179]. The selection of features is a fundamental issue in many fields. All components may be necessary for some problems. Feature selection decreases the dimensionality of the feature space and eliminates redundant, obsolete, or noisy data so that a small subset of features is essential for particular goal definitions. This method is selected because it can calculate the information gain for each attribute for the output variable. Those traits that contribute more information have a higher information gain value and can be chosen, while those that do not give much information have a lower score and can be deleted [178].

3.7.2.5 Meta classifier

Meta classifier includes a wide variety of classifications. The number of attributes and the number of values per attribute determines the complexities of time and space. The first approach is multi-scheme from meta-rule; this class selects a classifier from a set of many using cross-validation on the training data. The training data's performance, which is assessed by percent accuracy (classification) mean squared error. The second algorithm is Bagging, this type of class is for bagging a classifier to reduce variance, and it can do classification and regression depending on the base learner. The third algorithm, CVParameterSelection, is a meta-classifier that can optimise over an arbitrary number of parameters, with only one drawback apart from the apparent explosion of possible parameter combinations [162].

3.7.2.6 Misc classifier

The category Misc contains only two classifiers unless additional corresponding WEKA packages are enabled. The InputMappedClassifier is a wrapped classifier that addresses incompatible training data by building a mapping between the training data that a classifier is built with and the incoming test instance structure. The Serialised classifier loads and uses a model that is serialised to a server for prediction. It has no impact to provide new training data sets since it summarises a static model [162].

3.7.2.7 Rule classifier

The association rules are used to determine a correct link between all of the characteristics. They usually can predict more than one outcome. However, the number of records to be estimated correctly by an association rule is called coverage. Support is characterised as coverage divided by several records in total [180]. The rules are easier to understand compared to the giant trees. For every path from the root to the leaf, one root is created. Each pair of attributes along the path is a conjuncture. The leaf holds the prediction of class. Rules are mutually exclusive to each other. Each time a rule is learned, tuples remove from the rules. OneR - This classifier will choose one characteristic and determine the optimal classification rule based on that attribute. The rule will then predict the value of the target attribute based on the value of this attribute for a specific instance. ZeroR-this is the simplest of the rule-based classifiers and is the majority class classifier. The ZeroR rule classifier takes a look at the target attribute and its possible values. Also, it will always output the value that is most commonly found for the target attribute in the given data set [181].

3.7.3 Statistical chi-squared method

A chi-square (x^2) statistic is a test that evaluates how well a model compares to actual observed data. However, the data used to calculate a chi-square must be random data, raw, mutually exclusive, drawn from independent variables, and removed from a large enough sample. The Chi-Square Goodness of fit test is a non-parametric test used to determine how significantly the observed value of a process differs from the expected value. In the Chi-Squared goodness test, the term goodness of fit equates the sample distribution observed with the expected probability distribution. The x^2 statistic appears quite different from the other statistics, which have been used in the previous hypotheses' tests. It also appears to show little similarity to the previously reported theoretical chi-square distribution. The chi-square statistic is the same for both goodness of fit test and the test of independence. For each of these tests, all the data's categories are used. The observed numbers of cases refer to the data received from the sample. These are the frequency of occurrences for each of the data types. In the chi-square tests, the null hypothesis states how many cases are to be expected in each category if this hypothesis is correct. The chi-square test is based on the difference between the observed and the expected values for each category [182].

Procedure for Chi-Square Goodness of Fit-Testing

Set up the hypothesis for the Chi-Square fitness test:

a) Null hypothesis: in the Chi-Square goodness test, the null hypothesis suggests no substantial difference between the expected and the observed value.
b) Alternative hypothesis: in the Chi-Square goodness test, the alternative hypothesis suggests a substantial difference between the observed and the expected value.

Calculate the value of the Chi-Square test using the following formula:

$$x^2 = \sum \frac{(O_i - E_i)^2}{E_i} \qquad \text{Eq (3.19)}$$

Where

A chi-square (x^2) a statistic is a test that measures how a model compares to actual observed data.

An observation (O_i) in statistics of cases in category i is a value of something of interest you're measuring or counting during a study or experiment.

The expected value (E_i) is the expected number of instances in category i, and it is computed by multiplying each potential result by the chance that each event will occur and then adding all of those numbers.

The calculation shows that the Chi-Square statistic is based on the difference between observed and predicted data if there were no links between the variables. This chi-square statistic is calculated by subtracting the observed number of instances from each category's predicted number of cases. This difference is squared and divided by the expected number of cases in that category. These values are added for all the categories, and the total is referred to as the chi-squared value.

Chi-square distribution

General chi-square tests for goodness of fit of an observed variable to a theoretical one, the independence of two parameters for qualitative data classification, and confidence interval estimation for a population standard deviation of a normal distribution from a sample standard deviation using the chi-square distribution [183].

The reason for using a chi-squared test rather than other tests like T-test, is that a chi-square test requires categorical variables, each of which may have any number of levels. But the T-test requires two variables, one must be categorical and have exactly two levels, and the other must be quantitative and be estimated by a mean.

3.8 Related studies

Recently, ANNs reported being a successful modelling technique in different contexts, including numerous geotechnical engineering speciality areas. An ANN can deal with complexity and record the non-linear functions adopting the substantial computer potential to carry out very iterated work. An investigation conducted by [184] focused on the ANN as an alternative approach to evaluating the chloride diffusivity of high-performance concrete (HPC). The use of the ANN technique is described in [185] to analyse relationships between several input parameters and observed corrosion-reinforcing damage. We have collected data sets on the effects of environmental conditions, concrete structure and properties on the degree of damage caused by steel corrosion on 11 concrete bridge structures in a Croatian moderate continental climate. The primary causes of deterioration were chloride ions from de-icing salts and accelerated carbonation due to higher carbon dioxide concentration on highways and in towns [185]. The ANN is defined in [186] as a tool for classifying damage and predicting the expected future degree of damage. However, in further work [187] the author investigated the Nord test method for rapid chloride permeability to determine the chloride ion penetration of high-calcium fly ash (HCFA)-containing concrete for partial replacement of Portland cement. The test results are used as a training set for generating rules describing the relationship between material composition and chloride resistance. Multiple techniques for generating rules have been used and compared. The rules of the WEKA workbench algorithm J48 provided the means for an adequate classification of plain concrete and concretes modified with high calcium fly ash as components of good, unacceptable or acceptable resistance to chloride penetration [187]. In [188] the researcher investigated rules for the automatic categorisation of concrete quality using selected machine learning methods of artificial intelligence. While many researchers highlighted the use of ANN in geotechnical engineering, there are still significant gaps in the subject knowledge. The slow convergence rate, the need to constantly change training, and getting stuck in the local minima are major drawbacks associated with the conventional artificial neural network [188]. In practice, both supervised classification and ANN techniques can provide good results to predict the outcome variable. Researchers are interested in their modelling with many machine learning methods for the prediction of different properties of concrete structures [189] [190] [191]. However, it utilised ANN methods based on experimental data to estimate the chloride permeability of the concrete [192]. It found that the ANN technique provided very accurate results for predicting corrosion in concrete structures [193] [194].

Additionally, we chose the parameter for the input based on trial and error. In the current study, a new methodology has been presented using concrete specimens in different saltwater concentrations and exposed to microwave sensors. A chlorimeter tool was used as a partially destructive method to determine the level of chloride in different depths. Then, the ANN approach was used to evaluate between the microwave sensor data and the chlorimeter tool's experimental data. The choice of input parameter has been discussed using microwave sensor data in five different saltwater concentrations to identify the most important frequency point to determine the chloride ion level in concrete. The choice of output parameter was select using the three different depths of chloride penetration experimental data work.

3.9 Summary

The literature study's specifics are covered in this chapter to give the reader a quick assessment of the viability of computational intelligence methods. The viability of computational intelligence (CI) applications is highlighted and addressed. It could apply the CI methods effectively to provide a predictive model when the relationships between model inputs and outputs are nonlinear. The number of dependent and independent variables, number of neurons, training system, and data set size are the key parameters influencing model convergence, according to the topology and factors affecting the construction and training phase of the ANN model. To avoid over-fitting and ensure the trained networks' good generalisation capability, other essential aspects of the model must be defined after the model has been configured, such as the standardisation mechanism and the data set division process. In addition, we discussed the technique of feed-forward error back-propagation as a highly effective method in modelling nonlinear relationships. Also, most of the equations used by the MATLAB algorithm to calculate the hidden neuron output, output layer through the combination of weight calculations and back-propagation during the whole training process were described. A root mean square error (RMSE), mean absolute error (MAE), and determination coefficients (Pearson's R and P) were chosen as the critical statistical measures for measuring the efficiency and generalisation capabilities of the trained network. The back-propagation work and supervised LM employed were also introduced and discussed. The algorithm of ANN for the entire process mentioned above was presented by flowchart.

Moreover, the classification techniques used in these projects and WEKA workbench software was discussed in detail. For data collection classification, Meta, Misc, Rules and Trees classifiers were discussed in detail. Finally, studies of some related projects reported on chloride ion penetration in concrete structures.

Chapter Four: Electromagnetic Waves and Microwave Sensor

The electromagnetic waves, namely microwave sensing systems, will be introduced in this chapter as a proposed technique for detecting the level of chloride ions in reinforced concrete. This chapter will discuss various antenna types and evaluate their qualities for transmitting and receiving microwave signals to identify the most appropriate antenna for this study. The experimental work was carried out as preliminary work to select the optimal angular frequency. This section of the experiment is conducted to see whether the S_{21} and S_{11} parameters could be used with concrete samples and if there was a link between skin depth and concrete penetration depth. In terms of demonstrating the state of the art, those preliminary experiments were utilised to improve the methodology and justify the rest of the experimental work.

4.1 Background

In general, microwave spectroscopy is defined as a study of those interactions between radio waves and matter, of wavelengths between fractions of a millimetre and several metres [195]. In a massive theoretical development in 1873, James Clerk Maxwell proposed the presence of electromagnetic waves and mathematically predicted their properties before anyone had ever noticed such a phenomenon or even heard of it. Science and communications engineers have since utilised this radiation for many different kinds of determination. EM waves can be defined characteristically as having three types of physical property, i.e. wavelength (λ), frequency (f), and photon energy (E). Figure 4.1 shows the full spectrum of electromagnetic waves that cover an entire span of visible and non-visible light signals comprising magnetic and electric fields that are perpendicular to one another and perpendicular to the propagation direction with all their frequencies and wavelengths. During its early stages, microwave spectroscopy was

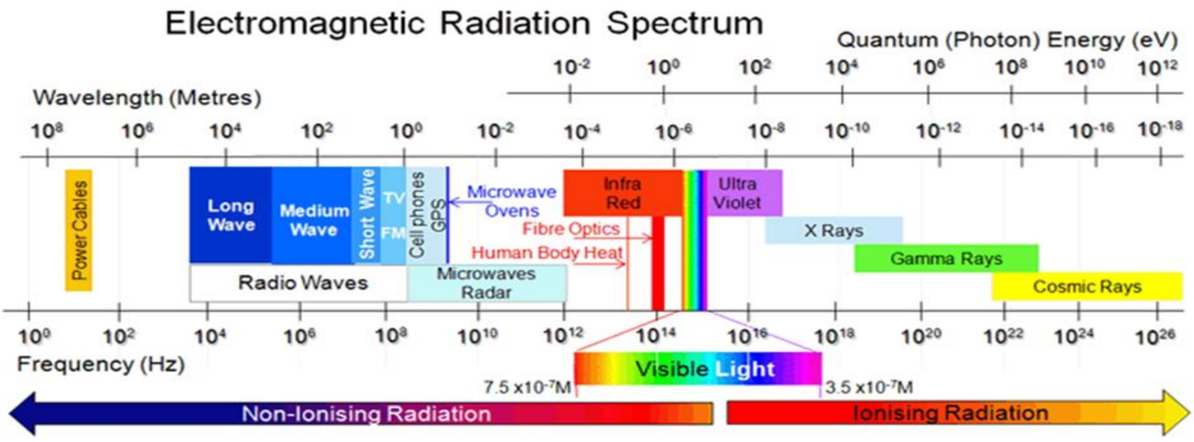

Figure 4.1: Electromagnetic waves with their full frequencies and wavelengths [160]

introduced to determine dielectric matter properties with experimentation carried out via Hertzian waves. Microwaves are commonly classified as electromagnetic waves with a frequency between 300 MHz and 300 GHz; the wavelength of these electromagnetic waves are identified as well within the range varying from one metre to one millimetre [196].

Microwaves are used in many applications, but in 1934 the first use was as a microwave radiotelephone network that worked at a frequency of 1.8 GHz between France and England. The magnetron was invented in 1937 and used in a high power microwave generation device currently used in microwave ovens [197]. Since the Second World War (WW2), the utilisation of microwave spectroscopy has had prominence with radar and various other technical developments in techniques for the generation of microwaves. This technique is utilised in a broad range and wide variety of applications such as food quality testing, milk quality, and testing of pollutants in water [198] [199] [200] [201]. The author of [202] investigated chloride ions in the hardened mortar by using microwave non-destructive testing. Drying structures using high-frequency electromagnetic radiation or microwave technologies are gaining much more use [203]. Electromagnetic sensing techniques help analyse civil infrastructures, such as transportation, in terms of static and dynamic behaviour during, before, and after a disaster like an earthquake. The technique of electromagnetic sensing provides knowledge about the materials investigated in terms of the amplitude and phase of gathered signals, which in effect consist of the materials' electromagnetic properties [204].

The electromagnetic waves provide a fast and non-intrusive diagnosis that is useful at the prevention level as a precautionary diagnosis of both strategic buildings and transportation infrastructure and they can be a critical issue in seismic risk mitigation. Furthermore, they may serve as a valuable tool for quickly mapping the damage to civil structures and facilities (highways, bridges, and dams) during the crisis, allowing for preliminary estimates of which areas are safe for rescuers [204] [205]. Therefore, the timely assessment, monitoring and recovery of bridges may reduce overall direct costs and indirect costs in terms of the potential destruction of property and life of the bridge. While we cannot avoid natural disasters, NDT can greatly reduce the total direct and indirect costs associated with bridges' destruction due to internal flaws or design defects. The electromagnetic technique can also be used for detecting the excess moisture content in building fabrics [207] [208], as well as in public health for monitoring insecticide levels in developing countries [209]. The authors in [210] report that microwave spectroscopy is used for non-destructive monitoring of meat drying and water holding capacity.

Microwave propagation within concrete depends upon dielectric properties that are, in turn, a function of free water amounts that are present within the material. There is a significant reduction in free water amounts during hydration, which makes methods for the absorption of microwaves powerful as tools for monitoring that process of hydration. There are various applications of microwave technology, such as determining water activity within fresh meat within the food industry [211]. Microwaves are used within medicine for the determination of breast cancer [212]. Within the water industry, microwaves can be used to detect underground water leaks [213]. Microwave spectroscopy is a non-ionizing, low-cost, high-penetration technology with considerable design flexibility, and it is a non-destructive, real-time measurement approach.

4.2. Dielectric properties of concrete at microwave frequency

Concrete is defined as a dielectric material that will store energy when exposed to an electromagnetic signal. Therefore, the concrete can be described by its dielectric properties using the EM wave field. Exposure of a dielectric material (not a perfect conductor) to an electromagnetic field, results in a change in the configuration of its microscopic electric dipole composed of negative and positive charges, whose centres do not always coincide. Material dielectric properties are associated with other material characteristics and can detect properties such as bio content, bulk density, chemical concentration, and moisture content. When exposed to an EM field, a change in the relative positions of the internal bound positive and negative charges against regular molecular and atomic forces causes polarisation, storing electrical energy [214]. The latter is represented by the real part of the material's complex permittivity or (dielectric constant). Whereas the (dielectric constant) real part reflects the amount of material polarisation, the imaginary component or (loss factor) reflects the losses caused by conductivity and water dipole relaxation. Hence a perfectly dry dielectric material with no moisture would have an imaginary part of zero.

Two independent electromagnetic properties can be defined by a dielectric, namely complex permittivity (ε^*) and complex permeability (μ^*).

Definition of permittivity: The permittivity of a material is a property that quantifies the resistance it generates when an electric field develops. It is explained as the ratio of the electric displacement to the electric field intensity. The SI unit of permittivity is Farad per metre. The vacuum has the lowest possible permittivity, which is approximate $8.85 \times 10^{-12}\,\mathrm{Farad/metre}$.

Definition of Permeability: Permeability is the property of the material which supports the formation of the magnetic field. The temperature, field strength, field frequency and humidity affect the permeability of the material. The material's permeability is directly proportional to the conduction of the magnetic force surfaces. Permeability is defined as the ratio of the flux density to the material's field strength. The permeability constant is the permeability of free space. It is represented by μ_0, and it is approximately equal to $4\pi \times 10^{-7}$ Henry/metre

Nevertheless, most dielectric materials, including concrete and wood, are non-magnetic, making the permeability very near free space permeability. The discussion is therefore limited to the complex permittivity (ε^*) this is defined as [215]:

$$\varepsilon^* = \varepsilon' - j\varepsilon'' \qquad \text{Eq (4.1)}$$

Where ε' is the real part of the complex permittivity, ε'' is the imaginary part of the complex permittivity and $j = \sqrt{-1}$. Then the equation 4.1 divided by the permittivity of the free space ε_0 the property becomes dimensionless and relative to free space:

$$\varepsilon_r^* = \frac{\varepsilon^*}{\varepsilon_0} = \varepsilon_r' - j\varepsilon_r'' \qquad \text{Eq (4.2)}$$

Where ε_r' is the real part of the relative permittivity known as dielectric constant and ε_r'' is the imaginary part of the relative permittivity known as the loss factor.

However, the dielectric constant continuously measures how much energy is extracted by material from an external electric field. The loss factor is a function of how dissipative material is, due to current conduction to an external electrical field.

The ratio of the lost energy to the accumulated energy in materials is given as a loss tangent:

$$tan\delta = \frac{\varepsilon_r''}{\varepsilon_r'} \qquad \text{Eq (4.3)}$$

Where $tan\delta$ is the loss tangent, loss tangents could change with temperature, moisture, frequency and mixture, and compression [216] [217]. The following section defines the basic working principle of the microwave sensors technique.

4.2.1 The working principle of microwave sensors technology

Different forms of microwave sensors are being produced, and more developed. Most of their principles are generally known, while some others are new. Microwave sensors use electromagnetic fields and a device that internally operates at a frequency from 3 MHz to the terahertz scale [218]. Microwave sensing technology is a widely used engineering method for many different industrial applications, such as for non-destructive measurements in real-time. This method's theory is based on the interactions between microwaves and material under test (MUT), which directly affects the speed of the signal, i.e., reflects the signal or attenuates it. Because of this change, the material permittivity also varies, resulting in the incident electromagnetic signal becoming attenuated or shifting frequency. By considering how the reflected (S_{11}) and transmitted (S_{21}) microwave power differ at discrete frequency intervals, the signal shift can be related to the composition of the object under test [219]. Buschmüller (2008) explored microwave resonance technologies using the interaction between water molecules and shifting electromagnetic fields.

The measuring frequency of the employed sensor is predetermined by the resonance wavelength of the microwave-induced resonator. However, the frequency of resonance depends on the geometries of the sensors employed. When the resonator is loaded with materials an increasing storage of electric field energy can be observed, resulting in a decreasing frequency of resonance. The permittivity, which is excited by the energy storage, significantly changes concerning the water content. Moreover, the wet material disposed of the resonator energy, which results in an increasing width of the resonance waves because resonators respond very sensitively, measurement accuracy can be high. Thus, water content leads to a decreasing frequency resonance; the frequency bandwidth increases simultaneously (see Figure 4.2). The broadening of the observed resonance frequency band is induced by the moisture of the substance and the material load in the sensor's focus. By simultaneously considering frequency and bandwidth and comparing it to the unstressed resonator in air, two independent properties are available, which allow the determination of an MUT in terms of the moisture content. Hence, a material's moisture content can be obtained using microwave spectroscopy [220]. In using microwave sensors, the primary advantages are that there can be a broad range of applications that are cheap and non-destructive and yet effective whilst measuring in a non-invasive way from close by as the waves penetrate without the creation of any hazards to health [221].

Even though this microwave sensor type is at a lower range of frequency to a level of a few tens' worth of GHz, there are no hazards to health for either humans or animals. Furthermore, they may easily retrofit them to existing set-ups within the industry.

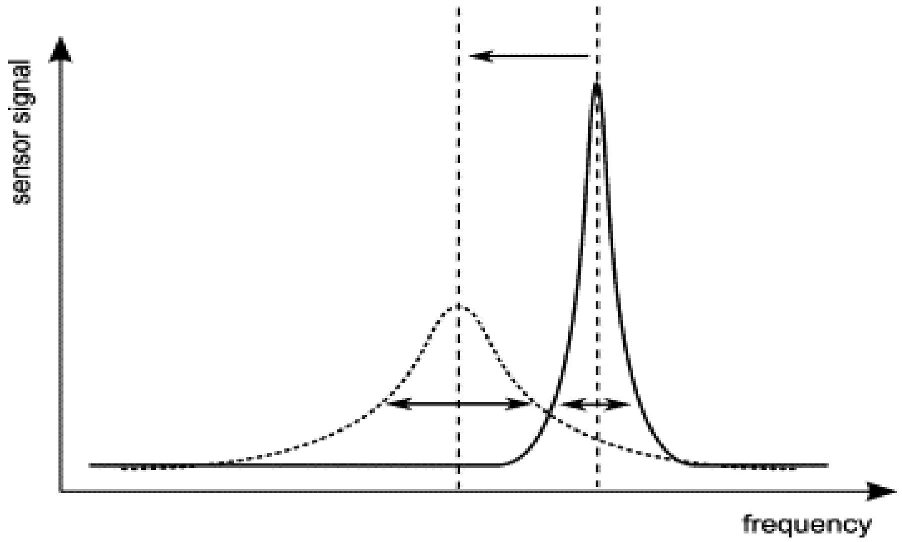

Figure 4.2: Microwave resonance curves, resonance curves in the air (solid line), resonance curve in wet material (dash line) [220].

A typical microwave system comes in three parts: the graphical user interface (GUI), a vector network analyser (VNA), and a sensor. See Figure 4.3 for a block diagram of a microwave sensor network. VNA is a commonly used instrument for the design applications for Radio Frequency (RF). It allows the output of RF and microwave devices to define network scattering parameters or S-parameters. VNA data can be presented using complex data (real and imaginary), magnitude and phase.

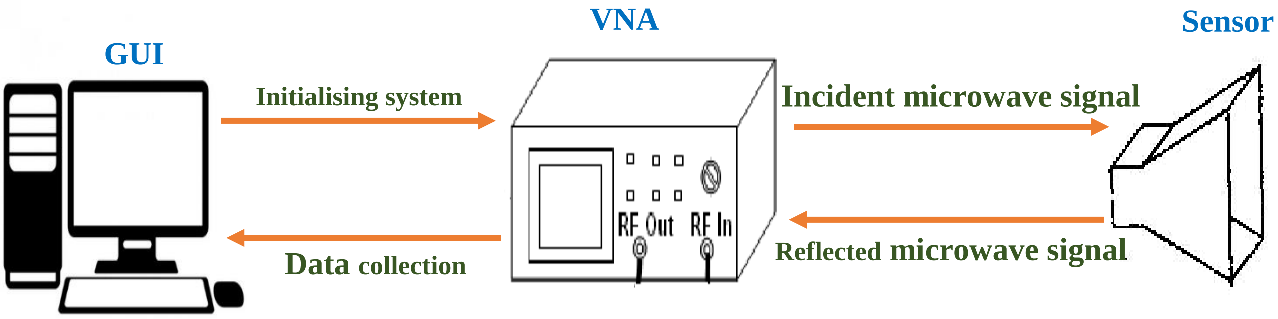

Figure 4.3: Microwave sensor technique.

The graphical user interface has complete control of the system. It initialises the VNA, configures the desired parameter (e.g. frequency range, S-parameters, etc.). Hence, it collects the most valuable information from a sensor via VNA, analyses data/reflected signal, and displays appropriate parameters/information on a laptop /PC screen (e.g. numeric data or expected measurement values / plotted).

4.3 Maxwell equation relation with electromagnetic waves

A nineteenth-century physicist named James Clerk Maxwell developed a theory that clarified the relationship between electricity and magnetism, stating that visible light makes up electromagnetic waves. Electromagnetic waves might exert forces on charges at a great distance from their source, making them detectable. There are two main components to EM waves, i.e., a magnetic field (H) and an electric field (E). As shown in Figure 4.4, these fields oscillate in phase in perpendicular ways to the energy propagation energy (z) and each other [212]. Within a vacuum, all EM waves travel at the speed of light. EM radiation is a repetitious periodic wave. Frequency relates to the repetitions per second for the waveform, the measurement of which is in Hertz (Hz). Wavelength (λ) refers to the distance travelled by a wave in one of its complete cycles.

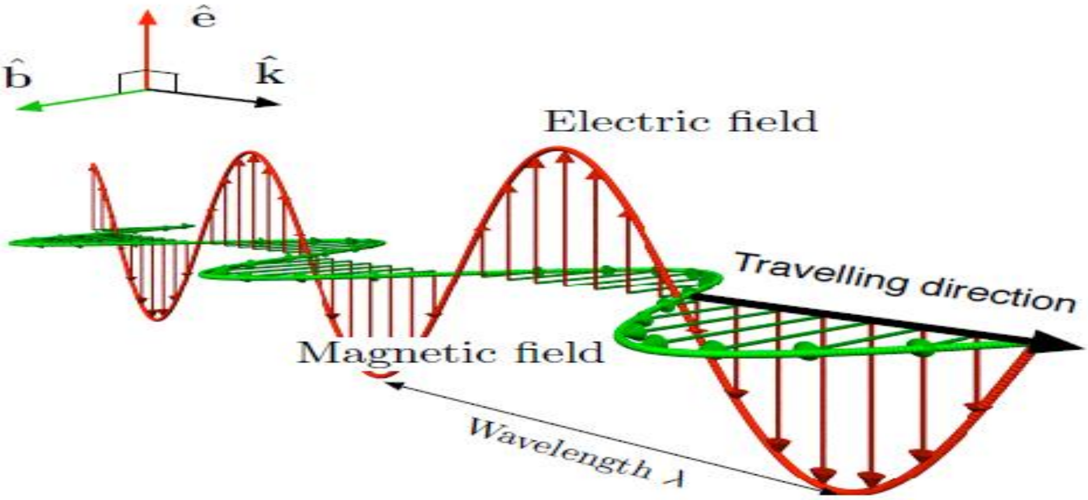

Figure 4.4: Electromagnetic waves components [222]

The distance travelled by a wave for completion of a single cycle is considered as the signal wavelength. If a periodic signal has a frequency (f) travelling at the speed of light, shown as (c), then equation 4.4 gives the associated wavelength (λ) [223] [224].

$$\lambda = \frac{\mathbf{c}}{\mathbf{f}} \qquad \text{Eq (4.4)}$$

All kinds of EM waves travel at the same speed within a vacuum, i.e. the speed now known as the speed of light 2999792458 m/sec; Maxwell calculated that electromagnetic waves would propagate at speed given by the equation 4.5:

$$c = \frac{1}{\sqrt{\varepsilon_{\circ}\mu_{\circ}}} \qquad \text{Eq (4.5)}$$

Where c is the speed of light, dielectric air constant is represented by ε_o, with a value of 8.85×10^{-12} Farad/metre and magnetic air permeability is represented by μ_o, with a value of $4\pi \times 10^{-7}$ Henry/meter. When travelling through other materials, however, the EM wave speed is reduced by a factor of $\sqrt{\varepsilon_r \mu_r}$. Equation 4.6 shows the effect upon wavelength [223, 224].

Speed of light c: A fundamental physical constant that is the speed at which electromagnetic radiation propagates in a vacuum has a value fixed by the international convention of 299,792,458 metres per second.

Dielectric air constant (ε_o): The dielectric constant is a measurement of the amount of electric potential energy stored in a particular volume of material under the action of an electric field in the form of induced polarisation.

Magnetic air permeability (μ_o): The property of the material allows the magnetic line of force to pass through it.

$$\lambda = \frac{c}{\sqrt{\varepsilon_r \mu_r}\, f} \qquad \text{Eq (4.6)}$$

4.4 Frequency and electromagnetic wave

A wave transfers energy from one place to another without moving material between the two places, or a wave is a disturbance that carries energy from place to place. A typical example of a wave is a wave on the ocean, where they take energy, as they cause erosion on the shore. Still, material such as water cannot continuously transfer onto the shore. Therefore, electromagnetic waves do not require a medium to travel through. They transfer energy without transferring particles and also travel by transferring energy between electric and magnetic fields. An electromagnetic wave transports its energy through a vacuum at a speed of 3.00 x 108 m/s. However, the propagation of an electromagnetic wave through a material medium occurs at a net speed that is less than 3.00 x 108 m/s. Some waves must have a medium to move through; these are called mechanical waves [225]. The number of occurrences per unit of time of a repeating event in which a periodic function repeats the same sequence of values during a unit variation of the independent variable, namely temporal frequency. This confirms the disparity between spatial frequency and angular frequency; the period is an interval of one cycle in a repeating event. Thus it can be concluded that the frequency is the reciprocal of the period [226].

Moreover, in the case of increasing frequency, the result is a shorter wavelength, whereas in the case of decreasing frequency, the wavelength will be longer, but at the same time, the resolution will change related to frequency. Therefore, the use of a high-frequency antenna will get high resolution but will achieve low depth. So, selecting an antenna is based on work conditions and requirements. If greater skin depth measurement is required, it will tend towards a low-frequency antenna and conversely [225]. The depth at which electromagnetic waves can be effective is the function of factors like water content, material conductivity, antenna gain and efficiency, receiver sensitivity, and transmitter pulse width [225]. Attenuation reduces signal strength during transmission, and attenuation is represented in decibels (dB). In the case of dB, it is ten times the logarithm of the input signal power divided by the signal power output of a unique medium. Consequently, positive attenuation causes signals to become weaker when travelling through the medium.

4.5 Frequency, wave velocity, and speed

Wave speed depends on the environment in which the wave is moving. It varies in solids, liquids, and gases. The distance a wave travels in each unit of time, such as the number of metres it travels each second, is known as wave speed. The following is a mathematical formula for calculating wave velocity:

Wave speed = wavelength (metres) x frequency (Hz). In many dry materials, such as concrete, sand, and soil, when small amounts of water are used in the mix, the dielectric of the wet material becomes higher and thus, the microwave velocity will decrease. For example, dry clayey soils have microwaves, which travel twice as fast as wet clayey soils [227]. The electromagnetic properties of the material govern the velocity of propagation in the material.

As a result, the signal speed is often reduced by the square root of the material's relative permittivity. Speed is described as a scalar quantity since it has magnitude but no direction. They have a magnitude and no specific direction, according to the definition of a scalar quantity. Speed has no defined direction and just one magnitude, making it a scalar quantity. Velocity is a quantity having magnitude and acting in a specific direction and is described as a vector. Equation 4.7 shows the relation between the velocity and speed of light.

$$v = \frac{c}{\sqrt{\varepsilon_r}} \qquad \text{Eq (4.7)}$$

4.6 Scattering parameters

Return loss and insertion loss can also be specified using S-parameters. If a microwave signal is an incident on the sample's surface, some signals reflect and transmit through the sample. Therefore, the ratio of the reflected signal to the incident signal is the reflection coefficient. The ratio of the transmitted signal to the incident signal is the transmission coefficient. In section 4.7, Figure 4.5 demonstrates the transmission and reflection coefficients. However, the transmission and reflection coefficients are specified in both directions as follows:

Port 1: Input Port

Port 2: Output Port

S_{11}: Input reflection coefficient

S_{12}: Reverse transmission coefficient

S_{21}: Forward transmission coefficient

S_{22}: Output reflection coefficient

S_{11} is the signal reflected at input port 1 as a ratio of the signal incident at input port 1. S_{12} is the signal output at port 1 as a ratio of the signal incident at port 2. S_{21} is the signal output at port 2 as a ratio of the signal incident at port 1. S_{22} is the signal reflected at port 2 as a ratio of the signal incident at the same port 2. Therefore, to measure S_{11} of a single horn antenna and S_{21} parameter between two antennas, experimental work was conducted to measure dry concrete samples, wet samples with tap water and salt water, and both parameters compared. S-parameters are used to describe how energy can propagate through material properties. S-parameters describe the relationship between different ports when it becomes especially important to describe a network in terms of amplitude and phase versus frequency, rather than voltages and currents. The author of [228] demonstrated this in an experimental study using a GPR method as a transmitted and received signal for monitoring moisture and chloride ingress into concrete. In [229] demonstrated this similarly in an experimental study using near and far-field microwave non-destructive methods for the determination of chloride content in concrete, citing the reflection (S_{11}) and transmission (S_{21}) coefficients of a concrete planar sample [229]. Moisture content inside concrete structures can be studied from the data of their interactions with microwaves. This interaction can be revealed in the form of a unique signal spectrum known as reflection (S_{11}) and transmission (S_{21}) coefficients [230]. The authors demonstrated further similar findings in their study, using two horn antennas, and investigated the propagation of EM waves through the concrete blocks and their interaction with water. Therefore, based on this research, in this study, two horn antennas and microwaves were experimentally used to investigate the propagation of EM waves through the concrete samples and their contact with different saltwater concentrations.

4.7 RF or microwaves and the concrete sample

A microwave must travel across free space to reach the receiver and detector. However, some obstacles are commonly encountered within the propagation area, such as buildings, windows, bridges, metallic structures, fog, and walls. When an EM or radio wave comes across changes to a medium, some or all of it could propagate into the new kind of medium as refraction, dispersion or absorption, whilst the microwave remainder reflects. With the hitting of obstacles by microwaves, there is an irredeemable loss of energy; however, that fact means that precise detection of refracted or reflected microwave energy can provide valuable information concerning the character in electromagnetic terms ($\varepsilon_2, \mu_2, \sigma_2$). The rules that govern the reflection of radio waves are, as with those that govern light waves, quite simple.

Figure 4.5 illustrates three media with equivalent transmission lines that encounter characteristic impedance forms, respectively shown as Z1, Z2, and Z3. The representation of the thickness of the wall is shown by d. As a reflection occurs, the incidence angle, the representation of which is θ_i, has a value that is the same for both the incident and the reflected rays. Furthermore, absorption usually causes a degree of loss whilst the signal is a passage through the medium. In real transmission paths for radio waves, often there is a reflection by a variety of different surfaces. So, there are multiple reflections and transmissions at the boundaries. There is a summarising of all reflected waves into the reflected wave, and all transmitted waves summarise into the transmitted wave [231].

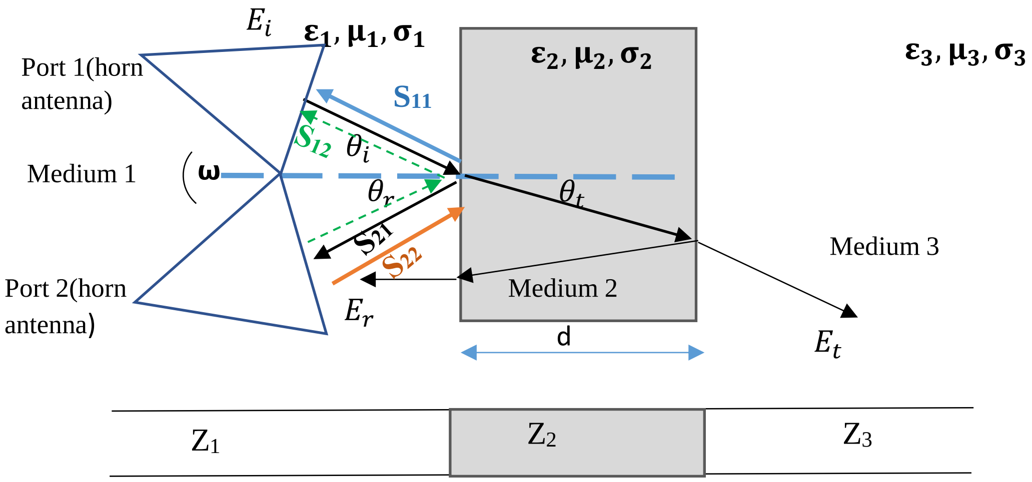

Figure 4.5: Microwave penetration and reflection are demonstrated using a schematic design

In general, transmitted and reflected waves will change the amplitude and phase of the incident wave. Typically, the transmitter and the reflected wave frequency will be the same as the incident wave frequency. The phase and amplitude of the transmitted and reflected components are examined by the known related Fresnel coefficients, which are dependent on dielectric material characteristics and the microwave signal incidence angle to the material [232]. S-parameters are complex as they are both magnitude and phase. The outside wall reflects the wave, which represents loss from a receiver within the building. A further loss comes from the nature of the building material, which leads to transmitted wave attenuation because of absorption of the transmitted wave with its propagation through that material. The absorption causes ohmic heating, the absolute amount of which is extremely small because the radio signal energy flux is also extremely small; however, serious signal attenuation may be caused by the mechanism. Attenuation, calculated in decibels, has simple proportionality with a material depth that the signal propagates through. As such, total attenuation depends upon the radio wave incidence angle for the building material.

The real part is the magnitude, and the imaginary part is the phase angle. Quite often, it is the case that more interest focuses on the magnitude, and there may only be references made to that. Both magnitude and phase change with load, input frequency, and sensor size alteration together with the source's impedance. In general, this research project was the only measurement of the S_{21} parameters; more discussion can be found within sections 4.6 and 4.7.

4.8 Antenna

An antenna is completed by using a conductor, which is usually made of a rod or wire and is used to receive or transmit radio waves. The performance is through a transition structure between free space and a device for guiding, such as a transmission line. The transmitter radiates EM energy into free space from where the receiver collects it. The same design of antenna may be utilised for both transmission and reception. However, there is a certain degree of resistance to radiation for every antenna, referred to as antenna impedance. The impedance of the transmission line and radio must be adequately matched to the antenna's impedance in order for a radio (transmitter or receiver) to supply power to it. Voltage standing wave ratio VSWR and also referred to as Standing Wave Ratio (SWR). The parameter VSWR measures numerically describe how well the antenna impedance matches the radio or transmission line it connects to VSWR. It represents the power reflected from the antenna and is a function of the reflection coefficient. The following equation defines the VSWR if the reflection coefficient is supplied by (Γ) [233]:

$$VSWR = \frac{1+|\Gamma|}{1+|\Gamma|} \qquad \text{Eq (4.8)}$$

S_{11} or return loss is another name for the reflection coefficient. Most antenna types have designs with an impedance of 50Ω; this is standard for microwave and RF systems. Most antennas are devices that are resonant and efficiently operate across the bandwidths of relative frequency. More ready radiation of power at high frequencies is comparable to the antenna dimensions and acceleration of charges to the maximum extent because the changes within an electric field are faster [234].

Antenna characteristics are determined by the type, shape, and size of the material employed. Various types of antenna can use for transmitting and receiving microwave signals; these are considered below, i.e. aperture antennas [235], microstrip antennas [236], wire antennas [236].

4.8.1 Aperture antennas

Several kinds of aperture antennas exist, such as the pyramidal horn, the conical horn, and the rectangular waveguide. Horn antennas come in various shapes and sizes, with examples including the pyramidal and conical types, the pectoral horn (H plane and E plane), the exponential horn, the ridged horn, the corrugated horn, the aperture-limited horn and the septum horn [237] [238] [239]. A horn antenna is a flared-out waveguide with better directivity and less diffraction. However, a microwave horn antenna produces a phase front that is uniform with an aperture that is larger than the associated waveguide and has a greater degree of directivity. Pyramidal horn antennas flare on both of their sides. If flaring is undertaken to both walls (E plane and H plane) of a rectangular waveguide, it produces a pyramidal horn. Flaring aids in matching the impedance of antennas to the impedance of free space so that there is better radiation; with avoidance of standing wave ratio, greater directivity is provided along with the narrower width of the beam. Horn antenna flare angle is a key factor for consideration; if it is overly small, then the wave that results, instead of being planar, will be spherical, and the beam that radiates would not be directive [240].

Thus, the angle of the flare ought to have an optimum angle value that is related closely to its length. Horn antennae have the primary advantage, however, of providing very significant levels of gain and directivity. For greater gain levels, horn antennae ought to have larger apertures. Also, to achieve maximum gain for a particular size of the aperture, the taper ought to be longer for the wavefront phase to be almost as constant across the aperture as is possible [235]. The basic kind of pyramidal shape is shown in Figure 4.6.

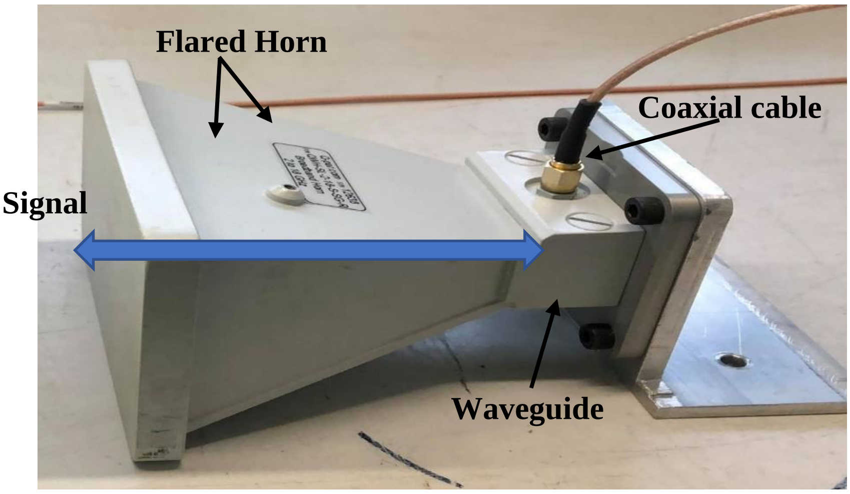

Figure 4.6: Pyramidal horn antenna [LJMU Lab sensor]

Horn antennas feature a directed radiation pattern with a high antenna gain, which may reach up to 25 dB in certain circumstances but is more common around 10-20 dB. Horn antennas have a wide impedance bandwidth, implying that the input impedance slowly varies over a wide frequency range (which also implies low values for S_{11}). The bandwidth for practical horn antennas can be in the order of 20:1 (for instance operating from 1 GHz -20 GHz), with a 10:1 bandwidth not being uncommon. Sometimes the gain of the horn antenna increases (and the beam diameter decreases) as the operating frequency increases. Because the horn aperture's size is often measured in wavelengths, the horn antenna is electrically larger at a higher frequency and has a smaller wavelength. The horn antenna is probably the most simple and most commonly used type of microwave antenna; it provides the transition between the propagation of waves within a line of transmission and radiating surface within free space. Horn antennas have very little loss, so the directivity of the horn antenna is roughly equal to its gain [241].

The advantage of using a horn antenna, in terms of the EM waves, is that it has a higher gain and directivity, as mentioned before. This means it can penetrate further into the concrete compared to the other antennas, such as the patch antenna, which can only penetrate the samples a few centimetres and only provide the surface information; that is why the horn antenna is used in this project. However, the previous research [208] used a wide-band 2-18 GHz pyramidal horn antenna to detect moisture content in the building fabric. The previous researcher used sensor technology to detect moisture levels in concrete structures. According to the findings, this technology can detect moisture. As a result, this technique will be used in this study to investigate the detection of chloride ions in concrete structures to determine whether they are also durable, as they can detect moisture. Due to its penetration depth capability, the preliminary usage of horn antennas allows us to measure the entire concrete sample rather than just the surface. Because the chloride level has a significant impact on the reinforcement concrete, it can induce corrosion depending on the amount and depth of penetration. As a result, the horn antenna had to monitor chloride ions at different penetration depths in this study.

4.9 Design consideration for horn antenna

Horn antennas are the simplest and most widely used microwave antennas, and they find applications in wireless communications, electromagnetic sensing RF heating [242]. Because the waveguide feeder has an impedance of 377 ohms and the horn antenna has a tapered or flared end, it may be used as an RF transformer or impedance match between it and free space. Horn antenna offers several benefits when employed. It helps inhibit signals travelling via undesirable modes in the waveguide from being radiated, providing a high amount of directivity and gains, and matching the guide's impedance to that of free space [243]. While it serves as an entry medium for signal interception for processing in receiving systems, it helps to clarify the dish antenna from its focal area in the case of transmitting, estimated from the parabolic dish's f/d parameters [244]. Dual-mode feed horns often provide excellent performance over a wide range of microwave bands [245]. Conical and pyramid horn antennas are the two primary kinds of horn antennas. It is very appropriate to have the correspondence of impedance with transmission lines of radiofrequency. Standing waves result in increased loss levels and frequently lead to failure of transmission [246]. The design has an optimal flare angle for various horns, which helps minimize all of the problems mentioned above. Horn antennae designed with consideration for the optimum flare angle is known as Optimum Horns [247].

4.10 Skin depth of concrete

The penetration of a planar electromagnetic wave into a substance is defined as the skin depth. The field's magnitude in the material is proportional to $e^{-X/\delta}$. Where δ = skin depth, x = distance into the material from the incident wave's surface. Skin depth is when the transverse electric and magnetic fields decay to 1/e of their amplitudes upon value entering the surface. The skin depth of EM waves is based upon the efficacy of the antenna radiation, the microwave foundation signal frequency, and the subsurface electrical characteristic. However, the skin depth is calculated from the real part of material permittivity and the loss tangent. The concrete or cement's loss tangent is illustrated by [56]:

$$\tan\delta = \frac{\varepsilon_r''}{\varepsilon_r'} \qquad \text{Eq (4.9)}$$

There can be an expression of concrete skin depth with:

$$\sigma_s = \frac{\mathbf{1}}{\boldsymbol{\alpha}}\,(\mathrm{m}) \qquad \text{Eq (4.10)}$$

Where the constant of attenuation (α) can be provided by:

$$\alpha = \frac{\omega}{c*\sqrt{2}} * \sqrt{\varepsilon_r'\mu_r'} * \sqrt{\sqrt{1+\tan^2\delta}-1} \qquad \text{Eq (4.11)}$$

Where c equates to a speed of light, ε_r' is the relative concrete permittivity, μ_r' is the relative concrete permeability set to equal 1 for concrete, and ω is the angular frequency.

Speed of light c: Light waves travel at various speeds through different materials. The speed of light in a vacuum, in particular, is 299,792,458 metres per second.

Relative permittivity ε_r': Relative permittivity is the factor that determines how much the electric field between charges reduces in comparison to the vacuum. The relative permittivity of concrete typically varies from 6 for naturally dry concrete to 12 for saturated concrete.

Relative permeability μ_r': The simplicity with which a fluid may pass through a porous substance is referred to as permeability.

Angular frequency ω: The angular frequency is defined as the angular displacement of any wave constituent per unit time.

There is a need to calculate attenuation constants and the skin depth for both dry and wet samples of concrete. So that there was an independent note of response to the electromagnetic field to both dry and wet types of concrete, for this study, the magnetic and dielectric properties were derived from S-parameter measurements upon representative samples placed within the waveguides [248, 249] and use of the algorithm of Baker-Jarvis [250]. The skin depth for the dielectric property of the electromagnetic wave signal for the marine concrete structure has been suggested, with the nominal cover ranging between 55-75 mm in terms of the civil engineering requirement. Therefore, the skin depth for the EM waves point of view has been selected and applied to satisfy the requirement from civil engineering for measuring the nominal and effective cover. This technology can be used in the civil engineering field for more inspection purposes. Also, more details about the skin depth, the nominal cover has been provided in chapter two, Literature review section 2.11. Because our focus was initially on the marine concrete structures, this parameter needs to be taken into consideration, but this could be further investigated for other civil engineering applications like bridges on a motorway, where the skin depth has to be 35 to 45 mm according to the BS EN 1992-2:2005 [65].

4.10.1 Rectangular waveguide used with different bands

Rectangular waveguides are one of the earliest types of transmission lines. They are used in many applications. Many components such as isolators, detectors, attenuators, couplers and slotted lines are available for various standard waveguide bands from 1 GHz to above 220 GHz [251]. The fields in a rectangular waveguide consist of several propagating modes that depend on the waveguide's electrical dimensions. These modes are broadly classified as either transverse magnetic (TM) or transverse electric (TE). The shape of the rectangular waveguide is as shown in Figure 4.7. A material with permeability and permittivity fills the inside of the conductor. However, a rectangular waveguide can't propagate below certain frequencies; this frequency is the cut-off frequency [252]. A rectangular waveguide is a structure that guides waves, such as electromagnetic waves or sounds, by limiting energy transmission to one direction, with little energy loss.

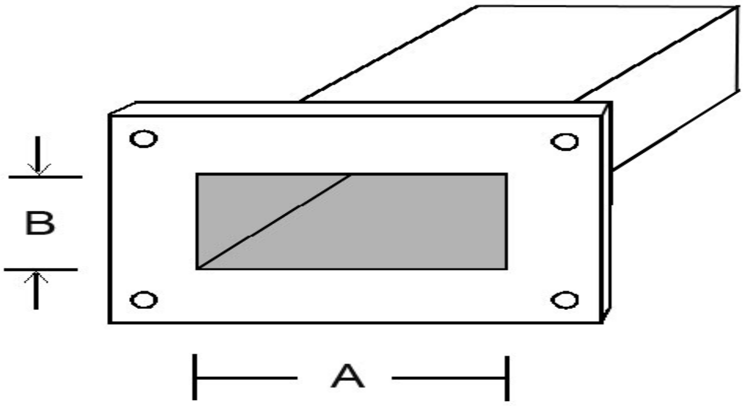

Figure 4.7: The shape of rectangular waveguide

In this project, three different bands are used, and only the dimensions of these three bands are changing and the frequency range because this project requires the establishment of a frequency for the operational use of the sensor. The purpose is to investigate the microwave signal reaction over various frequencies to the concrete structure with various chloride levels. The bands used in this project ranged from 2.35 GHz to 2.85 GHz within the S-band, 4 GHz to 7 GHz within the C - band and 8 GHz to 12 GHz within the X - band. A rectangular waveguide has different cross-sections based on various bands, such as the S-band of WR340 with dimensions of 86.36 mm by 43.18 mm, the C-band of WR159 with dimensions of 40.38 mm by 20.19 mm and the X-band of WR90 with dimensions of 22.86 mm by 10.16 mm. Chapter 5, section 5.3.2 explains the experiment as a Proof-of-Concept work with these different bands, and the findings are discussed in detail.

4.10.2 Used electromagnetic sensor working principle.

The primary principle of the horn antenna, operating at radio wave or microwave frequency range, is founded on signal interaction with a material sample medium under examination with various concentrations of salt water. Interactions between medium materials and the microwave signal may take the form of a phase shift or amplitude attenuation, and it determines the relative permittivity with moisture content and different saltwater concentrations. Figure 4.8 shows an experimental set-up involving a microwave horn antenna connected to a vector network analyser by Rohde and Schwarz and a PC that collected raw data and stored it through software developed within LabVIEW. The schematic diagram is presented in Figure 4.9 (a), and the developed sensor is shown in Figure 4.9 (b).

Also, a sample of wet concrete was monitored upon a scale to measure the lost weight due to drying whilst the experiments were undertaken. Because the microwave signal spread from the edge of the horn antennas, the microwave sensor was set 20 mm from the sample's surface to avoid monitoring any other items adjacent to the concrete sample during the experimental test. The surface of the scale was metal, and it is a good wave reflector.

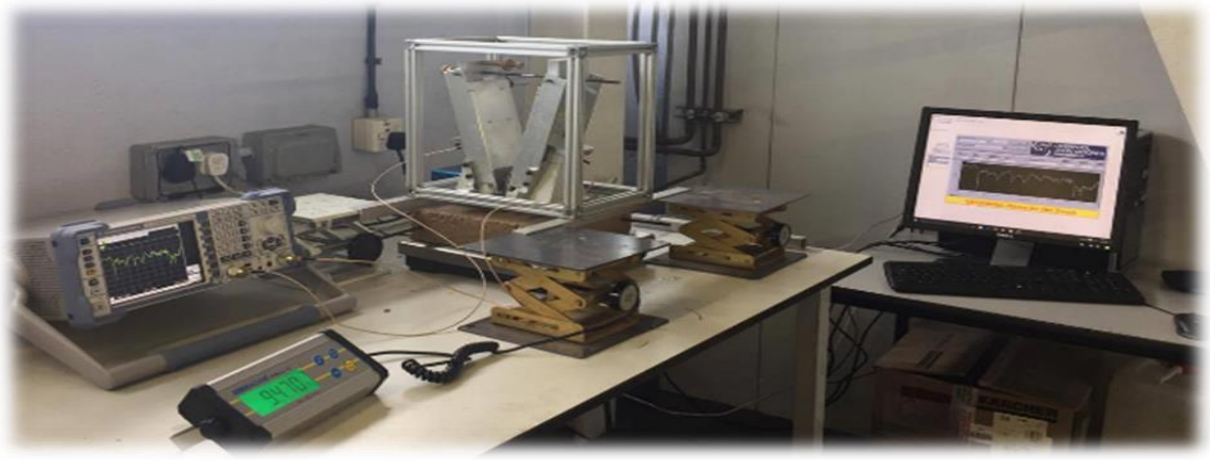

Figure 4.8: The experimental set-up for microwave sensing

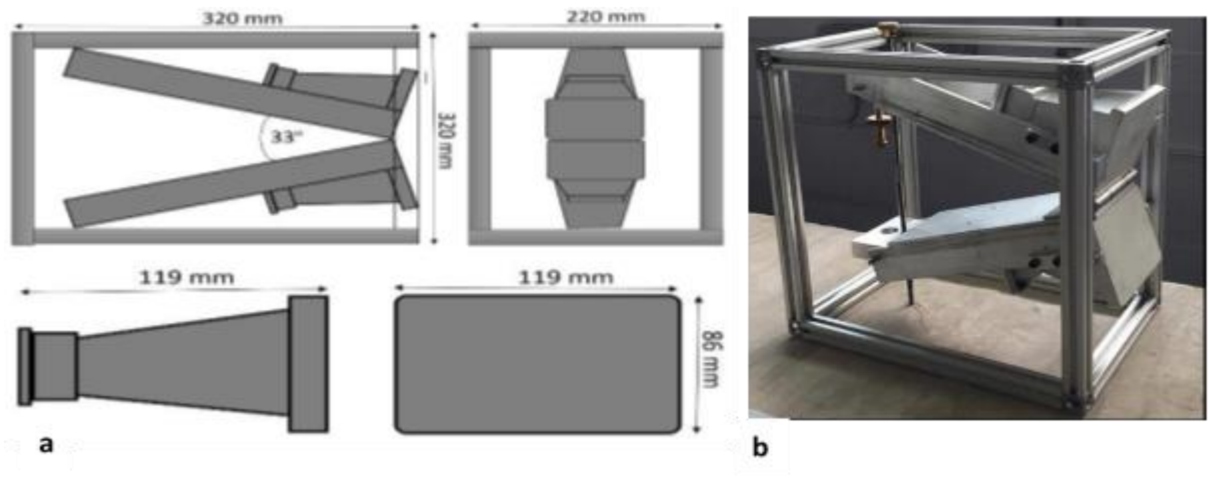

Figure 4.9: (a) Sensor Schematic, (b) Sensor Prototype

4.11 Summary

This chapter introduced the electromagnetic waves, which could potentially measure moisture and chloride ion levels in concrete. As part of electromagnetic waves, the microwave spectrum was highlighted as the most suitable frequency range for this investigation, mainly the 2-12 GHz frequency range. According to the previous study, it explained the concepts and theory for the most common electromagnetic sensors. Microwave sensing technology is a widely used engineering method for many different industrial applications (see section 4.2 for more details). Concrete is defined as a dielectric material, which will store energy when exposed to an electromagnetic signal. Therefore, the concrete can be described by its dielectric properties using the field method of electromagnetic waves. A dielectric material can define two independent electromagnetic properties: complex permittivity (ε*) and complex permeability (μ*). These definitions are well explained in section 4.2.1. S-parameters describe the relationship between different ports when it becomes essential to describe a network in terms of amplitude and phase versus frequencies, rather than voltages and currents. Moisture content inside concrete structures can be studied from the results of their interactions with microwaves. This interaction can be revealed in the form of a unique signal spectrum known as the reflection coefficient (S_{11}) and the transmission coefficient (S_{21}) (see section 4.6).

The pyramidal horn antenna was chosen as the most suitable type and structure of the current sensors due to its capability, low cost of production, and, most importantly, high penetration compared to other antennas due to higher gain and directivity and its design flexibility. The advantages of using horn antennae and their selection in this project are explained in sections 4.8.1 and 4.9. The skin depth of EM waves is based on the antenna radiation's efficacy, the microwave foundation signal frequency, and the subsurface electrical characteristic. The skin depth for the dielectric property of the marine concrete structure's electromagnetic wave signal has been suggested. According to the Eurocode, the nominal cover ranges between 55-75 mm in terms of the civil engineering requirements. A rectangular waveguide measures the concrete samples' skin depth, one of the earliest transmission lines. They are used in many applications. In this project, three different bands are utilised, the only experimental variations for the waveguides. Therefore, the operational frequency changes as well. The research methodology is described in greater detail in the following chapter: the sample preparation, experiment set-up, data analysis, and a description of how the sensor data was validated with the collected data using a partially destructive approach and an ANN model.

Chapter Five: Experimental Work

5.1 Introduction

This research aims to investigate and validate the use of Electromagnetic (EM) waves as a non-destructive technique to determine the chloride level in reinforced concrete structures. This chapter will describe the introduction, namely, the research methodology, the overall experimental regime (preliminary and primary tests), concrete mix design preparation, initial surface absorption test, experimental approaches, and data analysis. However, the chapter will start with section 5.2, the research methodology and provide the flow diagram of the research methodology. Then, section 5.3 will introduce the overall experimental regime including preliminary and primary tests, and Table 5.2 contains the number of samples and purpose of use in this research. This chapter will provide, in sections 5.4.1 and 5.4.2, the first measurements taken after the preliminary test and preparation of concrete mix design, in detail. Section 5.4.3-5.4.5 will demonstrate the experimental set-up of the continuous monitoring of the curing and drying process approach undertaken in this investigation. Section 5.5.1 will present the experimental set-up under various salt-water concentrations. Section 5.5.2 and 5.5.3 will introduce the chloride content preparation to submerge the concrete samples individually and demonstrate measurements taken of 5 water concentrations. Section 5.5.4 will show the chlorimeter tool as a partially destructive method to detect chloride levels in concrete. Then we will discuss Finlay, section 5.6, techniques for data processing, and the development of validation models based on collected data.

5.2 Research methodology

Develop the approach outlined below to meet the goal and objectives outlined in Chapter One:

- The first stage of this investigation was understanding the essential principles of the mechanism of chloride ion attack and the problems associated with chlorides present in concrete structures. Studied the theory to provide an understanding of the corrosion process and some electrochemical corrosion rate measurement techniques; also, an understanding of the impact of chloride content, moisture, and temperature on the dielectric constant of the concrete structures. We have carried out a literature review to understand the existing NDT technologies for detecting the level of chlorides in concrete structures and EM theory, including waveguides and antennas. The literature review established that a commercially available technique to detect the chloride level in a concrete sample is time-consuming, high cost, and mainly destructive. In addition, there are revised new techniques for chloride ions detection. However, they still have not met the industrial requirements, and some of the methods were more costly than the current state of the art, and others were unworkable due to sampling preparation requirements of the techniques. A previous researcher has reported that the electromagnetic wave sensor could be used as an alternative non-destructive method for identifying water content in concrete structures [253]. Journal papers, conference papers, and textbooks are used as the primary sources of background information. A flow diagram of the research methodology is presented in Figure 5.1.

- The next stage was to experimentally test a system with moisture and chloride detection to determine the signal spectrum. It was necessary to select the optimised angle of horn antennas as a transmitter and receiver system operating when the concrete sample was under the sensor involved optimising parameters, including the substantial sample size depending on the horn antenna surface. The sweet number point, frequency range, and power electronic (dBm) are linked by a coaxial wire and interfaced to a PC or laptop running National Instruments (NI) LabVIEW software to show the signal spectrum.
- A preliminary test of the concrete paving slabs submerged in water and salt water was carried out. Each concrete slab was immersed in salt water and tap water for 24 hours, then underwent a drying process, and the concrete samples were monitored every minute for 24 hours. The initial findings show that there are some differences and noticeable changes in the microwave signal. Still, it is significant enough to continue performing more experiments to understand further what changes can be seen in the electromagnetic wave signal.
- An experiment was constructed that utilised previously observed parameters to investigate changes of EM waves at microwave frequency with tap water and salt water in the paving slabs in an hour. It is also necessary to know the age of the concrete structures to check the propagation of EM waves through typical constructions. The main constructions that were studied in this project were concrete samples with and without reinforcement. The previous related studies recommended using two horn antennas. Therefore, in the current study, two horn antennas have been used to investigate the moisture content and level of chloride in the concrete samples. The first horn antenna transmits the waves, and the second one receives the signal reflected from

the studied material. The frequency range utilised in these investigations was 2 to 12 GHz. A machine learning technique in the new area of artificial intelligence aims to develop patterns to explain engineering applications. Hence, the developed design would be able to generalise the behaviour of complex engineering systems [254]. Over the last few decades, many machine-learning methods have been present. To validate the results of the electromagnetic sensor and the gold standard approach, we will combine the WEKA workbench classification and ANN methodology with each other.

Figure 5.1 A flow diagram illustrating the methodology development.

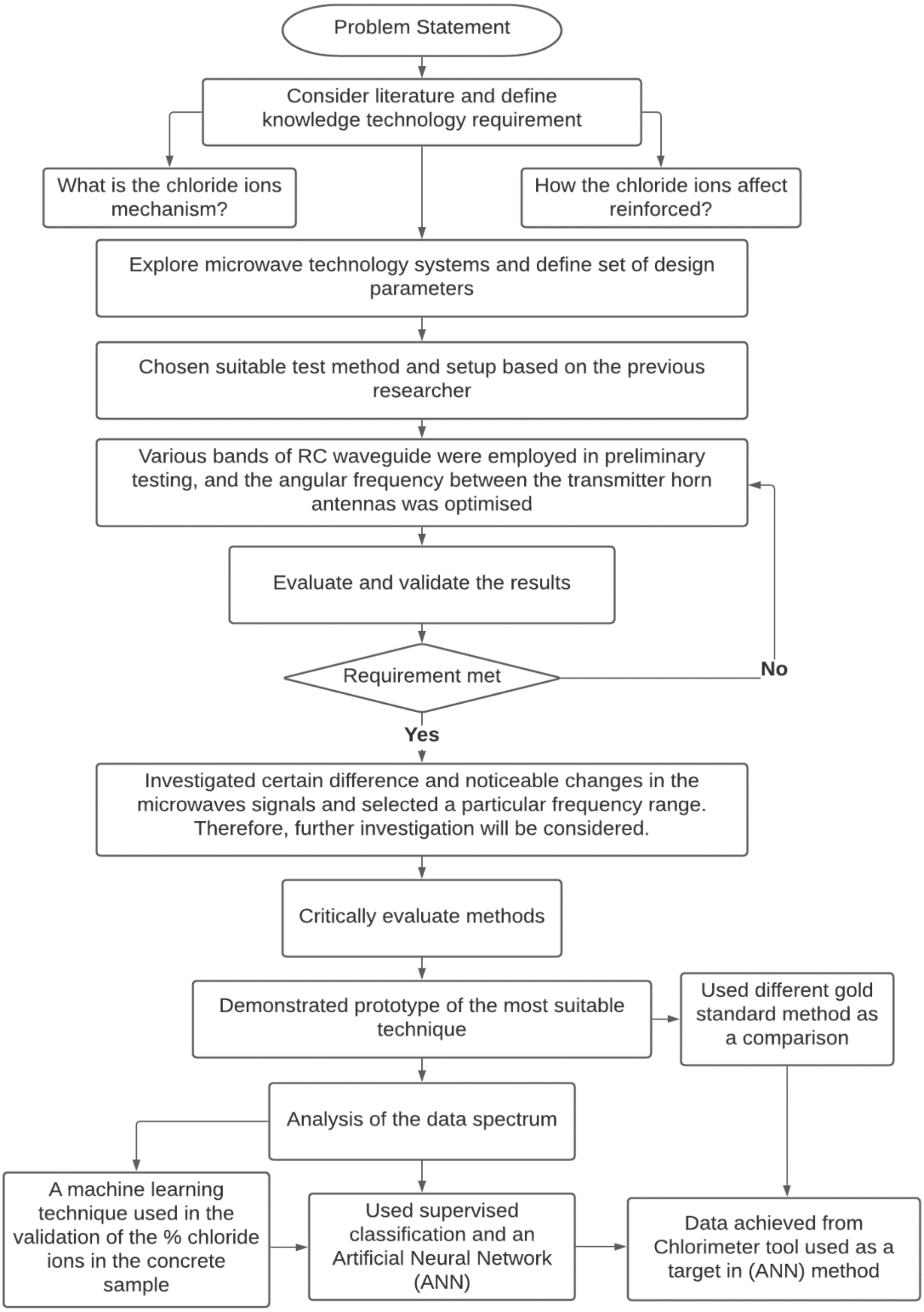

Figure 5.1: Overview of research methodology

5.3 Overall experimental regime (preliminary and primary tests)

This section demonstrated the number of samples that were prepared and used in preliminary and primary tests. Each section will discuss the experimental work and set-up on each of the groups separately. Table 5.1 indicates all the samples that were used for the test during this project. However, Table 5.2 indicates the main characteristics of each group of the concrete samples.

Table 5.1: The number of concrete samples exposed to microwave sensors

Group	Number of samples	Size of samples (mm)	Purpose
A	3	150 x 150 x 150	These three samples used to determine the permeability of the concrete and compressive strength.
B	4	250 x 250 x 60	These samples used as a preliminary test to measure the skin depth of the EM waves that need to penetrate the concrete blocks according to the civil engineering requirement; used three different bands of rectangular waveguide. In addition, using these samples was to establish the angular frequency between the two-horn antenna for the rest of the experimental work. Hence, these experimental set-ups and results are discussed in the following section 5.3.1in detail.
C	2	600 x 600 x 40	These two pavement slabs use as a preliminary experimental test to determine the effect of chloride ions and moisture on electromagnetic waves. The results of this test are shown in Chapter 6, section 6.2.
D	10	250 x 250 x 60	Then, following the same process as the three trial cubes in the lab, ten concrete slab combinations with and without reinforcement were made and cast. The electromagnetic waves are reflected by the reinforced concrete and varied reinforcement areas inside the

			concrete samples. In Chapter 6, the findings of two concrete samples without reinforcement after curing and drying are discussing. In addition, chapter 6 discusses two of the examples that have two rebars. Appendices D show the raw data results of six samples with reinforcement rebar at various saltwater concentrations.
E	5	300 x 300 x 150	Five unreinforced concrete slabs were mixed and poured. The proportions 1:1.5:3:0.7 kg were used in the standard concrete mix, which is more typical in European countries. The data from these five samples was used to determine the skin depth and reinforcement depth concerning the access depth reinforcement required for maritime concrete structures, ranging from 70mm to over 100mm depending on the concrete mix design. In Chapter 6, the results of all five samples with five different saltwater concentrations are discussed.

Table 5.2: Demonstrated the main characteristics of each group of concrete samples

Group	**The weight proportion of concrete mix design Kg/m^3**	**Compressive strength Mpa, after**		**The dry density of concrete Kg/m^3**	**Superplasticizer kg**
		7 days	**28 days**		
A	1:1.80:3.71:0.4	26.29	39.86	2416	0.032
B	1:1.82:3.69:0.4	=	=	2347	0.126
C	n/a	n/a	n/a	2216	-
D	1:1.82:3.69:0.4	=	=	2349	0.0126
E	1:1.5:3:0.7	n/a	n/a	2592	-

5.3.1 Initial surface absorption test (permeability test)

This test was undertaken to ascertain the permeability of the concrete samples and how fast they absorbed the water and salt water during the curing process. For experimental investigations on the air permeability of construction materials, surface layers, mainly concrete, the Torrent Permeability Tester (TPT) made by a Swiss company, Proceq, was used. The TPT is a modern device that is applicable for a non-destructive determination of the concrete air permeability. The equipment is used in conjunction with a vacuum pump for on-site and laboratory measurements. The basic parts of the device are a two-chambered vacuum cell and pressure regulator that regulates the air flowing into the internal chamber located perpendicular to the concrete surface. A further component of the measuring device is an indicator with a liquid crystal display, permitting data recording for up to 200 measurements. The initial surface absorption test (ISAT) is standardised in Great Britain as in BS 1881:208 [255] [256]. Under a pressure head of 200 mm, movement down a capillary tube attached to a cup monitors the rate at which water absorbs into the concrete.

When water comes into contact with dry concrete, it is absorbed via capillary action at a rapid pace at first, then at a slower rate as the water fills the capillary's length. The basis of initial surface absorption, is defined as the rate at which water flows into concrete per unit area at a stated interval from the start of the test at a constant applied head at room temperature. The measuring method relies on calculating both the permeability coefficient K_T and length L constants and is performed with numerical integration and derivation using an indicator tool. The issue is to establish the constant open concrete porosity, which is different for various concrete types. The developer of the TPT device and a team of co-workers established the measurement limits (see Table 5.3), based on comprehensive permeability tests conducted.

The air permeability factor K_T calculations with the TPT used the mean value of open porosity = 0.15, that was measured by the developer from a comprehensive set of tests[257]. However, three trial cubes of 150 × 150 × 150 mm with 10 mm limestone aggregate and 0.4 w/c ratios for the compressive strength and initial surface absorption test (permeability test) were prepared. Therefore, experimental work was further conducted with two concrete samples to conduct permeability testing in this project. The reason for doing this test in this project was to show how fast the water and salt water will penetrate the concrete sample, based on the porosity of the concrete. Figure 5.2 shows the experimental work of permeability testing. The experiment results are explained in chapter 6, section 6.1.

Table 5.3: Classification of the quality of the concrete cover according to K_T [256]

Classification of the concrete cover quality		K_T **Measured at 28 days [e^{-16} m^2]**
1	Very good	$K_T < 0.01$
2	good	$0.01 < K_T < 0.1$
3	normal	$0.1 < K_T < 1.0$
4	bad	$1.0 < K_T < 10$
5	Very bad	$K_T > 10$

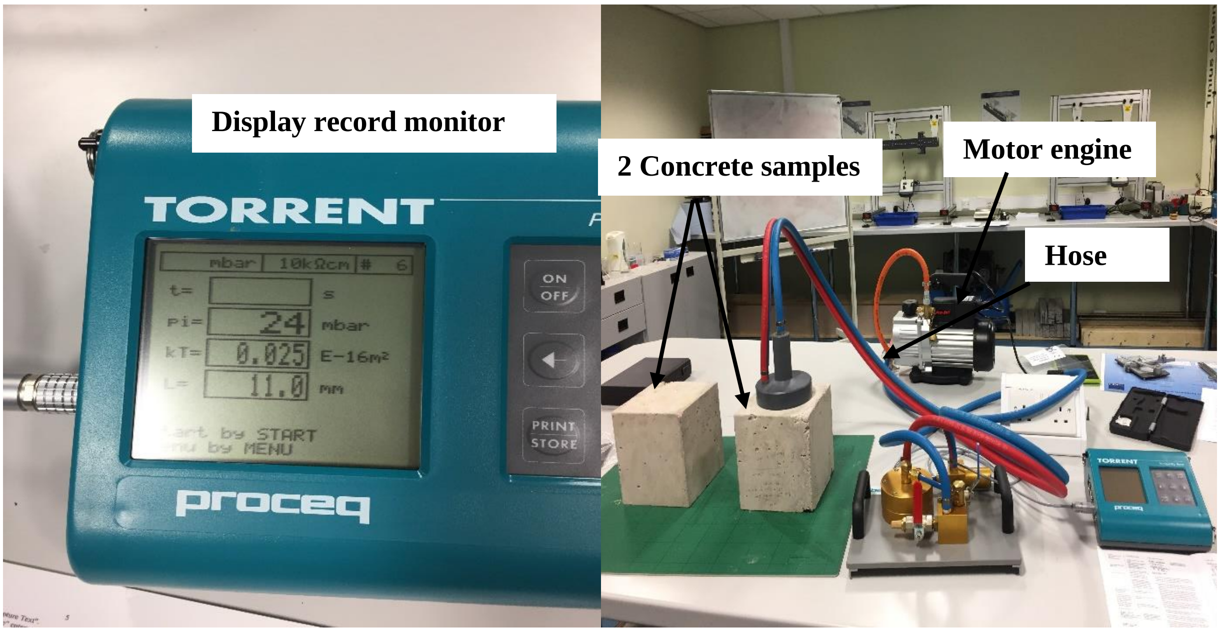

Figure 5.2: The experiment set-up of the permeability test

5.3.2 Proof of concept experiment

Experiments were conducted to determine the imaginary and complex relative permittivity of dry and wet concrete samples with water and salt water. The measurement of S-parameters through reflection and the transmission of three different band frequencies is mentioned in section 4.10.1. Two concrete specimens (250 mm x 250 mm x 60 mm), were prepared, both with water-cement ratio w/c 0.4, produced using tap water and Ordinary Portland Cement type II. These specimens were then left in the hydration room for 24 hours and left to cure, one in tap water and the other in a saltwater solution of 3.5% for 7 days. Table 5.4 shows the specific gravity of the components and the specifications of the mixed proportions of the concrete. Using limestone aggregate in the concrete mixtures of this experimental work is due to some benefits of the aggregate, such as the low possibility of an alkali-silica reaction, good strength, and, more importantly, decreasing the drying shrinkage in concrete [258]. After 7 days of curing, the samples were cut very carefully to make sure they fit within the S, C and X band waveguides without leaving any gaps. The samples are cut into the following: a) 101.52 mm length that fitted into the section of S-band waveguide, b) 120.87 mm length that fitted into the section of C-band waveguide, c) 40.75 mm length that fitted into the section of X-band waveguide.

Table 5.4: The concrete composition with OPC [259]

Material used	**Kg**	**Specific gravity (g/cc)**
Ordinary Portland cement OPC (CEM II)	3.10	3.12
Fine aggregate	5.66	2.65
Coarse aggregate size (10 mm)	11.48	2.70
water	1.24	1.0 at 4C°
Superplasticizer	24.8 grams	1.19-1.24 at 25C°

However, whilst cutting the samples, a slight excess remained on the cross-sectional area affecting the sectional fit in the metal waveguide, as nearly all samples were chipped away during their cutting. The air gaps are a primary reason for inaccuracies within such measurements [260]. Figure 5.3 shows the experimental set-up for the 3 different bands.

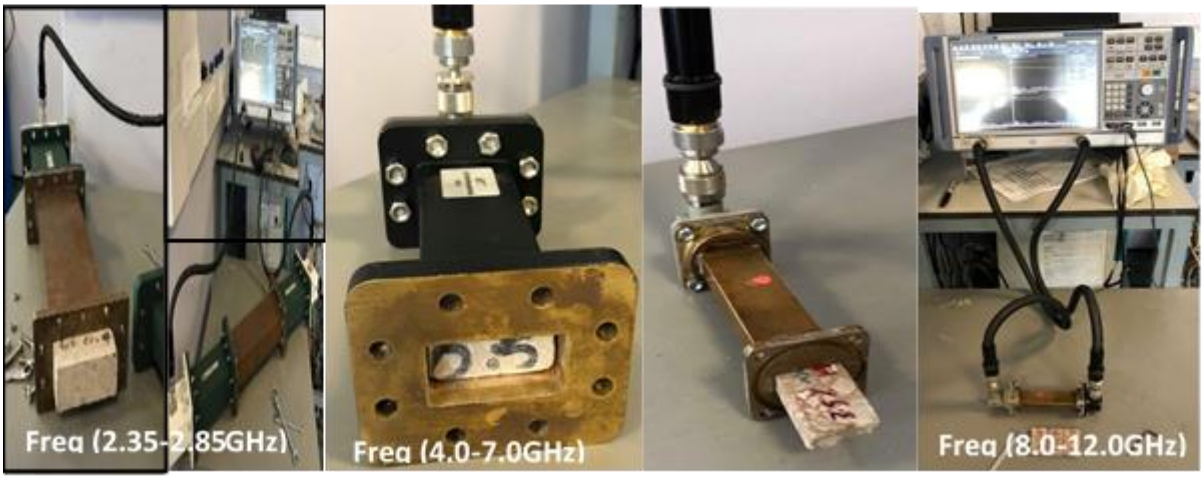

Figure 5.3: Experimental set-up with RC Waveguide

The data presented in [56] refers to the imaginary and real parts of the complex permittivity for the hardened concrete. The complex permittivity data characteristics for varied water-cement ratios and water volume absorption situations are recorded. There was a recording of the results at 24 GHz, 9 GHz and 3 GHz. In the compelling case of when concrete may be considered dry or as having a tiny amount of water content, the imaginary part and the complex permittivity are found to be between 0.1 and 0.7. The real component discoveries range from 5.0 to 7.0. Also, concrete that may be considered fully saturated or wet, the imaginary part of complex permittivity can vary from 1.5 to 2.9 and the real part from 9.0 to 20.0 [261, 262]. Figure 5.4 and Figure 5.5 (a, b & c) show concrete permittivity, and the loss tangent (tanδ) and the real part (ε_r') in the selected bands; see equation 4.2 in chapter 4 section 4.2.1 for definition. Also, as the evaporation process in the saltwater-soaked samples continues, the salinity of the remaining solution increases. At 2.35 -12 GHz, the dielectric properties of salt water are markedly different from tap water. It can be seen from the figures that tanδ and ε_r' for the concrete begin to fall as the frequency rises, a type of behaviour that is well-recognised for polar dielectrics such as with water [260]. The relative permittivity of tap water is only slightly higher than that of salt water with 3.5% NaCl. However, the loss tangent of salt water with 3.5% NaCl is significantly higher than tap water. These differences get larger as long as the NaCl solution of water increases and as more pore liquid evaporates.

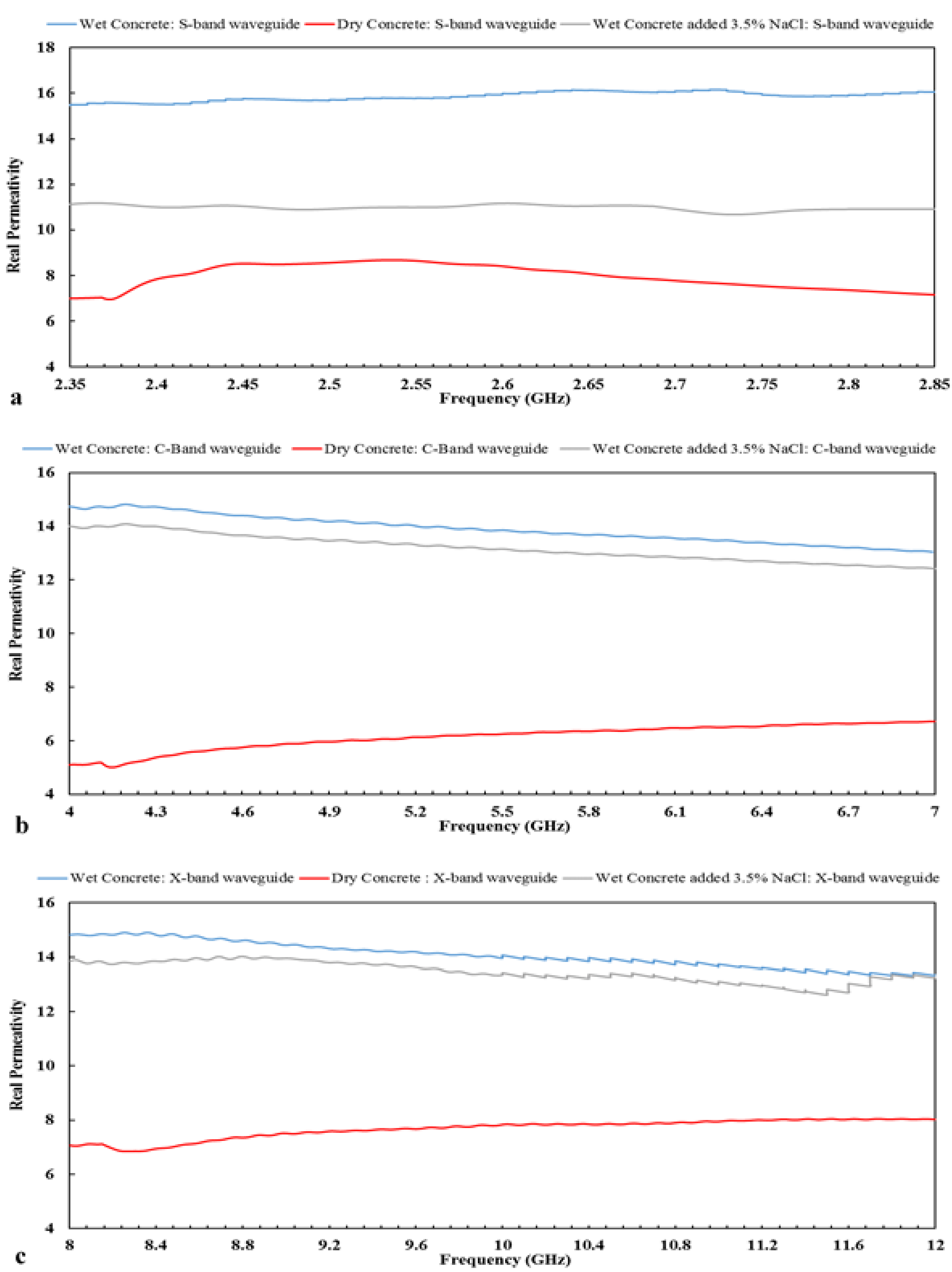

Figure 5.4: A dielectric permittivity of concrete samples dry, wet with tap water and 3.5% NaCl inserted into three different bands respectively with a temperature of ± 21 C

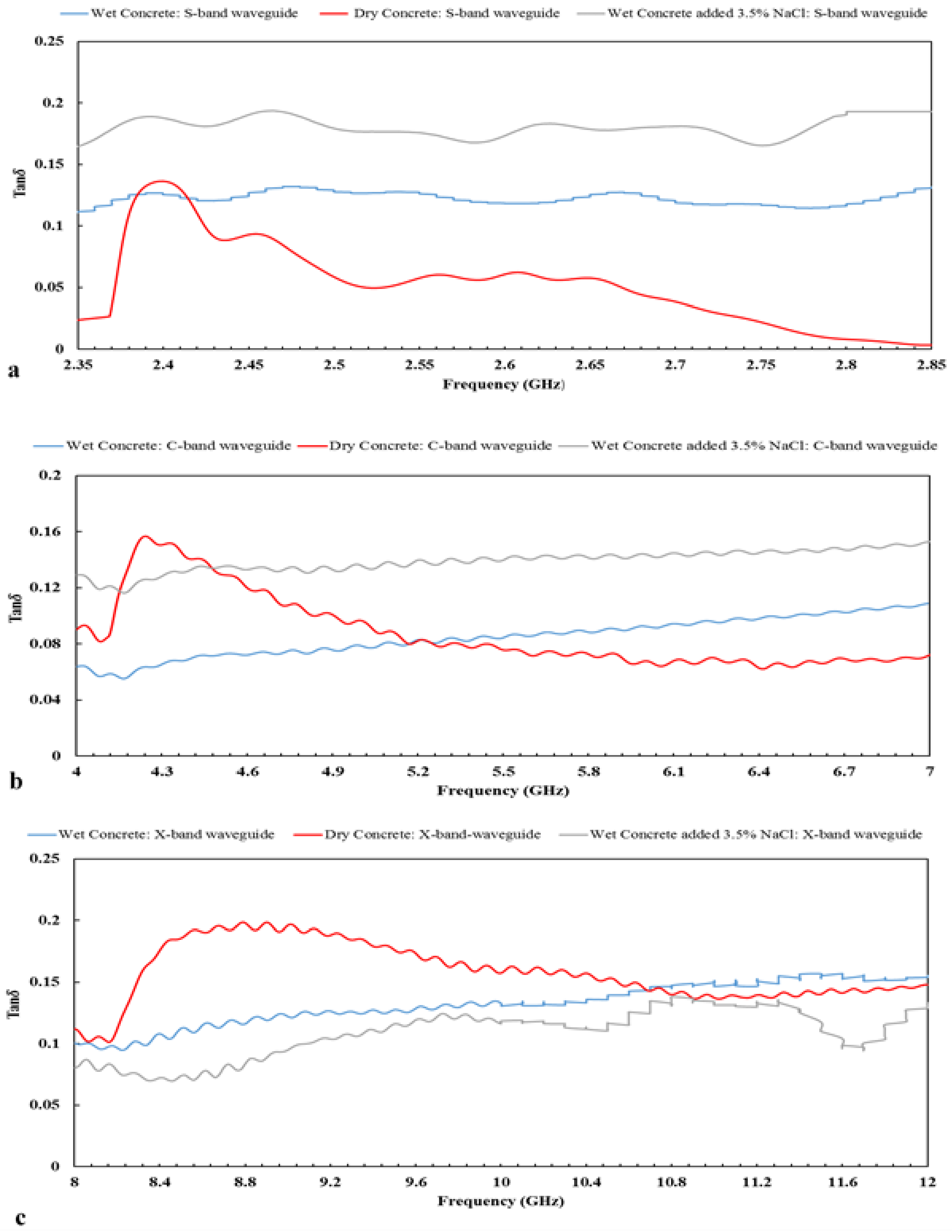

Figure 5.5: Lost tangent concrete samples dry, wet with tap water and 3.5% NaCl inserted into three different bands respectively with a temperature of ± 21 C

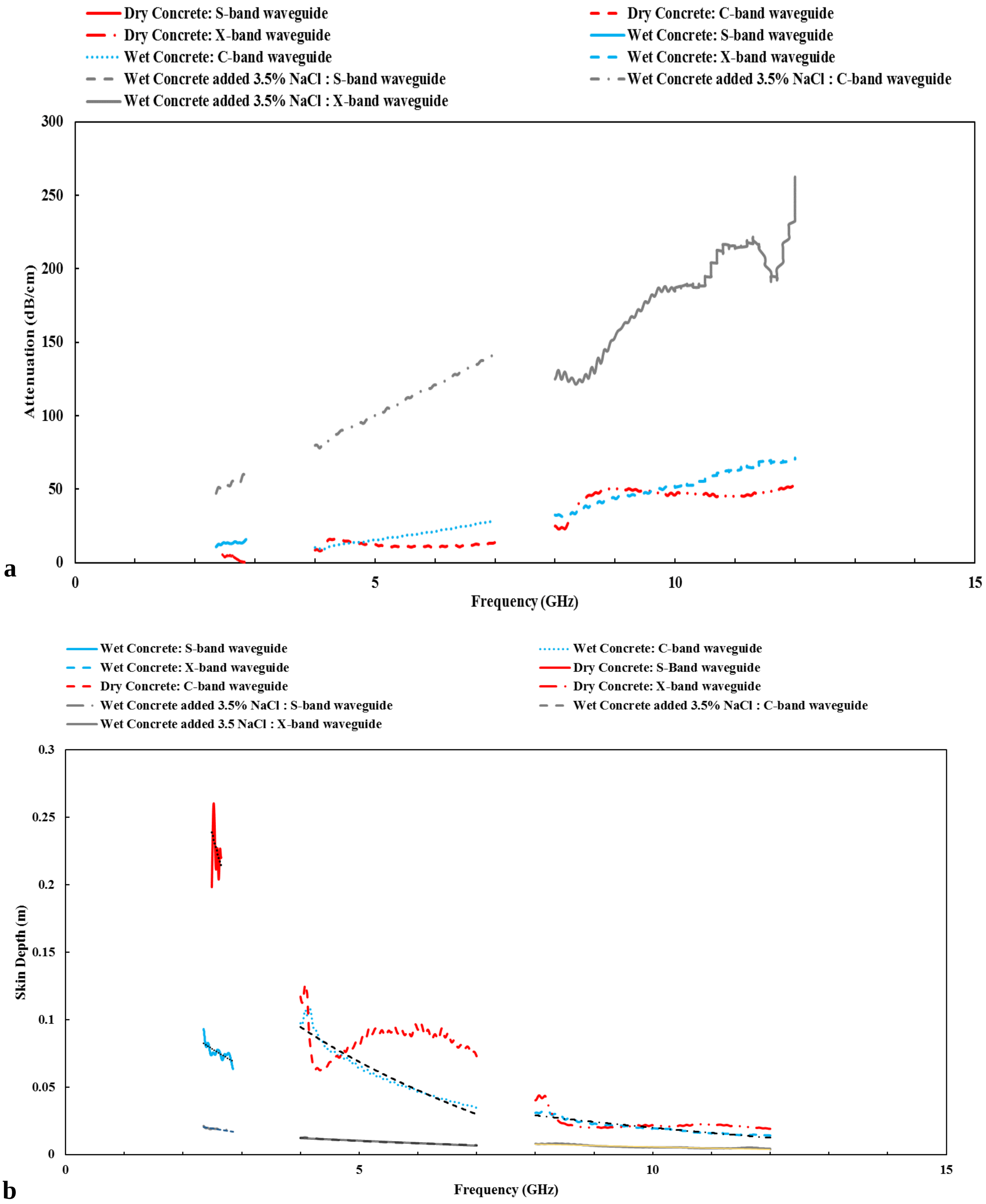

Figure 5.6: (a) Presented the skin depth and (b) attenuation constant of dry, and wet with tap water and salt water, concrete data measurements from three different bands.

In Figure 5.6 above, a) refers to the skin depth for concrete with tap water, salt water and dry samples within the 3 different bands, i.e. S-band, C-band and X-band, with the waveguide holder of the sample as a frequency function. Previous research has calculated the attenuation constant for concrete samples and the skin depth at different humidity levels [56]. The data for this investigation for dry and wet concrete do align, therefore, to previous research. For the aims established for this experimental undertaking, it has been necessary to discover to what depth the electromagnetic wave propagation needs to penetrate through the slabs of concrete for the detection of ions of chloride. However, for condition XS3 of marine exposure, the rule for the standard depth for reinforced concrete for chloride detection within the field of civil engineering is around 70 mm.

As a result, the optimum angle between both horn antennas determines using these civil engineering requirements for concrete structures exposed to chloride ion conditions and skin depth calculations. Also, if the reinforced concrete has light aggregate within it, the cover depth should increase to 80mm due to the increase in porosity. Furthermore, the goal of the cover thickness is not just to protect the reinforcement but also to ensure concrete and composite structural action of steel and provide fire protection and resistance to abrasion. In practical terms, the cover thickness should not exceed 80-100 mm [263]. This research has considered concrete as a dielectric material with both real complex permittivity and effective conductivity.

Figure 5.6 (b) clearly shows the calculated skin depth of dry and wet concrete samples from the measurements of the C-band waveguide, which enables EM wave propagation in concrete at 5.42GHz for up to 70mm-80mm. Figure 5.5 (a) shows the frequency curve of the attenuation constants for dry and wet concrete samples (a). The constants of attenuation for concrete samples are determined by the loss tangent and complex relative permittivity; if the loss tangent increases, the attenuation increases with a higher frequency because they are directly related. Whilst there is an increase in the attenuation, the skin depth begins to fall with increased frequency due to the inverse proportionality of skin depth to the constant of attenuation, as in equation 4.6 section 4.10 in chapter 4.

5.3.3 Preliminary experimentation with the horn antenna

This section did this experimental work as preliminary work to see if the S_{21} and S_{11} parameters could be used with concrete samples and to see if there was a relationship between the skin depth and the concrete penetration depth. In demonstrating the state of the art, those preliminary experiments are utilised to improve the methodology and justify the rest of the experimental work. Figure 5.7 shows a set of horn antennas and one single horn antenna via which the microwave signals are reflected and transmitted while penetrating the concrete sample in both directions.

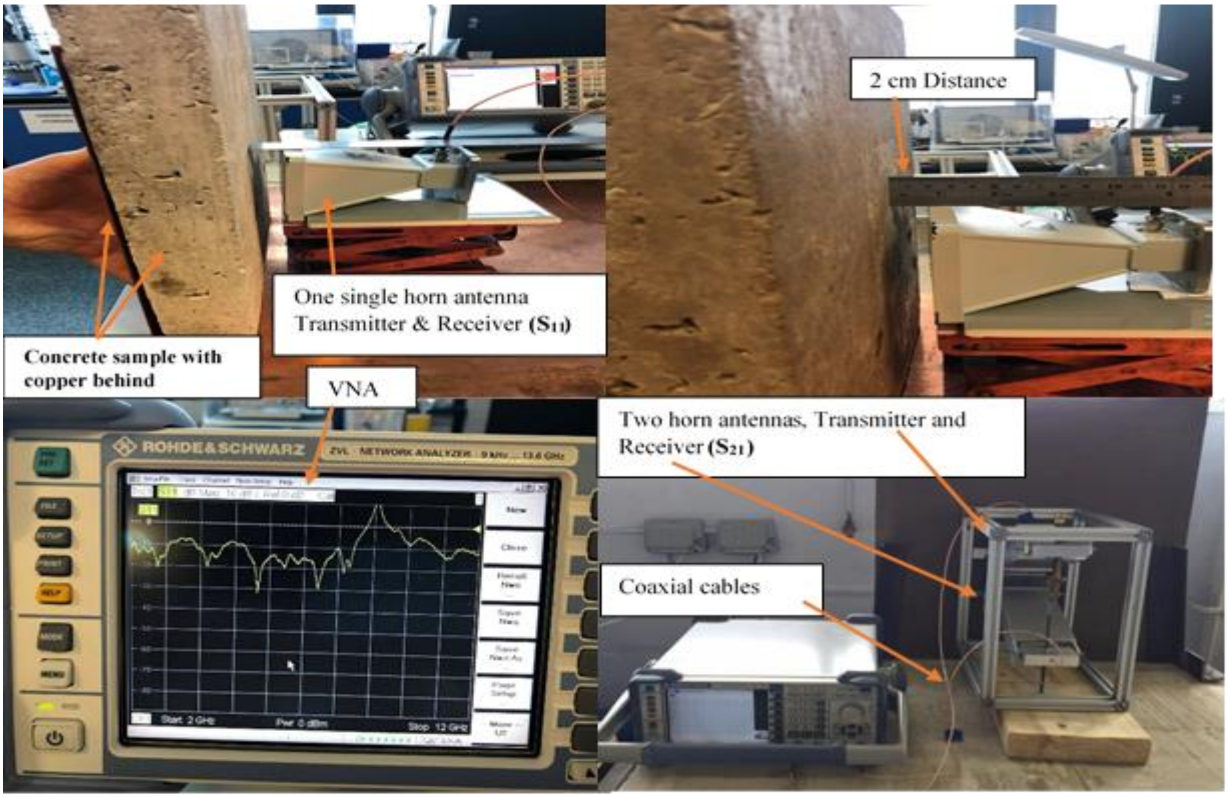

Figure 5.7: Experimental set-up for both single horn antenna & two horn antennas to measure S-parameter

Figure 5.8 (a and b) demonstrates the comparisons of S_{21} of a set horn antenna and S_{11} of single horn antenna measurements at a distance of 2cm from the surface of the concrete block, taken every one minute with five repetitions. The effects of microwave contact on chloride ions and moisture content inside concrete structures can be investigated. This interaction can be described as being in the form of a unique signal spectrum known as a reflection coefficient (S_{11}) and the transmission coefficient (S_{21}) [230]. It can be seen there is a noticeable change in the EM wave's signature. The amount of water and salt water is assumed to decrease or evaporate during the drying process, causing the change. Therefore, the figure clearly shows a steady amplitude shift at the frequency between 2-12 GHz. The relative permittivity of tap water is slightly higher than the samples with salt water with 3.5% NaCl and dry concrete. However, the relative loss factor of salt water is significantly higher than that of tap water. The value of S_{21} with the same distance, 2 cm, from the concrete surface is more elevated than -60 dB, which can still be detected by a VNA. Therefore, the peaks on both figures represent the amount of water, salt water and material properties in the concrete specimens, which significantly influences the microwave signal. However, the method will be used for further examination in this research project to evaluate the level of chloride ions in concrete structures, based on previous research results and this preliminary experimental work on a set of horn antennas.

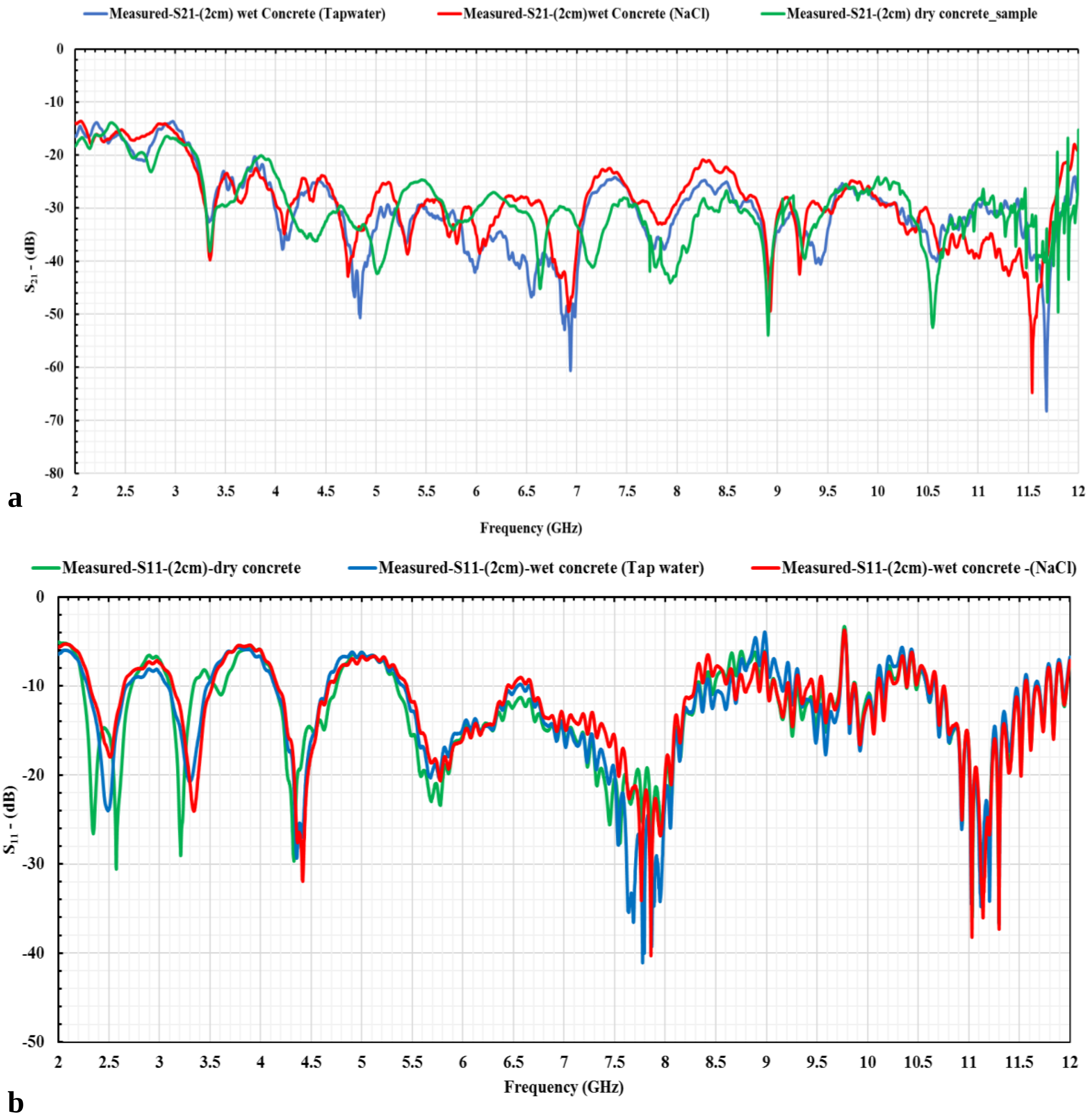

Figure 5.8: (a) S_{21} measurement, (b) S_{11} measurement.

5.4 Electromagnetic wave sensor test procedure

5.4.1 Initial experiment

In this test, a square pavement limestone aggregate concrete slab with dimensions 600 x 600 x 40 mm is used as the sample material. Figure 5.9 shows an experimental set-up diagram. Figure 5.10 shows a weighted and submerged sample in water, and Figure 5.11 shows an experimental set-up. The frequency is set to between 2 - 12 GHz due to the horn antenna limits on operational frequency. The microwave sensor was placed 2cm in front of the concrete paving to avoid monitoring any other items around the sample during the test. The signal radiated from the side of the horn antenna and the horn antenna was directly connected to the Rohde & Schwarz Vector Network analyser (VNA) and a PC. The VNA was connected to the PC via a crossover Ethernet cable. The remaining moisture content in the concrete samples was calculated by using equation 5.1 [262]. The equation used the weight of the dried samples before being submerged into the solutions and wet samples after being taken out of the solutions. Table 5.5 presents the calculations related to moisture in the paving slab concrete.

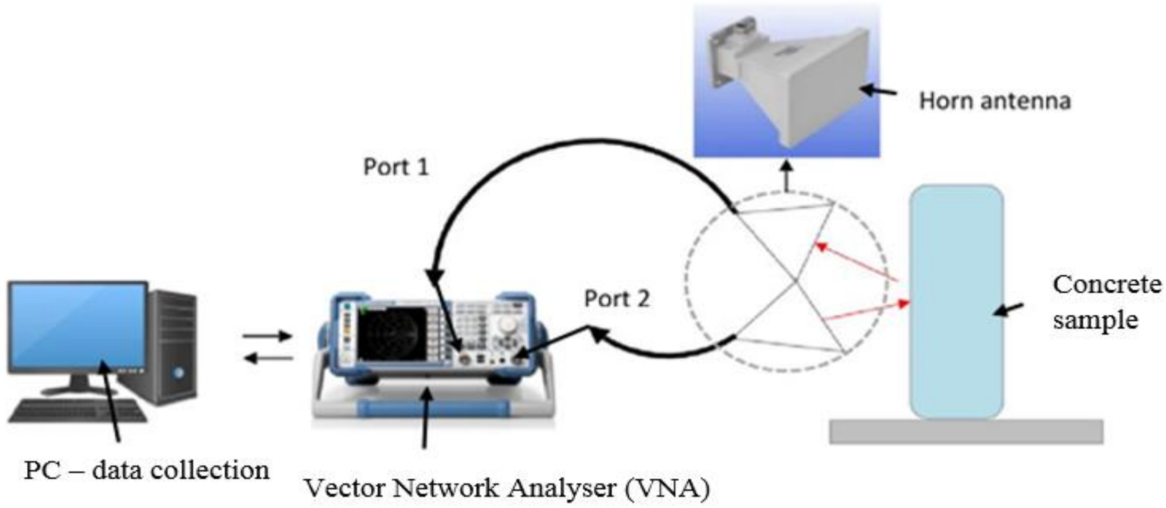

Figure 5.9: The experimental set-up is illustrated schematically

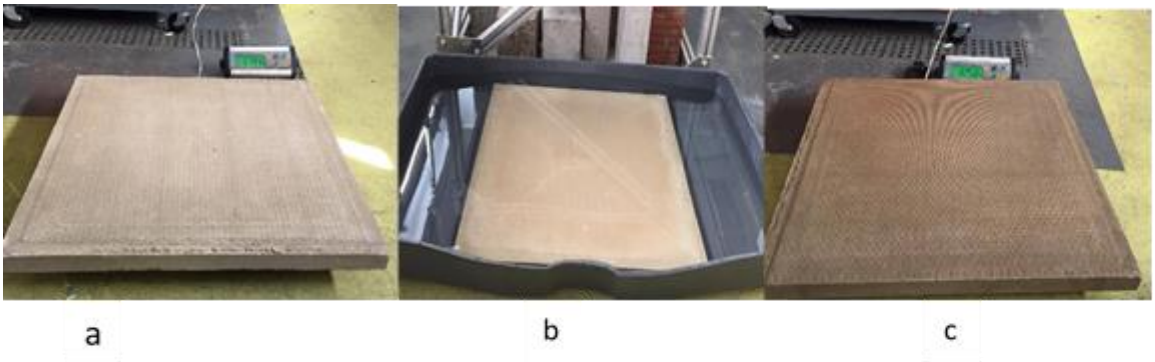

Figure 5.10: (a) Dry concrete paving sample being weighed. (b) The sample was submerged in tap water for 24 hours. (c) Using a scale to weigh the wet sample after being submerged in tap water

Figure 5.11: An experimental set-up

$$\mathrm{M} = \left(\frac{\mathrm{W_{wet}} - W_{dry}}{\mathrm{W_{dry}}}\right) \times 100 \qquad \text{Eq (5.1)}$$

Where Ww_{et} = mass of specimens at the time of measurements
W_{dry} = dried sample

Table 5.5: Demonstrated the percentage of moisture absorption and evaporation,

Type of water	The original weight of the dry sample (Kg)	Weight of wet sample (Kg)	Weight of sample after drying off (Kg)	Amount of water absorption by sample (%)	Amount of water evaporated after 24hours (%)
Fresh Water	31.92	32.58	32.08	2.068	1.56
Salt water	32.20	32.48	32.26	0.870	0.682

The second preliminary test was conducted for the pavement slab concrete submerged in the saltwater solution for 24 hours with 2.53% salinity (in this stage, table salt (NaCl) has been used). The conductivity meter (Hanna Instruments) was used to measure the electrical conductivity of the solution. It is commonly used in freshwater systems to monitor the amount of salt in the water. The amount of table salt added into the tap water to simulate seawater's conductivity was measured, approximately 50 mS/cm [264]. Table 5.6 shows the results of the conductivity test obtained for tap water and mixed with salt. The purpose of this table is to show how much salt was added to the 500 ml tap water to simulate the conductivity of seawater. In these quick tests, there are only 26 grams of salt added to one litre of tap water with a measured conductivity of 40.22 mS/cm, which is below the conductivity of seawater, which is approximately 50mS/cm, to see how this rate of salt affected the electromagnetic waves. To reach the conductivity of seawater, it needs 35 grams of salt to be added to one litre of tap water because the seawater contains 35 grams of NaCl in one litre. But in this experiment only 26 grams of NaCl was added into one litre of tap water; this is shown in further experimental work.

Table 5.6: The conductivity measurement test results obtained.

Amount of NaCl (gram)	Conductivity test, (mS/cm)
0	0.018
3	8.20
5	15.08
5	16.92
Total salt (26) in one Litre	40.22
Seawater contains (35) in one litre	50

5.4.2 Preparing the concrete mix design

Mix design prepared three trial cubes of 150 x 150 x 150 mm for the compressive strength and initial surface absorption test (permeability test). Hence, the cubes must be fully compacted. After 24 hours, the cubes were taken from the moulds and immersed in tap water at ambient room temperature (20±1C°) for 7 or 28 days to test cubes in saturated and dry surface conditions. Then 10 concrete slab mixtures of size 250 x 250 x 60 mm with and without reinforcement were prepared and cast, using the same procedure for preparing the three trial cubes in the lab according to British standard BS 8500-1:2006 [59]. The rebar size used in these concrete slabs was 6 mm. Hence, we selected the size of rebar to add to the concrete slab because of the thickness. A water-cement ratio (w/c) of 0.4 was used, and the detailed mixture proportions of the concrete studied, and the specific gravity of materials is given in Table 5.7.

Specimens were exposed to several curing solutions procedures to acquire varying levels of water absorption:

Curing a: Four specimens, one cast with one rebar, one with two rebars, one with crossing rebars and one with mesh rebars, were submerged in regular tap water at the ambient room temperature (20±1C°) for 28 days.

Curing b: Four specimens, one cast with one rebar, one with two rebars, one with crossing rebars and one with mesh rebars, were immersed in a saltwater solution (NaCl) with 3.5% salinity at average room temperature for 28 days, to investigate how much electromagnetic wave energy is absorbed by adding a different amount of salt into the tap water. The other two plain concrete slabs were separately submerged in their respective solutions to within 3.2 mm of their top surface and were used as reference test specimens for monitoring the effects of the tap water and rock saltwater solution during the curing period for 28 days. Figure 5.12 shows the preparation of 10 concrete sample castings. Figure 5.13 shows the submerged concrete samples in different saltwater concentrations. Figure 5.14 shows the experimental set-up for the curing process for over 28 days.

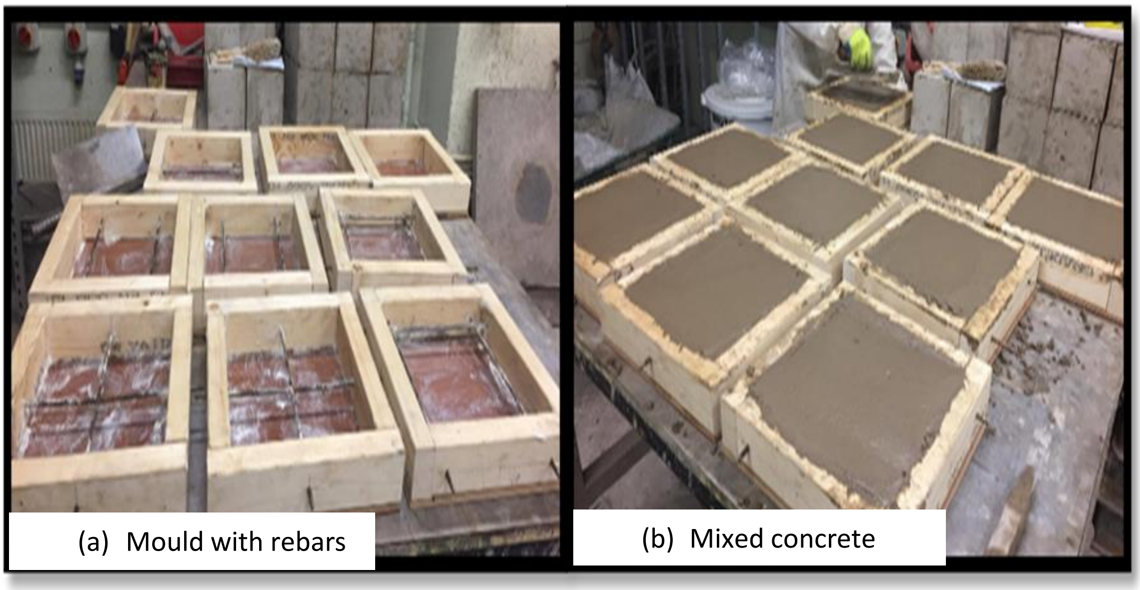
(a) Mould with rebars
(b) Mixed concrete

Figure 5.12: (a) Mould with rebars, (b) Mixed concrete ratio (1:1.82:3.69:0.4)

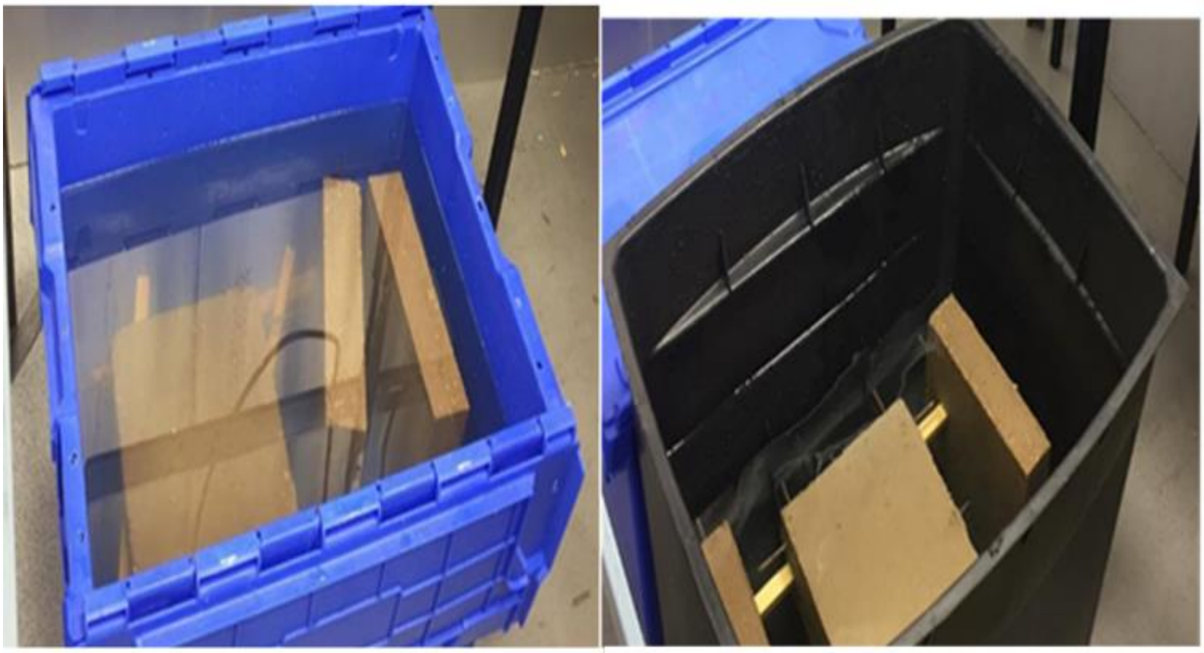

(a) 5 samples submerged in NaCl

(b) 5 samples submerged in Tapwater

Figure 5.13: The concrete samples immersed in tap water and saltwater for 28 days

Table 5.7: The concrete composition with OPC [259] [59]

Constituent used	Concrete Mix Design_(Kg)	Specific Gravity (g/cc)
Ordinary Portland Cement OPC (CEM II)	15.5	3.12
Fine aggregate (saturated surface dry)	28.3	2.65
Coarse aggregate size (10 mm)	57.4	2.70
Water	6.2	1.0 at 4C^{o}
Superplasticizer	0.124	1.19-1.24 at 25C^{o}

Step 1: Experimental set-

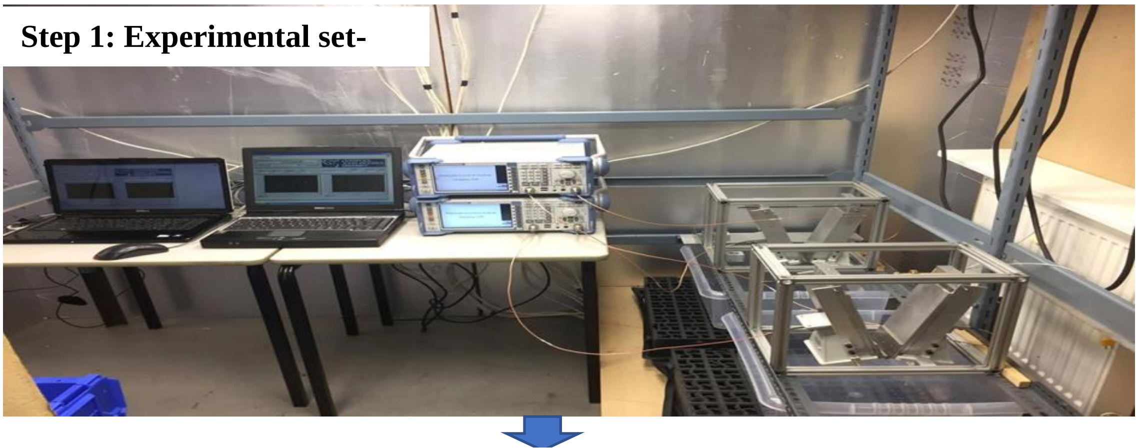

Step 2: Using both tap and salt water to fill the containers.

Step 3: The surface of the concrete samples was exposed to the microwave sensors as a dry during the measurement.

Step 4: After evaporations, both containers were refilled.

Figure 5.14: An experimental set-up for curing process over 28 days

5.4.3 Curing process experimental measurement

The curing experiment was undertaken for two concrete samples without reinforcement out of the 10 concrete samples. For 28 days, one sample was immersed in tap water and the other in salt water. This curing test aimed to determine how the concrete samples absorbed the tap water and salt water by monitoring them using a microwave sensor for 28 days. The microwave sensor was placed 20mm from the top surface of each slab. For this experiment, the operating frequency was set between 2 and 12 GHz. The sensor was connected directly to the Vector Network Analyser and laptop, which obtained and stored data via software developed in LabVIEW, as shown in Figure 5.14. The results show that both samples have a very significant effect on the microwave signal. As described in section 5.4.4, the drying-off method will be the next experimental operation performed on these two samples.

5.4.4 Measurements of the drying-off process in the laboratory

This experiment is conducted to monitor the water content and salt-water solutions in the concrete affecting the electromagnetic wave signal during the 72- hour drying off period. The initial experiment mentioned shows some differences in the microwave signal, so further investigations on the drying off process are significant for better understanding the material's properties.

In addition, wet concrete sample monitors were placed on a scale to measure the weight lost during drying off for over 72 hours. The microwave sensor was placed 20mm above the sample's top surface. The operating frequency was set to between 2 and 12 GHz for this experiment. Over 72 hours, the data are recorded every minute. The surface of the scale was metal, and it was a good wave reflector and the horn antenna was directly connected to the Rohde & Schwarz Vector Network analyser (VNA) and a PC. The VNA was connected to the PC via a crossover Ethernet cable, as shown in Figure 5.15. The concrete sample was not moved during the experimental work, and all other conditions such as temperature and light remained technically the same during the test procedure. The test was conducted in the small chamber structure, which was initially made for a different purpose; the subsequent experimental work was carried out with two concrete samples containing two rebars described in section 5.4.5.

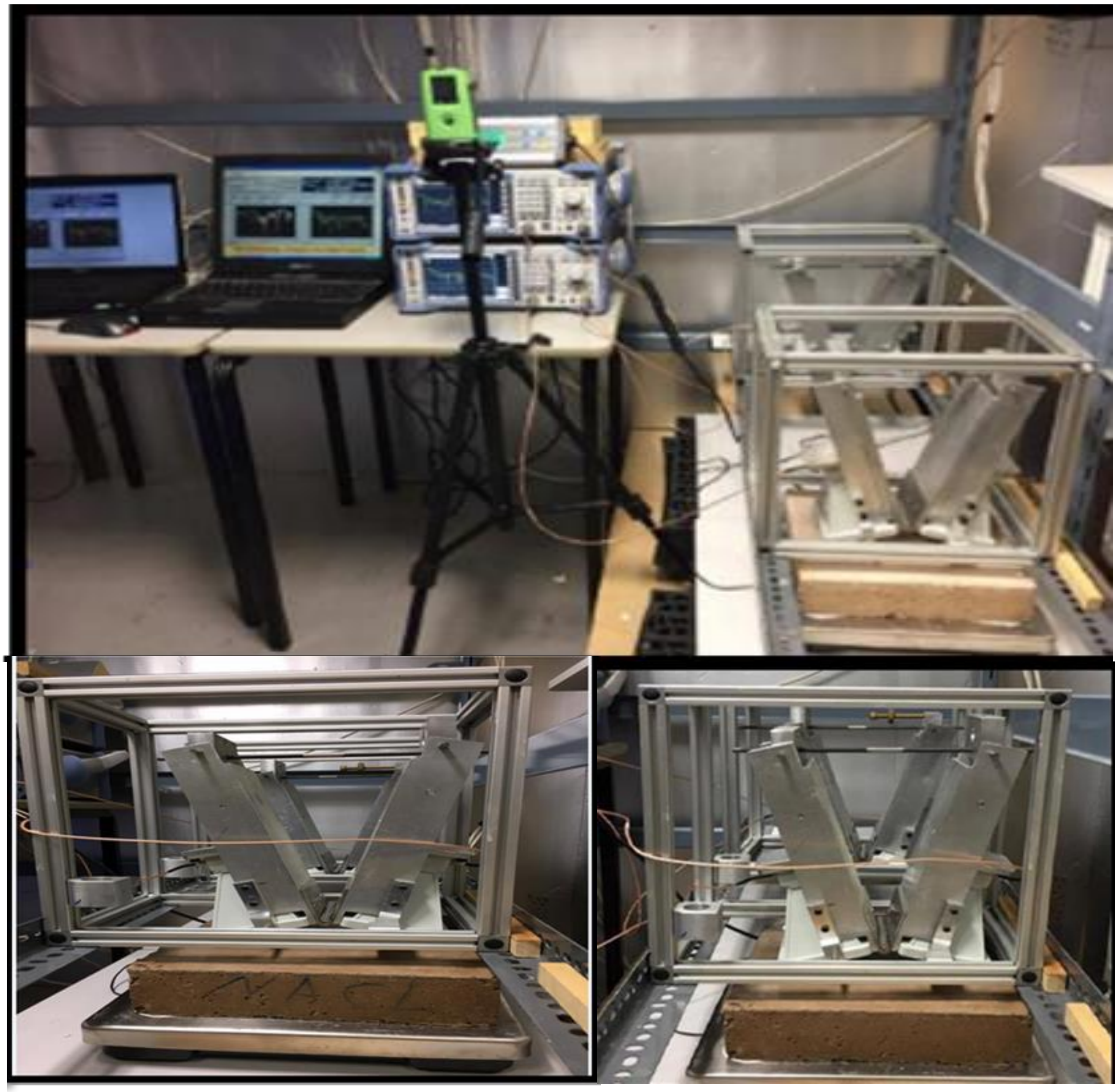

Figure 5.15: The drying off a measurement is carried out on both samples for 72 hours after the curing procedure is completed.

5.4.5 Drying measurements of samples with two rebars

Experimental work was carried out for two concrete slabs with the same size and material properties, with two rebars included, to investigate the different effects of tap water and saltwater solutions on concrete with reinforcement rebars and how the rebars in concrete structures affect the electromagnetic wave signal. As a result, due to the varying dielectric characteristics and texturing of the measured objects, changes in the microwave spectrum can be observed. Also, the sensor will enable the investigation of the location of the rebar in the concrete structure. The test set-up is presented in Figure 5.16. The microwave sensor was placed 20 mm from the top surface of the concrete slab. The sensor is directly connected to the Vector Network Analyser (VNA) and PC, which captured and stored data via software developed in LabVIEW as demonstrated in Figure 5.17. Before and after being submerged in tap water and salt water, each slab's moisture percentage was calculated using Equation 1. Table 5.8 shows the percentages of moisture absorption and evaporation.

Table 5.8: Demonstrate how much moisture is absorbed and evaporated.

Type of water	**The original weight of the dry sample (Kg)**	**Weight of wet sample (Kg)**	**Weight of sample after drying off (Kg)**	**Amount of water absorption by sample (%)**	**Amount of water evaporated after 24hours (%)**
Fresh Water	9.05	9.29	9.21	2.66	0.81
Salt water (3.5%)	9.30	9.47	9.42	1.88	0.53

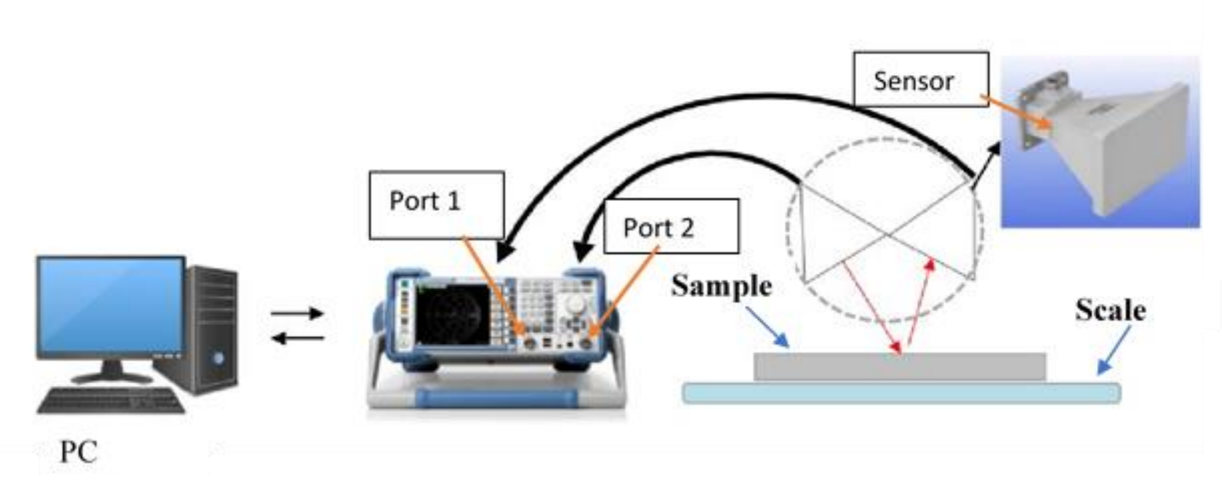

Figure 5.16: An illustration of the experimental set-up

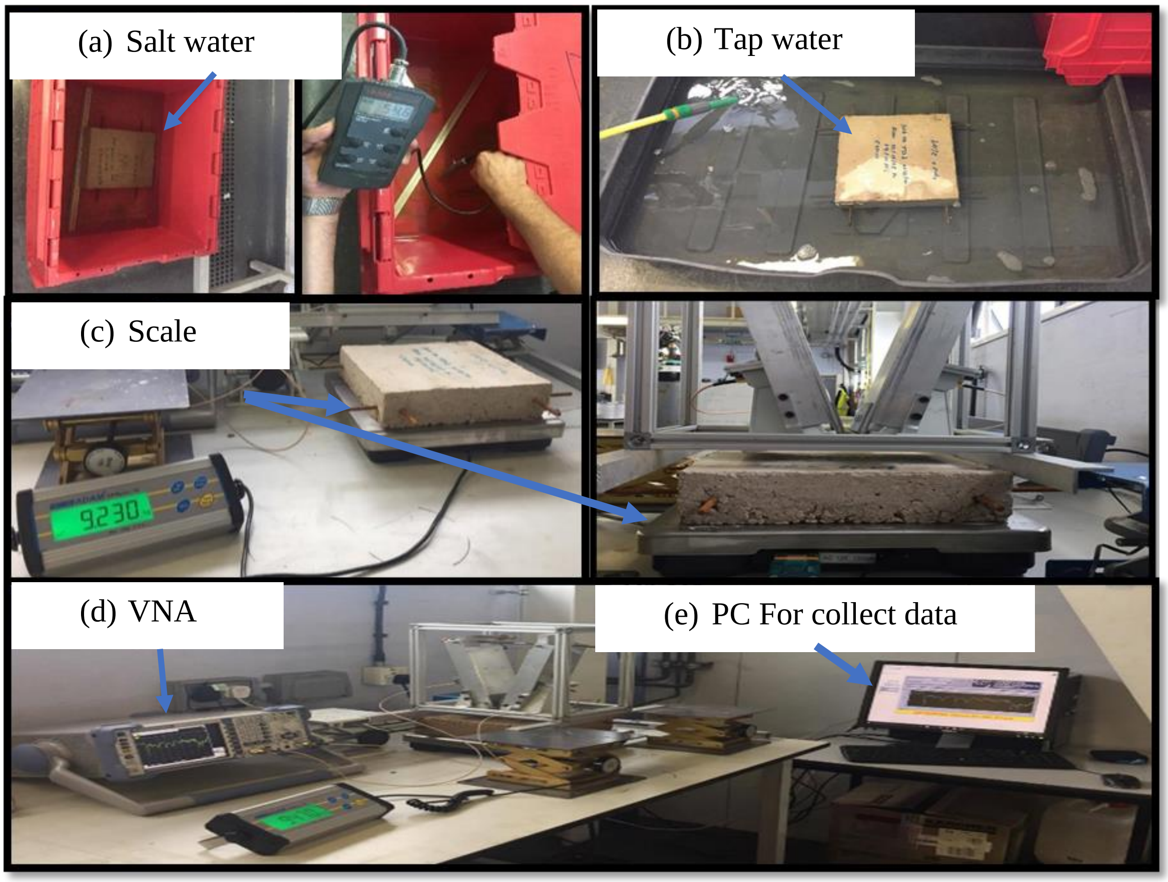

Figure 5.17: An experimental set-up for both samples' drying processes with reinforcement

5.5 Experiments under various salt-water concentrations

5.5.1 Concrete Sample

Five concrete slabs of size 300 x 300 x 150 mm without any reinforcement were prepared and cast. The standard concrete mix ratio used was in proportions 1:1.5:3:0.7 Kg, which is more common in European countries. The concrete was mixed correctly using tap water and filled the concrete mould in three layers in which each of the layers was compacted 25 times. This mix design used a limestone aggregate to compare how the different saltwater concentrations penetrated the concrete samples. Each of these samples was submerged into 5 different saltwater concentrations to detect the level of chloride by using microwave spectroscopy at the 2-12 GHz frequency range. Table 5.9 shows the concrete composition with OPC. The data for these five samples were collected to define the skin depth to the required reinforcement depth for marine concrete structures, which can range from 70mm to over 100mm depending on the concrete mix design.

Table 5.9: Presents the concrete composition with OPC (CEM II 32.5R)-Kg [46]

Constituent used	**Concrete Mix design (kg)**	**Specific gravity (g/cc)**
Type of cement (OPC)	CEM II	-
Cement dosage Ordinary Portland Cement	35.48	3.12
Fine aggregate	53.22	2.65
Coarse aggregate size (10mm)	106.44	2.70
W/C	0.7	1.0 at $4C^0$

5.5.2 Chloride Content

Five different saltwater concentrations were prepared to submerge the concrete samples individually for 5 days at the ambient room temperature. A plastic sheet covered the containers with different saltwater concentrations to avoid water evaporation during the curing process. The samples submerged in tap water and saltwater solutions are indicated in Figure 5.18. Sodium (Na+) and Chloride (CL-) was selected and mixed with the tap water from (0.0%, 0.5%, 1.5%, 2.5% and 3.5%). Every kilogram of (one litre by volume) of salt water has approximately 5 grams of dissolved NaCl. The tap water had an initial conductivity of 0.176 mS/cm, but the conductivity of the tap water was raised once the salt was added, and stirred to ensure that it was dissolving. Conductive readings were then taken for each saltwater concentration with a Hanna Instruments HI933000 conductivity meter at various points to ensure that the NaCl dissolved well and the estimated conductivity was correct across the saltwater concentration. For comparison, normal conductivity levels in drinking water are limited by legislation to 0.25 mS/cm, and seawater has a conductivity of roughly 50 mS/cm. The conductivity measurements with different saltwater concentrations are indicated in Table 5.10.

Table 5.10: Conductivity measurements of five saltwater concentrations

Saltwater concentration %	Conductivity reading (mS/cm)
(One litre of water has 0.0)	0.176
(One litre of water has 0.5)	9.40
(One litre of water has 1.5)	26.6
(One litre of water has 2.5)	43.1
(One litre of water has 3.5)	50.2

Figure 5.18: Concrete samples submerged into different saltwater concentrations for up to 5 days

5.5.3 Five concrete samples were tested with varying saltwater concentrations

Experimental work was conducted in a laboratory environment. An electromagnetic sensor was positioned 20 mm from the concrete sample surface to perform non-destructive testing to determine chloride content at various penetration depths. In total, we prepared 5 concrete specimens and repeated each configuration 3 times. In addition, the concrete specimens were examined during the drying off period to understand the relationship between moisture content and the electromagnetic spectrum concerning the chloride concentration. Each concrete sample was also weighed continuously during the experiment to establish a consistent mass indicating equilibrium moisture content conditions [207, 208, 265]. The experimental set-up contained a weigh scale under the concrete specimen, a vector network analyser (VNA), and a computer running LabVIEW software to continuously collect data every 15 minutes. The parameter (S_{21}) was detected from the transmitted and received horn antennas connected to the VNA. The experimental set-up is shown in Figure 5.19.

The concrete sample was not moved during the experimental work, and all other conditions such as temperature and light remained technically the same during the test procedure. Because of the difference in concrete thickness and curing time, measurements were taken every 15 or 30 minutes. Because water and salt water evaporate slowly, measurements can be made every 30 minutes to an hour if the concrete depth is greater.

However, if the sample thickness is lower, the weight of the sample drops rapidly in the first few hours, and the sample loses its integrity and the weight drops steadily after that. Essentially, the concrete sample loses weight faster due to its lower thickness. It is necessary to monitor the data more frequently to analyse and establish the relationship between the operation and the electromagnetic signal.

The wet concrete sample is monitored on the scale during the drying process to measure the weight loss for up to 24 hours or 72 hours. Usually, the water and salt water do not evaporate very fast from the concrete; therefore, the microwave signal continuously remains the same until the samples' amount of water is reduced. In addition, the water can evaporate from the first layer of the concrete quite fast. However, while the water ingress continued to greater depths, it took time to evaporate through the pores, depending on the concrete water-cement ratio and permeability.

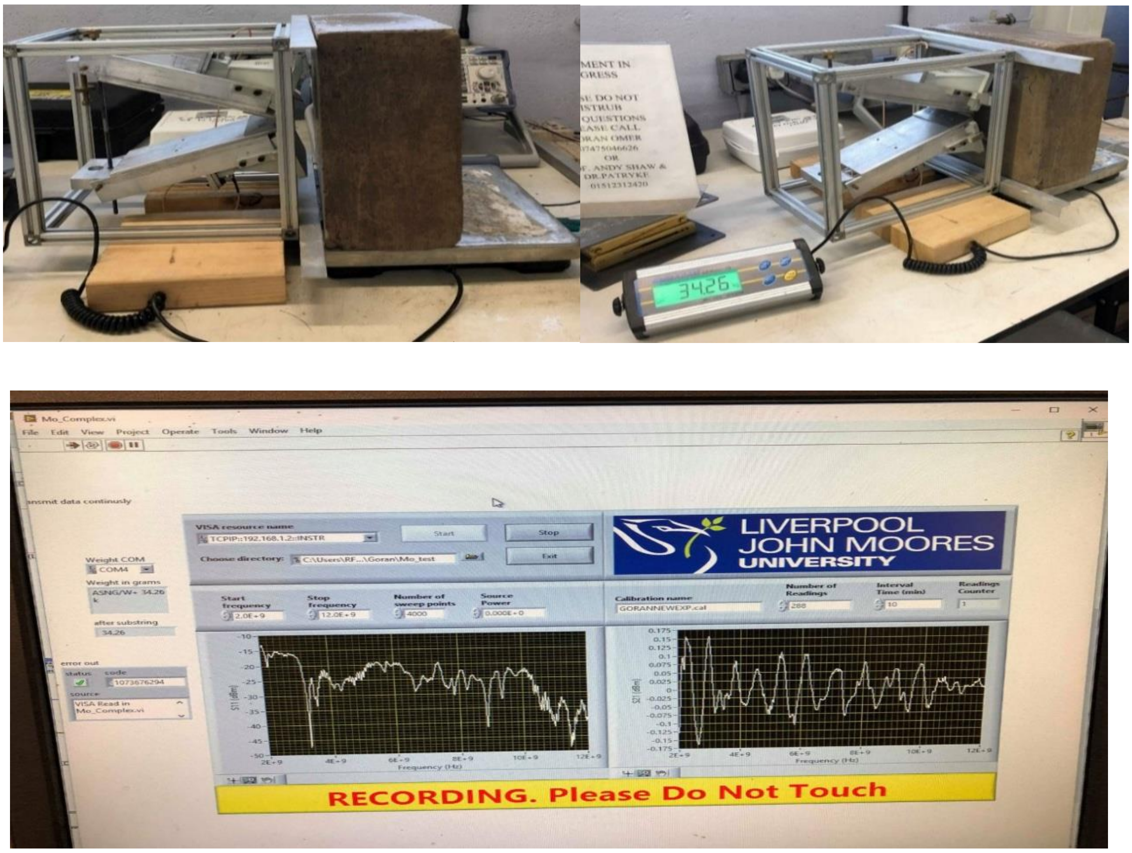

ansmit data continusly

VISA resource name: TCPIP::192.168.1.2::INSTR

Choose directory: C:\Users\RF...\Goran\Mo_test

Weight COM: COM4

Weight in grams: ASNG/W+ 34.26 k

after substring: 34.26

error out: status ✓ code 1073676294

source: VISA Read in Mo_Complex.vi

Start frequency: 2.0E+9

Stop frequency: 12.0E+9

Number of sweep points: 4000

Source Power: 0.000E+0

Calibration name: GORANNEWEXP.cal

Number of Readings: 288

Interval Time (min): 10

Readings Counter: 1

Figure 5.19: Presents the experimental set-up and LabVIEW interface for data acquisition

5.5.4 Chlorimeter tool

The Chlorimeter tool is the gold standard technique, and a model number C-CL-3000 is used as a partially destructive method to detect the amount of chloride in the concrete sample. The Chlorimeter test system offers a fast and accurate determination of the total chloride content in concrete. The test was carried out to determine the presence of chloride ions in the concrete and their penetration. The samples were immersed subsequently in 5 different solutions for 5 days. The concentration of the NaCl solution was kept constant during the time of immersion. It was necessary to drill to three different levels of the concrete sample to obtain a chloride profile. All five samples were drilled at three different depths, namely 18, 40 and 70 mm. The chosen depths of sampling aimed to incorporate a suitable range to allow interpolation and prediction between commonly used nominal depths of cover under various exposure conditions, for instance, near the top surface, a little deeper and very close to the rebar position. The 3 grams of dust were collected separately at three depths (18mm, 40mm and 70 mm). The

3 grams of dust were weighed using the digital scale provided in the kit. The device needs calibration before performing any chloride tests. The kit contains the five different percentage solutions used to calibrate the instrument. This calibration can hold only for 2 hours. After collecting the 3 grams of dust from each hole separately, the 3-gram dust test sample was slowly added into the 20ml of chloride extraction liquid in stages to avoid excessive fizzing from the limestone present in concrete.

After mixing well, the plastic jar lid was opened and the probe was put into the liquid to read the chloride percentage. This measurement takes up to 2 to 3 minutes to display the percentage of chloride on the chlorimeter screen. The probe should be washed well with deionised water for every measure and then used for another measurement to avoid reading errors. The accuracy of this chlorimeter tool covers a wide range from 0.002% to 2% chloride per weight. This procedure was repeated for all the samples after completing the drying off and recorded all the results during the experiments to measure the level of chloride ions in the concrete blocks. Figure 5.20 indicates the masonry drill used to collect the 3 grams of dust. Figure 5.21 displays the chlorimeter calibration tool and chloride measurement experimental set-up.

Figure 5.20: Drilling the sample to collect 3 grams of dust at 3 different depths

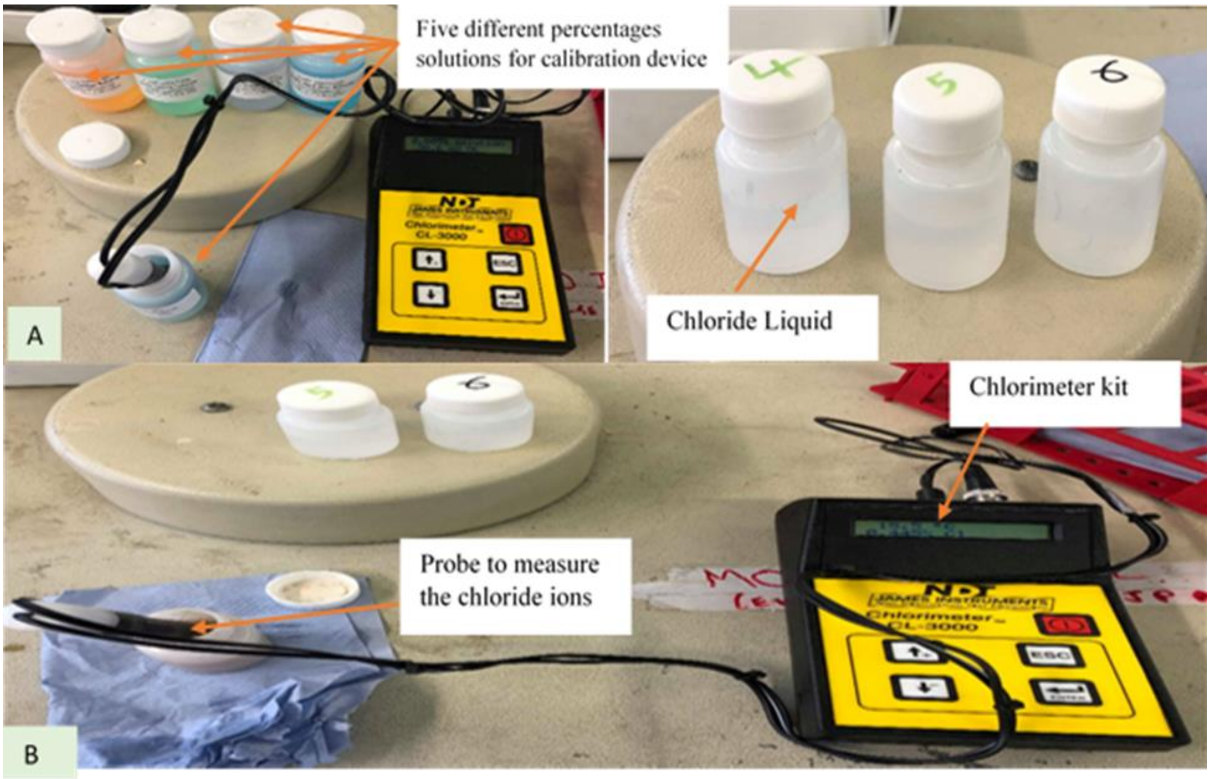

Figure 5.21: Presents (A) calibration device and (B) Chloride measurement taken

5.6 Data processing and validation models

The initial preliminary experiment was conducted for a pavement slab in different saltwater concentrations and tap water to identify the drying process and the amount of salt penetrating the pavement slabs on the electromagnetic wave signal. According to the data obtained from this initial experiment, it is shown that the EM signal can interact with concrete exposed to salt water and tap water predictably. During the data processing, the most important task was selecting the optimum correlation between the transmitted signal and changes in the concrete sample, such as weight loss, with the spectrum containing 4,000 sweep points. The data is provided in detail in chapter 6, section 6.2.

The final stage of this project is a comparison of this non-destructive technique with gold standard techniques, which are commonly used in the industry. However, to compare these techniques, we must process the data via machine learning and an Artificial Neural Network (ANN) to create a validation model. The ANN technique was selected for this data inspection due to its ability to handle many input variables and multiple outcomes simultaneously.

5. 6.1 Validation techniques include machine learning and artificial neural networks (ANN)

One of the main aims of this research is to develop and train a consistent validation model using the Levenberg-Marquardt (LM) algorithm to fully capture the percentage of chloride at three different depths of penetration with high efficiency. For this reason, back-propagation is possibly the most used algorithm in ANNs. Still, the Levenberg-Marquardt (LM) method is known to attain a much-improved performance by converging more often and making training much faster. The planned training algorithm is a data-driven computing tool, which can be used when the relationship between model input and output parameters is complex [266]. Also, the LM algorithm can capture the nonlinear functions and the substantial computer capacity can be applied to implement extremely iterated work [267].

One of the understandable advantages of the LM method is that no internal training parameters are required to be modified during the training process. This avoids many complications and barriers noted in using the classical algorithms, such as the slow rate of convergence, learning rate, and local minima and correcting learning epochs [268].

The ANN analysis was carried out using the MATLAB R2019a software. To conduct the analysis, the neural network fitting was selected; Figure 5.22 shows the search path of MATLAB.

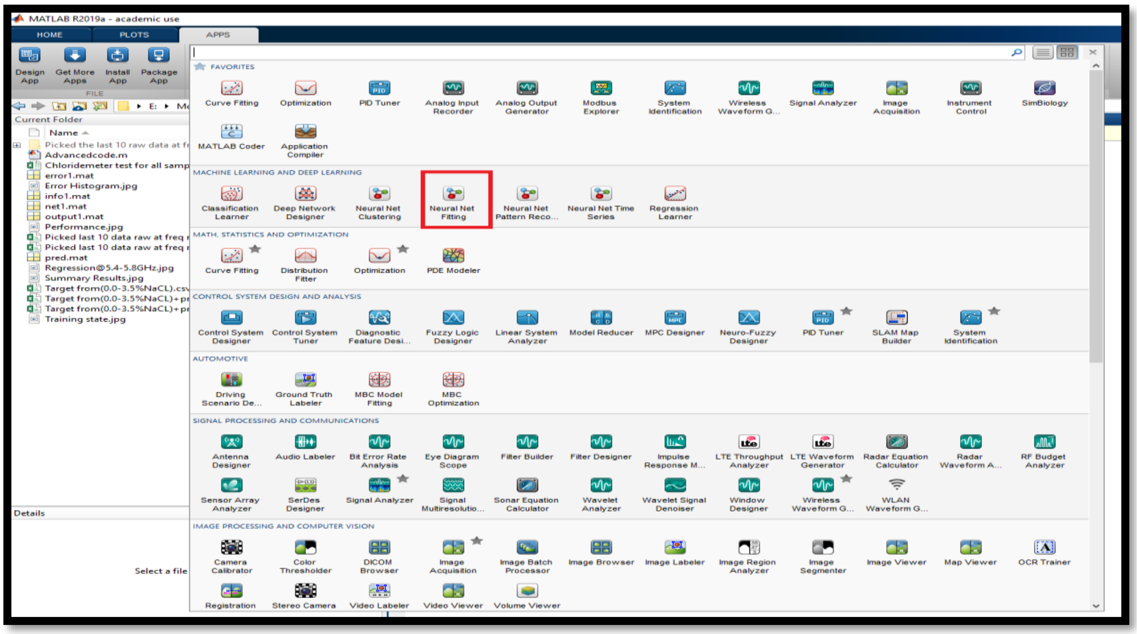

Figure 5.22: The Neural Net fitting was selected from MATLAB (LJMU Library)

5.6.2 ANN Training

Throughout the training process, data sets are handed to the input layer and then passed from layer to layer, upholding the system of the forward pass. However, in this type of system, each neuron in the hidden layer receives inputs from input layer neurons, which are already being multiplied using the adjacent weight, after which they are then summed up. In some cases, it is modified by using adding bias. After that, the inputs pass through the transfer function and provide values for the output layer.

Errors are calculated by comparing the target and output values. In addition, errors are minimized with iteration, and just in case of back-propagation, these propagate backwards to regulate or update the weight for higher accuracy. The following Figure 5.23 flow diagram shows the entire process summarised.

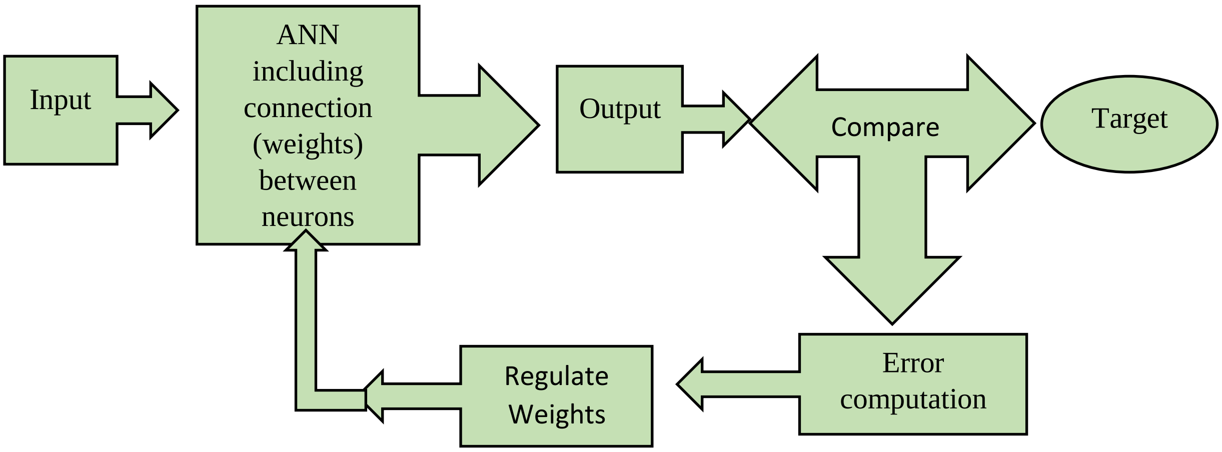

Figure 5.23: The Flow diagram of the training process of an ANN

5.7 Summary

This chapter defined the research methodology design process, which will be used to complete this research project. Several approaches will be used in this study. The first will be numerical calculations to select the optimum angle and frequency between the two horn antennas to monitor the concrete samples. This portion can be completed after determining the skin depth that the electromagnetic wave must penetrate in the concrete samples. In section 4.10 of Chapter 4, we defined the skin depth. The initial surface absorption testing findings are shown in chapter 6, section 6.1, to determine the permeability of the concrete samples and how quickly they absorbed water and salt water throughout the curing process. The preliminary experimental work aimed to decide whether or not we should use S_{21} or S_{11} characteristics with concrete samples. This experiment works to establish the relationship between the skin depth and the penetration depth of the concrete, thus demonstrating the state of the art.

This study used three bands with different frequencies ranging from 2.35 GHz to 2.85 GHz in the S-band, 4 GHz to 7 GHz in the C-band, and 8 GHz to 12 GHz X-band to determine the attenuations and skin depth of EM waves. Therefore, preliminary experimentation was used to improve the methodology for the rest of the experimental work. After the preliminary testing, the initial experimental work was conducted with square pavement limestone aggregate concrete slabs with dimensions 600 x 600 x 40 mm. This experiment aimed to see how the reduction of water and salt water affects the microwave signal when using pavement slabs that were just 40mm thick. Following that, 10 concrete slabs with and without reinforcement, size 250 x 250 x 60mm, were constructed and cast using the same technique as the three trial samples, under BS 8500-1:2006. These ten samples were tested independently for drying time and how electromagnetic waves reflect the concrete's reinforcement and the various reinforcement areas inside the concrete. After the concrete samples were constructed, the curing process was tested in two different saltwater concentrations for up to 28 days without reinforcing. The purpose of this curing process test is to determine when the concrete sample has gained sufficient strength, is fully saturated, and how quickly water and salt water enter into the concrete after 28 days. Then, the expanded experiment included monitoring the amount of water and saltwater solutions in the concrete and how they altered the electromagnetic signal during the 72-hour drying off period.

Two concrete samples with mesh rebar were subjected to an experiment. This experiment aimed to see how different solutions of tap water and salt water affect concrete with reinforcement rebars and how rebars in concrete structures affect electromagnetic signals. The final experiment used five concrete slabs with 300 x 300 x 150 mm and no reinforcing. The data from these five samples was used to determine the skin depth and establish a reinforcement depth to determine the depth of reinforcement required for maritime concrete structures. However, it illustrated the comparison between the data processing and validation procedures employed in this study. Finally, the data generated from the microwave sensor and the partially destructive chlorimeter tool approach were compared using ANN, which revealed no significant difference between the two methods.

Chapter Six: Results and Discussion

This chapter will demonstrate the experimental results using horn antennas to monitor the level of chloride ions in the concrete samples during the curing and drying processes. In addition, a chlorimeter tool is used as a gold standard method to detect the level of chloride in concrete and is compared with a microwave technique as a non-destructive method. The supervised LM algorithm, trained via multilayer feed-forward back-propagation, has been developed and applied in the present study. This sort of ANN comprises fully interconnected parallel neurons or processing elements (PEs), which are connected in three layers, following the order: the input layer, the hidden layer and finally, the output layer. Results obtained from all the experimental work will be processed, plotted, and analysed using an artificial neural network (ANN) to develop a validation model for monitoring chloride ions in different saltwater concentrations and at different depths during the curing process drying off.

6.1 Results of the initial surface absorption test (permeability test)

The initial surface absorption test is the most commonly used non-destructive test for evaluating primary concrete durability factors like absorption, permeability (air, gas, and water), and migration-related concerns. The permeability coefficient is calculated using the assumption of unidirectional airflow. The coefficient permeability of each sample shows in Table 6. 1. This method's readings frequently show an explicit reliance on the current wetness of the surface layer being investigated, which must be observed simultaneously. However, this technique is used to assess the concrete cover's resistance to infiltration by various aggressive agents' methods and determine the age of concrete constructions. The concrete cover's air permeability coefficient is directly connected to the pressure rise rate, Pi (measurement starts at t = 60 s). This approach has the advantage of being speedier and fully non-destructive. The value of the K_T is used to determine the quality of the concrete cover (coefficient of permeability). This study shows that the measured permeability is lower in the case of wet concrete, indicating that the concrete quality appears to be too good. The purpose of this test is to determine the permeability of the concrete. The coefficient of permeability is lower, indicating that fluids (water or other chemical substances/chloride) cannot easily travel through the pores of the concrete. However, this low permeable concrete was exposed to a microwave horn antenna to test the sensor's accuracy. Microwave sensors successfully detect chloride ions in concrete structures. Figure 6.1 [271] shows the concrete quality class defined by K_T in a nomogram. If the permeability coefficient is less than 0.01x10^{-16} m^2, the quality of the concrete cover is excellent.

Table 6.1: Shows the permeability results obtained

Concrete sample	**Time (second)**	**Pi (mbar)**	**K_T(10^{-16} m^2)**	**Length (mm)**	**Permeability**
1	720	26	0.017	11	Very low
2	720	24	0.11	11	Low

Where, Pi is the pressure rise in the inner cell (mbar), K_T; is the coefficient of air permeability (m^2).

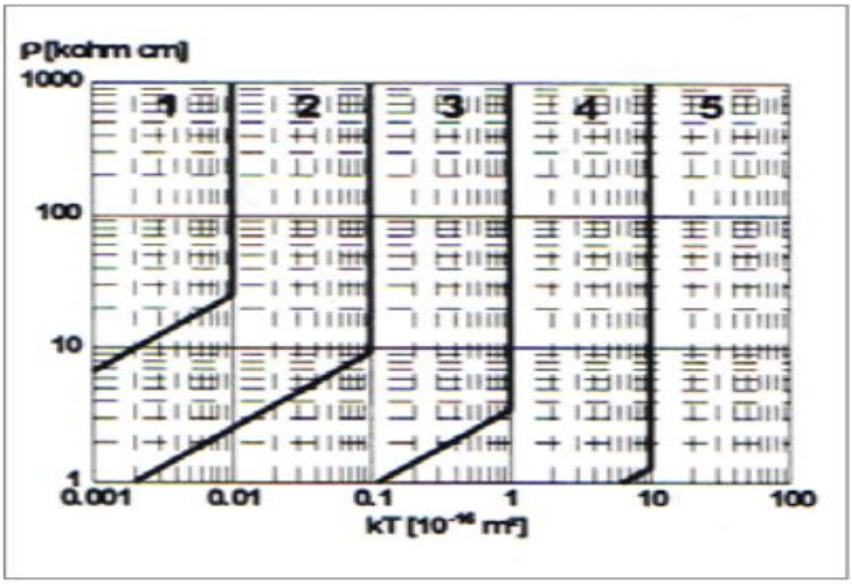

Figure 6.1: The nomogram for the concrete quality class [269]

6.2 Initial measurement results

For both samples, measurements of the S_{21} parameter are taking over the complete spectrum range of the VNA and sensor frequencies between (2 GHz and 6 GHz). It was found that there was a change in the response for pavement samples with different saltwater concentrations at the same frequencies of the S_{21} parameter. Areas of interest for further analysis are highlighted in both Figure 6.2 and Figure 6.4. Zoomed in the regions highlighted in Figure 6.2 and Figure

6.4 for the S_{21} signal, identified frequencies of 3.6 GHz and 4.15 GHz, as seen in Figure 6.3 and Figure 6.5, respectively. The reason for choosing the lower frequency region for the microwave response was to avoid complex signals with higher-order modes and measurement complexities at high frequencies, more suitable for industrial use. There is a noticeable change in EM signature appearing after the concrete absorbed water and salt water, particularly at the 3.6 GHz and 4.15 GHz frequency range. According to this experimental data, the change is caused by the concrete's decreasing amount of water and salt water.

During the experimental work, the sample was not touched or moved, and all other conditions, such as temperature and light, remained consistent during the test. Water absorbs electromagnetic waves very well because water has a high dielectric value, which enables the observation of changes in the microwave spectrum. After all, any minor change in water content could significantly impact the electromagnetic wave response curve (see Figure 6.3). In addition, the changes in electromagnetic waves are caused by differences in chloride ions concentration in the concrete. When the concrete samples are exposed to the microwave sensors, the result of sample S_{21} measurements in Figure 6.3 compares to the sample S_{11} measurements in Figure 6.4. It can be seen that there is a significant steady amplitude shift at the frequency ranges 2 GHz-12 GHz and 2 GHz and 6 GHz. The decrease in the amount of water in the concrete samples strongly influences the microwave response when the samples start drying off, hence a significant shift. However, for the S_{21} parameter of the concrete sample, this was best detected in the range of 3.6 GHz to 4.15 GHz; the change in amplitude increased from -40 dB to -34 dB as the moisture content decreased. However, when the moisture content decreased, the amplitude of the S_{11} parameter of the concrete sample illustrated in Figure 6.4 decreased from -5 dB to-9 dB in the same region. The S_{21} parameter was chosen for use in the entire experiment due to these findings and previous research.

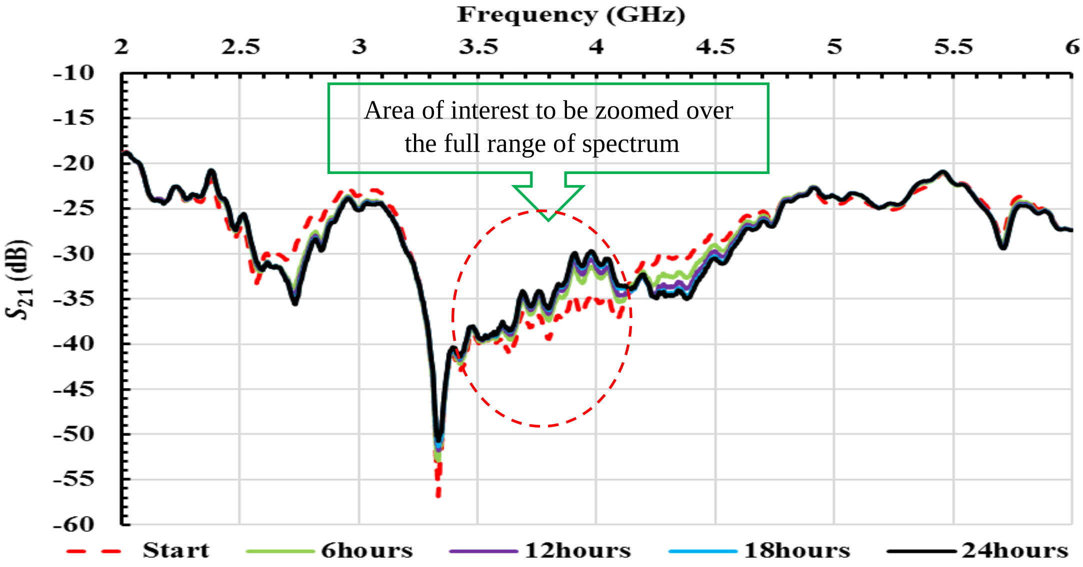

Figure 6.2: The electromagnetic wave sensor: measurements were taken every one hour in the frequency range (2-6 GHz), Tap water

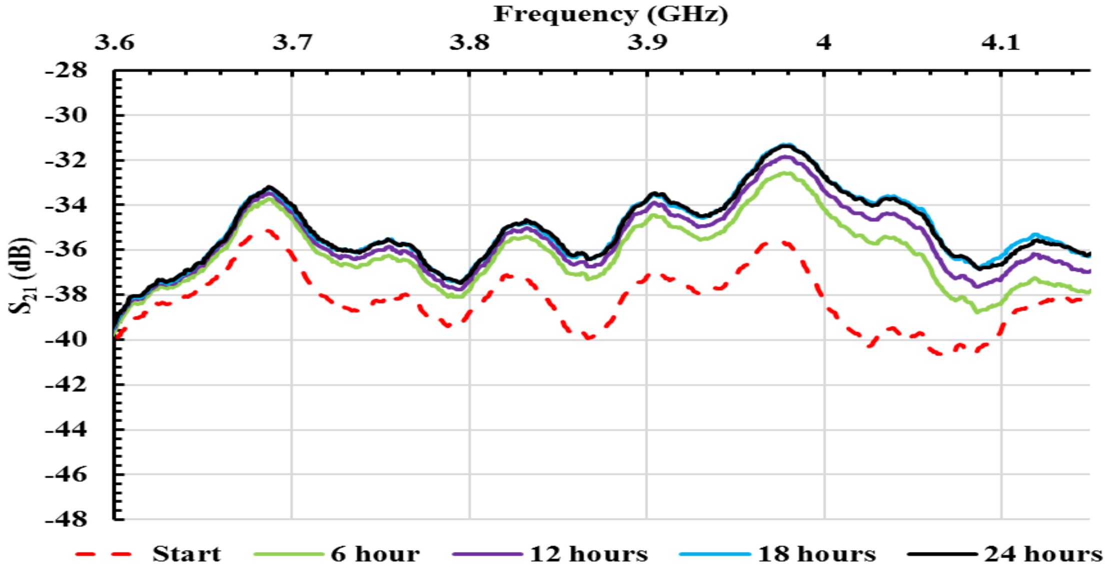

Figure 6.3: The electromagnetic wave sensor: measurements were taken every one hour in the frequency range (2-6 GHz), but for clarity data measurements from 6 hour intervals and from 3.6-4.15 GHz are presented (Tap water)

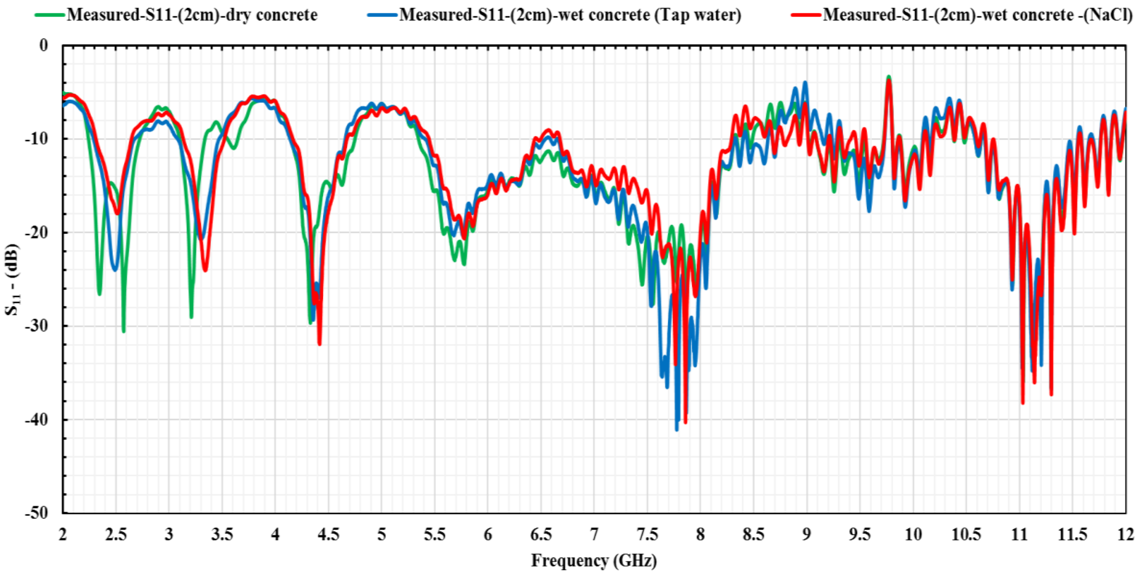

Figure 6.4: The electromagnetic wave sensor: measurements are taken in the frequency range (2-12 GHz)

Figure 6.5 shows that the amplitude measurement of the microwave signal changes depending on the material properties, environmental influence and the amount of water and salt absorbed by the concrete over 24 hours. Data analyses allow the identification of the level of chloride ions in the concrete specimens during the experiment.

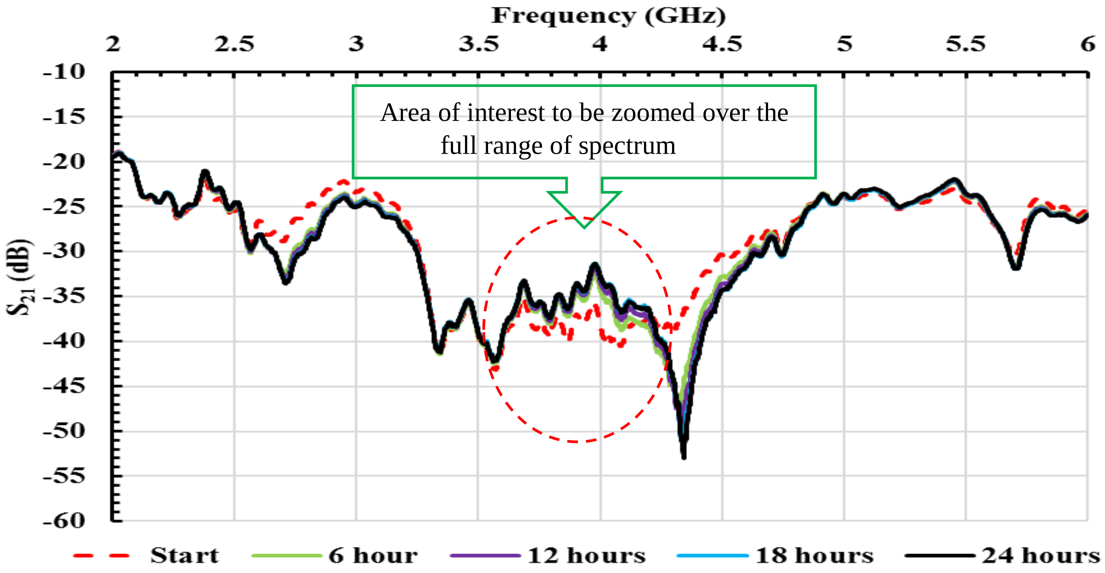

Figure 6.5: The electromagnetic wave sensor: measurements were taken every one hour in the frequency range (2-6 GHz), (Salt water)

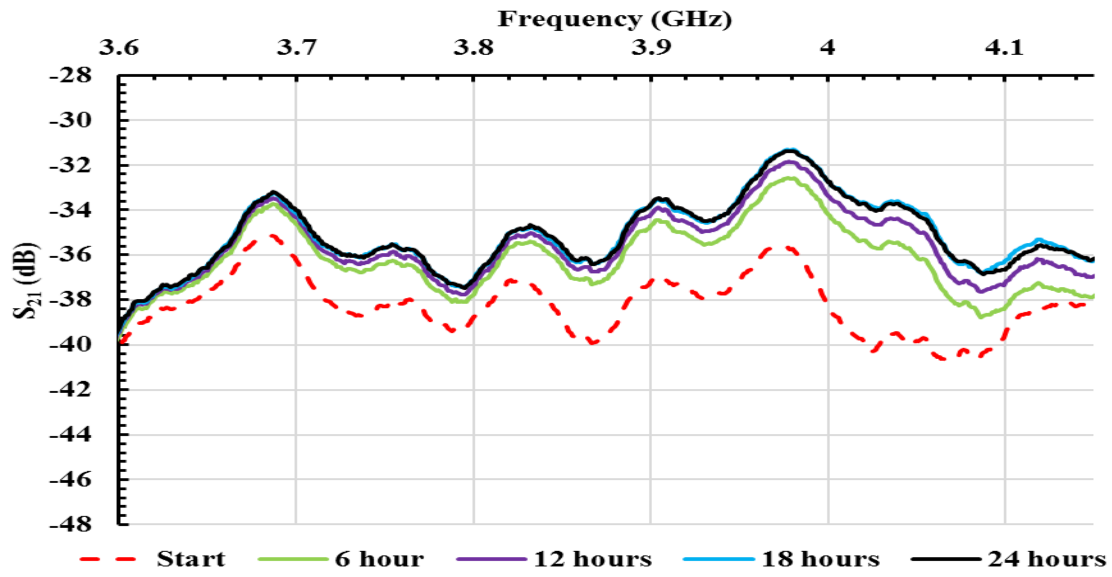

Figure 6.6: Microwave sensor measurements were taken every one hour in the frequency range (2-6 GHz), but for clarity data measurements from 6 hour intervals and from 3.6-4.15 GHz are presented (Saltwater).

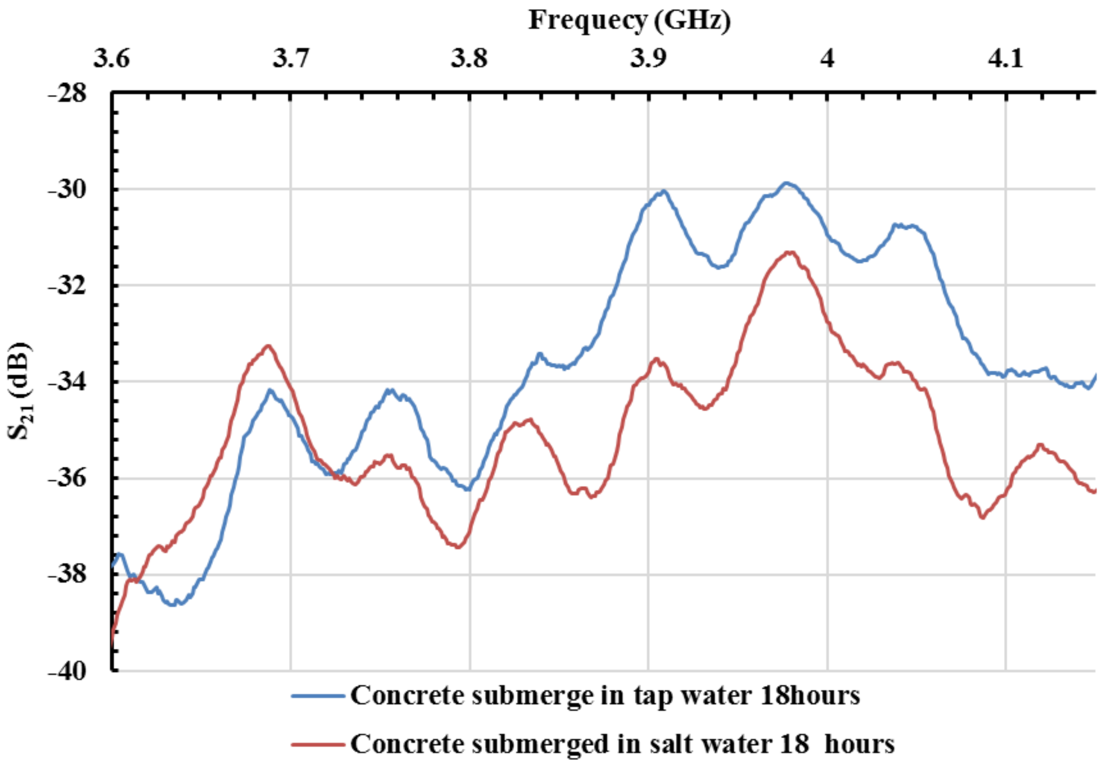

Figure 6.7: S_{21} measurement comparison between two plain concrete samples

In Figure 6.7, the legend shows both concrete samples with different saltwater concentrations after passing 18 hours of drying off. Since water has a high dielectric value, any slight change in its amount could significantly impact the microwave response curve. The above Figure 6.7 shows a steady amplitude shift in the frequency between 3.6 and 4.15 GHz. Noticeable changes of microwave signal power levels between the 3.6 and 4.15 GHz frequency range can easily be observed after the 18 hours drying process. However, these changes in the spectrum were caused by the dielectric properties of the water and salt water, and when the amount of water is reduced, then less EM energy is absorbed; this technique can identify the state of the water content and amount of salt during the drying process. From Figure 6.7, it can easily be seen that the spectrum changes between both samples, with tap water and salt water after the 18-hour drying process. After the water has evaporated, the sample containing NaCl absorbs more EM wave energy because of the amount of salt remaining inside the sample. It can be noticed in these initial results that the horn antenna could identify different saltwater concentration ingress in the concrete samples under test, hence providing the proof of concept.

6.3 Curing process experimental measurement

The experiment curing process was demonstrated in Chapter 5 Table 5.1 using two concrete samples without reinforcement out of ten concrete samples (Group D). Both concrete samples were measured for S_{21} and S_{11} parameters over the complete spectrum range of the VNA, between 2 GHz and 12 GHz. The reason for commencing the test from 2 GHz is due to the horn antenna limitation and non-response zones within the spectrum, with higher noise levels found below 2 GHz. The results of both S_{21} and S_{11} measurements are shown in Figure 6.8, Figure 6.10, and Figure 6.12, respectively. The spectrums were carefully examined to identify the change of the magnitude in the full range to investigate the condition of the concrete samples with different saltwater concentrations in terms of the microwave signals. It was found that there was a change in the frequency response of concrete samples with varying concentrations of salt water at the same frequencies for the S_{21} and S_{11} parameters. Areas of interest for further investigation are highlighted in Figure 6.8, Figure 6.10 and Figure 6.12 and zoomed in the highlighted areas for the S21 and S11 parameters, identified in the frequency range of 2.5 GHz -3 GHz. It can be seen in Figure 6.9, Figure 6.11, and Figure 6.13 that there is a noticeable change in the EM signature between the frequency range 2.5 GHz and 3 GHz, especially at a frequency of 2.7096 GHz. The change is affected by the amount of water and salt water absorbed in the concrete sample during the 28-days curing period. Because moisture and chloride are two constituents that have the most prominent effect on the dielectric properties of concrete, while the volumetric content of water in a concrete mixture is small, it has a very important bearing on the velocity and attenuation of electromagnetic waves in the concrete. Owing to water having a high dielectric property, microwave signal changes and electromagnetic (EM) wave absorption are very dependent on the water salinity and temperature. Because the dielectric characteristics of water and the concrete mixture as a whole are affected only by the chlorides present in solution at any particular time, dissolved chlorides start to reduce the real part of the complex dielectric permittivity of water, which directly affects the microwave velocity and greatly increases the imaginary part, affecting the attenuation of microwave signal waves. The sample was not touched or moved during the experimental work, and all other conditions such as temperature and light nominally remained the same during the test. When both concrete samples were placed under the sensors, increasing storage of electric field energy can be observed, which leads to a decreasing resonance frequency. While the concrete sample started to absorb the water and salt water, the amplitude increased simultaneously.

The speed of the EM waves is higher than that of sound waves and strongly depends on the permeability(μ)the permittivity (ε), the conductivity (σ) and the density of the volume charge (ρ) [270]. In addition, these parameters change with the type of water, so the wave propagation speed varies. It was also taken into account that seawater's dielectric constant changed with changes in frequency, temperature, and salinity [271] [272]. High attenuation due to water conductivity is the crucial problem with underwater communication using electromagnetic waves. As the frequency increases, this attenuation increases as well [273].

An experimental investigation was conducted to determine the skin depth of the penetration of electromagnetic waves into the concrete samples with different saltwater concentrations. The results and discussion were presented in detail in Chapter 5, Section 5.3.2.

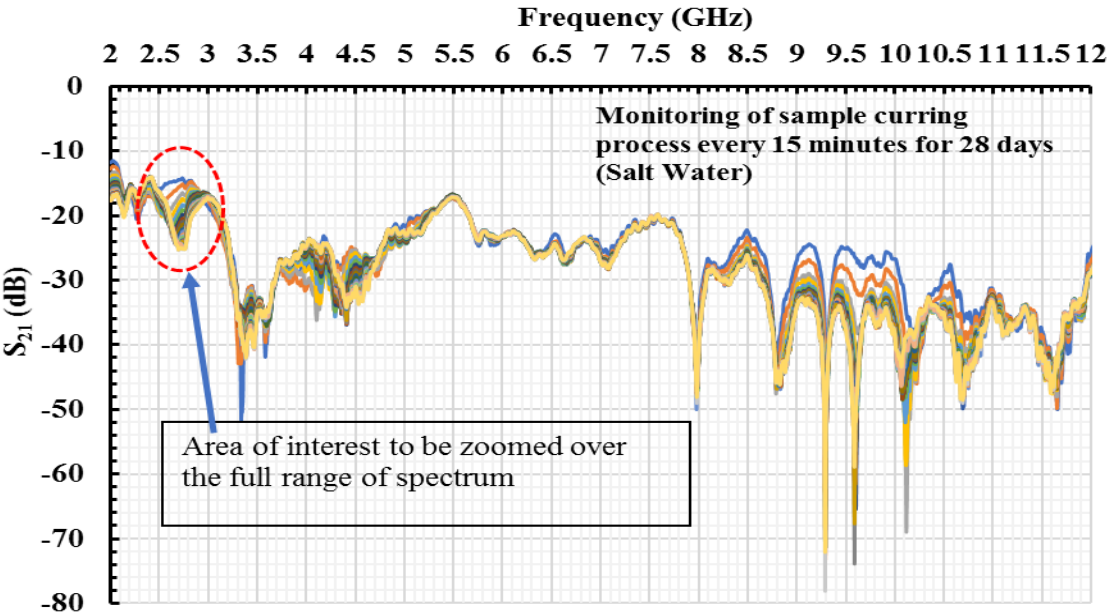

Figure 6.8: The electromagnetic measurements were taken every 15 minutes in the frequency range (2-12 GHz), (Saltwater)

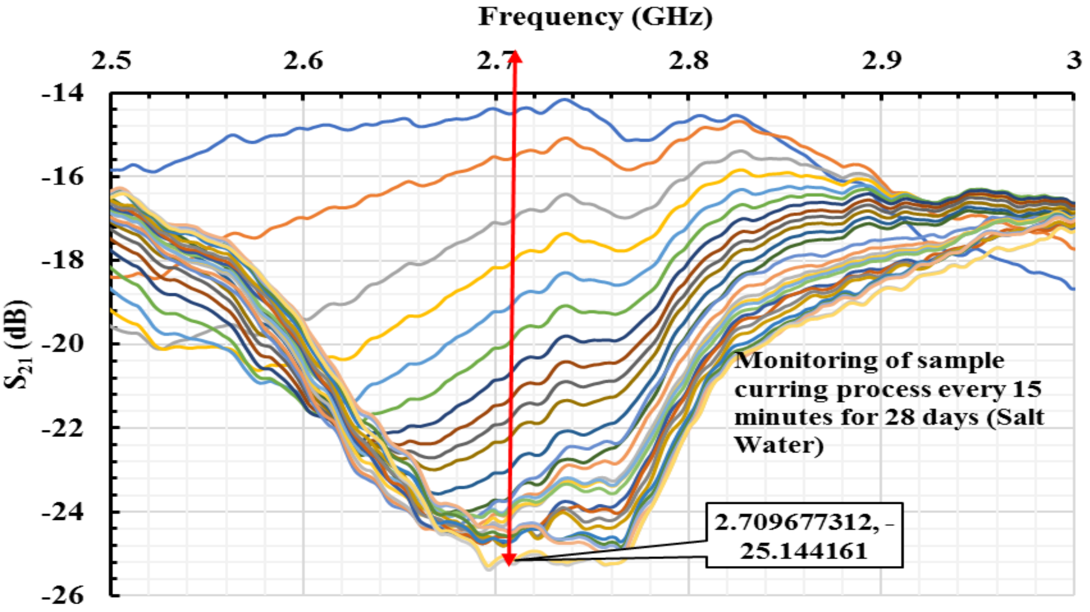

Figure 6.9: S_{21} measuments from the electromagnetic wave sensor were taken every 15 minutes in the frequency range (2-12 GHz), but for clarity data from 2.5-3 GHZ is presented with measurements from 24 hour intervals (Saltwater)

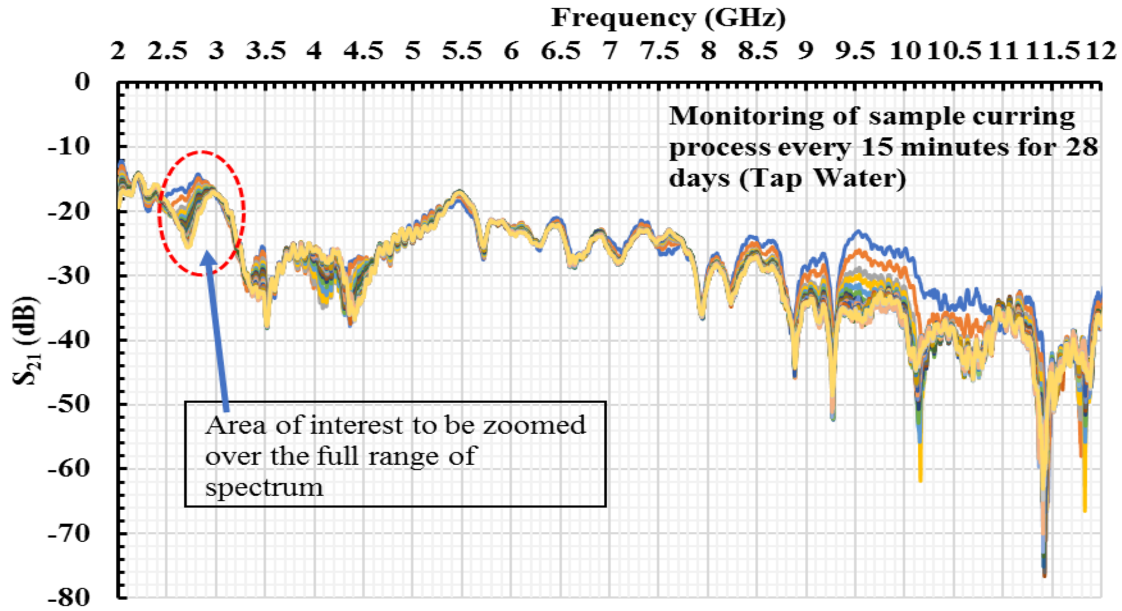

Figure 6.10: Readings from the electromagnetic wave sensor; measurements were taken every15 minute for 28 days in the frequency range (2-12 GHz) (Tapwater)

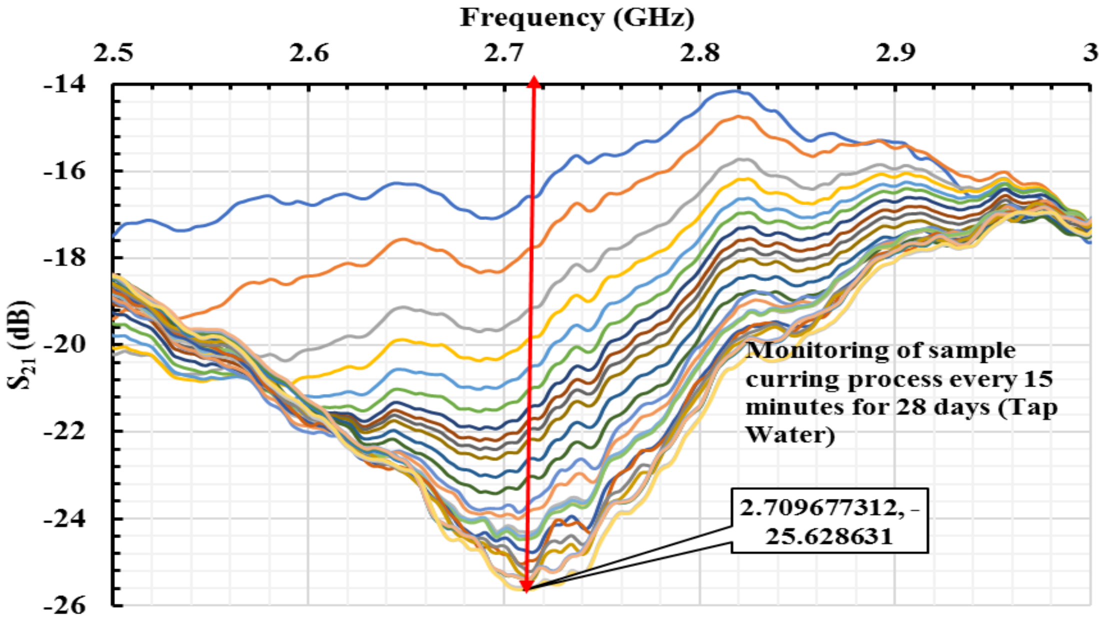

Figure 6.11: S_{21} measurements were made every 15 minutes for 28 days in the frequency range (2-12 GHz), although data measurements at 24 hour intervals and from 2.5-3.0 GHz are shown for clarity (Tapwater)

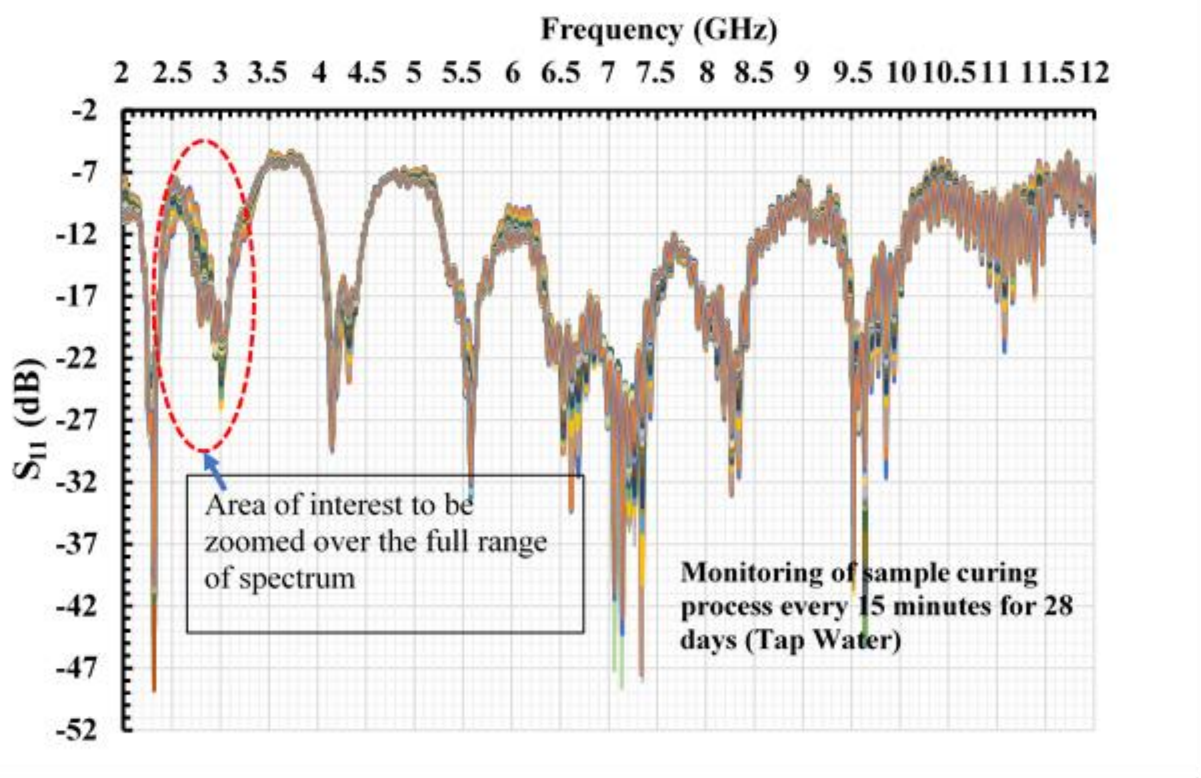

Figure 6.12: Transmitted power S_{21}measurements using microwave sensor for the full range of frequencies (2-12 GHz) were taken every15 minute for 28 days (Tapwater)

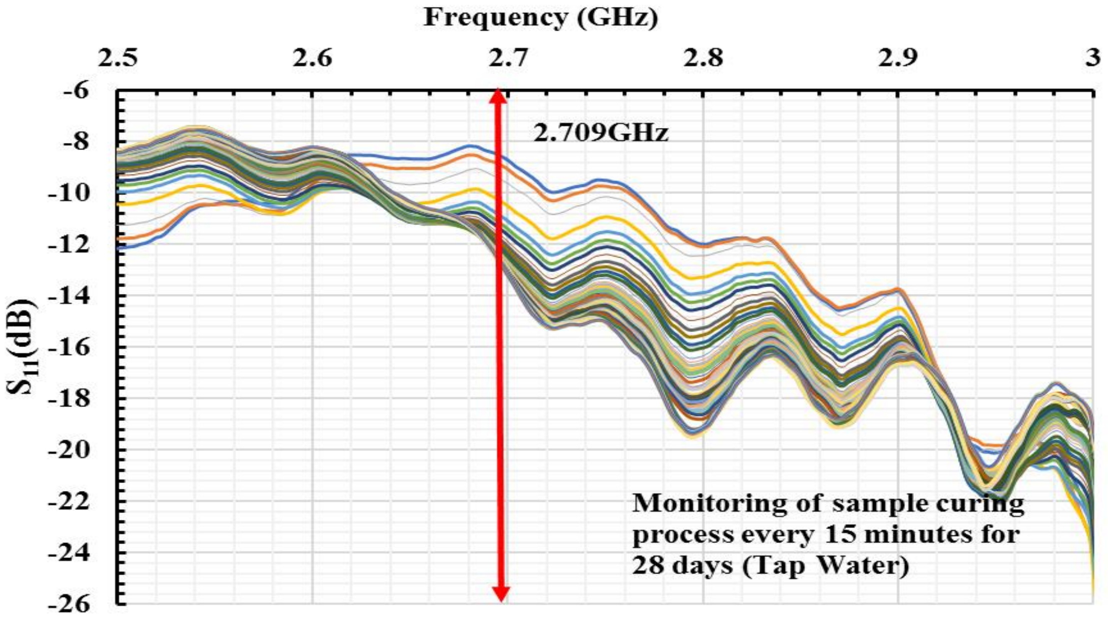

Figure 6.13: The microwave sensor measurements were taken every15 minute for 28 days in the frequency range (2-12 GHz), but for clarity, data measurements from 24-hour intervals and 2.5-3.0 GHz are presented (Tapwater)

The results also show that the saltwater-soaked samples gained more in mass per unit volume as a function of the increasing number of cycles. This is due to two main factors: a) More salt is deposited into the concrete slabs through the pores after each soaking cycle. b) Adding salt to the pores decreases the speed at which liquid water evaporates from concrete slabs.

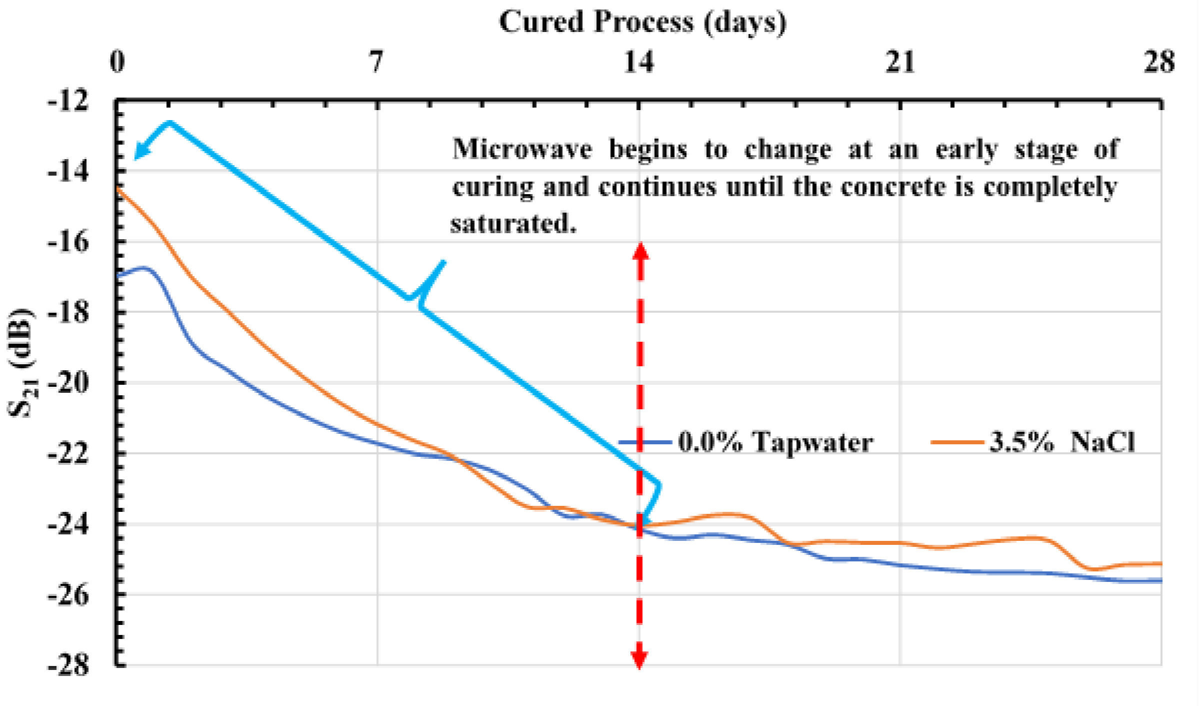

Figure 6.14: At 2.709 GHz, the microwave signal begins to alter at an early stage

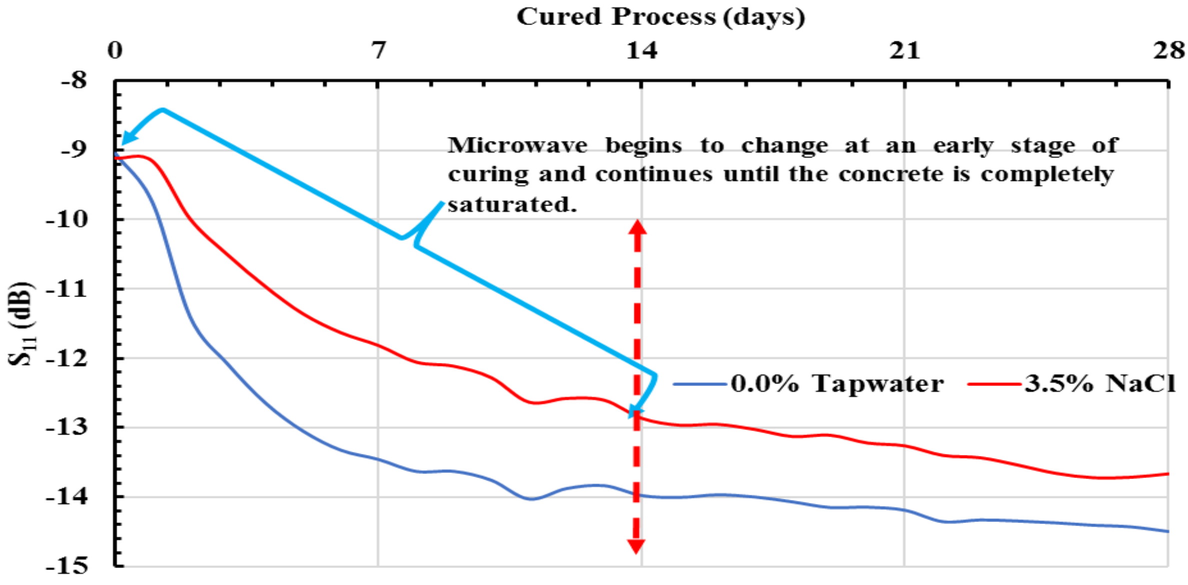

Figure 6. 15: At 2.709 GHz, the microwave signal begins to alter at an early stage

The above Figure 6.14 and Figure 6.15 show that the microwave signal starts to change at the early age of curing until the concrete gets fully saturated because concrete strength increases with age as moisture and a favourable temperature are present for cement's hydration. Therefore, it can easily be seen that the microwave power level rate of change differed at 14 days for both concrete samples curing in normal tap water and salt water.

6.4 Data analysis of drying process

The experimental work was undertaken with a set of horn antennas to monitor the drying process of both concrete samples with two different saltwater concentrations. Measurements of both concrete samples were via the S_{21} and S_{11} parameters. In the first instance, readings were captured over the full spectrum range of the VNA between the 2 GHz and 12 GHz frequency range. Figure 6.16, Figure 6.18, Figure 6.20, and Figure 6.22 illustrate the S_{21} and S_{11} measurements taken every minute during the 72 hours. In addition, they were taking the measures of the weight loss of both the concrete samples simultaneously for 72 hours. The spectrums were carefully examined to identify the resonant frequency wave in the full range to study the response of saltwater concentration ingresses into the samples compared to the microwave signals. The microwave frequency response at the same S_{21} and S_{11} parameters changed with varying saltwater contents in both samples. Areas of interest for further analysis are highlighted in Figure 6.16, Figure 6.18, Figure 6.20, and Figure 6.22, then zoomed in the highlighted areas for the S_{21} and S_{11} parameters, identified in the frequency range of 2.5 GHz -3 GHz; this can be seen in Figure 6.17, Figure 6.19, Figure 6.21, and Figure 6.23. The reason for selecting the microwave response region in this frequency range is that in Figure 6.17, Figure 6.19, Figure 6.21, and Figure 6.23, there is a noticeable change in EM signal in both samples. The amplitude decreases as the moisture content of the concrete sample decreases; additionally, the data obtained from this experimental work can demonstrate that in the concrete sample submerged in salt water. The amplitude does not drop rapidly because there is still salt inside the concrete after the water has evaporated from the specimen's surface.

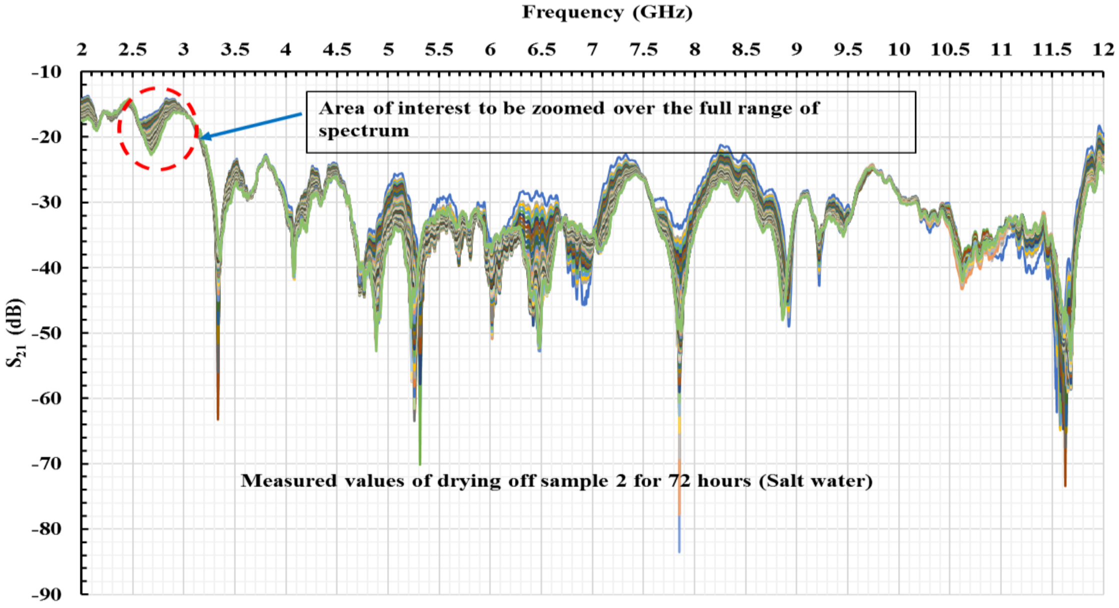

Figure 6.16: Transmitted power S_{21} measurements from electromagnetic wave sensor were taken every hour in the frequency range (2-13 GHz), salt water

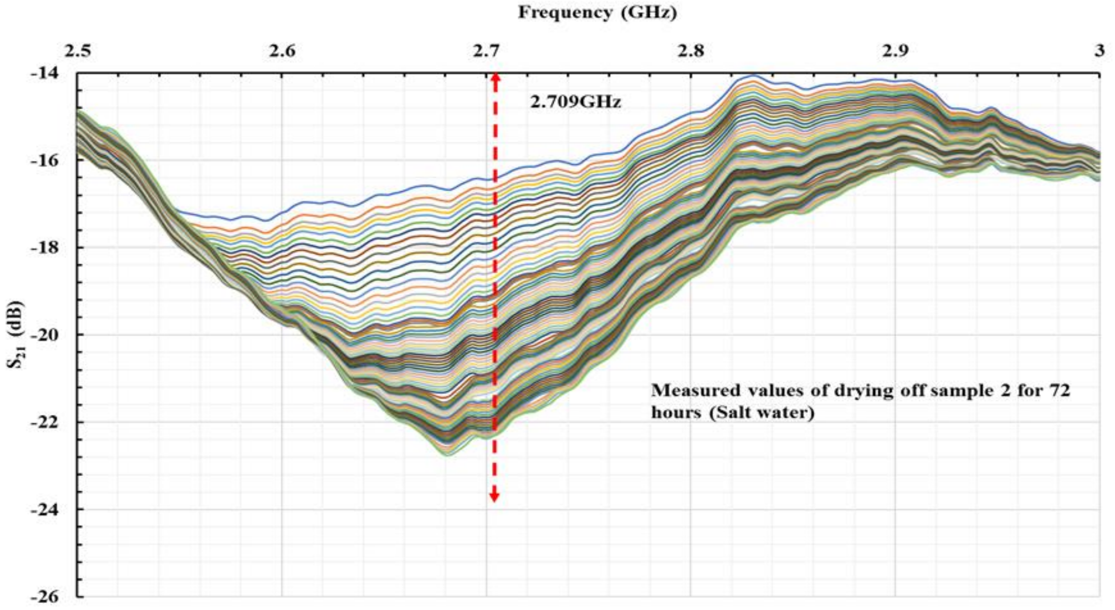

Figure 6.17: Readings from the electromagnetic wave sensor: measurements were taken every hour in the frequency range (2-13 GHz), but for clarity, data from 2.5-3 GHz are presented (Salt water).

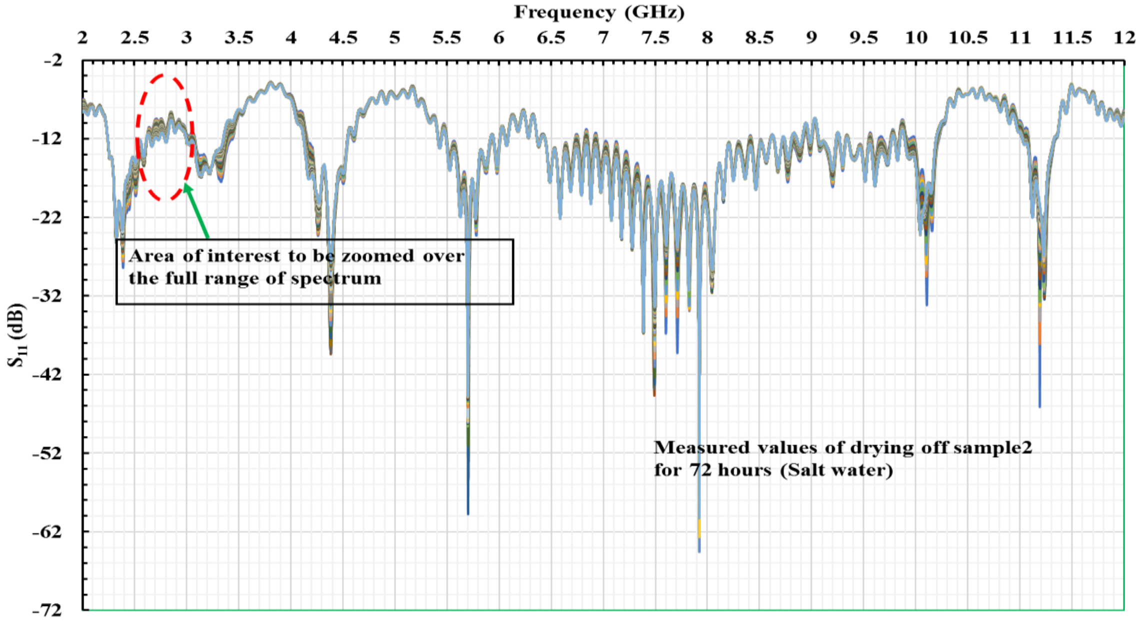

Figure 6.18: Readings of reflected power S_{11} measurements using microwaves were taken per hour for the full range of frequencies, 2-12 GHz (Salt water)

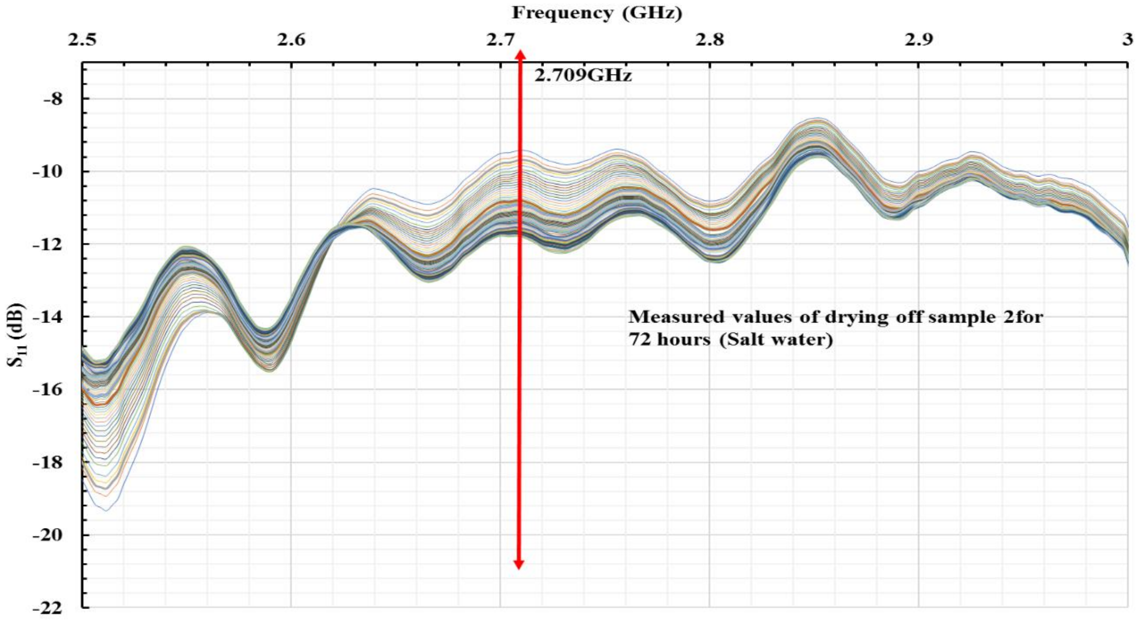

Figure 6.19: Reflected power S_{11} measurements of the material response to the microwaves were at the frequency 2.5-3 GHz are presented (Salt water)

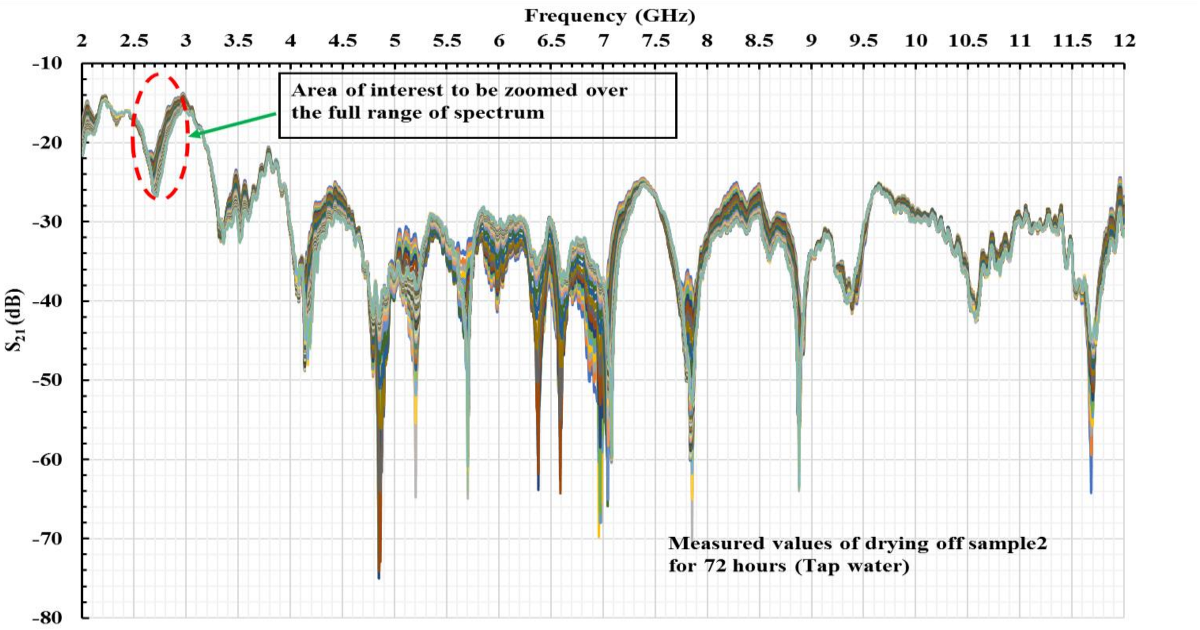

Figure 6.20: Transmitted power readings S_{21} measurements using the electromagnetic wave sensor; were taken every hour in the frequency range (2-12 GHz) (Tap water)

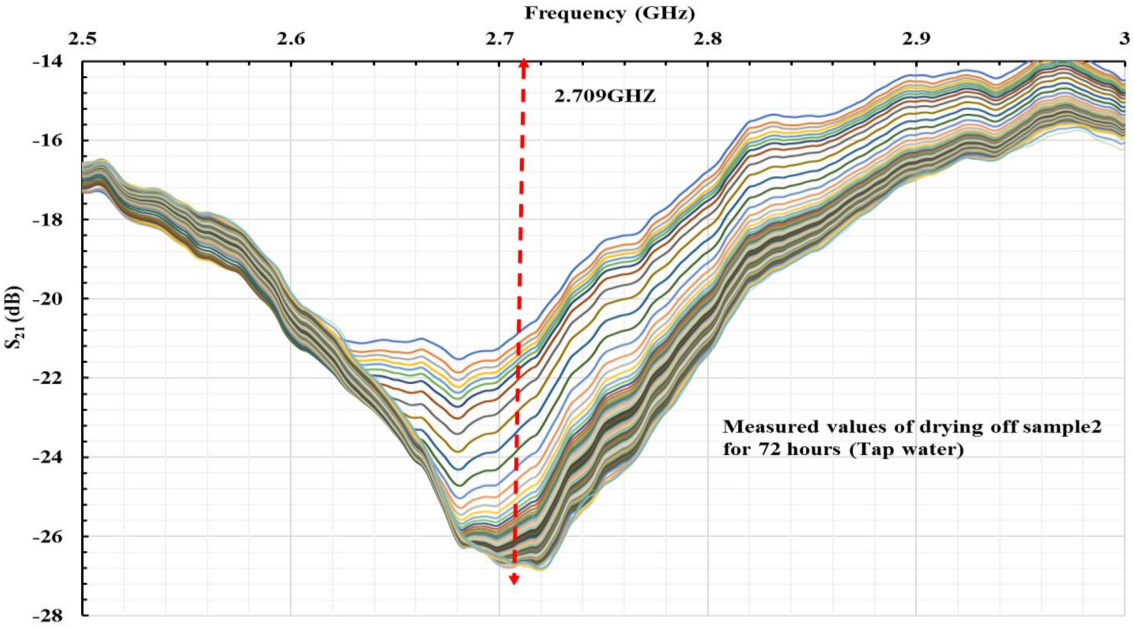

Figure 6.21: Transmitted power S_{21} measurements were taken every hour using electromagnetic wave sensor for the entire frequency range (2-12 GHz), but for clarity data from 2.5-3 GHz are presented (Tap water)

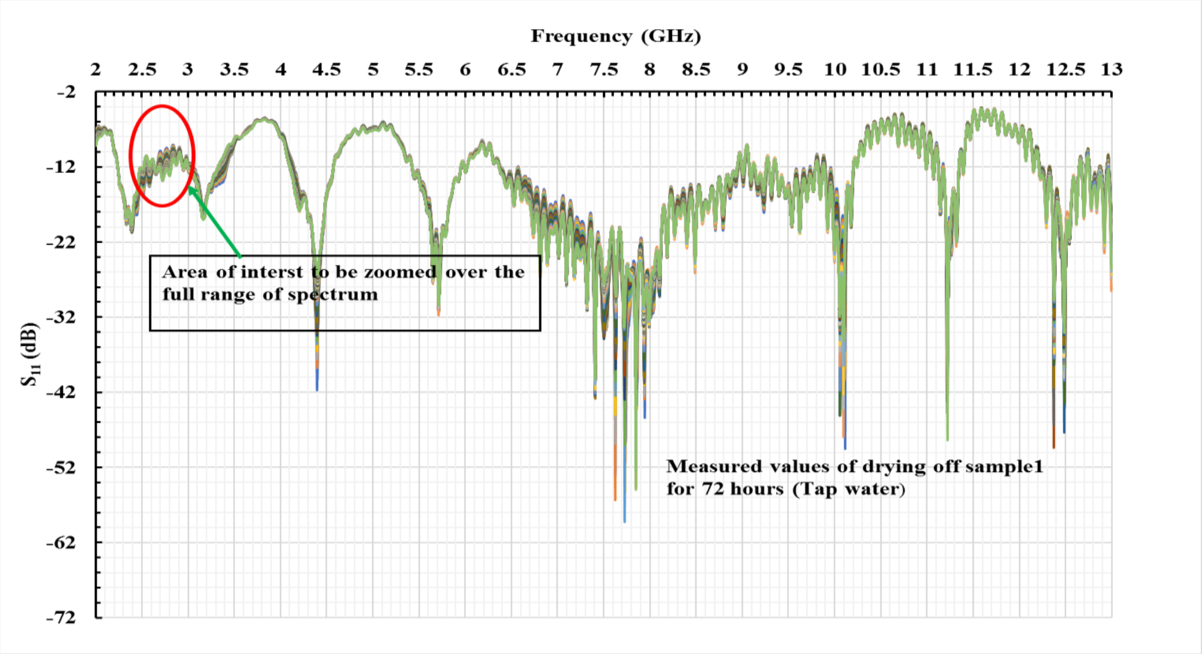

Figure 6.22: Readings of reflected power S_{11} measurements using microwaves were taken per hour for the full range of frequencies, 2-12 GHz (Tap water)

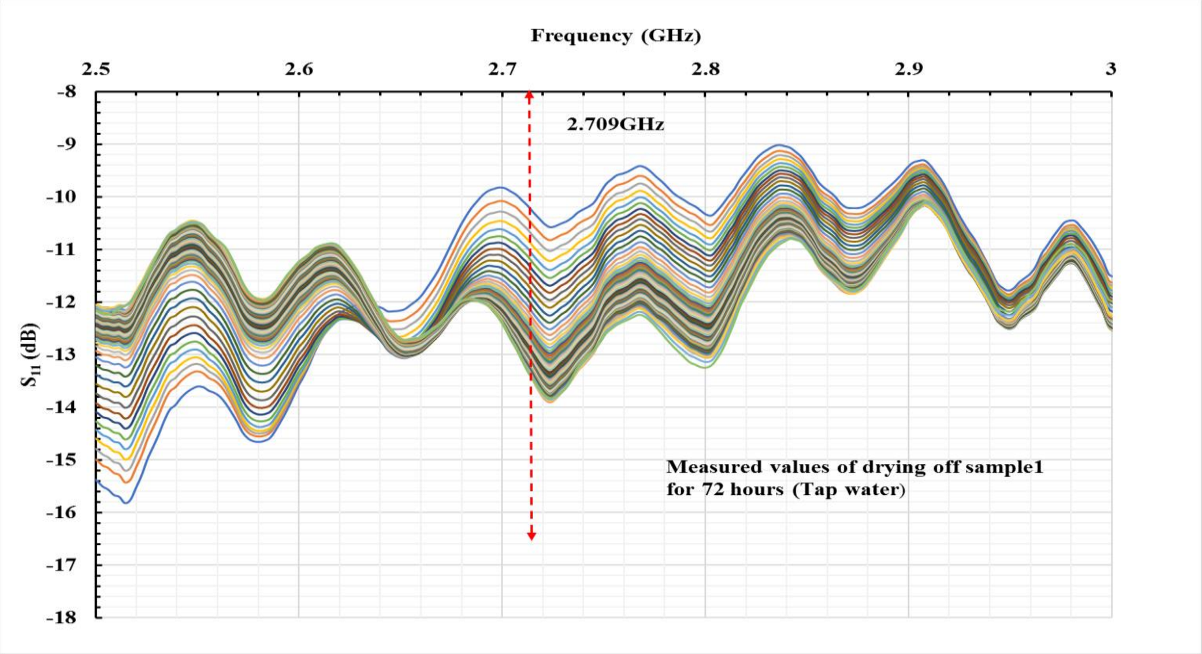

Figure 6.23: Reflected power S_{11} measurements using microwaves were taken per hour for the entire of frequencies, 2-12 GHz, but for clarity data from 2.5-3 GHz are presented (Tap water)

Table 6.2: The weight value of the sample before and after wetting

Concrete Samples without Rebar	Different water concentration	Weight samples before submerged in different water concentrations (Kg)	Weight samples after 28 days cured in different water concentrations (Kg)	Weight of sample after drying off 72 hours (Kg)	Amount of water absorbed by the sample (%)	Amount of water& salt water loss over 72 hours (%)	Amount of remaining water in the sample after 72 hours (%)
Sample 1	Fresh water	8.96	9.06	8.98	1.11	0.89	0.22
Sample 2	Salt water	8.99	9.28	9.18	3.22	1.09	2.13

Chloride penetrates concrete by the ingress of water containing the salts and by diffusion of the water's ions and absorption. This results in a high concentration of chloride ions at the surface of the concrete, which can ingress with time to reach the reinforcing steel. Chloride can ingress to a considerable depth while the concrete is permanently submerged, but there will be no corrosion unless oxygen is present in the cathode area. If the concrete is sometimes exposed to seawater and is occasionally dry, then salt ingress is progressive. In this experiment, both samples were not fully submerged in tap water and salt water. However, both the concrete samples were immersed in their respective solutions within (6 mm) of their top surface. Water and seawater was absorbed or evaporated from the edge of the concrete sample to the middle after 10 days of curing.

Dry concrete takes in salt water by absorption and, under some conditions, may continue to do so until the concrete has become fully saturated. If the external conditions then change to dry, the direction of movement of water becomes reversed, and water evaporates from the ends of capillary pores open to the ambient air. However, it is only pure water that evaporates, the salts being left behind. Consequently, the concentration of salts in the water left behind increases near the surface of the concrete. It can be seen that as an outcome, the salt moves inward, and the water moves outward. Then the next cycle of wetting with salt water will bring more salt present in solution into the capillary pores [274]. Nevertheless, if the wetting duration is short and the drying restarts very quickly, the ingress of salt water will carry the salts well into the interior of the concrete. Subsequently, drying concrete will get rid of pure water, leaving salts behind.

The ingress of salt water depends on the length of the wetting and drying durations. Also, it should remember that the wetting occurs very rapidly with salt water, but the drying is slower. Hence, the interior of the concrete never dries out, and it should also be noted that the diffusion of ions during the wet periods is relatively slow [263].

Table 6.2 shows the percentage of remaining moisture and salt water in both concrete samples. The concrete sample submerged in salt water still has 2.13% moisture remaining after 72 hours drying off; in comparison, the other sample submerged in tap water has only 0.22% moisture remaining after 72 hours drying off. The reasons for 2.13% remaining in the concrete sample depend on the duration of the drying period and the external relative humidity. It is likely for most of the water in the outer zone of the concrete to evaporate. The water remaining in the internal area will become saturated with salt, and the excess salt will quickly form as crystals.

Where the salt water penetrated more extensively into the concrete sample, the conductivity of the sample increased, which led to the decrease of the penetration ability of the microwave signal. Thus, the sensitivity of the measurement was decreased. Figure 6.24 and Figure 6.26 present the correlation coefficient (R^2) between weight loss and S_{21} and S_{11} parameters change across the entire frequency spectrum, i.e. from 2 GHz to 12 GHz frequency range. R^2, the correlation between every single frequency point from 2 to 12 GHz compared to the second parameter, which could be either the amount of moisture lost or the amount of chloride concentration, was displayed using the LabVIEW software. LabVIEW generates a graph ranging from 0 to 1, with 0 representing no correlation and 1 representing a strong correlation, and 2.709 GHz presenting the highest correlation. The strongest (polynomial) correlation coefficient determined between S^{21} and S^{11} where it changes at 2.709 GHz for weight loss, with $R^2 = 0.91$ and $R^2 = 0.96$ for the saltwater sample and $R^2 = 0.97$ and $R^2 = 0.92$ for the tap water sample, as shown in Figures 6.25 and 6.27.

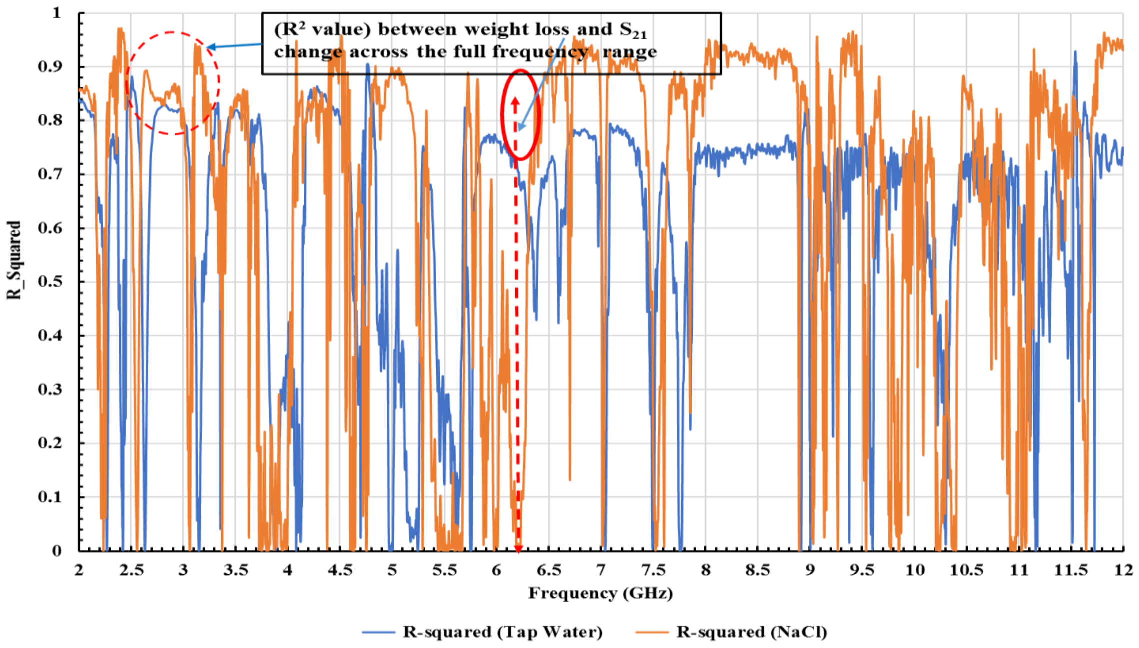

Figure 6.24: R^2 between both concrete sample weight loss and S_{21} change across the full frequency spectrum

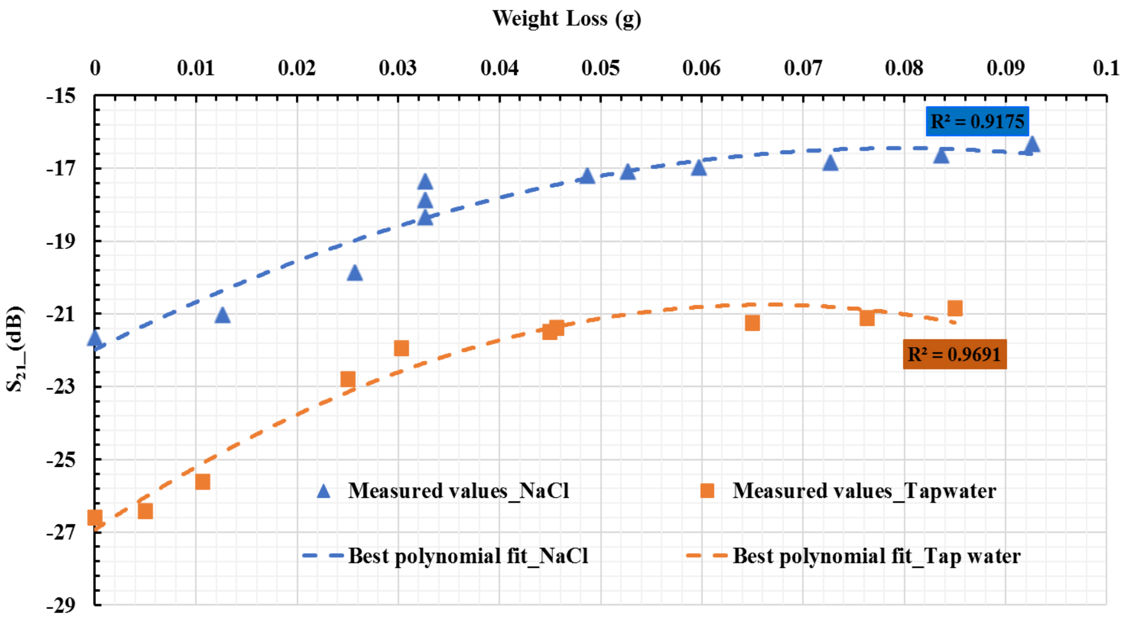

Figure 6.25: Polynomial correlation coefficient best fit between weight loss and S_{21} change at 2.709GHz, with R^2 =0.91, for salt water sample and R^2=0.97 for tap water sample

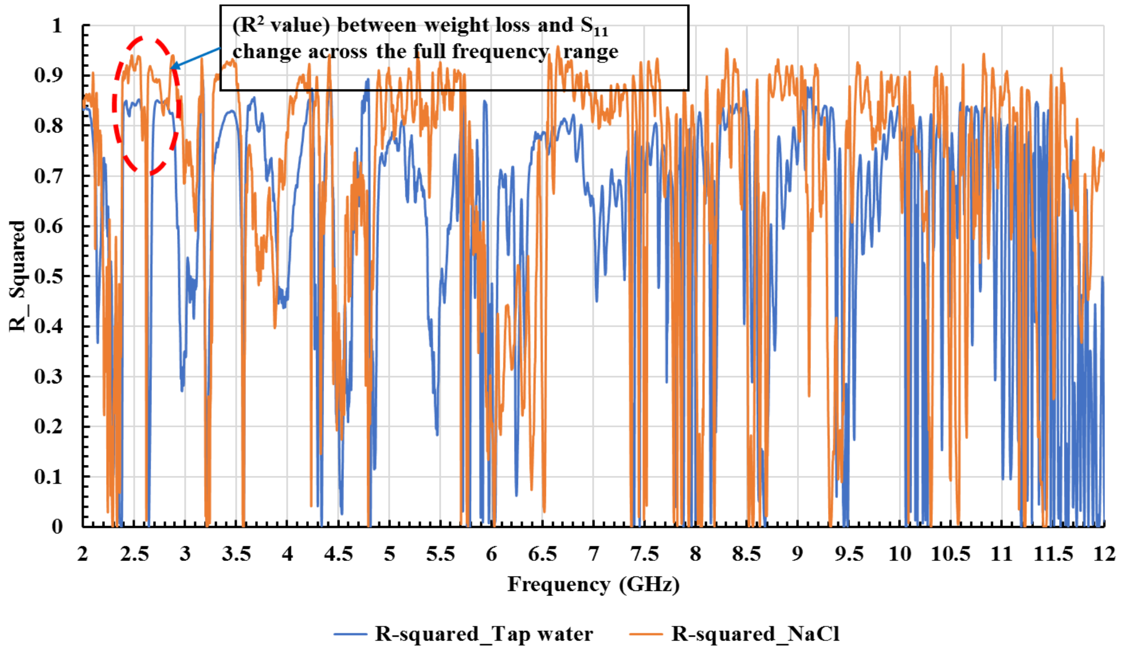

Figure 6.26: R^2 between both concrete sample weight loss and S_{11} change across the full frequency spectrum

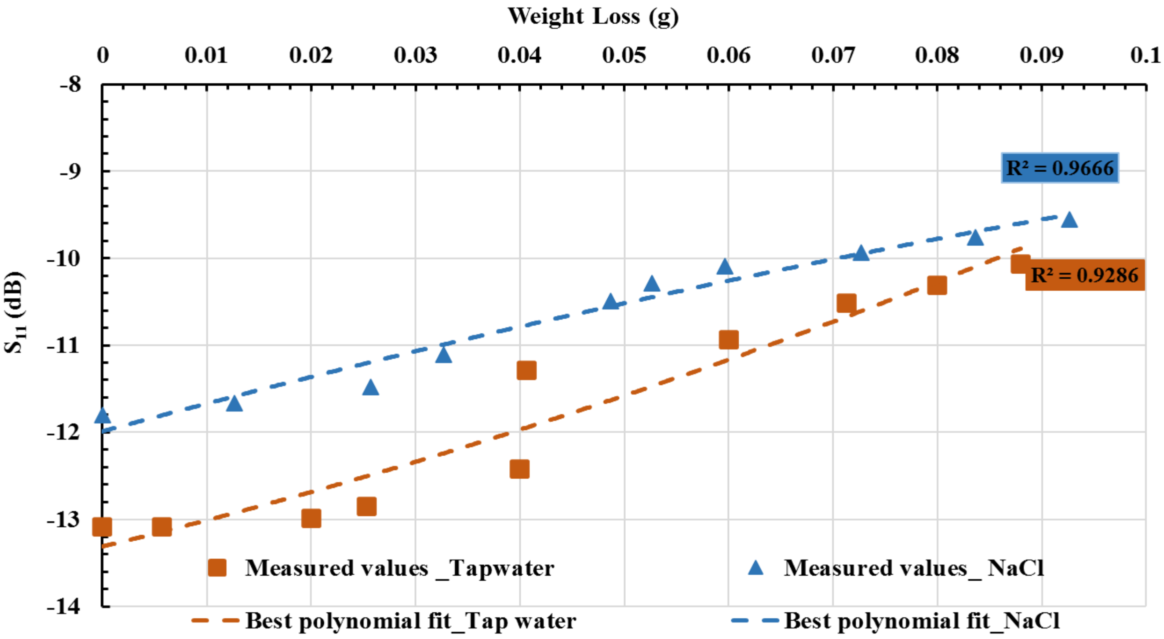

Figure 6.27: Polynomial correlation coefficient best-fit weight loss and S_{11} change at 2.709 GHz, with R^2=0.96, for saltwater sample and R^2=0.92 for tap water sample

Absorption is driven by moisture gradients [275]. Furthermore, the durability of concrete is mainly dependent on the capacity of a fluid to penetrate the concrete structure, which is known as permeability. High permeability leads to the introduction of molecules that react and destroy the structure's chemical stability [276]. Moreover, the low permeability of concrete can improve resistance to the penetration of water, sulphate ions, chloride ions, alkali ions, and other harmful substances which cause chemical attack [277]. Chloride ions can be absorbed quickly but not as rapidly as moisture; moisture always comes first, followed by chloride. This is due to the difference in dynamic viscosity between water and salt water; salt water's viscosity is substantially higher and denser than water without salt [278]. Therefore, the data analysis from the drying process experiment has proven that the sample containing only moisture was drying off much faster than the concrete sample containing chloride ions which were always last because of the crystals of salt that blocked the water from escaping from the surface of the concrete. Hasted (1948) conducted an experimental study on the dielectric properties of saltwater solutions and observed a dielectric decrement with salt concentration. That means the addition of sodium chloride to water results in a drop in electrical permittivity.

6.5 Data analysis of drying process (two rebars)

An experiment was carried out using two concrete slabs of the same size and the material properties that contained two rebars. These represented two samples out of 10 samples (group D) see Table 5.1 in Chapter 5. The details of the concrete properties are mentioned in Chapter 5, Section 5.4.2. We investigated the difference between tap water and saltwater solutions on the concrete with reinforcement and how the rebars in concrete structures affect the microwave signal. As a result, it is possible to observe changes in the microwave spectrum due to measured objects' different dielectric properties and textures. In the first instance, we took measurements of both concrete samples for the S_{21} parameter, and all samples were captured over the full spectrum range of the VNA between 2 GHz and 12 GHz. across the VNA's complete spectrum range between 2 GHz and 12 GHz. Figure 6.28 and Figure 6.31 illustrate the S_{21} measurements, which were taken every minute for 24 hours, taking the weight loss measurements of both the concrete samples simultaneously for 24 hours. The spectrums were carefully examined to identify the resonant frequency wave in the full range, to study the response of saltwater concentration ingresses into the samples compared to the microwave signals and to study the response of saltwater concentration ingress to the microwave signal. The microwave frequency response at the same S_{21} parameters changed with varying saltwater contents in both samples. Areas of interest for further analysis are highlighted in Figure 6.28 and Figure 6.31, then zoomed in the highlighted areas for the S_{21} parameters, identified in the frequency range of 3.45-3.55 GHz and 4.2 GHz – 4.6 GHz, for both concentrations of salt water respectively and can be seen in Figure 6.29, Figure 6.30, Figure 6.32 and Figure 6.33.

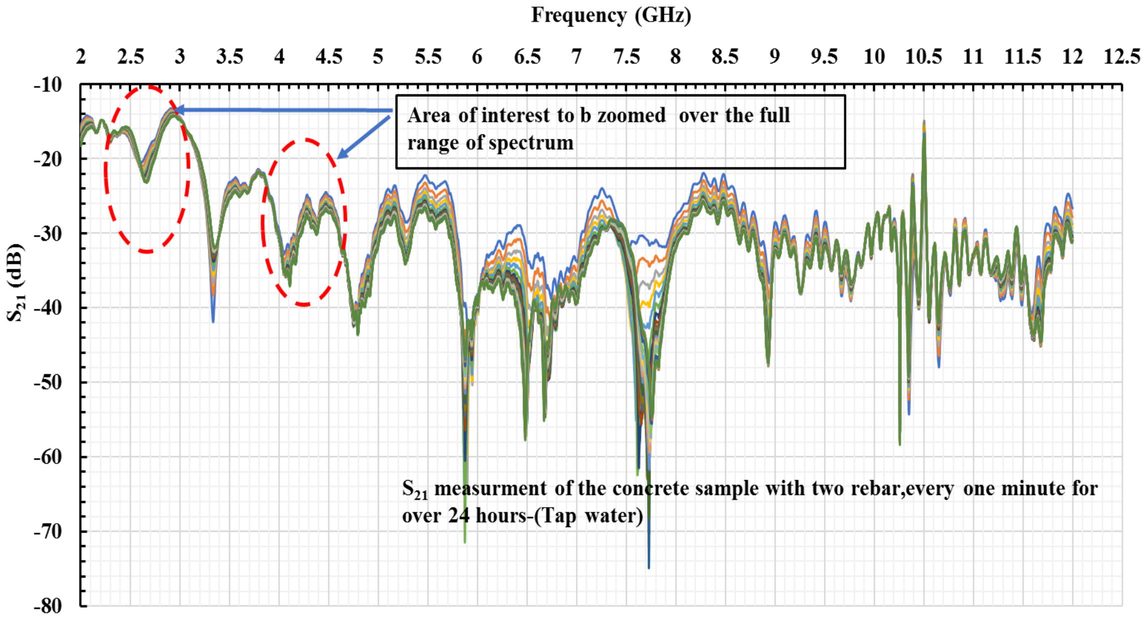

Figure 6.28: Transmitted power S_{21} measurements using microwave were taken every one minute for the full range of frequencies, 2-12 GHz (Tap water)

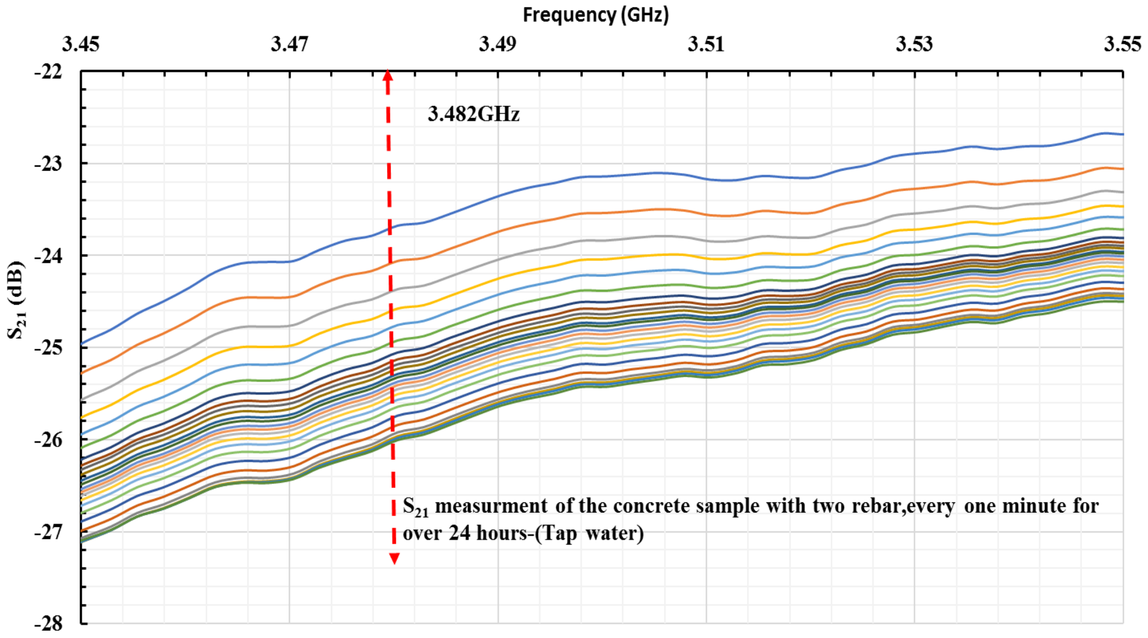

Figure 6.29: Readings of transmitted power S_{21} measurements responses of the concrete using microwave were taken per minute for the full range of frequencies (2-12 GHz), but for clarity, data measurements from 3.45-3.55 GHz are presented (Tap water).

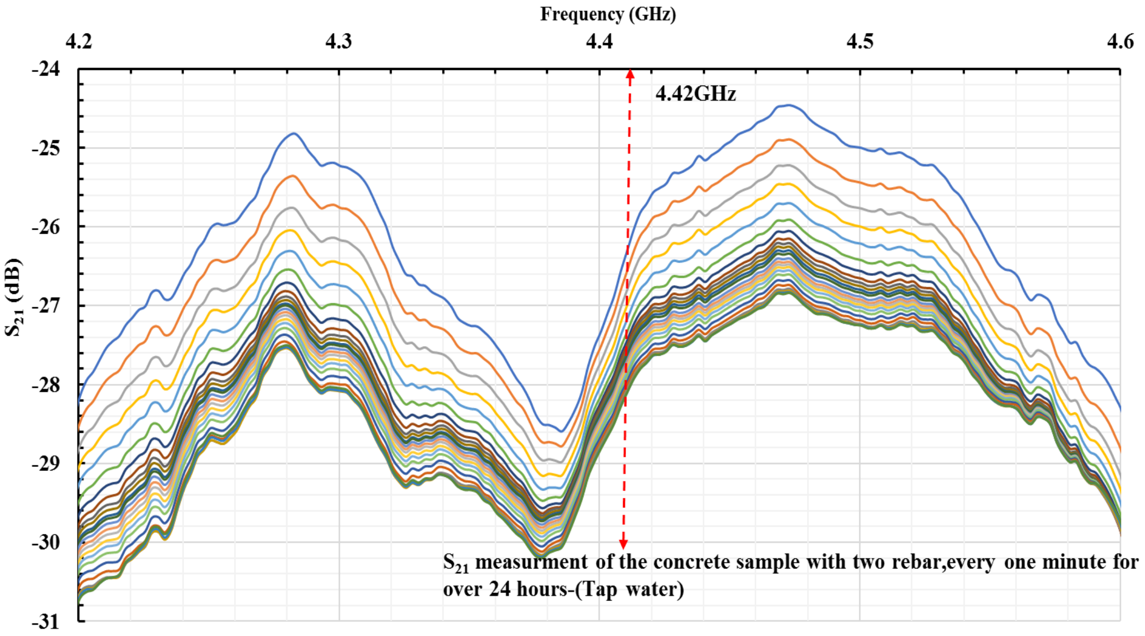

Figure 6.30: Transmitted power S_{21} measurements using microwave were taken per minute for the full range of frequencies, (2-12 GHz), but for clarity data measurements from every hour intervals and 4.2-4.6 GHz are presented (Tap water)

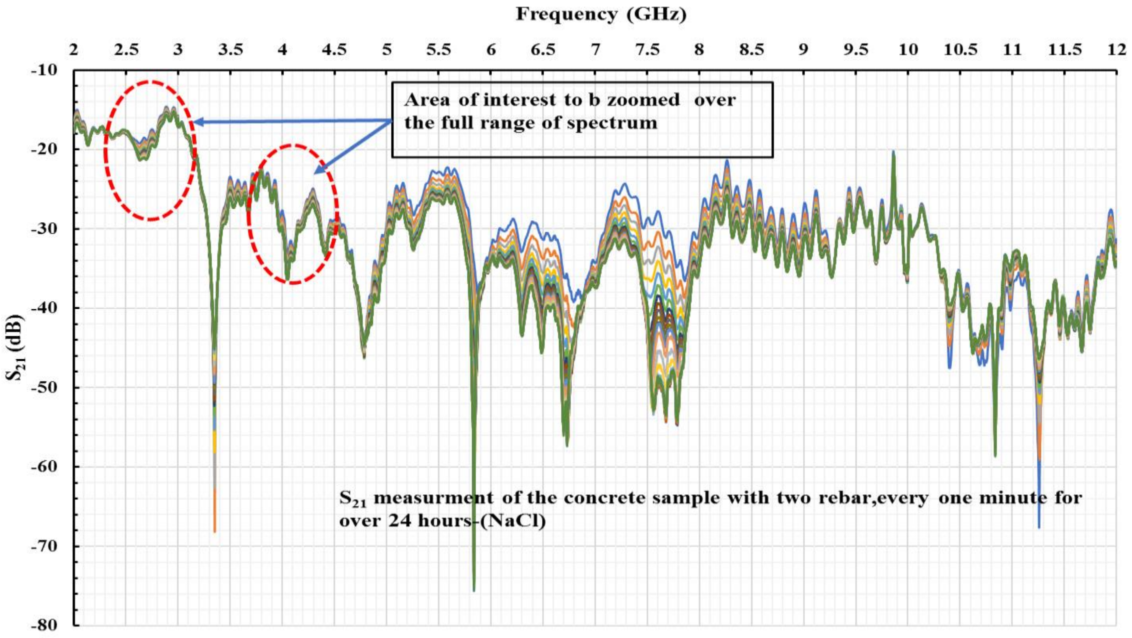

Figure 6.31: Readings of transmitted power S_{21} measurements using microwave were taken every one minute for the full range of frequencies, 2-12 GHz (Salt water)

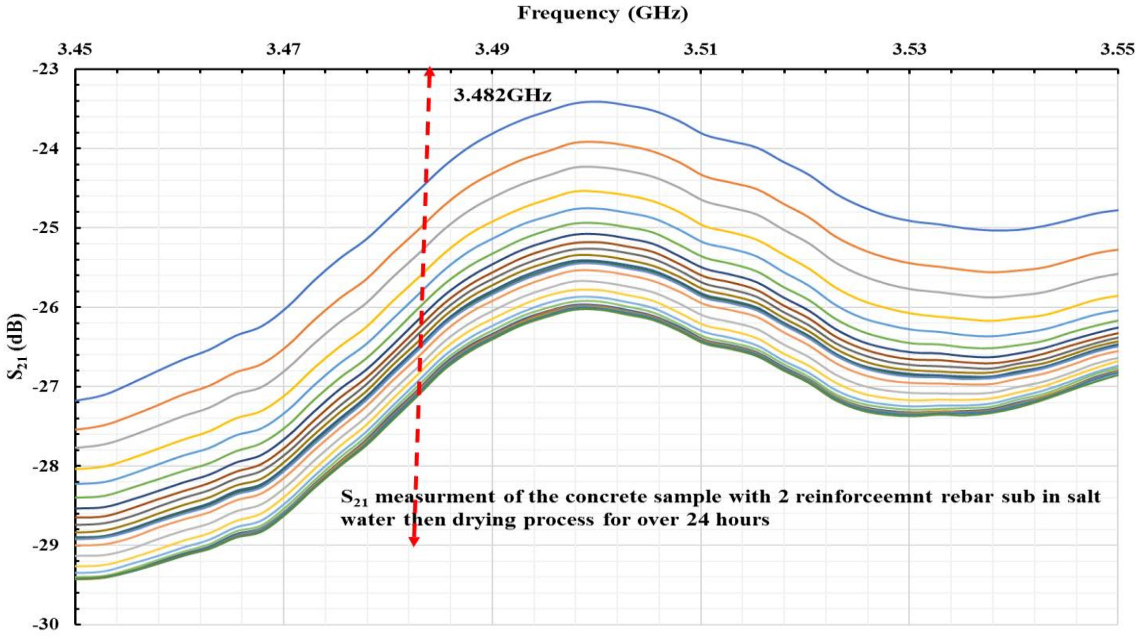

Figure 6.32 Microwave measurements of transmitted power S_{21} were taken every minute over the entire range of frequencies (2-12 GHz), but clarity data readings from every hour intervals and 3.45-3.55 GHz are presented (Salt water)

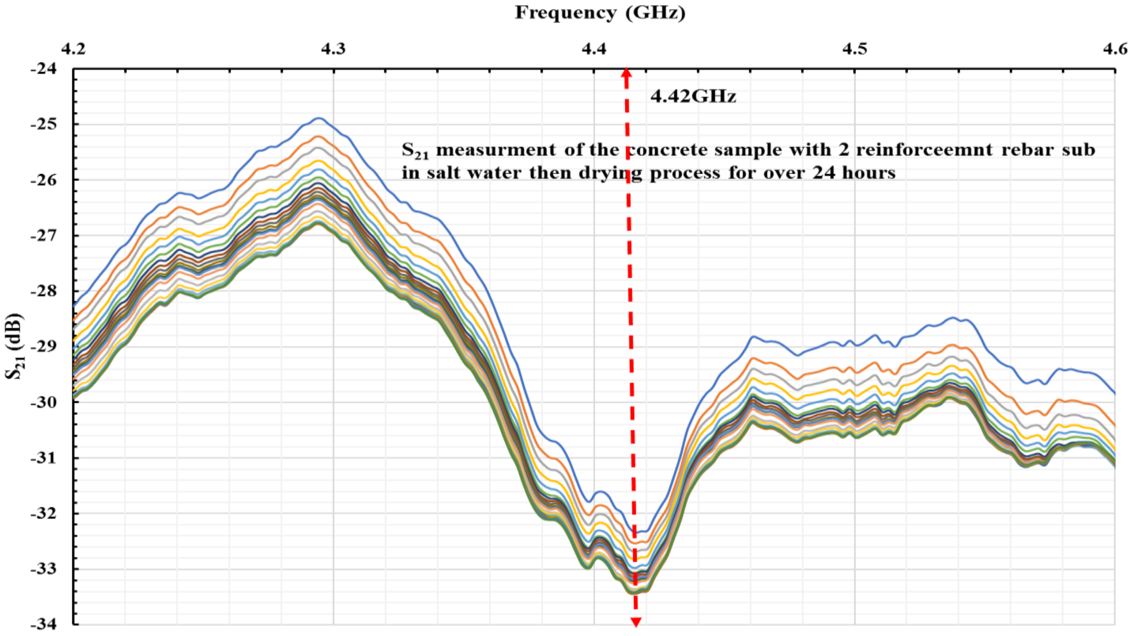

Figure 6.33: Readings of transmitted power S_{21} measurements of the response concrete using microwaves were taken per minute for the full range of frequencies (2-12 GHz), but for clarity data measurements from every hour intervals and 4.2-4.6 GHz are presented (Salt water)

The conductivity of the concrete sample increased as the salt water penetrated further into the concrete, which contributed to a decrease in the microwave signal’s penetration power. Thus, the measurement sensitivity decreases. The linear association (R^2) between weight loss and the S_{21} parameter varies over the entire frequency spectrum, i.e. the frequency ranges from 2 GHz to 12 GHz, as shown in Figure 6.34. In comparison with the second parameter, the LabVIEW program was used to display the R^2 value that is the correlation between every single frequency point from 2-12 GHz. This could be either the amount of moisture lost or chloride concentration, and LabVIEW produces a graph between 0-1, where 0 is not correlated, and 1 is the strong correlation. It shows about 3.482 GHz and 4.42 GHz with the highest correlations. The strongest (polynomial) correlation coefficient association between S_{21} shifts at 3.482 GHz and weight loss, with R^2 = 0.78 with the salt water and R^2 = 0.90 of the sample with tap water, can be seen in Figure 6.35. The strongest (polynomial) association between S_{21} shifts at 4.42 GHz and weight loss, with R^2 = 0.71 with the saltwater and R^2 = 0.89 of the sample with tap water, can be seen in Figure 6.36.

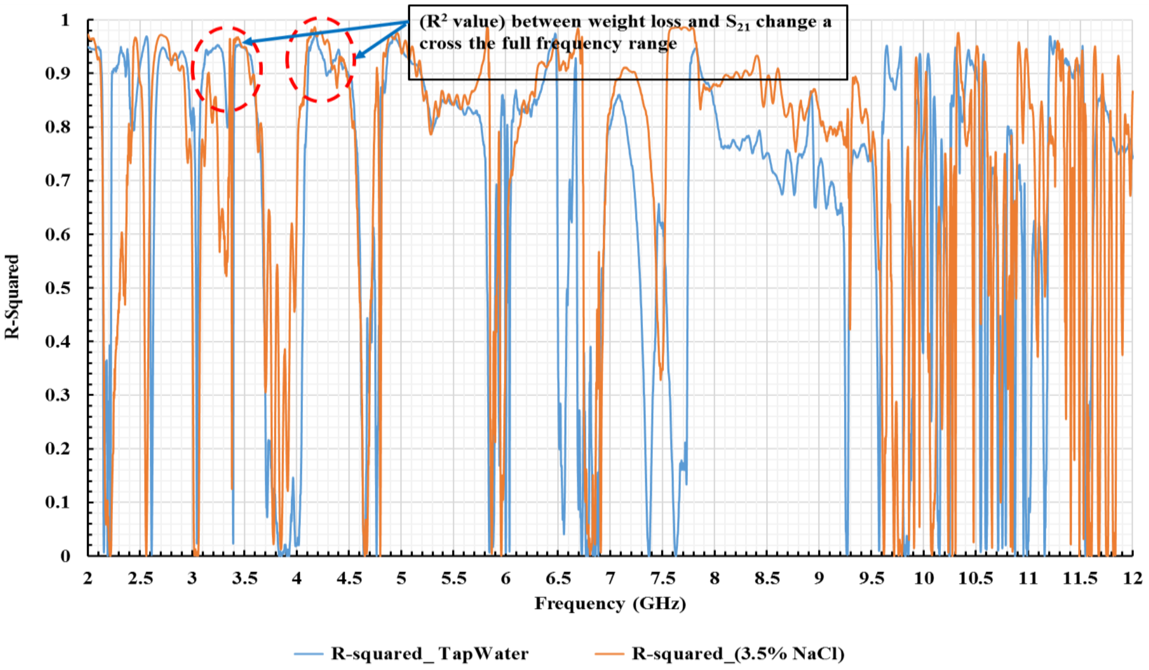

Figure 6.34: R^2 between both concrete sample weight loss and S_{21} change across the full frequency spectrum

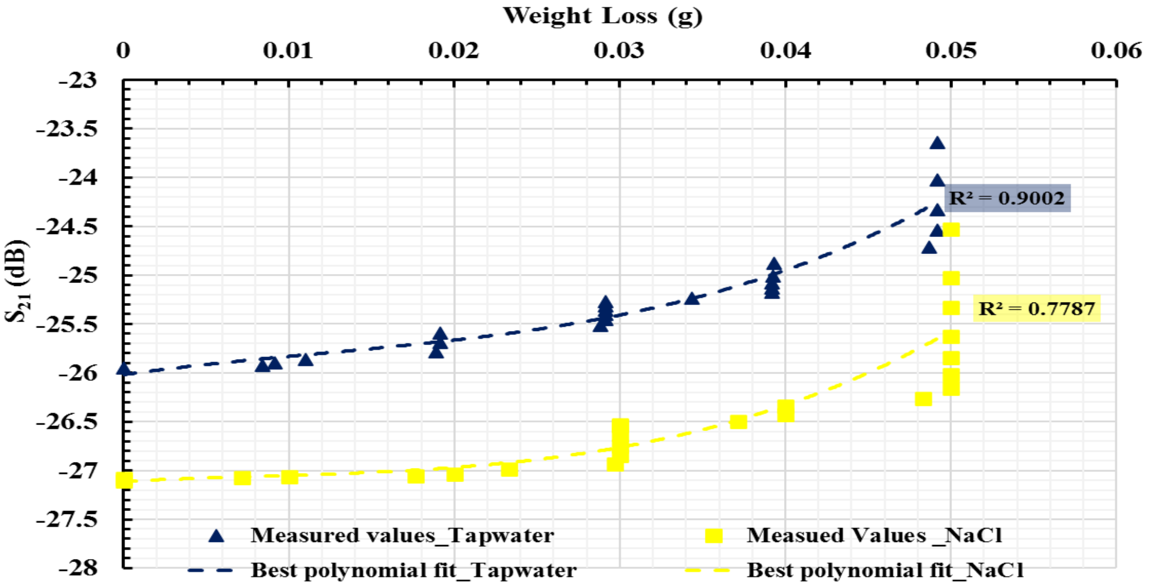

Figure 6.35: Polynomial correlation coefficient best fit between weight loss and S_{21} change at 3.482 GHz, with R^2 =0.77, for salt water sample and R^2=0.90 for tap water sample

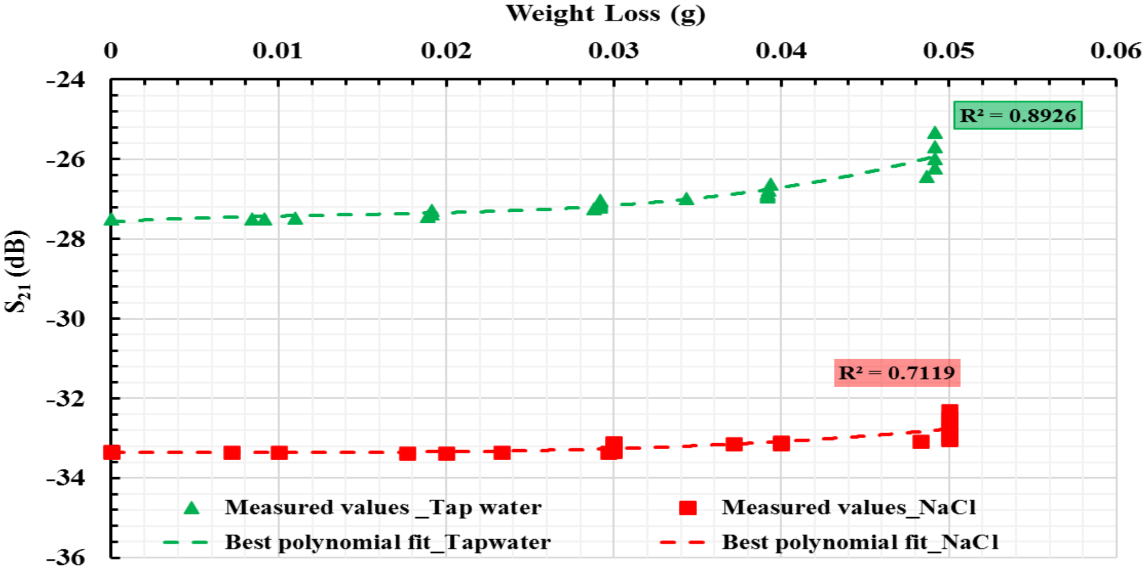

Figure 6.36: Polynomial correlation coefficient best fit between weight loss and S_{11} change at 4.42 GHz, with R^2 =0.71, for salt water sample and R^2=0.89 for tap water sample

Collecting the signature of the microwave spectrum was necessary to recognise the characteristics of the concrete structure. Therefore, measurements taken with and without reinforcement for the concrete samples can be seen in Figures 6.37 and Figure 6.38. Both sensors were located 20 mm from the measured area surface, and data was collected over 24 hours during the concrete sample drying off period. The S_{21} parameter was used for the measurements, and the plots indicate the reflected amplitude signal from the measured material properties. Data illustrated in Figure 6.37 shows that microwave attenuation changes because the moisture content in the concrete sample is reducing. This experiment is to confirm that the concrete sample without the reinforcement has its specific pattern. The second experiment also showed this for the concrete sample with two reinforcements, where data sets were collected with the two horn antennas. Figure 6.38 shows results from the sensor. The antenna was arranged in the same parameter S_{21} configuration and placed at the same distance from the surface of the concrete samples. The identical concrete pattern remains constant at the rebar location before the sensor position is adjusted. The unique signal starts to change due to reducing water and the dielectric properties of the steel rebar. The role and form of the material inside the concrete structure can be identified using these phenomena.

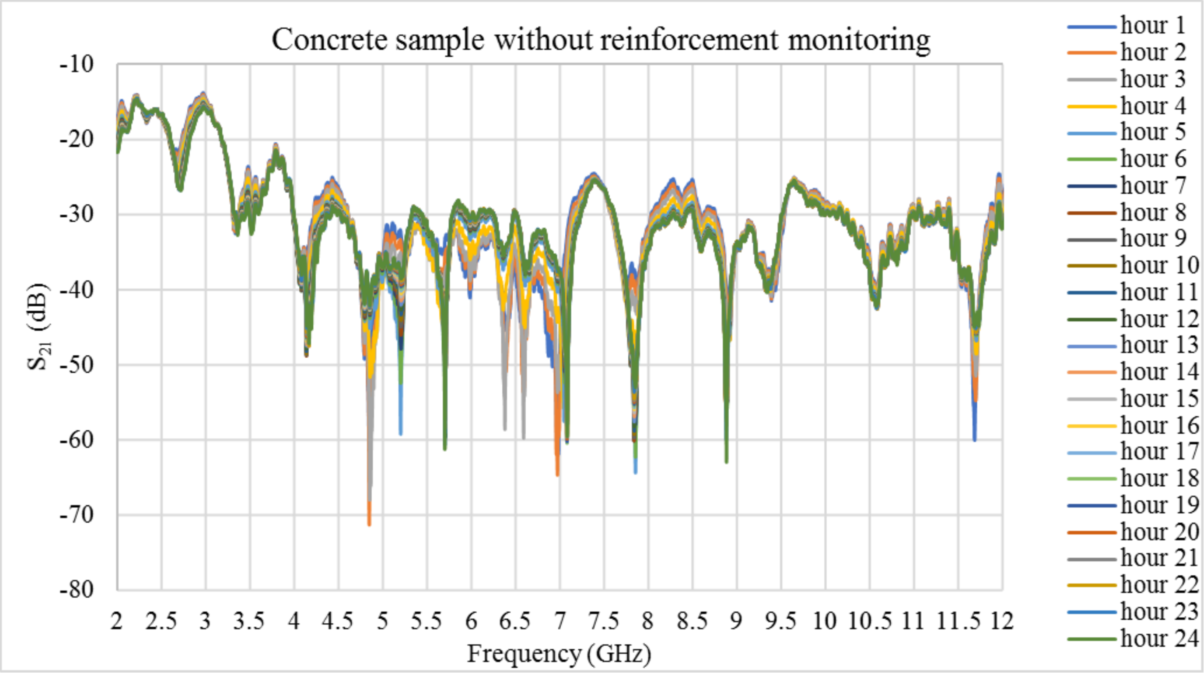

Figure 6.37: Transmitted power S_{21} measurements of concrete sample drying off without reinforcement for the full range of frequencies, 2-12 GHz (Tap water)

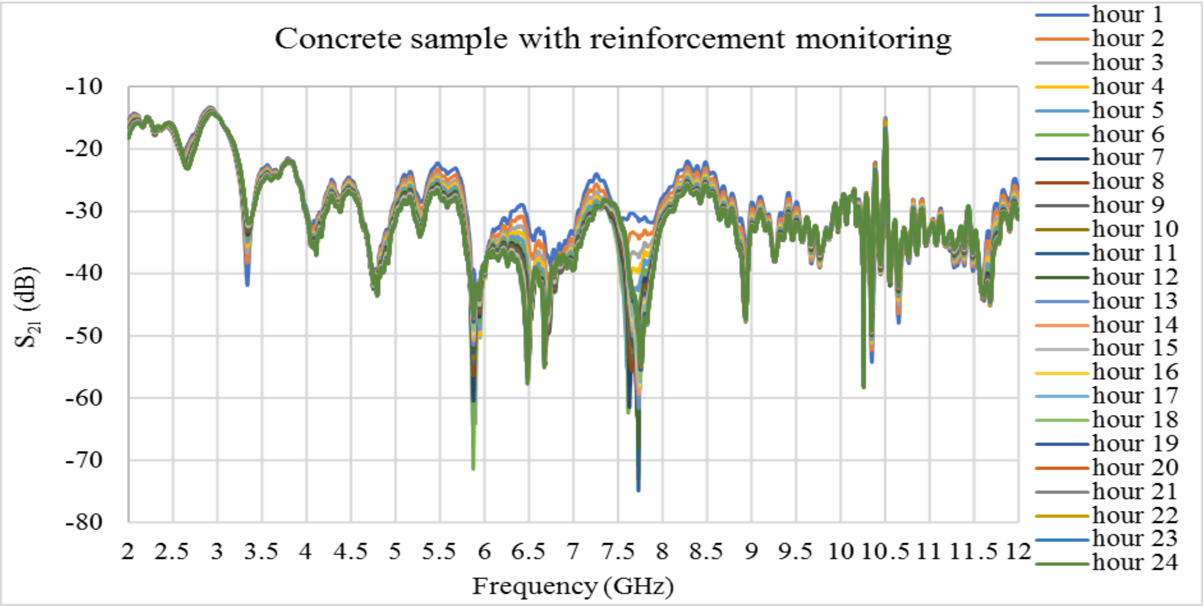

Figure 6.38: Transmitted power S_{21} measurements of concrete sample drying off with reinforcement for the full range of frequencies, 2-12 GHz (Tap water)

A comparison between two concrete samples with reinforcement and without reinforcement has been shown in Figure 6.39. Sensors were put in the middle of the sample from the start of the measurements. In comparison, results observed that the specific microwave configuration shifted to the left, and the amplitude level of the microwave signal has also changed due to the presence of the steel rebar. Concrete samples absorb different amounts of microwave energy without reinforcement. Appendix D contains the raw data results for the remaining samples with one rebar, crossing rebars, and mesh rebars.

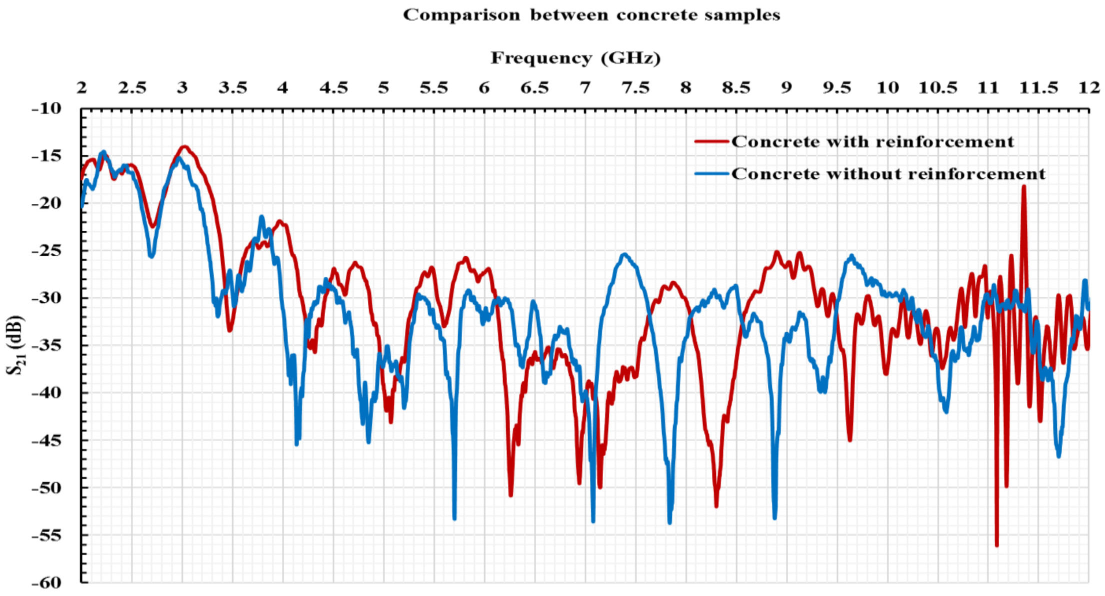

Figure 6.39: Comparison between concrete samples with and without reinforcement

6.6 Data analysis of 5 concrete samples with 5 different saltwater concentrations

Figure 6.40 illustrates the S21 measurements of the reflected signal for five concrete samples. The measurements shown in the figure were taken every 15 minutes for 48 hours. The change of the antenna response is thought to be caused by the different saltwater concentrations from (0.0%, 0.5%, 1.5%, 2.5% and 3.5%). The data was processed in two steps to select the optimum electromagnetic frequency for chloride ion concentrations test in concrete samples. The first step used an Info Gain Attribute Eval, which employs the Ranker search method from the Weka workbench select attribute to reduce the dimensionality of the data from 4,001 features to 3,003 features based on the five different classes such as (0.0%, 0.5%, 1.5%, 2.5%, and 3.5%) saltwater concentrations [179]. The selected method is able to calculate the information gain for each attribute for the output variable. Those attributes that contribute more information have a higher information gain value and can be picked, while those that don't give much information have a lower score and can be eliminated. The second step applied 10 machine learning algorithms in four different classifiers (Meta, Misc, Rules, and Tress). These methods and associated algorithms have been described in detail in Chapter 3 Section 3.7.2. The final algorithm, J48, is the Class for generating an unpruned or pruned C4.5 decision tree. The knowledge model depends on how the classifier is constructed, and it can be represented by classification rules algorithms AQ21 [279], decision trees e.g algorithm C4.5 [280] or many other representations. Table 6.3 presents the set of algorithms that have been previously described above within various classifiers having less mean square error and a higher percentage of accuracy to establish the most important frequency across the Class of five different saltwater concentrations. This research concentrated on the most popular decision tree classifiers, the algorithm J48 of the last publicly available version of the C4.5 method developed by J.Rose Quinlan [280]. This algorithm was compared to selected algorithms available in Weka workbench [281]. Figure 6. 41 shows the procedures for collecting and processing the data.

Table 6.3: Results obtained for different classifiers from the Weka workbench

The different classifier has been used for these algorithms	Accuracy (%),	Means Absolute error (%)	Root means square error (%)
MultiScheme	20	0.3	0.4
Bagging	20	0.32	0.4002
CVParameterSelection	20	0.32	0.4
InputMappedClassifier	20	0.32	0.4
OneR	20	0.32	0.5657
ZeroR	20	0.32	0.4
REPTree	20	0.32	0.4
RandomTree	72	0.112	0.2366
DecisionStump	40	0.24	0.3464
J48	86	0.056	0.2266

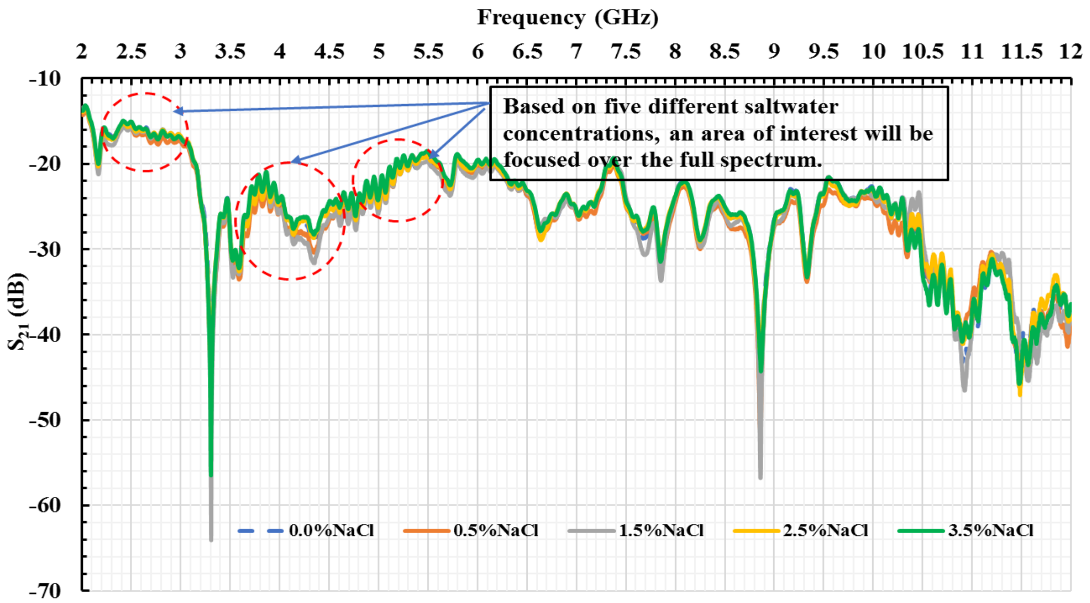

Figure 6.40: The microwave horn antenna; the measurements were taken for the frequency range 2-12 GHz.

The best accuracy equalling 86% and least means absolute error and root mean square error was obtained utilising the J48 algorithm. The decision tree generated by the J48 algorithm is illustrated in Figure 6.42, which shows the most crucial frequency point for the different saltwater concentrations. The first number in brackets indicates the number of examples from the training set covered by a select leaf; the second value directly after the sign (10,0) reflects the number of incorrectly categorised (see Figure 6.42) created by the Weka workbench algorithm. These numbers are based on the frequency values indicated in Figure 6.41. The trees generated by algorithm J48 show the frequency point that is the most significant point determining the level of chloride ions in the concrete samples.

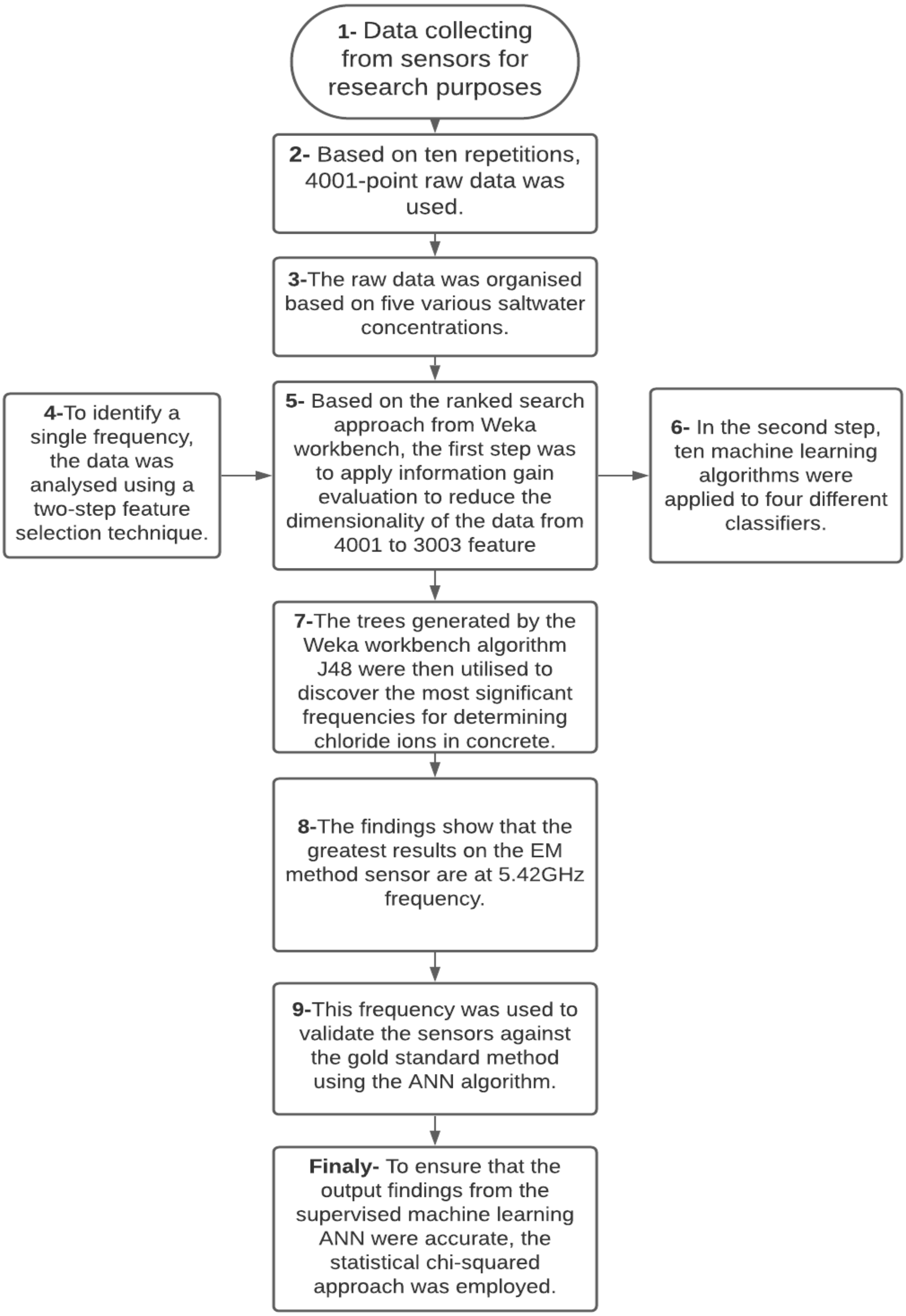

Figure 6.41: Flow diagram of data processed with machine learning classification.

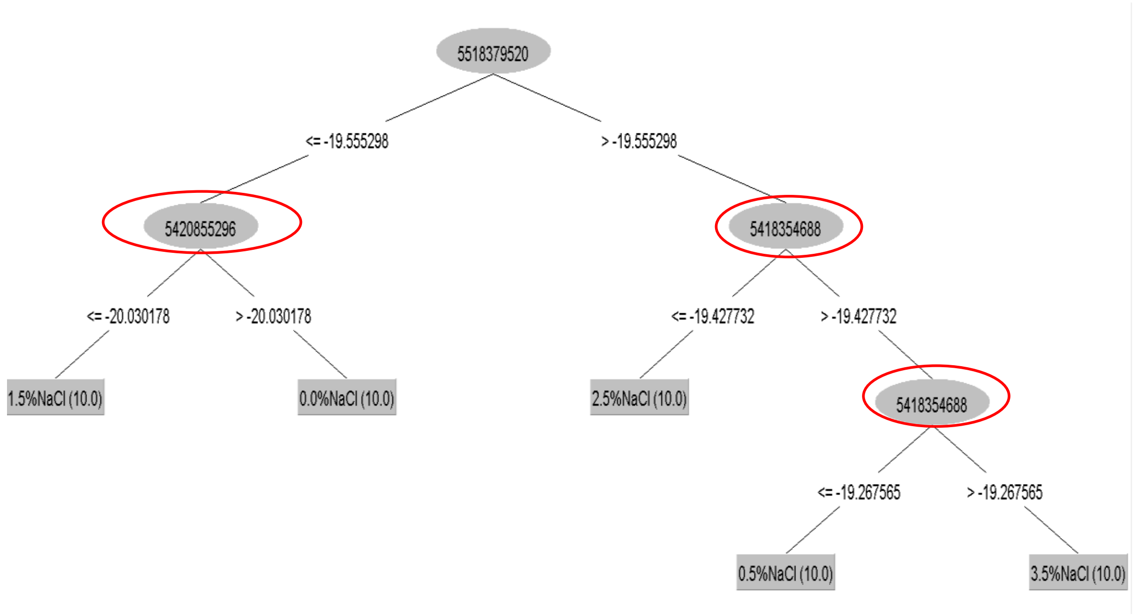

Figure 6.42: Indicates the classification of algorithm J48 decision tree graphic

The obtained decision tree can be easily transformed into the following rules:

Salt concentration = 0.0%, 05%, 1.5%, 2.5% and 3.5%

Rule 1 [freq (5518379520 <= -19.555298)] and [5420855296>-20.030178]: *p* = 10, n = 0

Rule 2 [freq (5518379520 <= -19.555298)] and [5420855296<=-20.030178]: *p* = 10, n = 0

Rule 3 [freq (5518379520 > -19.555298)] and [5418354688<=-19.427732]: *p* = 10, n = 0

Rule 4 [freq (5518379520 > -19.555298)] and [5418354688<=-19.427732] and [5418354688<=-19.267565]: *p* =10, n = 0

Rule 5 [freq (5518379520 > -19.555298)] and [5418354688<=-19.427732] and [5418354688<=-19.267565]: *p* = 10, n = 0

Where *p* denotes the number of positive examples covered by the rule and n denotes the number of negative ones. The obtained decision rules determine that at 5.42 GHz frequency the best results are obtained for the sensor that has been used in this project. The number of test examples is equal to 50 (n = 50). The accuracy classification obtained was equal to 86%. The results obtained from a test set are often displayed as a two-dimensional matrix with a column and row for each class. Each matrix element shows the number of test examples for which the actual class is the row, and the predicted class is the column. In addition, the sum of the numbers from down the main diagonal of the confusion matrix with a red arrow divided by the total number of test examples determines the classification accuracy. Table 6.4 presents the confusion matrix of the solved problem.

Table 6.4: The confusion matrix for the leave-one-out validation of classification

Classified as	**0.0% NaCl added**	**0.5% NaCl added**	**1.5% NaCl added**	**2.5% NaCl added**	**3.5% NaCl added**
0.0% NaCl	9	0	0	1	0
0.5% NaCl	0	8	0	0	2
1.5% NaCl	2	0	8	0	0
2.5% NaCl	0	2	0	8	0
3.5% NaCl	0	0	0	0	10

Figure 6.43 illustrates the S_{21} measurements taken for the frequency range 2-12 GHz, but for clarity, data from 5.4-5.6 GHz is presented after the trees generated by algorithm J48 from the WEKA workbench. The frequency point 5.42 GHz is the most significant point determining the level of chloride ions in the concrete sample. The reason for choosing the 5.42 GHz frequency point was the skin depth EM wave calculation for marine concrete cover depths up to 70 mm. In terms of civil engineering requirements, the skin depth for the dielectric property of the electromagnetic wave signal for the maritime concrete structure has been suggested, with the nominal cover ranging 55-75 mm. As a result, the skin depth for the EM waves point of view was chosen and applied to meet the civil engineering requirement for assessing the nominal and effective cover. This technology could be utilised in civil engineering to do additional inspections. However, because our initial focus was on maritime concrete structures, this parameter should be taken into account. However, this criterion can still apply to other civil engineering applications, such as motorways and pavement where the skin depth must be between 35 and 45 mm, per BS EN 1992-2:2005. As demonstrated in Figure 6.41, other potential frequencies can be employed to determine the concentration of chloride ions. A decision tree constructed by the J48 algorithm was used to choose these frequencies, as shown in Figure 6.42. Weka workbench algorithm J48 has been used to select the other frequency point based on five different saltwater concentrations, allowing us to narrow down the frequency range. Appendix E contains the results of the WEKA workbench and the ANN techniques.

Based on the readings from the microwave horn antenna, the measurements were taken for the full frequency range 2–12 GHz, however, data from 5.4–5.6 GHz is given in Figure 6.43 for clarity. After the full data set of frequency analysis through the algorithm for the Weka workbench classification and via the trees produced by algorithm J48, a different frequency point has been selected and shown in Figure 6.42. However, each single frequency point is significant to determine the level of chloride ions in the concrete samples. The skin depth calculations and theory shown in Chapter 5 section 5.3.1, along with the ANN technique used to analyse the sensor data, has selected the most significant frequency (5.42 GHz).

In addition, at this frequency point, the EM wave enables penetration of the concrete sample up to 70 mm skin depth. Therefore, after selecting the most significant frequency point, there is a need to compare with the gold standard chlorimeter tool (destructive method) by applying the ANN technique to evaluate this frequency. The frequency chosen from algorithm J48 was compared to the target value determined from chlorimeter tool data gathered during the experiment. In addition, the single frequency point was used as input, and the chloride data at three different depths such as 18, 40 and 70 mm were collected from the chlorimeter tool and used as output.

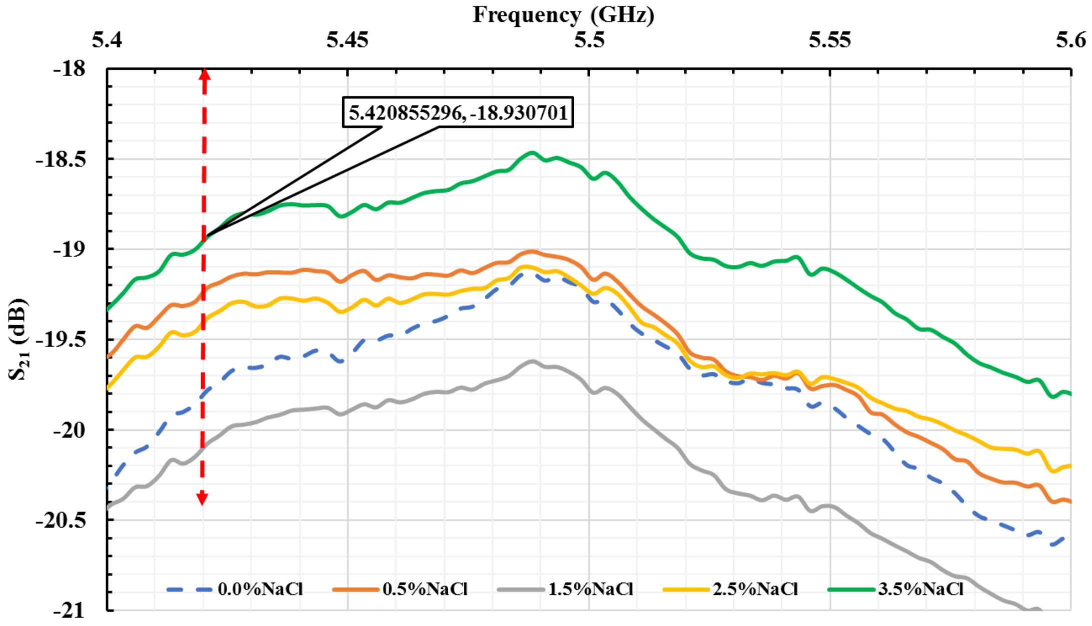

Figure 6.43: Readings from the microwave horn antenna; measurements were taken for the frequency range 2-12 GHz, but for clarity data from the 5.4-5.6 GHz is presented

Firstly, the full data spectrum was analysed by the WEKA workbench classification method and the most significant frequency point was selected. Then, based on the outcome of results generated from the decision tree J48 algorithm shown in Figure 6.42, the area of interest for the full spectrum needed to be zoomed in on, shown in Figure 6.43. Thus, the differences between each concrete sample, based on five different saltwater concentrations, especially between 5.4-5.47 GHz, are shown in Figure 6.43.

Table 6.5 demonstrates the percentage of chloride ions that have been collected from the laboratory work undertaken by the destructive method (chlorimeter tool) at three different depths in five different saltwater concentrations.

Table 6.5: The Percentage of chloride per weight of 3 grams of dust in five different saltwater concentrations at three different depths (destructive method)

	5 samples with 5 different percentages of saltwater concentration. Chloride content per weight of 3-gram dust				
3 varying depths of cover (mm)	**0.0% NaCl added**	**0.5% NaCl added**	**1.5% NaCl added**	**2.5% NaCl added**	**3.5% NaCl added**
18	0.03%	0.85%	0.94%	1.18%	1.65%
40	0.02%	0.66%	0.81%	0.92%	0.48%
70	0.02%	0.62%	0.72%	0.76%	0.40%

6.6.1 Variables selected for neural networks

Following the selection of the most significant frequency by the WEKA workbench algorithm J48, supervised machine learning classification methods were employed to detect the level of chloride ions in specimens. Therefore, this frequency point was selected for the determination of chloride ions' content in the concrete samples. The selected single frequency data sets were used in the ANN method to validate the sensors and the gold standard method as commonly used in industry. In this research, ANN was developed and performed under MATLAB programming. To simplify the back-propagation (BP) neural network's learning process and reduce the time required for training, the learning algorithm adopted to train the network model in this study was the Levenberg–Marquardt algorithm [144]. The ANN model was developed, trained, tested, and validated using 50 data sets. To assess the reliability and accuracy of the models, 70% of the 50 data sets were randomly selected as training sets, 15% of the 50 data sets selected for testing and 15% selected for validation. For modelling, data on the level of chloride ions in the specimen at three different depths is interpreted as output.

In addition, the raw data of electromagnetic waves for concrete samples in 5 different saltwater concentrations were considered as input parameters. The data was formatted into a 5x3 matrix to fit the ANN model. Table 6.6 gives the list of the ANN inputs and outputs. The supervised machine-learning algorithm used in the study was gradient descent with adaptive learning back-propagation. This network training function updates weight and bias values according to gradient descent with an adaptive learning rate. The error incurred during the learning process was expressed in terms of mean squared error (MSE). Many researchers have described the structures of the ANN [282] [283] [194].

To determine and validate the percentage of chloride ions in the concrete samples, five different saltwater concentrations are used as input layer neurons: 0.0% NaCl, 0.5% NaCl, 1.5% NaCl, 2.5% NaCl and 3.5% NaCl. Measurements of chloride ions' content via chlorimeter tools at three different depths were used as the output layer neurons. However, there is no rule currently for determining the optimal number of neurons in the hidden layer or the number of hidden layers, except through experimentation [284]. The number of hidden layers in a Feedforward Neural Network (FNN) design is the most significant factor to consider. A single hidden layer is very satisfactory for many problems. A single hidden layer for FNNs is sufficiently close to the corresponding outputs desired by the approximation theorem. Increasing the number of hidden layers may increase the accuracy in the test set. This can causes the network to overfit the training set, that is, it will learn the training data. However, the analysis also verifies that the complex non-linear problem at hand can be solved with a single hidden layer, so there is no substantial need for two or more layer architectures [285]. The architecture of the validation model for the percentage of chloride ions in the concrete sample consists of three layers as shown in Figure 6.44.

Table 6.6: The Input and output parameters of the ANN at one single frequency (5.42GHz)

Input Variable		**Target (output)**		
5 different percentages of salt water concentration	**Averaged (10) Number of S_{21} at (5.42GHz), (dB)**	**% of Chloride ion per weight of cement**		
		18mm depth	**40mm depth**	**70mm depth**
0.0% added (NaCl)	-19.78067 (Stdev)	0.0059	0.0047	0.0039
0.5% added (NaCl)	-19.21289 (Stdev)	0.1667	0.1291	0.1222
1.5% added (NaCl)	-20.07625 (Stdev)	0.1855	0.1589	0.1421
2.5% added (NaCl)	-19.38039 (Stdev)	0.2316	0.1821	0.1506
3.5% added (NaCl)	-18.93071 (Stdev)	0.3256	0.0952	0.0786

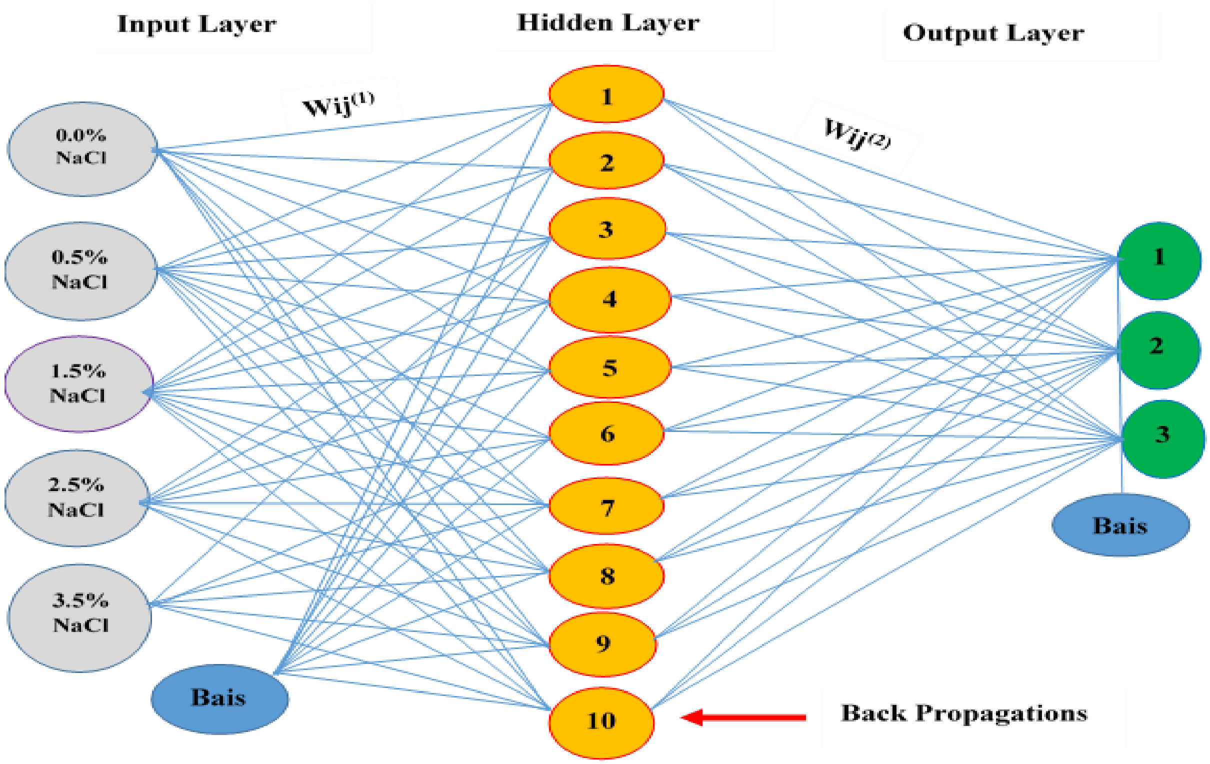

Figure 6.44: The characteristic structure of the ANN model inputs and output variables for a single frequency (5.42GHz)

The most challenging part is selecting the number of neurons in the hidden layer in the total network development process. Therefore, neural networks were trained with different hidden layer neurons to determine the optimal number of hidden layer nodes. Thus, the data from the training set were used to determine the number of neurons in the hidden layer, which resulted in the most negligible error between the neural network output and the experimental data. The hidden layer neuron number was varied, and the resulting mean square errors (MSEs) between the network outputs and the corresponding experimental outputs were determined and plotted in Figure 6.45. It can be shown that when the number of neurons is 10, the error is the lowest.

Figure 6.45: The error generated by different numbers of neurons

Table 6.7 demonstrates the % of chloride per weight of cement and concrete at different depths using the destructive method (chlorimeter) as per equation (6.2) [75, 286]. Table 6.7 indicates the percentage of chloride per weight of cement.

$$\%\mathrm{CL}_{\mathrm{Per\ WCement}} = \frac{W_c \times \%Cl_3}{W_d} \qquad \text{Eq (6.2)}$$

Where; W_c represent the weight of cement per sample, Cl_{3gram} represents the percentage of chloride per weight of 3-gram dust, W_d is the weight of dust per hole.

We used Equation 6.2 to determine the amount of chloride per weight of cement for each sample in different saltwater concentrations and at different cover depths.

Table 6.7: The %chloride per weight of cement in five different saltwater concentrations at three different depths.

	5 samples with 5 different percentages of saltwater concentration. % Chloride content per weight of Cement				
3 varying depths of cover (mm)	**0.0% NaCl added**	**0.5% NaCl added**	**1.5% NaCl added**	**2.5% NaCl added**	**3.5% NaCl added**
18	0.006	0.167	0.185	0.232	0.326
40	0.005	0.129	0.159	0.182	0.095
70	0.004	0.122	0.142	0.151	0.079

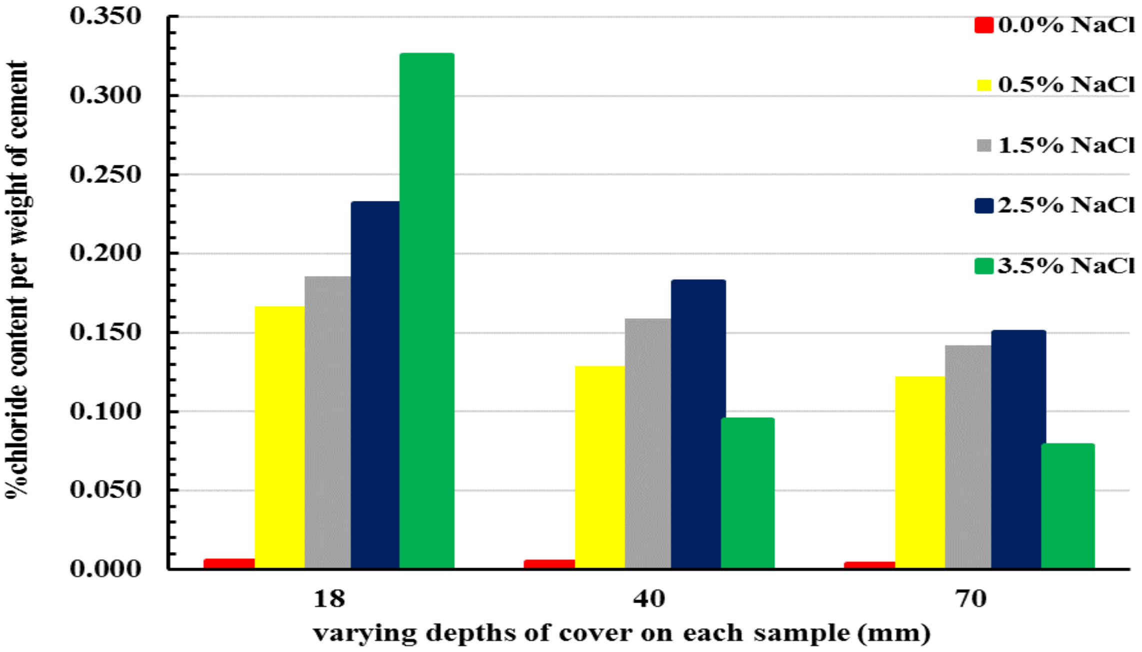

Figure 6.46: The % chloride per weight of cement

Chloride penetration at various concentrations reduces as the concrete cover increases, as seen in Figure 6.46. This is due to the saltwater concentration's viscosity, the concrete's permeability, and the fact that it was compacted well during the casting process. Furthermore, as the water drained through the concrete's surface, the salt stayed inside the concrete and formed a crystal, inhibiting capillary absorption and allowing the solution to reach the reinforcement and begin the corrosion process.

6.6.2 The developed ANN model made use of electromagnetic wave sensor data

Table 6.8 shows a summary of model output for optimisation of a single frequency for chloride prediction. A total of 50 data samples were employed in the ANN model training (70%), validation (15%), and testing (5%). (15%). The results compared model findings with those acquired using the destructive approach and correlated with predicted and measured values (chlorimeter tool).

Table 6.8: The ANN model's summary findings

		Per weight of cement	
Parameter	**Samples**	**MSE**	**R^2**
Training (70%)	34	2.22469×10^{-7}	0.99984
Validation (15%)	8	5.00873×10^{-6}	0.999557
Testing (15%)	8	1.49404×10^{-6}	0.999814

Table 6.9 presents the validation percentage measurement of chloride per weight of cement in the concrete specimens using electromagnetic (EM) wave spectroscopy.

Table 6.9: Validated percentages of chloride per weight of cement

	The percent chloride per weight of cement was validated at a single frequency (5.42GHz)				
3 varying depths of cover (mm)	**0.0% NaCl added**	**0.5% NaCl added**	**1.5%NaCl added**	**2.5% NaCl added**	**3.5% NaCl added**
18	0.006	0.167	0.185	0.232	0.326
40	0.005	0.129	0.159	0.182	0.095
70	0.004	0.122	0.142	0.151	0.079

Figure 6.47 demonstrates the validated chloride per weight of cement that was obtained by using the ANN technique. The validation values obtained using the ANN for the testing percentage of chloride in different saltwater concentrations at three different depths per weight of cement are listed in Table 6.9. The Chi-squared test can be used to determine the relative error between the validation values and the measured chloride percentage values using the gold standard chlorimeter tool. The following procedure has been carried out to calculate the Chi-squared value and the P_Value, confirm the validation values obtained through the developed ANN model, and use the Hypotheses test to verify the significance. That means the null

hypothesis was accepted, and the H1 hypothesis was rejected because it can be seen that there is no significant difference between the validation values and target values. The following section describes more about the Chi-Squared statistical method and the calculation technique to determine the Chi-Squared value

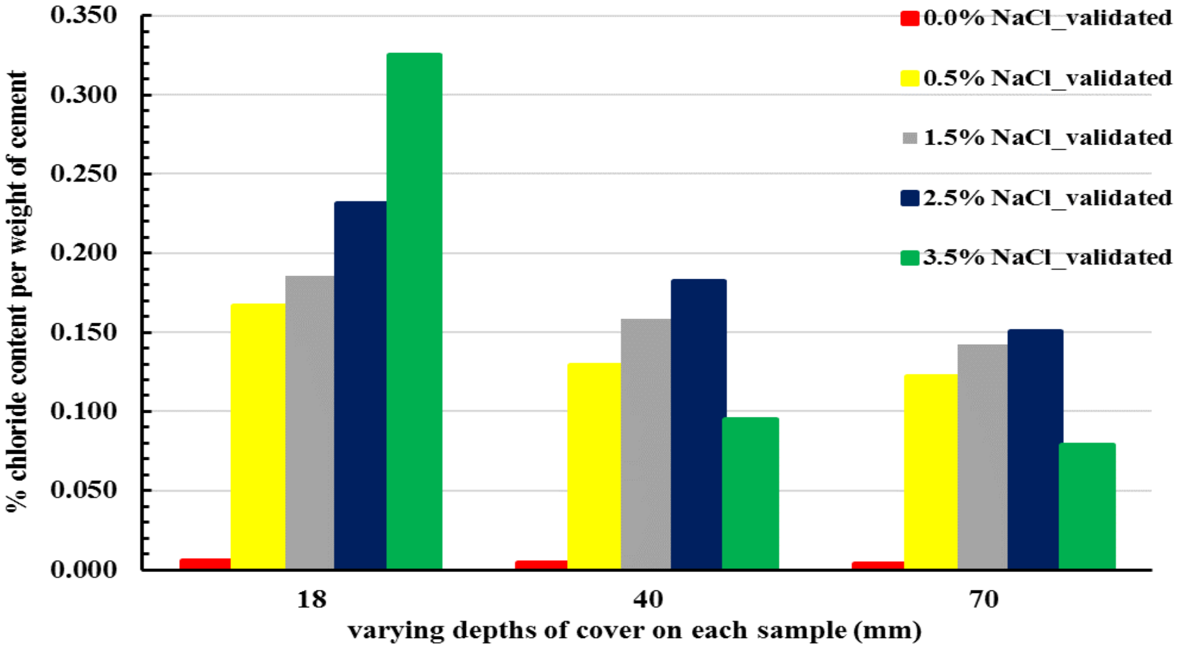

Figure 6.47: Validated % chloride per weight of cement obtained from the ANN model for 5 different saltwater concentrations and taken at 3 different depths using the selected single frequency.

6.6.3 Error calculations using the chi-squared method

The Chi-square test is based on a statistic that calculates the difference between the observed results and the values expected under the null hypothesis of no correlation. It involves calculating the expected values based on the results. The observed values used were taken from the data collected from the laboratory testing. Then the expected values were calculated from the observed value.

Table 6.10 and Table 6.11 show the total observed values obtained from the laboratory and calculated expected values.

Chi-squared test

Table 6.10: Data on the observed value obtained from the (chlorimeter tool)

Observed	**Actual percentages of chloride content per weight of cement**					
Varying depths of cover (mm)	**0.0% NaCl added**	**0.5% NaCl added**	**1.5% NaCl added**	**2.5% NaCl added**	**3.5% NaCl added**	**Total**
18	0.005913	0.166747	0.185471	0.231593	0.325609	0.9153324
40	0.004730	0.129101	0.158863	0.182120	0.095199	0.5700132
70	0.003942	0.122202	0.142109	0.150584	0.078643	0.4974804
Total	0.014585	0.418049	0.486443	0.564297	0.499451	1.9828260

The following calculation demonstrates how to obtain the expected value:

0%NaCl at 18 mm = (0.014585 *0.9153324)/(1.9828260) = 0.0067331

0%NaCl at 40 mm = (0.014585 *0.5700132)/(1.9828260) = 0.0041929

0%NaCl at 70 mm = (0.014585 *0.4974804)/(1.9828260) = 0.0036594

Same method used for the rest of (0.5%NaCl, 1.5%NaCl, 2.5%NaCl and 3.5%NaCl) to obtained expected value.

Table 6.11: The expected value is derived from the total number of observed values.

Expected value					
Varying depths of cover (mm)	**0.0% NaCl added**	**0.5% NaCl added**	**1.5% NaCl added**	**2.5% NaCl added**	**3.5% NaCl added**
18	0.0067331	0.1929841	0.2245567	0.2604967	0.2305619
40	0.0041929	0.1201787	0.1398402	0.1622215	0.1435799
70	0.0036594	0.1048863	0.1220459	0.1415792	0.1253097

The following equation has been used to find out the Chi-Squared:

$$x^2 = \sum \frac{(O_i - E_i)2}{E_i}$$

The calculation shows Chi-squared for (0%NaCl)

0% NaCl at 18 mm $\longrightarrow X^2 = \sum \frac{\mathbf{(0.005913 - 0.0067331\ )2}}{\mathbf{0.0067331}} = \mathbf{0.000101}$

0% NaCl at 40 mm $\longrightarrow X^2 = \sum \frac{(\mathbf{0.004730} - \mathbf{0.0041929})\mathbf{2}}{\mathbf{0.0041929}} = \mathbf{0.000070}$

0% NaCl at 70 mm $\longrightarrow X^2 = \sum \frac{(\mathbf{0.003942} - \mathbf{0.0036594})\mathbf{2}}{\mathbf{0.0036594}} = \mathbf{0.000022}$

The same method was used for the rest of (0.5% NaCl, 1.5% NaCl, 2.5% NaCl and 3.5% NaCl) to obtain Chi-Squared. Table 6.12 shows the total Chi-Squared calculation values for 5 different saltwater concentrations at three different depths.

Table 6.12: The total Chi-Squared calculation values

Chi-Squared					
Varying depths of cover	**0.0% NaCl added**	**0.5% NaCl added**	**1.5% NaCl added**	**2.5% NaCl added**	**3.5% NaCl added**
18	0.000101	0.003568	0.006799	0.003208	0.039174
40	0.000070	0.000663	0.002586	0.002441	0.016299
70	0.000022	0.002859	0.003297	0.000573	0.017375
Total	0.099				
P_Value	0.99999				

In statistical research, under the assumption that the null hypothesis is correct, the p-value is the probability of obtaining test results at least as extreme as the findings observed. Therefore, a very small p-value ($P < 0.05$) means that the test hypothesis is false or should be rejected. If ($p > 0.05$), this means the probability is that the null hypothesis is true. The reason why this test was carried out was to find out any significant difference between the actual data values achieved from the laboratory and the validated trained data from the ANN technique.

Degree of freedom (df) (number of rows – 1) x (number of columns – 1) = (3-1) x (5-1) = 8. Table 6.13 shows the critical values of the chi-square distribution with degrees of freedom and 95 % confidence ranges.

Table 6.13: Chi-Square and P-Value are displayed.

X^2	0.0990338
Df	8
x^2 critical	15.51
P_value	0.999999759 > 0.05

Chi-squared is one of the statistical tests widely used to compare quantities and define if observed values differ from those expected under a specific hypothesis. It was used to check (H0) and (H1)

H1 = there is a difference between the age range years for the three options (alternate hypothesis). H0 = when there's no dissimilarity (Null Hypothesis)

0.099 < 15.51; therefore, Rejected H1 and accepted H0. The chi-squared value needed to reject the (hypothesis) rises because it is shown there is no significant change between the Observed value and Expected value.

The same method is used to calculate the Chi-Squared %chloride per weight of cement and the predicted %chloride per weight of cement. Table 6.14 indicates the final calculations of chi-squared values for the predicted percentage of chloride ions in five different saltwater concentrations specimens at three different depths. The results demonstrate that the electromagnetic (EM) wave spectroscopy can suitably predict the chloride ion content across the range of values investigated and the percentage error in relation to the destructive method (chlorimeter tool) as a gold standard in the industry is 0.034%.

Table 6.14: The total Chi-Squared values and %of error

Parameter	% of Chloride	Chi-Squared	% Error
Chlorimeter Tool	per weight of cement	0.099000000	
Microwave spectroscopy_	per weight of cement @ 5.42GHz	0.099033791	**0.034**

According to the CHI Squared calculation, there is no significant change between observed and expected values. It can be seen in Table 6.14 that the % of error is calculated with the CHI Squared values. The following equation is used to calculate the percentage error.

Per weight of cement @ 5.42GHz $\longrightarrow$ $\%\text{Error} = \frac{(0.09900000-0.099033791)}{(0.099000000)} * 100 = 0.034$

6.6.4 Comparison of actual value and confirmed chloride ion percentages at 5.42 GHz frequency

Figure 6.48 demonstrates the % of chloride per weight of cement in different saltwater concentrations at three various depths. The Chlorimeter tool is used as the gold standard method to measure chloride ions at three different depths. The accuracy of this Chlorimeter tool covers a wide range from 0.002% to 2% chloride per weight. It can be seen in both figures that the penetration of chloride increased with the increased percentage of salt water at the 18 mm depth. But after the cover depth increased, the chloride penetration decreased because of the material properties such as less permeability, being well compacted, the high viscosity of the solution, and the water-cement ratio.

In the case of chloride intrusion, chloride ions have only a small influence on the pH of the pore solution. Nevertheless, when the chloride content in the pore solution exceeds a critical value (chloride threshold), it can destroy the passive layer. However, it has proved rather difficult to establish a threshold chloride concentration below which there is no risk of corrosion as it depends on numerous factors, including [287]: a) The concentration of hydroxyl ions in the pore solution and pH of concrete. Therefore, above a critical ratio of chloride and hydroxy ions, corrosion can take place. Husman suggested 0.6 as the critical ratio [10]. In addition, the hydroxyl ion concentration in the pore solution mainly depends on the type of cement and additives. (b) The number of voids at the concrete reinforcement interface generally depends on the workability of the fresh concrete and the compacting procedure. Therefore, this may weaken the cement products deposited at the concrete reinforcement because of the voids.

However, the data analysis obtained on bridge structures in the UK, suggested that the level of chloride below 0.2% by weight of cement represents minimal risk of corrosion, while levels of chloride above 1.5% represent a very high risk as can be seen in Figure 6.49 [288]. The outcomes of similar work on U.S. bridges recommended a range between 0.17 and 1.4% (by weight of cement), on Danish bridges 0.3% and 0.7% (by weight of cement), while especially high threshold levels (from 1.8 to 2.2% by weight of cement) were reported in one survey of Austrian bridges [288].

Concrete cover specification according to the British standard BS EN 206-1 is the thickness of concrete cover based on the weather condition in which the structure is constructed. In addition the concrete strength and quality of concrete is dependent on cement and water-cement ratio [289].

According to the Complementary British Standard to BS EN 206 and European Committee for Concrete, for the limitation of the amount of chloride ion per weight of cement, there is a trigger point that should be 0.4%. Therefore, the proposed electromagnetic spectroscopy has determined the level below the critical level of chloride ion in the concrete structure. Consequently, the data demonstrated that the microwave sensor detects values below 0.4% per weight of cement, which means we can use this technology to predict when the structure is at the critical point for the repair [59] [290].

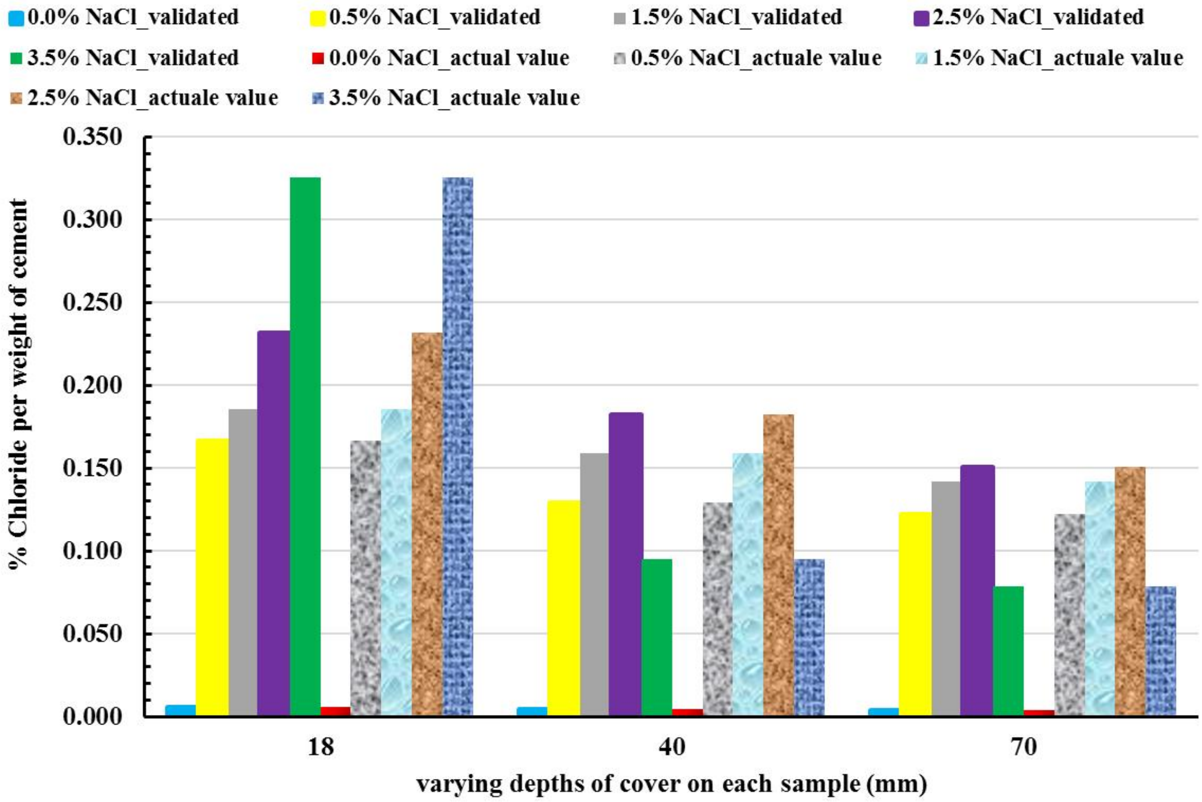

Figure 6.48: The comparison between actual and validated values of % chloride per weight of cement at one single frequency (5.42 GHz)

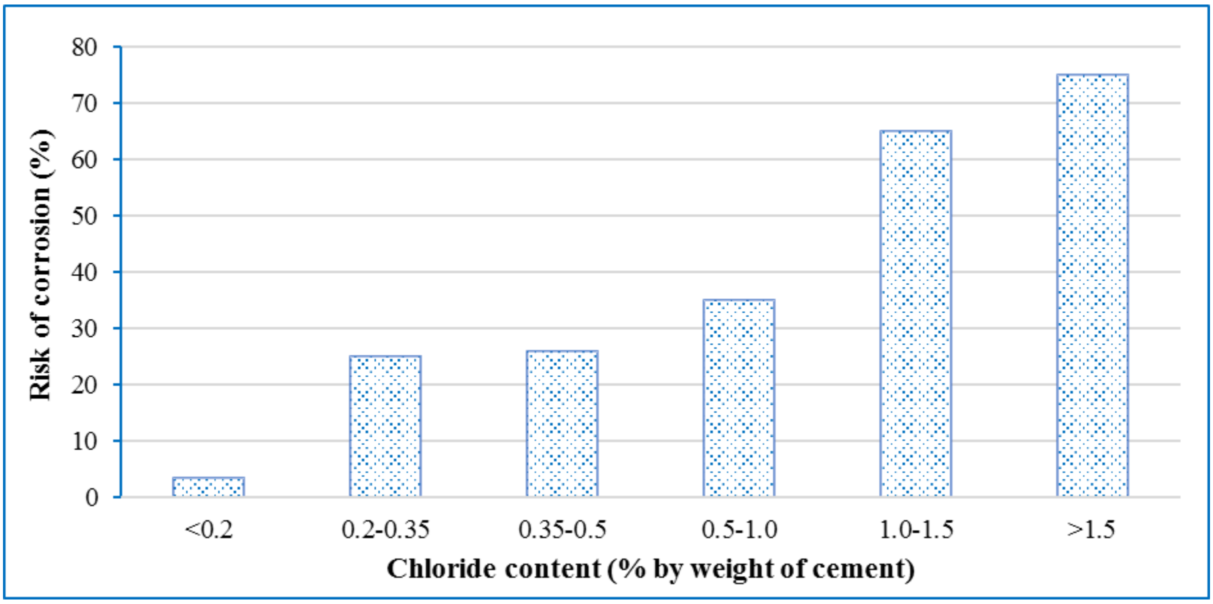

Figure 6.49: The corrosion risk determined on the UK bridges plotted as a function of chloride content according to BS EN 206.1 [291]

The chloride threshold value as a general rule for structures exposed to the atmosphere is assumed to be in the range of 0.4 to 1% by weight of cement, such values may significantly change, depending on the above parameters. For instance, the high degree of moisture content in the concrete leads to low oxygen content and a low value of the electrochemical potential of steel, in the submerged part of a marine structure. Therefore the chloride threshold is increased significantly [292].

6.6.5 ANN was used to analyse and validate five different saltwater concentrations

This section of the project presents and discusses the performance of the trained LM algorithm using the standard measuring performance indicator: mean square error (MSE), correlation coefficients (R^2). As previously demonstrated, the developing LM algorithm was considered a regularisation back-propagation scheme to train and develop the network due to its advantages over conventional methods. The neural network training stops when the error falls below a user-specified level or when the user-defined number of training iterations has been reached. In this case, 1,000 iterations were planned for the final training process, while it was found to be adequate in a series of test runs.

The validation performance and mean square error of the network starting at a large value and reducing to a small value is shown in Figure 6.50. A result is generated via the use of the software. The plot consists of three lines for three different steps of training, validation, and test. The training process on the training vectors continues until the model gets to the point where the training decreases the network error on the validation vectors, leading to avoiding the over-fitting of the data sets. As shown in Figure 6.50, the best validation efficiency occurs at epoch 5, and the process stopped at epoch 11 after 6 error repetitions. The results shown in Figure 6.50 illustrate the same ones as in Figure 6.51. The MSE value is 5.0087x10^{-06} of the data per weight of cement and stopped the training of the neural network. The training state for an Artificial Neural Network model is shown in Figure 6.50. As it is illustrated in the figure, the errors are repeated 6 times after epoch 5, and the test stopped at epoch 11. The error repeats starting at epoch 6 demonstrated over-fitting of the data. Therefore, epoch 5 is selected as the base, and its weights are chosen as the final weights. Moreover, because the errors are replicated 6 times before stopping the operation, the validation check is equivalent to 6. Figure 6.51 shows that at an epoch of 11, the error gradient was 7.04131x10^{-07}, while the mu factor and validation check were 1x10$^{-0.08}$.

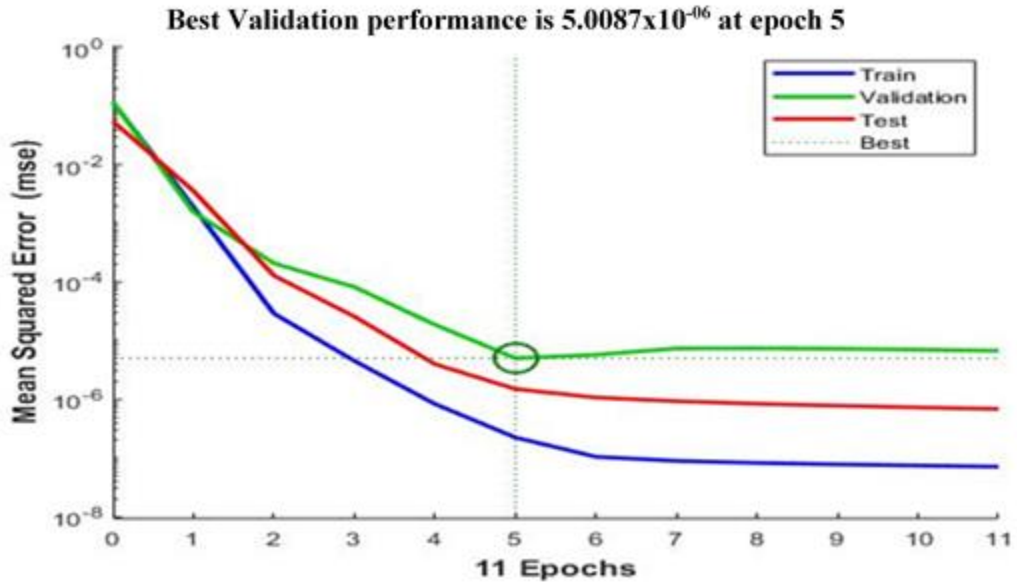

Figure 6.50: Best validation performance in Artificial Neural Network Model; Per weight of cement

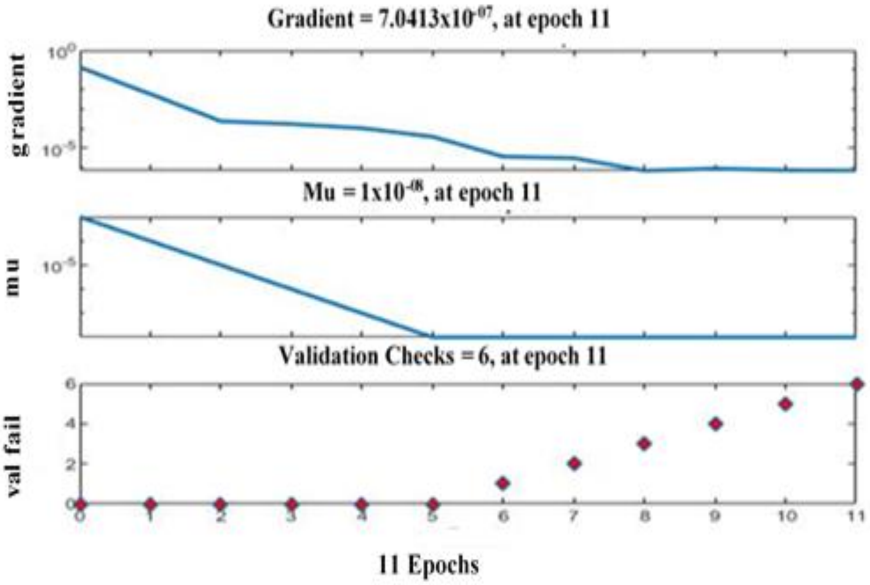

Figure 6.51: The gradient and maximum validation checks for the LM trained network; per weight of cement.

A further useful picture of the network profile can be seen in the error histogram (EH), as shown in Figure 6.52. Therefore, it is of value to see that the performance of the proposed algorithm can be very much affected by the presence of outliers. Figure 6.52 presents the error histogram with 20 bins for the three training, validation, and test steps in an Artificial Neural Network modelling. As is shown in Figure 6.52, the zero error is illustrated with a yellow line in the middle with 5 instances in the training set. Consequently, the training process is stopped straight away once the validation error starts to increase. Also, it can be shown that most data coincide with the zero-error line in the central bins of -0.00049 and $9.44 \times 10^{-0.5}$. However, the ANN technique generated the results from Figure 6.50 to Figure 6.52, with the data used of %chloride/weight of cement content from the microwave sensor. Also, this software calculated values based on the amount of data and matrix added into the software, and then the software algorithm started to calculate the values.

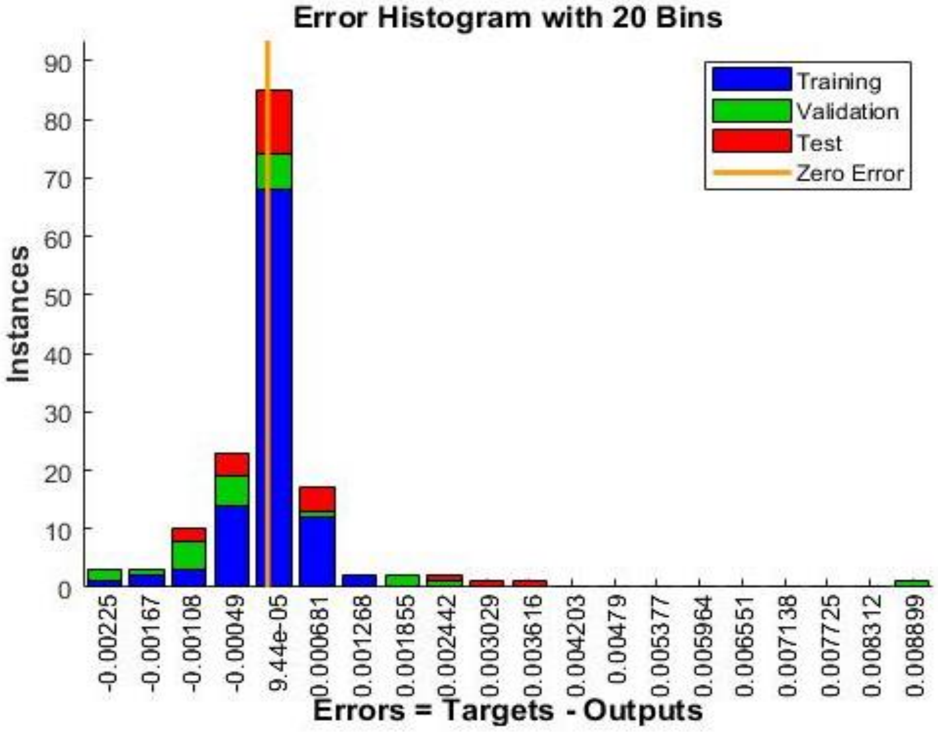

Figure 6.52: The plot of error histogram (EH) for the LM algorithm; per weight of cement.

The developed regression calibration plot for the training, testing and validation of all data sets to compare the measured and the validated percentage of chloride in three various depths, as demonstrated in Figure 6.53. The experimental results (Target) are shown on the horizontal axis and the output results on the vertical axis. There is an excellent correlation between the experimental and output values for the complete data set. The general equation of a straight line is y=mx+c, where m is the gradient and y=c is the value where the line cut the y-axis. Also, this number c is called the intercept on the y-axis. However, these equations are linked to those related to the LM algorithm used in ANN techniques that were discussed more in chapter 3. Figure 6.53 (a, b, c & d) represents the plots of coincidence between the target and output variables for training, validation, testing, and all our data steps, respectively. The “Target” values imply the “Measured Level of chloride ions from the concrete sample” and the “Output” values imply the “Validated level of chloride ions by MATLAB Software”. The dashed line in each plot represents the perfect result outputs = targets. Also, the solid line represents the best fit linear regression line between outputs and targets. The term “R” value is obtained by MATLAB Software which demonstrates the model efficiency. In Figure 6.53 (a, b, c & d) “R” confirms acceptable accuracies of the model in all the training, validation, and testing steps. If

R =1, this indicates an exact linear relationship between outputs and targets. If R is close to zero then there is no linear relationship between outputs and targets.

The points in all subdivisions (training, testing, and validation) are located close to the best line of equality (validated %chloride ions= β * measured actual value of %chloride ions+ α) with the high coefficients of determination of 0.99998, 0.99956, 0.9991, and 0.99992 for training, validation, testing and all data of the %Wt-cement. For this experimental work, the training data indicates a good fit. Also, the validation and test results show R values greater than 0.9. The results demonstrated that the ANN model is successful in learning the relationship between the different input and output parameters and show the ability of the network to validate the influence of varying saltwater concentrations on the microwave sensor in the concrete with different depths. The MATLAB code for those graphs has been shown in Appendix A, B and C.

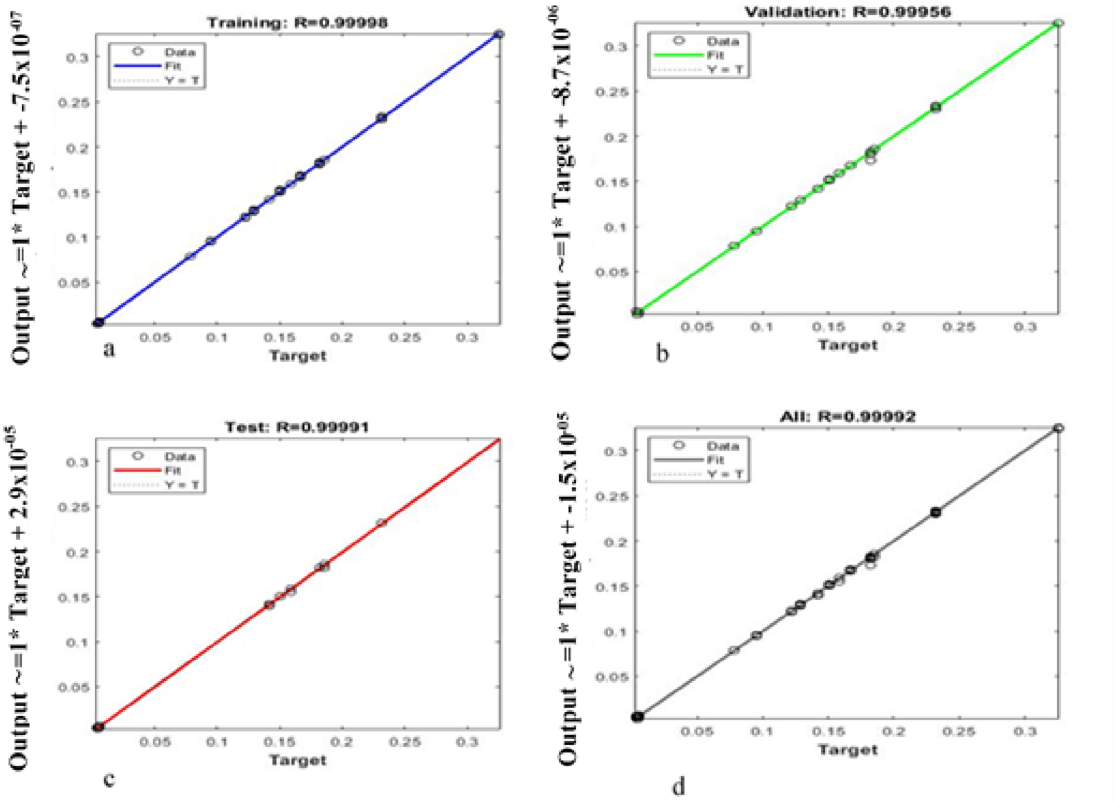

Figure 6.53: The regression graphs of the experimental results against the validated %Chloride ions per weight of cement

Furthermore, the performance of the LM algorithm is further examined using the target values versus the predicted values, as shown in Table 6.15. According to the results, the significant agreement can be observed between the targets measured versus predicted values with a Value of Normalised Absolute Error statistic (NAE), Value of Root Mean Square Error statistic (RMSE), and Value correlation coefficients (R2) with the amount of %chloride per weight of cement at three different depths being (0.000256, 0.000120 and 0.986709). The results have demonstrated that microwave spectroscopy can determine varying concentrations of NaCl in the concrete specimens at different depths. The single frequency can be ascertained by using classification feature selection and indicated a frequency of 5.42 GHz as a durable predictor for level chloride ions.

Table 6.15: The results for the observed data target and output values

%Chloride per weight of cement			
Varying depths of cover (mm)	**NAEs**	**RMSE**	**R^2**
18	0.000211	0.000135	0.960388
40	0.000303	0.000122	0.960397
70	0.000283	0.000106	0.960395
Total of three depth	0.000256	0.000120	0.986709

6.7 ANN was used to repeat the analysis of two different saltwater concentrations

An experiment was undertaken for two concrete slabs with the same size 250 x 250 x 60 mm and the same material properties with reinforced rebars to investigate the difference between tap water and saltwater solutions on the concrete with reinforcement rebar and how they affect microwave signal. Figure 6.54 shows the S_{21} measurements of the concrete slab1 and slab2 taken every minute over 24 hours to monitor the concrete drying off. It can be seen in Figure 6.54 that visible changes are appearing in the electromagnetic (EM) wave signature during the drying process of the concrete slab1 and slab2 while submerged in the salt water and tap water for 24 hours. The change is thought to be caused by the decreasing amount of water and the remaining salt in the concrete sample. There is a linear correlation R^2 value between the S_{21} change and weight loss across the full frequency spectrum ranges (2-12 GHz), but for clarity, data measurements shown in 5.4-5.6 GHz are presented in Figure 6.54. The same procedure of classification was applied to this experimental data work to identify the important frequency points. Then the ANN method was used to validate the data obtained from the sensor at 5.42 GHz frequency and compared with the gold standard method.

Then the destructive method (chlorimeter tool) was used as the gold standard method to measure the number of chloride ions at two different depths on both samples. Table 6.16 indicates the average of chloride ions in 3 grams of dust collected in three holes at the same depth of the concrete surface.

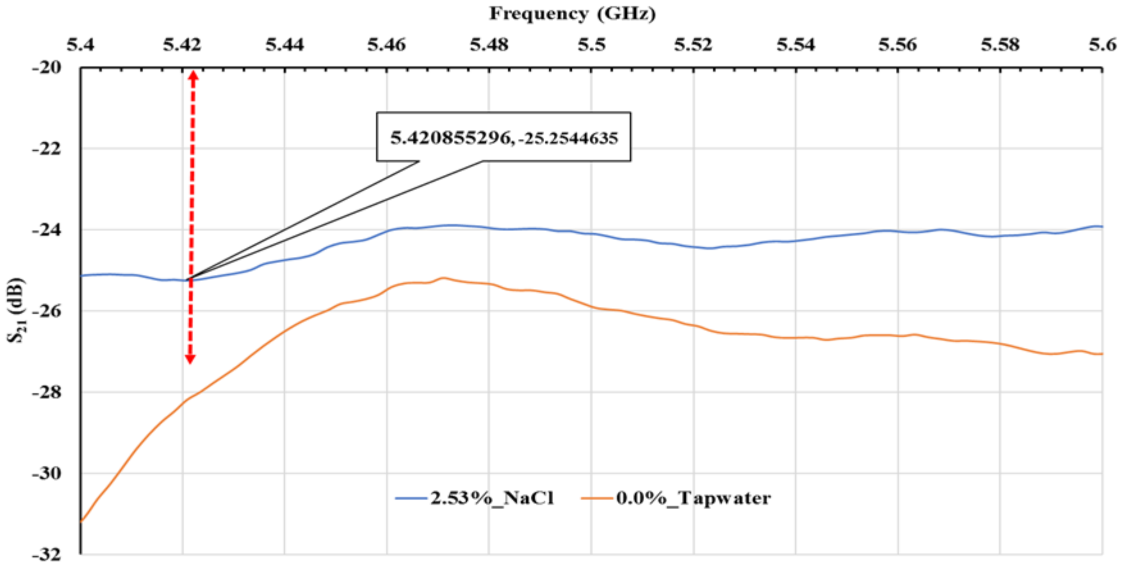

Figure 6.54: The measurement of microwaves horn antenna; for clarity, data from the 5.4-5.6 GHz is presented (Tap water & Salt water)

Table 6.16: The Percentage of chloride per weight of 3 grams of dust in 2 different saltwater concentrations at 2 different depths

2 samples with two different saltwater concentration, chloride content per weight of 3-gram dust		
2 varying depths of cover (mm)	**0.0% NaCl added**	**2.53% NaCl added**
18	0.03%	0.55%
40	0.00%	0.00%

The sample depth chosen was intended to include an acceptable range to allow interpolation and estimation between the commonly used nominal depth of cover under different exposure conditions, such as near the top surface, a little deeper, and very close to the rebar position. But for this experimental work, only two different depths have been selected because of the thickness of the concrete sample.

Also, because the surface of the concrete is usually flaky, the first 2-3 mm is easily removed due to the high-water content at the surface, so the 18 mm depth was chosen. As a result of the concrete cover's weakness and evaporation at the surface, 20 mm of cover is effectively reduced to 17-18 mm.

The variable selected for the Artificial Neural Network (ANN) technique was used to validate the amount of chloride in the concrete sample at different depths in different saltwater concentrations. Therefore, to visualize the performance of the Artificial Neural Network (ANN) models graphically, the measured values obtained from the laboratory measurement and its predicted values resulting from 5.4-5.6 GHz and only one single frequency are plotted and displayed in Figure 6.55. The ANN model exhibited a great capability to predict a level of chloride output with R^2 = 0.99 and with Mean Square Error of prediction very low. Furthermore, in order to approximate the number of hidden nodes in the hidden layer, neural networks were trained with different numbers of hidden layer neurons. Thus, the data from the training set was used to determine the number of neurons in the hidden layer, which resulted in the least error between the neural network output and the experimental data. See section 6.6.1 and Figure 6.45.

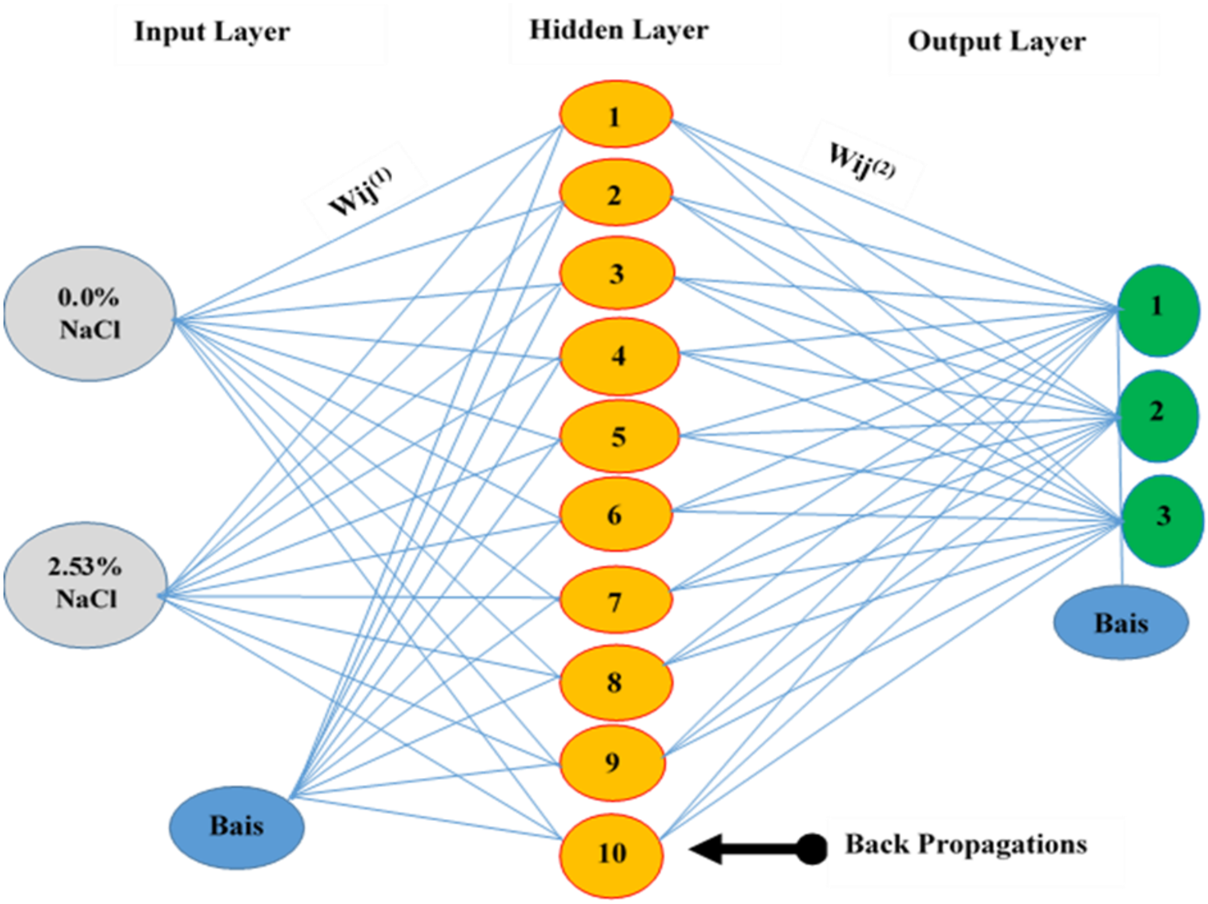

Figure 6.55: The characteristic structure of ANN model inputs and output variables for a single frequency (5.42GHz)

In addition, the raw data of electromagnetic waves on concrete samples in two different saltwater concentrations were considered as input parameters. The data was formatted into a 2x2 matrix to fit the ANN model. Table 6.17 gives the list of the ANN inputs and outputs.

Table 6.17: The input and output parameters of ANN at one single frequency (5.42GHz)

Input variables		**Target (Output)**	
2 different percentages of saltwater concentration	Averaged (10) Number of S_{21} (5.42GHz), (dB)	%Chloride Per weight of cement	
		18mm depth	40mm depth
0.0% NaCl added	-27.246 (Stdev)	0.0017	0.0013
2.53% NaCl added	-25.2545 (Stdev)	0.0282	0.0130

As declared in the experimental data collection, that destructive method was used to detect the level of chloride in two different depths by extracting using the drill press. Table 6.18 indicates the percentage of chloride per weight of cement. Moreover, in order to define the profile of penetration of chlorides, as shown in Figure 6.56, samples from different depths were extracted using a drill press.

Table 6.18: The %chloride per weight of concrete in different concentrations at 2 different depths

Actual value %chloride per weight of cement		
2 varying depths of cover (mm)	0.0% NaCl added	2.53% NaCl added
18	0.002	0.028
40	0.001	0.013

The above equation 6.2 was used to calculate the amount of chloride per weight of each concrete sample in different saltwater concentrations at two different depths shown in the above section 6.6.1.

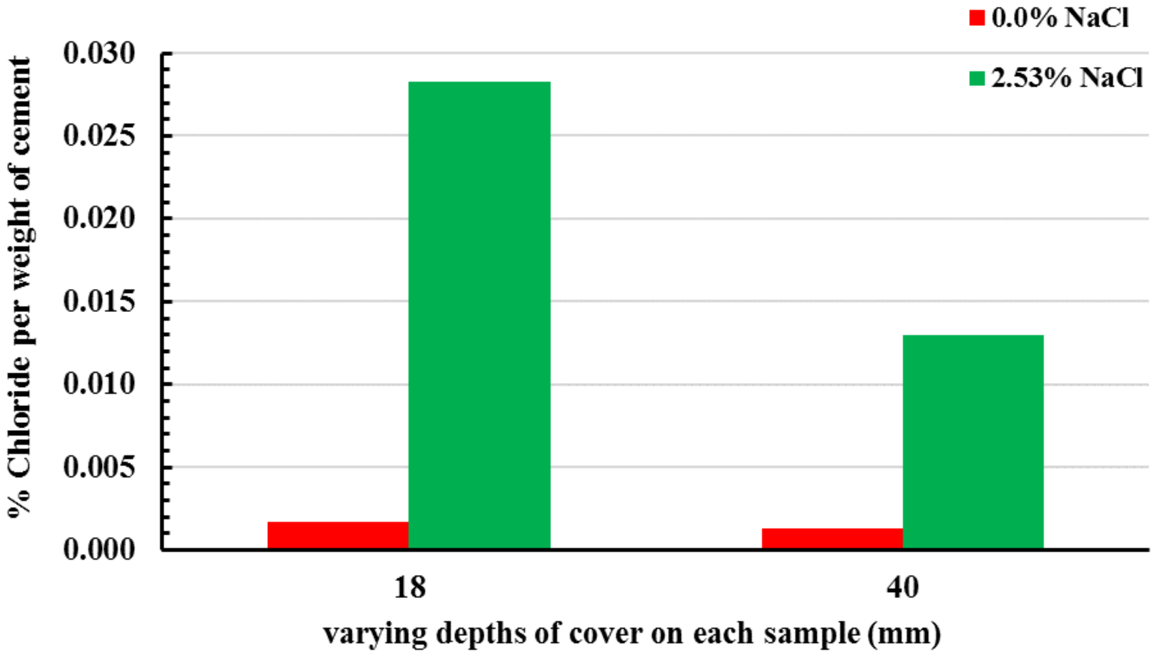

Figure 6.56: The % chloride per weight of cement

Figure 6.56 shows clearly that the transmission of chloride at different concentrations decreases by increasing the concrete cover. This is due to the salt water's high viscosity, the concrete's decreased permeability, and the fact that it was compacted thoroughly during the casting process. Moreover, while the water evaporated through the surface of the concrete, the salt remained inside the concrete and created a crystal, and it blocked the capillary absorption to let more penetration of the solution deeper to reach the reinforcement and start corrosion.

In Table 6.19, the description of the model performance for optimization of the best single frequency for chloride validation is presented. The ANN model divided the total data into three subsets of training, validation, and test. The proportion of training, validation, and testing are characterized based on the fact that the general structure of the model is constructed based on the training data set. The ANN model was developed, trained, tested, and validated using 20 data sets. To assess the reliability and accuracy of the models, 70% of the 20 data sets were randomly selected as training sets, 15% of the 20 data sets selected for testing and 15% selected for validation. Within minimizing the criteria function, the training process included iterative measurements of the weight coefficients. The network validated the outputs after each iteration use and validation. When the validation record's misclassification rate began to vary from the training record's misclassification rate, the training was stopped to avoid overfitting.

Table 6.19: Indicates the summary results of the ANNs model

		Per weight of cement	
Parameter	**Samples**	**MSE**	**R^2**
Training (70%)	14	$1.16923x10^{-12}$	0.999999
Validation (15%)	3	$4.09133x10^{-14}$	0.999993
Testing (15%)	3	$8.26223x10^{-13}$	0.999999

Table 6.20 presents the validated percentage of chloride per weight of cement in the concrete specimens using an electromagnetic (EM) waves sensor at microwave frequency. The difference between Table 6.20 and Table 6.18 is that the values in Table 6.18 were obtained from the measured chloride ion level directly from the concrete samples with the destructive method (Chlorimeter tool). But the values in Table 6.20 were obtained from the validated level of chloride ions from the ANN algorithm.

Table 6.20: The validated values of %chloride per weight of cement

percentage of chloride per weight of cement that has been validated throughout a single frequency range (5.42 GHz)		
2 varying depths of cover(mm)	**0.0% NaCl added_ validated**	**2.53% NaCl added_ validated**
18	0.0016907	0.0282383
40	0.0013456	0.0129729

Figure 6.57 demonstrates the validated chloride per weight of cement obtained from using the artificial neural network (ANN) technique after gaining the validated values of % chloride per weight of cement in two different saltwater concentrations at two different depths. The reason for choosing only two different depths was because the size of the concrete sample used was 250 x 250 x 60 mm in this experimental work. Then these results obtained need to prove that there are no significant differences between the results obtained by the chlorimeter tool as a destructive method and the microwave sensor as a non-destructive method by using the statistical technique called a Chi-Squared test. The statistical chi-squared approach was used to produce Chi-Squared values, P- values, and the hypothesis test to verify the data is more significant, in order to demonstrate the accuracy of the predicted model developed algorithm.

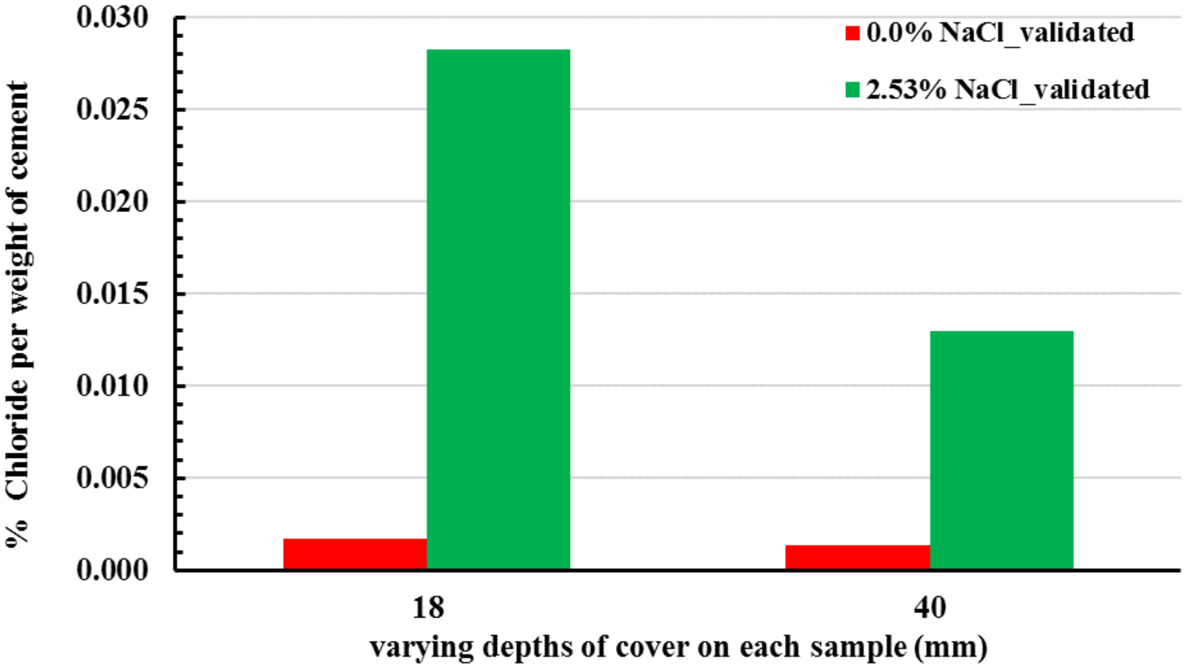

Figure 6.57: The validated value of percent chloride per (weight of cement) at various depths at a single frequency (5.42 GHz)

Chi-squared test

The Chi-Squared test is used to determine the Chi-Squared values and then can calculate the percentage of error within one single frequency point. The following Table 6.21, Table 6.22, and Table 6.23 show the observed, expected, and total Chi-squared values.

Table 6.21: Observed values obtained from the laboratory

Observed values	**Actual percentages of chloride content per weight of cement**		
2 varying depths of cover (mm)	**0.0% NaCl added**	**2.53% NaCl added**	**Total**
18	0.0016905	0.0282383	0.0299288
40	0.0013455	0.0129720	0.0143175
Total	0.0030360	0.0412103	0.0442463

Table 6.22: Expected values obtained from the calculation

Expecting values		
2 varying depths of cover (mm)	**0.0% NaCl added**	**2.53% NaCl added**
18	0.0020536	0.0278752
40	0.0009824	0.0133351

Table 6.23: Shows the total CHI Squared calculation values

Chi-Squared		
varying depths of cover (mm)	**0.0% NaCl added**	**0.5% NaCl added**
18	0.00004701	0.0000336
40	0.00009932	0.0000709
Total Chi-squared	0.00021296	
P_Value	0.988356615	

Degree of freedom (df) (number of rows – 1) x (number of columns – 1) = (2-1) x (2-1) = 1. Table 6.24 shows the critical values of the chi-square distribution with degrees of freedom and 95 % confidence ranges.

Table 6.24: The final chi-squared and P-value

X^2	**0.00021296**
Df	1
X^2 critical	3.841
P_value	0.988356615 > 0.05

In this case, H1 indicates that there is a variation in age between the three possibilities (alternate hypothesis). H_0 indicates that there is no variation (Null Hypothesis).

$0.0002 < 3.841$, therefore, we rejected H_1 and accepted H_0. The chi-squared value needed to reject the (hypothesis) rises because it is shown there is no significant change between the Observed value and Expected value.

The same method is used to calculate the Chi-Squared % chloride per weight of cement and the predicted % chloride per weight of concrete and cement. The following Table 6.25 indicates the final calculation of chi-squared values for the predicted percentage of chloride ions in two different saltwater concentration specimens at two different depths.

Table 6.25: The total Chi-Squared values and %of error

Parameter	% Chloride	Chi-Squared	% Error
Chlorimeter Tool_ (Destructive method)	per weight of cement	0.0002130084	
Microwave spectroscopy	per weight of cement @ 5.42 GHz	0.0002129655	**0.020**

According to the Chi-Squared calculation, there is no significant change between the observed values and expected values. The percentage error at the frequency point is very low. This means the relations between the predictions and actual values are very close to each other.

6.7.1 Comparison of % chloride ion between actual values and validated values

Figure 6.58 illustrates the comparison between the percentage of chloride per weight of cement in two different saltwater concentrations and at two different depths. Thus, the actual values of % chloride ions were collected by using the chlorimeter tools as a gold standard method at two different depths. It can be seen in Figure 6.58 that the penetration of chloride was increased with the increased percentage of salt water at the first 18 mm layer depth. The rate of chloride penetration in concrete in the marine environment depends mainly on the exposure situation that varies with the regular variation of the tide level. However, most of the concrete structures exposed to the tidal environment are in a non-saturated state, and also chloride ion transport is driven both by diffusion through concentration gradient through continuous pore water channel and convection via moisture through non-saturated pores. It also decreases the penetration of chloride ions into the concrete by increasing the concrete cover depth and using a lower water-cement ratio, being well compacted during casting, and high viscosity of the solution. Figure 6.58 presents the skin depth of electromagnetic waves and the ability to penetrate the concrete sample to validate the level of chloride ions with different saltwater concentrations at different cover depths.

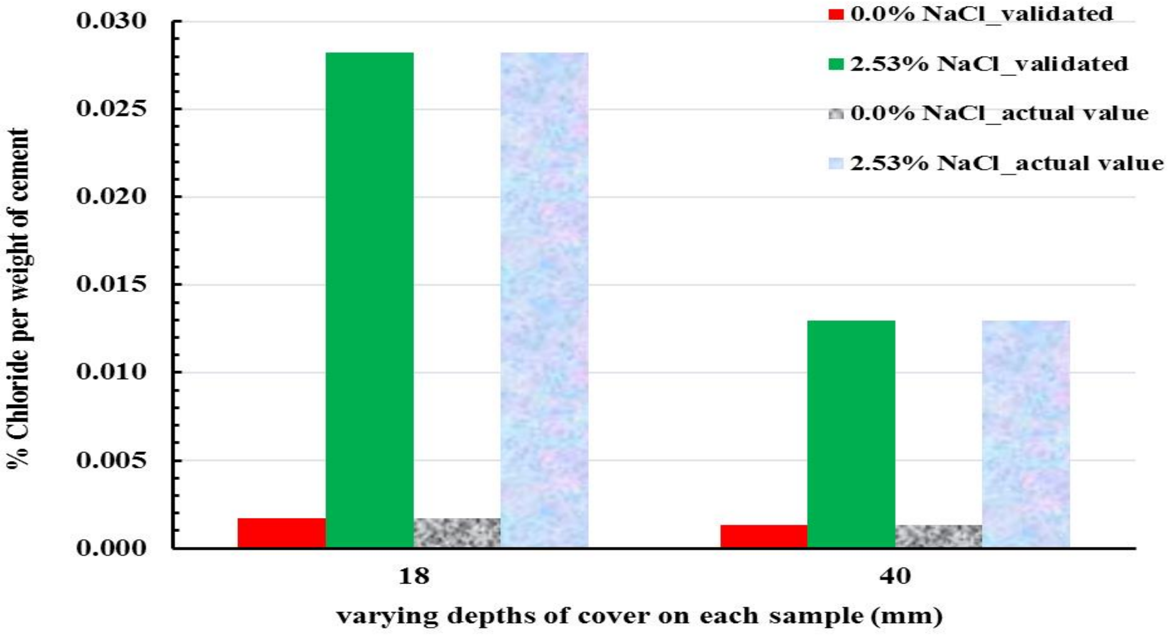

Figure 6.58: The comparison between actual and validated values of % chloride per weight of cement at one single frequency (5.42 GHz).

In general, the threshold chloride value for an exposed structure is assumed to be in the range of 0.4 to 1% by weight of cement. Still, such values may significantly change, depending on the parameters. For instance, the high degree of moisture content in the concrete leads to low oxygen content and a low value of the electrochemical potential of steel in the submerged part of a marine structure. Therefore, the chloride threshold is increased significantly [292].

However, according to the data set produced in this study, the microwave sensor can identify the level of chloride ions in the structure at different depths with different saltwater concentrations below the trigger point of 0.4%. This means that the technique can be used to predict when a structure's maintenance is at a critical stage.

In this experimental work, only two different saltwater concentrations are used to investigate how saltwater concentrations have affected the electromagnetic wave signal. The microwave signal has changed due to the variant level of saltwater concentrations. Therefore, we carried out further experimental work with five different concentrations of salt water.

6.7.2 ANN was used to analyse and validate two different saltwater concentrations

This section presents and discusses the performance of the trained LM algorithm using the standard measuring performance indicator: mean square error (MSE), correlation coefficients (R^2). Considering the analytical mechanism during the training process is vital for successful modelling. Figure 6.59 demonstrates the procedure of the training LM through the three stages testing, training, and validations. The epochs are one complete sweep of training, testing, and validation. The performance plot shows MSE in training, testing, and validation data. The MSE plot in the training data has a lower curve and has an upper curve invalidation data set. The network with minimum MSE invalidation is called the trained ANN model.

The training automatically stops when the validation error stops improving, as indicated by an increase in the MSE of the validation data samples. The results illustrate that the training process terminated when the validation errors number exceeded the allowed numbers. The technique of the training LM via the three stages of testing, training, and validations is represented in Figure 6.59. The epochs represent a whole training, testing, and validation cycle. MSE in training, testing, and validation data is shown in the performance plot.

From Figure 6.59, it can be seen that after 11 repetitions of the network training, the value of MSE had reduced to the specified level of 4.0913×10^{-14} of the data per weight of cement, then the training of the neural network was automatically stopped.

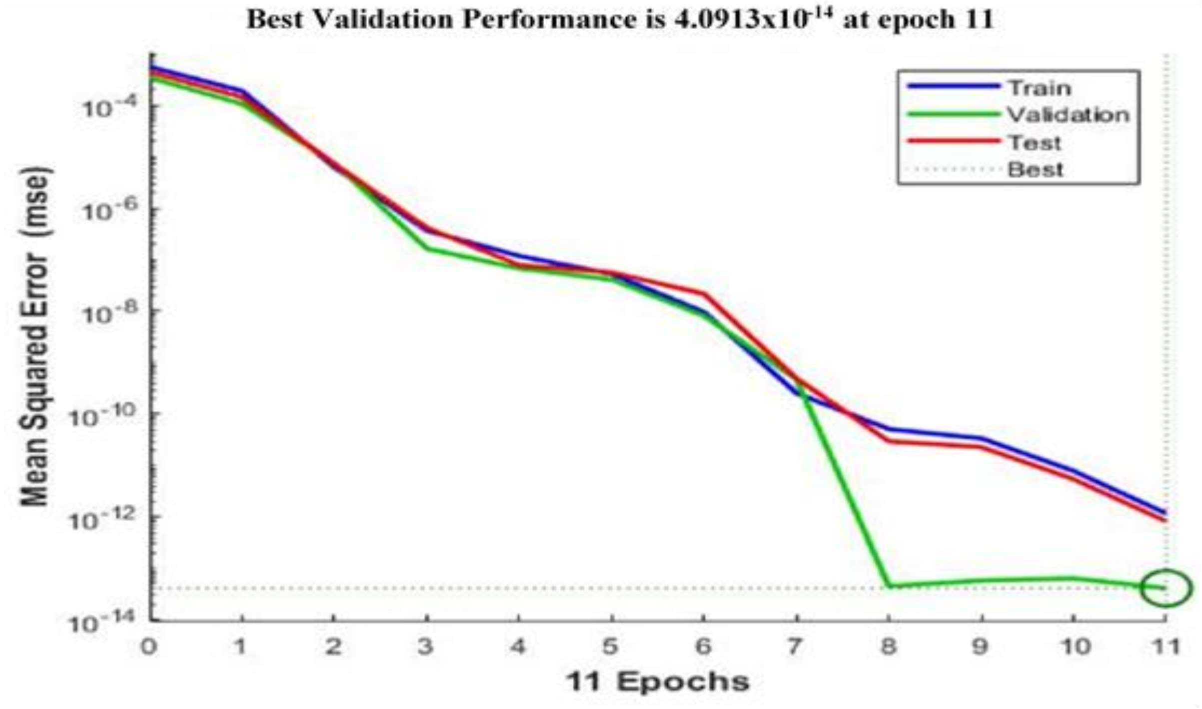

Figure 6.59: The performance plot of the LM algorithm for the concrete developed model during the training process; Per weight of cement.

Furthermore, the equivalent change of gradient and the Marquardt adjustment factor (mu) shows an important role in decreasing the mean square error percentage. As discovered in Figure 6.60, the gradient error decreases and reaches $4.8858x10^{-08}$. Significantly, the mu factor is decreased to a negligible value $1x10^{-14}$ after a few epochs, and the validation doesn't change at an epoch of 11. Additionally, Figure 6.61 demonstrates the error histogram (EH) plot to obtain further efficiency validation of network performance. Also, the EH can indicate outliers data features that appear to be inconsistent with other subsets observations [142]. Therefore, it is of value to see that the performance of the proposed algorithm can be very much affected by the presence of outliers. Consequently, the training process is stopped straightway once the validation error starts to increase. Also, it can be shown that the majority of data coincides with the zero-error line in the two central bins ($-1.2x10^{-07}$ and $4.93x10^{-08}$).

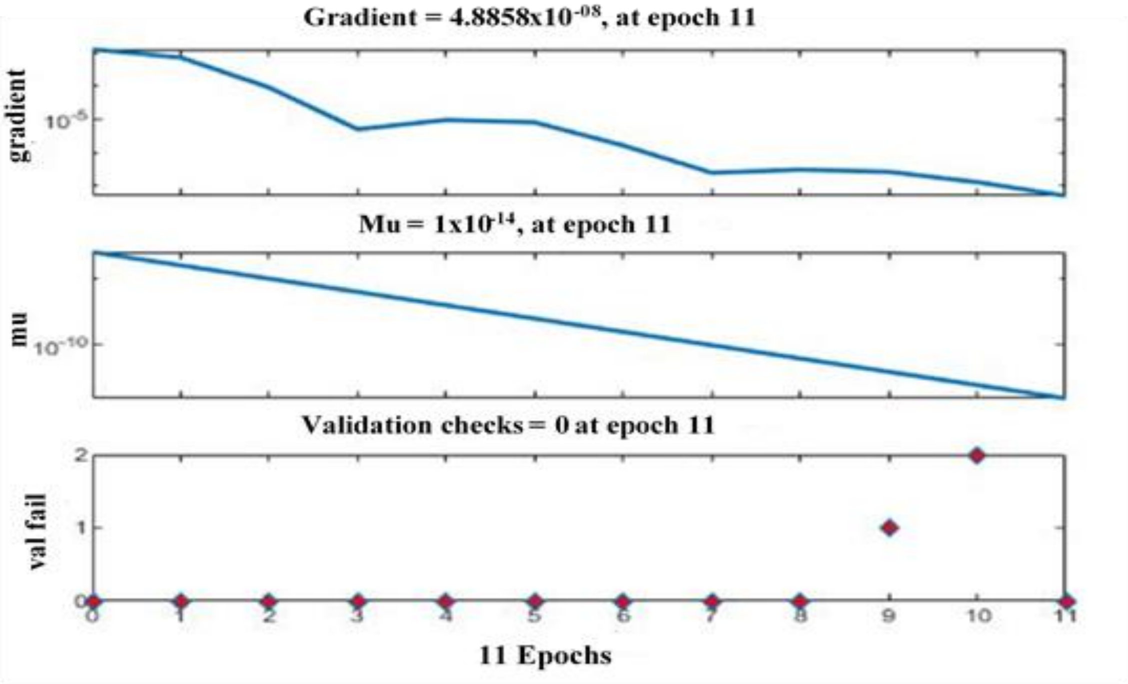

Figure 6.60: The gradient and maximum validation checks for the LM trained network; Per weight of cement

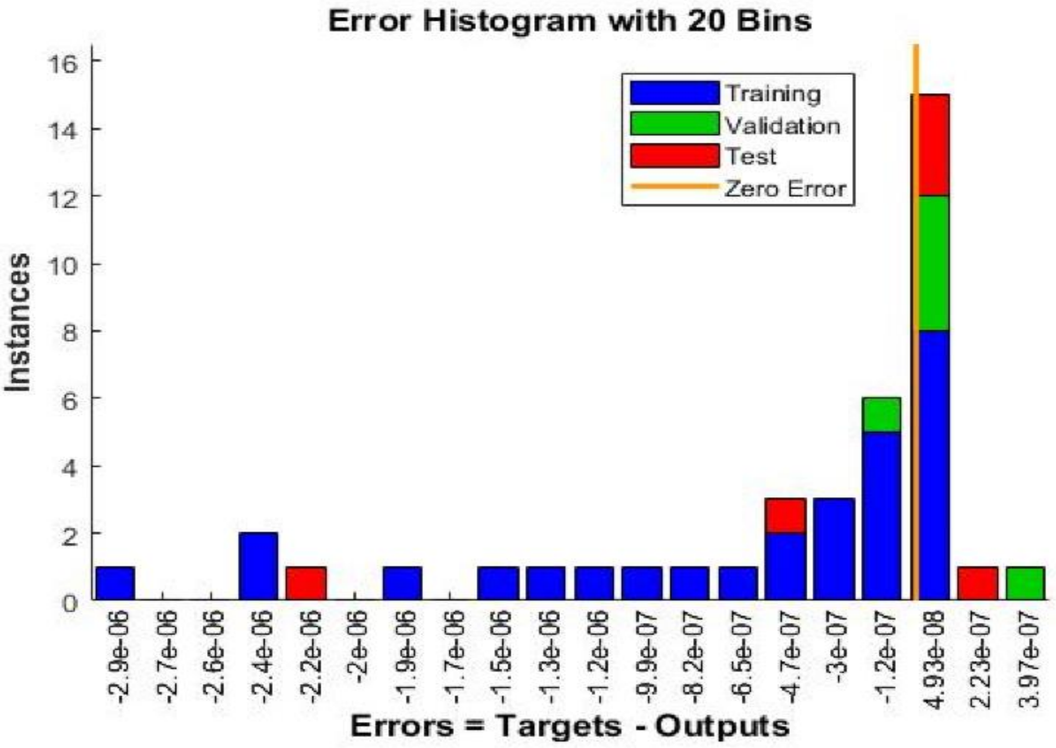

Figure 6.61: The plot of error histogram (EH) for the LM algorithm; Per weight of cement

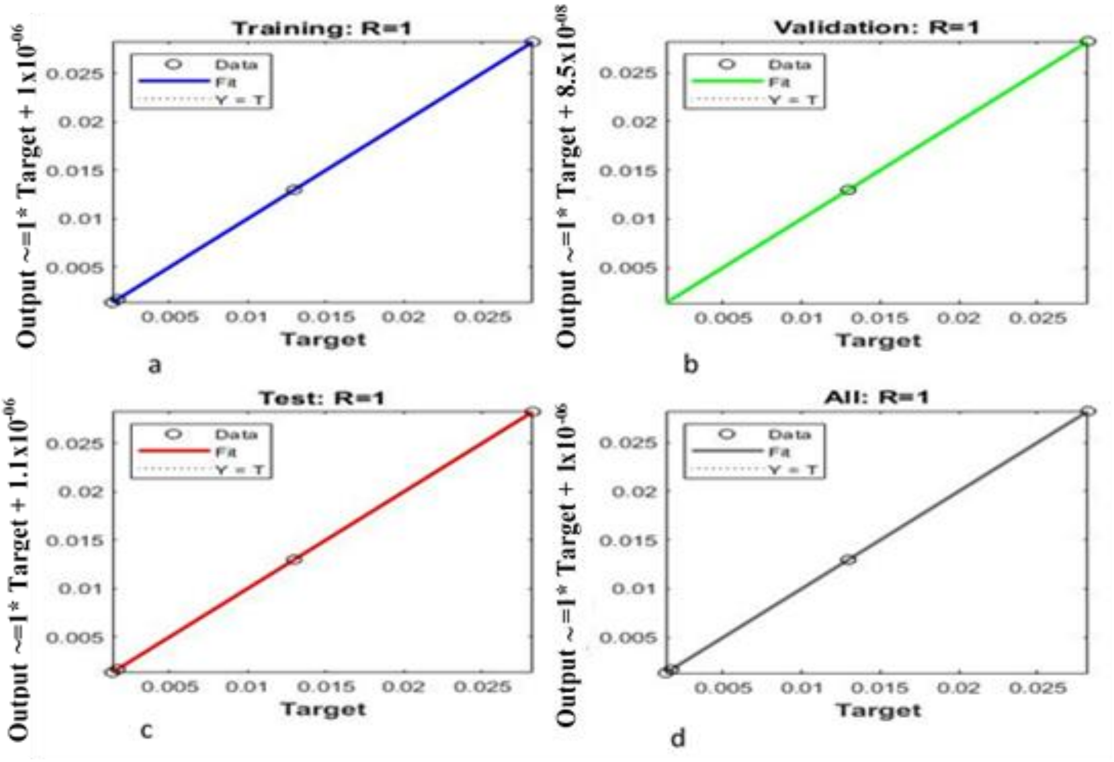

Figure 6. 62: The regression graphs of the experimental results against the validated %Chloride ions per weight of cement

Further useful figures concerning the correlation between the measured and the computational values such as training, testing, validation, and all data can be experiential in the regression plot of Figure 6.62 (a, b, c, & d). This Figure illustrates the relationship between the target and output variables for training, validation, and testing steps, respectively. The target values indicate the percentage of chloride ions in the concrete sample, and output values indicate the predicted percentage of chloride ions from the ANN algorithm in MATLAB Software. The points in all subdivisions (training, testing, and validation) are located close to the best line of equality (predicted %chloride ions= β * measured actual value of %chloride ions+α) with the high coefficients of determination of 1,1,1 and 1 for training, validation, testing and all data of the %Wt-cement. The term R is obtained by MATLAB Software which demonstrates the model efficiency. The MATLAB code for those graphs has been shown in Appendix A, B and C.

Furthermore, the performance of the LM algorithm is further examined using the target values versus the predicted values, as shown in Table 6.26. According to the results, the significant agreement can be observed between the targets measured versus predicted values with a Value of Normalised Absolute Error statistic (NAE), Value of Root Mean Square Error statistic (RMSE), and Value correlation coefficients (R^2) with the amount of %chloride per weight of cement at three different depths being (0.000138, 0.000272 and 0.9983905). According to the findings, microwave spectroscopy can assess variable amounts of NaCl in concrete samples at various depths. Furthermore, using supervised machine learning classification feature selection, a single frequency of 5.42GHz was identified as the most significant predictor for chloride ions.

Table 6.26: Presents the resulting data for the observed data target and validated values

%Chloride per weight of cement			
Varying depth of cover (mm)	**NAEs**	**RMSE**	**R^2**
18	0.000101	0.000212	0.997883
40	0.000215	0.000332	0.998898
Total both depth	0.000138	0.000272	0.9983905

6.8 Summary

The first experiment demonstrates that there is a considerable shift in the electromagnetic (EM) wave signature once the concrete absorbs water and salt water, notably at the 3.6 GHz and 4.1 GHz frequency range. The second experimental curing process was carried out for up to 28 days on two concrete samples of the same size and material properties. There is a noticeable change in EM signature between frequency range 2 GHz and 3 GHz, especially at frequency 2.7096 GHz. The change is affected by the amount of tap water and salt water absorbed in the concrete sample during the 28-days curing period. This is due to water's high dielectric property, which causes a microwave signal to change and electromagnetic (EM) wave absorption to depend highly on water salinity and temperature. However, the microwave signal changes early in the curing process and continues until the concrete is fully saturated. The third experiment used a set of horn antennae to monitor the drying process of both concrete samples with two different saltwater concentrations. There is a noticeable change occurring in the electromagnetic (EM) signal in both samples. Chose the frequency range of 2.5 GHz to 3.0 GHz because 2.709 GHz demonstrated the strongest linear correlation between the change in attenuation and weight loss of both concrete samples. The strongest linear correlation was found between S_{21} change at 2.709 GHz and weight, with $R^2 = 0.89$ for the saltwater sample and $R^2 = 0.88$ for the tap water sample. The fourth and fifth experiments used five concrete samples in five different saltwater concentrations. This study used two methods to detect the level of chloride ions in concrete samples based on the saltwater concentration. The first method employed an electromagnetic wave sensor, while the second, known as the chlorimeter tool, was used as the gold standard method to determine the amount of chloride in various cover depths.

In this project, we decided to use the Weka workbench to determine the most significant frequency point to investigate the level of chloride. The J48 algorithm, which displays the most important frequency point to detect the level of chloride ions in five different saltwater concentrations, obtained the best accuracy of 86 percent. Following the classification method's selection of a single frequency point, ANN prediction was used to analyse and develop the model. In addition, the Chi-squared, P-values, and error % between the actual and validated values of chloride ions were determined using the statistical Chi-squared test. According to the Chi-squared test, the percentage error between the actual and validated values per weight of cement is 0.036%. On the other hand, the ANN model accurately validated the level of chloride ions in five concrete samples at three different depths, with NAE = 0.000256 and $R^2 = 0.986709$, respectively.

Nevertheless, this study aims to see if electromagnetic (EM) waves could be used as a non-destructive method for determining chloride levels in reinforced concrete structures. The findings showed that the microwave sensor could detect chloride ions at different depths in concrete samples with saltwater concentrations less than the limited requirement of 0.4% chloride ion in the concrete structure.

Chapter Seven: Conclusions and Recommendations

7.1 Conclusions

- The presence of chloride ions in concrete structures is a significant source of reinforced steel corrosion, which leads to degradation. According to the present state-of-the-art limits, there is room for improvement since there is currently no easy-to-use yet strong technology to help in the NDT process. The most advanced field methods are destructive or somewhat destructive, limiting their continual usage by industry and requiring the extraction of the concrete pore solution. As a result, the researcher has been motivated to continue to study the application of innovative sensing technologies to create non-destructive ways for predicting the proportion of chloride ions in concrete buildings. A non-destructive measuring approach is required for real-time, consistent, and continuous monitoring of chloride-based degradation.
- Using microwave frequency and a horn antenna to detect chloride ions during the curing phase and drying process of concrete has been successfully tested and established. According to the literature study, horn antennas satisfied all of the design criteria for microwave sensors, including cost, flexibility, simplicity, and repeatability of results. As a result, the horn antenna was chosen for future research.
- The preliminary work began with the study of electromagnetic waves and the various types of microwave sensors used in different applications. This study selected two types of microwave sensors, the rectangular waveguide and the horn antenna, as possible sensing platforms to detect the amount of chloride ions in RC concrete structures. On the other hand, the dielectric property experiments were carried out to determine the imaginary and complex relative permittivity for concrete samples, both dry and wet, with fresh and salt water. To reach this conclusion, the S-parameters were measured by reflection and transmission using three different frequencies of rectangular waveguide bands. In Chapter 4, section 4.10.1, the bands utilised in this project are described and discussed.

  Due to the aims of this experiment, it was essential to find out how deep the electromagnetic wave propagation needed to go to detect chloride ions. However, the usual depth of reinforced concrete for chloride detection in the field of civil engineering is about 70mm for condition XS3, which involves exposure to salt water. Using civil engineering requirements for concrete structures exposed to chloride ion conditions and calculations of skin depth, the optimum angle between the two horn antennas was determined. It was then decided that the S_{21} and S_{11} parameters could be utilised with concrete samples and that there was a link between the skin depth of the concrete samples and the penetration depth.

Based on a literature review and preliminary experimental testing, a set of horn antennas were used in the lab.

- The first experiment used the transmitter and receiver horn antennas in the frequency range of 2 GHz and 12 GHz, respectively. Every hour for 24 hours, the S_{21} of wet processing pavement concrete was measured. A substantial shift in EM appears after both concrete samples absorbed water and salt water, particularly at the 3.6 GHz and 4.1 GHz frequency ranges. The changes are induced by a decrease in the amount of water and salt water in the concrete samples.
- In the second experiment, a 28-day curing process was carried out with a set of horn antennas. Measurements were collected every 15 minutes for 28 days while the concrete samples were immersed in both tap water and salt water. Especially around 2.709 GHz, there is a notable shift in the EM signature between the 2.5 GHz and 3 GHz range. The quantity of water and salt absorbed in the concrete samples throughout the 28-day curing period influences the EM wave changes. Results from the experimental curing procedure show that the microwave signal begins to alter at an early stage of curing and continues to do so until the concrete is fully saturated.
- S_{21} and S_{11} measurements of the drying process of both concrete samples in two different saltwater concentrations were taken after the curing process was complete. In both experiments, the EM signal shows a noticeable shift. There was a significant polynomial connection between the reflected signal and weight loss of both concrete samples and changes in the S_{21} parameter measurement at 2.709 GHz, with $R^2 = 0.91$ for the sample with salt water and $R^2 = 0.97$ for the sample with tap water for the transmitter and receiver sensors. At 2.709 GHz, the S_{11} parameter measurement changes from $R^2 = 0.96$ for the sample containing salt water and $R^2 = 0.92$ for the sample containing tap water.
- Two concrete slabs containing two rebars of the same size and material characteristics were compared in the fourth experiment. Figure 6.35 shows the greatest (polynomial) correlation coefficient between S_{21} shifts at 3.482 GHz

and weight loss, with $R^2 = 0.78$ for the saltwater sample and $R^2 = 0.90$ for the tap water sample. Figure 6.36 shows the greatest (polynomial) relationship between S_{21} shifts at 4.42 GHz and weight reduction, with $R^2 = 0.71$ for the saltwater sample and $R^2 = 0.89$ for the tap water sample.

  - The fifth experimental investigation, conducted between 2-12 GHz frequencies, used five concrete samples with five different saltwater contents. According to the data, the proportion of chloride ions at the concrete's surface was significantly greater, and it dropped as the concrete's cover increased. They have combined the data from both techniques to create a model for the percentage of chloride ions per weight of cement at three depths. It was found that the J48 algorithm provided the greatest accuracy of 86% and the lowest mean absolute error and the root mean square error. As shown in Figure 6.42, the decision tree created by the J48 algorithm is dependent on the varied saltwater concentrations. We used the ANN approach to analyse and construct the model once the most significant frequency point was selected. For the transmitter and receiver sensors, a single frequency point of 5.42 GHz was chosen to develop the validation model. The Chi-squared test was used to determine the Chi-squared value and percentage of error.
  - Additionally, the error % found was 0.034 per weight of cement. ANN model summary results show that the MSE and R^2 of the 70% training were $2.22469\text{x}10^{-7}$ and 0.99984 per weight of cement, respectively. For training, validation, testing, and the entire data set of the study, the coefficients of determination are 0.99998, 0.99956, 0.9991, and 0.99992, which are all high (per weight of cement). By using values for Normalised Absolute Error (NAE), Root Mean Square Error (RMSE), and Value Correlation coefficients (R^2). A significant agreement was found between the measured and validated values for the percent chloride per weight of cement at three different depths (0.000256, 0.000120 and 0.986709).

- Electromagnetic waves enable the measurement of chloride levels at different depths at a single frequency, and the findings achieved in this study were promising (5.42 GHz). There is, therefore, a requirement to create a portable sensor with a set of horn antennas as a transmitter and receiver that operates at a single frequency to employ this technology as an NDT technique for the large majority of prospective civil engineering users. A non-destructive method for determining chloride content in concrete structures was evaluated for the first time in this study using electromagnetic waves. When compared to existing industry gold standards, this novel approach may change the early detection of deterioration in steel-reinforced concrete structures. Because the microwave sensor detects values below 0.4% as a trigger threshold, this technology could be utilised to determine when concrete structures are at the critical point for repair, based on the data collected in this project. In order to confirm the amount of chloride ions in concrete samples, ANN was successfully utilised to analyse the microwave data and validate the results obtained.

7.2 Recommendations for future work

In light of results reported in this study and based on the experience gained during the research, several possible future studies are recommended as follows:

- Further work can be conducted to further test a larger number of laboratory concrete specimens to further validate the prediction model.
- The system can be taken to the marine environment to verify the technique on various structures with different chloride levels and depths of penetration.
- Incorporating this technology could enable the assessment of repairs to marine structures.
- Using this technology to detect the carbonation of concrete and reduce Ph levels could also be beneficial.
- Based on the findings and possible application, it is suggested to design a portable sensor device operating at 5.42GHz, including the VNA system for evaluation, all in one hand-held unit.
- The development of a mobile tool machine learning algorithm will provide further support for service life prediction.

References:

1. J.S. Damtoft, J.L., D. Herfort,D.Sorrentino,E.M. Gartner, Sustainable development and climate change initiatives. Cement and Concrete Research, 2008. **38**: p. 115-127.
2. Townsend, S.J.O.D.C.C.H.E., Atmospheric corrosion of di€erent steels in marine, rural and industrial environments. Corrosion Science, 1999. **41**: p. 1687-1702.
3. Luca Bertolini, M.C., Matteo Gastaldi, Federica Lollini, and Elena Redaelli. Corrosion of Steel in Concrete and Its Prevention in Aggressive Chloride-Bearing Environments. in 5th International Conference on Durability of Concrete Structures. 2016. Shenzhen: Department of Chemistry, Materials and Chemical Engineering “Giulio Natta”, Politecnico di Milano, Italy.
4. Montemor, M.F., A.M.P. Simões, and M.G.S. Ferreira, Chloride-induced corrosion on reinforcing steel: from the fundamentals to the monitoring techniques. Cement and Concrete Composites, 2003. **25**(4-5): p. 491-502.
5. Tuutti, K., Corrosion of steel in concrete in Department of Building Materials. 1982, Royal Institute of Technology, Stockholm: Swedish Cement and Concrete Research Institute, Stockholm.
6. G. Koch, M.B., N. Thompson, Y. Virmani, J. Payer, Corrosion costs and preventive strategies in the United States, Tech. rep., U.S. Department of tranportation Federal Highway Administration. CC Technologies Laboratories, Inc. and NACE international, 2002.
7. X. Shi, N.X., K. Fortune, J. Gong,, Durability of steel reinforced concrete in chloride environments. An overview, Construction and Building Materials, 2012. **30**: p. 125-138.
8. Duratinet. project context. 2012 [cited 2019 04/08]; Available from: http://durati.lnec.pt/en/publications.html.
9. W. J. McCarter, O.V., Sensor systems for use in reinforced concrete structures. Construction and Building Materials, 2004. **18**: p. 351-358.
10. A., H.D., Steel Corrosion in Concrete: How Does it Occur? Material Protection. 1967.
11. W. Morris, A.V., M. Vazquez, S.R. de Sanchez, Corrosion of reinforcing steel evaluated by means of concrete resistivity measurments. Corrosion Science, 2002. **44**: p. 88-99.
12. W. Morris, A.V., M. Vázquez, Chloride induced corrosion of reinforcing steel evaluated by concrete resistivity measurements. Electrochimica Acta, 2004. **49**: p. 4447-4453.
13. C.E. Locke, A.S., Electrochemistry of reinforcing steel in salt-contaminated concrete. D.E. Tonini, J.M. Gaidis (Eds.), Corrosion of Reinforcing Steel in Concrete, ASTM STP 713,American Society for Testing and Materials 1980: p. 3-16.
14. S.E. Hussain, A.R., A. Al-Musallam, A.S. Al-Gahtani, 1995. Cement and Concrete Research, Factors affecting threshold chloride for reinforcement corrosion in concrete. **25**: p. 1543-1555.
15. Alonso, C.A., M. Castellote, P. , Chloride threshold values to depassivate reinforcing bars embedded in a standardized OPC mortar. Cement and Concrete Research, 2000. **30**: p. 1047-1055.
16. D. Trejo, P.J.M., Corrosion performance of conventional (ASTM A615) and low-alloy (ASTM A706) reinforcing bars embedded in concrete and exposed to chloride environments. Cement and Concrete Research, 2005. **35**: p. 562-571.
17. M. Manera, Ø.V., L. Bertolini, Chloride threshold for rebar corrosion in concrete with addition of silica fume. Corrosion Science, 2008. **50**: p. 550-560.
18. Christopher J. Friend, Concrete Bridge Failures - Deterioration and Spalling. Website, 2013.
19. Bertolini., L., et al., Corrosion of Steel in Concrete and Its Prevention in Aggressive Chloride-Bearing Environments. 2016.
20. Friend, C.J. Concrete Bridge Failures-Deteriotions and Spalling. Causes of Concrete Deterioration & Spalling 2013 [cited 2017 01/07]; Available from: https://failures.wikispaces.com/Concrete+Bridge+Failures+-+Deterioration+and+Spalling.
21. Dhakal, D., Investigation of chloride induced corrosion of bridge pier and life -cycle repair cost analysis using fiber reinforced polymer composites. Article, 2014: p. 5-21.
22. Gonzalo, et al., State of the art – Methods to measure moisture in concrete. Article, 2011: p. 2-40.

23. Y. Zhou, et al., Carbonation-Induced and Chloride-Induced Corrosion in Reinforced Concrete Structures. Journal of Materials in Civil Engineering, 2015. **27**(9): p. 04014245.
24. Bioubakhsh, S., The penetration of chloride in concrete subject to wetting and drying, in Faculty of the Built Environment. 2011, Univerity College London: UCL (University College London). p. 355.
25. Kropp, J. and M. Alexander, Non- destrictive methods to measure ion migration. In: RILEM Report 40 Non-Destructive Evaluation of the Penetrability and Thickness of the Concrete Cover. 2007, RILEM TC 189-NEC: State of the art report. p. 13-34.
26. Verma, S.K., S.S. Bhadauria, and S. Akhtar, Review of Nondestructive Testing Methods for Condition Monitoring of Concrete Structures. Journal of Construction Engineering, 2013. **2013**: p. 1-11.
27. Humphreys, M., et al., Strategies for Minimising the Whole of Life Cycle Cost of Reinforced Concrete Brodge Exposed to Aggressive Environments. Report, 2008: p. 1-12.
28. Seminar. Control Of Corrosion On Underwater Piles. Seminar 2016 14 Feb; Available from: http://www.seminarsonly.com/Civil_Engineering/Control_Of_Corrosion.php.
29. M. Torres-Luque M, B.-A.E., Schoefs F, Sánchez-Silva M, Osma JF., Non-destructive methods for measuring chloride ingress into concrete: State-of- the-art and future challenges. Constr Build Mater, 2014: p. 68-81.
30. M.Torres-Luque, et al., Non-destructive methods for measuring chloride ingress into concrete: State-of-the-art and future challenges. Construction and Building Materials, 2014. **68**: p. 68-81.
31. Angst, U. and Ø. Vennesland, Detecting critical chloride content in concrete using embedded ion selective electrodes - effect of liquid junction and membrane potentials. Materials and Corrosion, 2009. **60**(8): p. 638-643.
32. Jin, M., L. Jiang, and Q. Zhu, Monitoring chloride ion penetration in concrete with different mineral admixtures based on embedded chloride ion selective electrodes. Construction and Building Materials, 2017. **143**: p. 1-15.
33. Gao, P., et al., Modification of chloride diffusion coefficient of concrete based on the electrical conductivity of pore solution. Construction and Building Materials, 2017. **145**: p. 361-366.
34. Andrade, C., R. d'Andrea, and N. Rebolledo, Chloride ion penetration in concrete: The reaction factor in the electrical resistivity model. Cement and Concrete Composites, 2014. **47**: p. 41-46.
35. Lam, C.C.C., et al., Optical Fiber Refractive Index Sensor for Chloride Ion Monitoring. IEEE Sensors Journal, 2009. **9**(5): p. 525-532.
36. R Falciai, A.G.M., A Vannini, Long period gratings as solution concentration sensors. Sensors and actuators B: chemical, 2001. **74**(1-3): p. 74-77.
37. F.de J Cano , T.W.B., R.P McGregor , B.J Balcom Magnetic resonance imaging of ^{1}H, ^{23}Na, and ^{35}Cl penetration in Portland cement mortar. Cement and Concrete Research, 2002. **32**(7): p. 1067-1070.
38. Ramírez-Ortíz, A.E., F. Castellanos, and P.F.d.J. Cano-Barrita, Ultrasonic Detection of Chloride Ions and Chloride Binding in Portland Cement Pastes. International Journal of Concrete Structures and Materials, 2018. **12**(1): p. 20.
39. Dérobert, X., et al., Evaluation of chloride contamination in concrete using electromagnetic non-destructive testing methods. NDT & E International, 2017. **89**: p. 19-29.
40. Hugenschmidt Johannes, L., Roman, Detection of chlorides and moisture in concrete structures with ground penetrating radar. Materials and Structures, 2007. **41**(4): p. 785-792.
41. 228, A.C., In-Place Methods to Estimate concrete strength. ACI Committee Reports, 2003: p. 41.
42. Dimitrios G. Aggelis, T.S., Shouhei Momoki, and Akinobu Hirama, Acoustic Emission and Ultrasound for Damage Characterization of Concrete Elements. International Concrete Abstracts Portal, 2009. **106**(6): p. 509-514.
43. Gradinarsky, L., et al., In situmonitoring and control of moisture content in pharmaceutical powder processes using an open-ended coaxial probe. Measurement Science and Technology, 2006. **17**(7): p. 1847-1853.
44. Korostynska, O., A. Mason, and A. Al-Shamma'a, Microwave sensors for the non-invasive monitoring of industrial and medical applications. Sensor Review, 2014. **34**(2): p. 182-191.

45. Adous, M., P. Quéffélec, and L. Laguerre, Coaxial/cylindrical transition line for broadband permittivity measurement of civil engineering materials. Measurement Science and Technology, 2006. **17**(8): p. 2241-2246.
46. P. Kot, et al., The feasibility of electromagnetic waves in determining the moisture content of concrete blocks, in Ninth international Conference on sensing Technology. 2015: New Zealand. p. 251-256.
47. Oh, B.H. and S.Y. Jang, Effects of material and environmental parameters on chloride penetration profiles in concrete structures. Cement and Concrete Research, 2007. **37**(1): p. 47-53.
48. Alonso, M.C. and M. Sanchez, Analysis of the variability of chloride threshold values in the literature. Materials and Corrosion, 2009. **60**(8): p. 631-637.
49. Rasheeduzzafar, S.E. Hussai, and s.s. Al-Saadoun, Effect of cement composition on chloride binding and corrosion of reinforcing steel in concrete. Cement & Concrete Research, 2009. **21**: p. 777-794.
50. Ahmad, S., Reinforcement corrosion in concrete structures, its monitoring and service life prediction—a review. Cement and Concrete Composites, 2003. **25**(4-5): p. 459-471.
51. Koleva, D.A., et al., Correlation of microstructure, electrical properties and electrochemical phenomena in reinforced mortar. Breakdown to multi-phase interface structures. Part I: Microstructural observations and electrical properties. Materials Characterization, 2008. **59**(3): p. 290-300.
52. T. Mohammed and H. Hamada, Corrosion of Steel Bars in Concrete with Various Steel. ACI Matrials Journal, 2006. **103**: p. 233-242.
53. L. Mammoliti, et al., The Influence Of Surface Finish Of Reinforcing Steel And Ph Of The Test Solution Of The Chloride Threshhold Concentraton For Corrosion Initiation In Synthetic Pore Solutions. Cement And Concrete Research, 1996. **24**(4): p. 545-550.
54. Raja, E.W. Concrete Cover for Reinforcement | Clear Cover | Nominal Cover | Effective Cover | Minimum Cover for Reinforcement. 2018 [cited 2020 01/06]; Available from: https://www.thecivilengineering.com/concrete-cover-for-reinforcement-clear-cover-nominal-cover-effective-cover-minimum-cover-for-reinforcement/.
55. Guedes, F. and R. Vaz Rodrigues, The effect of concrete cover on the crack width in reinforced concrete members-a code perspective. 2017.
56. Sung kim, J.S.a.J.B.-J., Electromagnetic Metrology on Concrete and corrosion. Journal of research of the national institute of standard and technology, 2011. **116**(3): p. 655-669.
57. Krause, A.P., Conductive concrete for electromagnetic shielding – methods for development and evaluation in Presented to the Faculty of The Graduate College at the University of Nebraska 2012, University of Nebraska-Lincoln, : Lincoln, Nebraska p. 68.
58. Bastidas-Arteaga, E., et al., Influence of weather and global warming in chloride ingress into concrete: A stochastic approach. Structural Safety, 2010. **32**(4): p. 238-249.
59. 8500-2:2006+A1:2012, B., Concrete. Complementary British Standard to BS EN 206-1. Specification for constituent materials and concrete. 2006, BSI Standards Limited 2012. p. 66.
60. Erdoğdu, Ş., I.L. Kondratova, and T.W. Bremner, Determination of chloride diffusion coefficient of concrete using open-circuit potential measurements. Cement and Concrete Research, 2004. **34**(4): p. 603-609.
61. Appleton, A.C.a., Chloride penetration into concrete in marine environment-part1 main parameters affecting chloride penetration. Materials and Structures, 1999. **32**: p. 252-259.
62. Vladim´ır Zivicaa, A.B., Acidic attack of cement based materials review. Part 1.Principle ofacidic attack. Construction and bBuilding Materilas, 2001. **15**: p. 331-340.
63. Marinoni, N., et al., The effects of atmospheric multipollutants on modern concrete. Atmospheric Environment, 2003. **37**(33): p. 4701-4712.
64. Zuquan, J., et al., Interaction between sulfate and chloride solution attack of concretes with and without fly ash. Cement and Concrete Research, 2007. **37**(8): p. 1223-1232.
65. Mancini, P.I.G. and P.d. Torino, EUROCODE 2 – Design of concrete structures Concrete bridges: design and detailing rules. EUROCODES, Bridges: Background and applications, 2005: p. 1-145.

66. Kulkarni, V.R., Exposure classes for designing durable concrete by exposure conditions. Indian concrete journal, 2009: p. 17.
67. Khan, M.U., S. Ahmad, and H.J. Al-Gahtani, Chloride-Induced Corrosion of Steel in Concrete: An Overview on Chloride Diffusion and Prediction of Corrosion Initiation Time. International Journal of Corrosion, 2017. **2017**: p. 1-9.
68. Abbas, Y., et al., No more conventional reference electrode: transition time for determining chloride ion concentration. Anal Chim Acta, 2014. **821**: p. 81-8.
69. A. Yousaf, F.K., and L. Reindl, "Passive Wireless Sensing of Micro coil parameters in fluidic environments,". Sensors and Actuators A: Physical, 2012. **186**: p. 69-79.
70. Larsen, K.r. Corrosion Effects on the Durability of Reinforced Concrete Structures. 2015 [cited 2019 09]; Available from: http://www.materialsperformance.com/articles/material-selection-design/2015/12/corrosion-effects-on-the-durability-of-reinforced-concrete-structures.
71. Serpelloni, E.S.a.M., "Wireless measurement technique for telemetry low-value resistive sensors," Procedia Engineering, 2011. **25**: p. 1261-1264.
72. Vu., K. and M. Stewart, Service Life Prediction Of Reinforced Concrete Structures Exposed To Aggressive Environments. Surveying & Environmental Engineering University of Newcastle Australia, 2002: p. 1-10.
73. M.Otieno, M.T., 7-Marine exposure envirnents and marine exposure sites. Marine Concrete Structures, 2016: p. 171-196.
74. Nireki, T.a.K., H, Monitoring and analysis of seawater content, in in Fourth International conference on Durability of Building materials and structures. 1987: Singapore. p. 531-536.
75. Adam, N., Chloride attack of reinforced concrete: an Overview. Materials and Structures, 1995. **28**: p. 63-70.
76. Damrongwiriyanupap, N., L. Li, and Y. Xi, Coupled diffusion of chloride and other ions in saturated concrete. Frontiers of Architecture and Civil Engineering in China, 2011. **5**(3): p. 267-277.
77. Gónzalez Fernández, J.A.a.M.V.J., Corrosión en las estructuras dehormigón armado:. Fundamentos, medida, diagnosis y prevención. 2007, Madrid,: Biblioteca de Ciencias.
78. R.G.Kelly, David W Shoesmith, and R.G. Buchheit, Electrochemical Techniques in Corrosion Science and Engineering. 2003.
79. McCafferty, E., Introduction to Corrosion Science. Springer, 2010.
80. R.T.L. Allen, J.a.F., A.P. Crane (Ed), The Investigation and Repair of Damaged Teinforced Concrete Structures,. scociety of Chemical Industry,London, 1983: p. 193-222.
81. Frankel, G.S., Pitting Corrosion of Metals A Review of the Critical Factors. 1998. **145**(6): p. 2186-2198.
82. H. Böhni, Localized corrosion of passive metals,. Second ed ed, ed. U.s.C.H. in: R.W. Revie (Eds.). 2000, USA: John Wiley & Sons.
83. Strehblow, P.D.H.H., Breakdown of passivity and localized corrosion: Theoretical concepts and fundamental experimental results. Journal Artical, 1984: p. 99-111.
84. Luca Bertolini, et al. Corrosion of steel in concrete and its Prevention in aggressive Chloride_Bearing Environment. in 5th International Conference on Durability of Concrete Structures Shenzhen University, Shenzhen, Guangdong Province, P.R.China Department of Chemistry, Materials and Chemical Engineering “Giulio Natta”, Politecnico di Milano, Italy.
85. Solgaard, A.O.S., corrosion of reinforcement bars in steel reinforced concrete structurees, in Department of Civil Engineering 2013, Department of Civil Engineering Technical University of Denmark: Department of Civil Engineering Technical University of Denmark. p. 151-157.
86. Altaf Ahmad and A. Kumar, Chloride ion migration/diffusion through concrete and test methods. 2013. **6**(3): p. 30.
87. Jennifer L. Kepler, David Darwin, and J. Carl E. Locke, Evaluation Of Corrosion Protection Methods For Reinforced Concrete Highway Structures, T.n.s. foundation, Editor. 2000: University of kansas center for research, inc.lawrence, kansas. p. 231.
88. Dhir, R.K., et al., Preconditioning in situ concrete for permeation testing Part 1: Initial surface absorption. Magazine of Concrete Research, 1993. **45**(163): p. 113-118.
89. McCann, D.M. and M.C. Forde, Review of NDT methods in the assessment of concrete and masonry structures. NDT&E International, 2001. **34**: p. 71-84.

90. Atkins., C.P., M.A. Carter., and J.D. Scantlebury, Sources of error in using silver/silver chloride electrodes to monitor chloride activity in concrete. Cement and Concrete Research, 2001. **31**: p. 1207– 1211.
91. G. de Vera, M.C., C. Ant´on, A. Hidalgo, C. Andrade,, Determination of the selectivity coefficient of a chloride ion selective electrode in alkaline media simulating the cement paste pore solution. Journal of Electroanalytical Chemistry 2010. **639**: p. 42-50.
92. Angst, U., et al., Critical chloride content in reinforced concrete—a review. Cement and Concrete Research, 2009. **39**(12): p. 1122-1138.
93. B. Elsener, L.Z., H. B¨ohni,, Non destructive determination of the free chloride content in cement based materials,. Materials and Corrosion, 2003. **54**(6): p. 440-446.
94. Elsener., B., Macrocell corrosion of steel in concrete – implications for corrosion monitoring. Cement & Concrete Composites, 2002. **24**: p. 65–72.
95. Basheer., P.A.M., et al., Monitoring electrical resistance of concretes containing alternative cementitious materials to assess their resistance to chloride penetration. Cement & Concrete Composites, 2002. **24**: p. 437–449.
96. Magda Marcela Torres-Luque, et al., Non-destructive methods for measuring chloride ingress into concrete: State-of-the-art and future challenges. Construction and Building Materials, 2014. **68**: p. 68-81.
97. K. Gowers and S. Millard, Measurement of concrete resistivity for assessment of corrosion severity of steel using Wenner technique. ACI Materials Journal, 1999. **96**: p. 536–541.
98. Plooy, R.L.D., The development and combination of electromagnetic non-destructive evaluation techniques for the assessment of cover concrete condition prior to corrosion. 2013, Universit´e de Nantes.
99. Maksimović, M., et al., Application of a LTCC sensor for measuring moisture content of building materials. Construction and Building Materials, 2012. **26**(1): p. 327-333.
100. H. Li, D.-S. Li, and G.-B. Song, Recent applications of fiber optic sensors to health monitoring in civil engineering. Engineering Structures, 2004. **26**(11): p. 1647-1657.
101. Li, H.-N., D.-S. Li, and G.-B. Song, Recent applications of fiber optic sensors to health monitoring in civil engineering. Engineering Structures, 2004. **26**(11): p. 1647-1657.
102. Kearey, P.a.B., M., An_introduction_to_geophysical_exploration. Department of Geology University of Leicester.
103. Davidson, N., Padaratz, I., and Forde, M., "Quantification of bridge scour using impulse radar.". International Symposium Non-Destructive Testing in Civil Engineering(NDT-C, E), 1995: p. 61-68.
104. M.Morey, R., Ground Penetrating Radar for Evaluting Subsurface Conditions for Transportation Facilities, in National Cooperative Highway Research Program. 1998, Transportation Research Board National Academy Press: Washington,DC:NCHRP Synthesis 255.
105. Rhee, J.-Y., J.-J. Choi, and S.-H. Kee, Evaluation of the Depth of Deteriorations in Concrete Bridge Decks with Asphalt Overlays Using Air-Coupled GPR: A Case Study from a Pilot Bridge on Korean Expressway. International Journal of Concrete Structures and Materials, 2019. **13**(1).
106. MASER, K.R., Integration of Ground Penetrating Radar and Infrared thermography for brdidge deck condition evaluation. NDTCE'09, Non-Destructive Testing in Civil Engineering, 2009: p. 1-8.
107. Cardimona, S., Willeford, B., Wenzlick, J. & Anderson, N. , Investigation of bridge decks utilizing ground penetrating radar, in In International conference on the application of geophysical technologies to planning, . 2000, St. Louis, MO, in press,: Design, Construction, and Maintenance of Transportation Facilities,. p. 1-10.
108. Varnavina, A.V., et al., An attempt to describe a relationship between concrete deterioration quantities and bridge deck condition assessment techniques. Journal of Applied Geophysics, 2017. **142**: p. 38-48.
109. Rodríguez-Abad, I., et al., Application of ground-penetrating radar technique to evaluate the waterfront location in hardened concrete. Geoscientific Instrumentation, Methods and Data Systems, 2016. **5**(2): p. 567-574.

110. Clemena, G.G., Hand book on non destructive testing of concrete structures "Short-pulse radar methods". 1991, , Boston, Chap.: CRC Press. 252-274.
111. NDT, J.I. Chlotimeter Chloride Field Test System. 2010 [cited 2018 1/4]; Available from: https://www.ndtjames.com/Chloride-Field-Test-System-p/c-cl-3000.htm.
112. Gu., P. and J.J. Beaudoin. Obtaining Effective Half-Cell Potential Measurements in Reinforced Concrete Structures. Construction Technology Update 1998 [cited 2017 15/04]; Available from: https://www.nrc-cnrc.gc.ca/ctu-sc/ctu_sc_n18.
113. Eunjong Ahn, et al., Principles and Applications of Ultrasonic-Based Nondestructive Methods for Self-Healing in Cementitious Materials. 2017. **3**: p. 278.
114. Elsener, B., et al., Half-cell potential measurements – Potential mapping on reinforced concrete structures. 2003. **36**: p. 11.
115. Clemena, G.G., Short-pulse radar methods. In Malhotra, V. M., N. J. Carino (Eds.), . 2nd ed. Handbook on nondestructive testing of concrete,. 2004, London: CRC Press, Boca Raton; . 386.
116. Tarawneh, B., Predicting standard penetration test N-value from cone penetration test data using artificial neural networks. Geoscience Frontiers, 2017. **8**(1): p. 199-204.
117. Morfidis, K. and K. Kostinakis, Seismic parameters' combinations for the optimum prediction of the damage state of R/C buildings using neural networks. Advances in Engineering Software, 2017. **106**: p. 1-16.
118. Xu, W.-Z., et al., Corroded pipeline failure analysis using artificial neural network scheme. Adv. Eng. Softw., 2017. **112**: p. 255-266.
119. Hagan, M.T., Demuth, H. B & Beale, M. H, Neural network design, ed. MABoston. 1996, PWSPublishing.
120. Rumelhart, D.E., G.E. Hinton, and R.J. Williams, Learning internal representations by error propagation, in Parallel distributed processing: explorations in the microstructure of cognition, vol. 1: foundations. 1986, MIT Press. p. 318–362.
121. Peng, J., Z. Li, and B. Ma, Neural Network Analysis of Chloride Diffusion in Concrete. Journal of Materials in Civil Engineering - J mater civil eng, 2002. **14**.
122. Jaeel, A.J., A.I. Al-wared, and Z.Z. Ismail, Prediction of sustainable electricity generation in microbial fuel cell by neural network: Effect of anode angle with respect to flow direction. Journal of Electroanalytical Chemistry, 2016. **767**: p. 56-62.
123. Abiodun, O.I., et al., State-of-the-art in artificial neural network applications: A survey. Heliyon, 2018. **4**(11): p. e00938.
124. Asghshahr, M.S., A. Rahai, and H. Ashrafi, Prediction of chloride content in concrete using ANN and CART. Magazine of Concrete Research, 2016. **68**(21): p. 1085-1098.
125. Majdi, A. and M. Beiki, Evolving neural network using a genetic algorithm for predicting the deformation modulus of rock masses. International Journal of Rock Mechanics and Mining Sciences, 2010. **47**(2): p. 246-253.
126. Shahin, M.A., Load–settlement modeling of axially loaded steel driven piles using CPT-based recurrent neural networks. Soils and Foundations, 2014. **54**(3): p. 515-522.
127. Rosenblatt, F., The Perceptron: A Probabilistic Model For Information Storage and Organization in the Brain. Psychological review, 1958. **65**(6): p. 386.
128. Gil, J.G., Artificial Neural Networks applied to the resolution of Regression and Classification Multivariate Analysis problems in the Agricultural and the Industrial fields, in Departamento de Teoría de la Señal y Comunicaciones e Ingeniería Telemática. 2012, Universida de valladolid. p. 117.
129. Kriesel, D., A brief introduction to neural networks. Zeta2-EN, 2005: p. 1-244.
130. Master, T., Practical neural networks recipes in C ++. Academic Press Inc, San Diego, 1993: p. 51.
131. Zhang, J., Hu, J., Zhang, C. & Wang, j., new deep neural network based on a stack of single-hidden-layer feed forward neural networks with randomly fixed hidden neurons. Neurocomputing,, 2016. **171**: p. 63-77.
132. Sazli, M., A brief review of feed-forward neural networks. Communications, Faculty Of Science, University of Ankara, 2006. **50**: p. 11-17.

133. Han, F., Zhao, M., Zhang, J. & Ling, Q., An improved incremental constructive single-hidden-layer feedforward networks for extreme learning machine based on particle swarm optimization. Neurocomputing,, 2017. **228**: p. 133-142.
134. A. J., A.-w., A. I. & Ismail, Z. Z., Prediction of sustainable electricity generation in microbial fuel cell by neural network: Effect of anode angle with respect to flow direction. Journal of Electroanalytical Chemistry, 2016. **766**: p. 56-62.
135. Feng, Y., Barr, W. f. & Harper, J., Neural network processing of microbial fuel cell signals for the identification of chemicals present in water. Environmental Management, 2013. **120**: p. 84-92.
136. Liu, W. and X. Zhang, Research on the Supply Chain Risk Assessment Based on the Improved LSSVM Algorithm. International Journal of u- and e- Service, Science and Technology, 2016. **9**(8): p. 297-306.
137. Haykin, S.O., Neural Networks: A Comprehensive Foundation,, n. Edition, Editor. 1999, Prentice Hall: McMaster University, Hamilton, Ontario, Canada.
138. Ravuri, S. and A. Stolcke. A comparative study of recurrent neural network models for lexical domain classification. in 2016 IEEE International Conference on Acoustics, Speech and Signal Processing (ICASSP). 2016.
139. Kriesel, D., A Brief Introduction Neural Networks, ed. ZETA2-EN. 2009.
140. Alizadeh, B., S. Najjari, and A. Kadkhodaie-Ilkhchi, Artificial neural network modeling and cluster analysis for organic facies and burial history estimation using well log data: A case study of the South Pars Gas Field, Persian Gulf, Iran. Computers & Geosciences, 2012. **45**: p. 261-269.
141. Tarawneh, B., Pipe pile setup: Database and prediction model using artificial neural network. Soils and Foundations, 2013. **53**(4): p. 607-615.
142. Yadav, A.K., H. Malik, and S.S. Chandel, Selection of most relevant input parameters using WEKA for artificial neural network based solar radiation prediction models. Renewable and Sustainable Energy Reviews, 2014. **31**: p. 509-519.
143. Rojas, R., Neural Networks, in A Systematic Introduction. 2005: Berlin Heidelberg NewYork,Hong Kong London, Milan Paris Tokyo. p. 505.
144. Nguyen-Truong, H.T.L., Hung M., An implementation of the Levenberg–Marquardt algorithm for simultaneous-energy-gradient fitting using two-layer feed-forward neural networks. Chemical Physics Letters, 2015. **629**: p. 40-45.
145. W. Schiffmann, M.J., R. Werner, Optimization of the Backpropagation Algorithm for Training Multilayer Perceptrons. 1994, Institute of Physics: University of Koblenz

146. Gurney, K., An introduction to neural networks. 2004, British Library Cataloguing in Publication Data: UCL Press.
147. Jebur, A.A., W. Atherton, and R.M. Al Khaddar, Feasibility of an evolutionary artificial intelligence (AI) scheme for modelling of load settlement response of concrete piles embedded in cohesionless soil. Ships and Offshore Structures, 2018. **13**(7): p. 705-718.
148. Levenberg, K., A method for the solution of certain problems in least squares,. Quart. Appl. Mach, 1994. **2**: p. 164–168,.
149. Morfidis, K.K., K., Seismic parameters' combinations for the optimum prediction of the damage state of R/C buildings using neural networks. Advances in Engineering Software, 2017. **106**: p. 1-17.
150. Wilamowski, B.M.Y., H., Improved cpmputaion for Levenberg-Marquardt. IEEE Transaction on Neural Network, 2010. **21**: p. 738-930.
151. Singer, P.Y., Advanced Optimization. 2016. p. 1-5.
152. Gratton, S., A.S. Lawless, and N.K. Nichols, Approximate Gauss–Newton Methods for Nonlinear Least Squares Problems. SIAM Journal on Optimization, 2007. **18**(1): p. 106-132.
153. Hao Yu, B.M.W., Levenberg–Marquardt Training. 2010. p. 1-16.
154. Premalatha, N. and A. Valan Arasu, Prediction of solar radiation for solar systems by using ANN models with different back propagation algorithms. Journal of Applied Research and Technology, 2016. **14**(3): p. 206-214.

155. Angela, K., S. Taddeo, and M. James, Predicting Global Solar Radiation Using an Artificial Neural Network Single-Parameter Model. Advances in Artificial Neural Systems, 2011. **2011**: p. 751908.
156. Al-Janabi, K.R., Laboratory Leaching Process Modeling in Gypseous Soils Using Artificial Neural Networks (ANNs), in Building and Construction Engineering Department. 2006, University: Iraq.
157. Stojanovic, B., et al., A self-tuning system for dam behavior modeling based on evolving artificial neural networks. Advances in Engineering Software, 2016. **97**: p. 85-95.
158. Madhiarasan, M. and S.N. Deepa, A novel criterion to select hidden neuron numbers in improved back propagation networks for wind speed forecasting. Applied Intelligence, 2016. **44**(4): p. 878-893.
159. Tom´aˇs Mareˇs, Eliˇska Janouchov´a, and Anna Kuˇcerov´a, Artificial neural networks in calibration of nonlinear mechanical models Advanced in Engineering Software, 2016. **95**: p. 68-81.
160. Hashim, K.S., et al., Defluoridation of drinking water using a new flow column-electrocoagulation reactor (FCER) - Experimental, statistical, and economic approach. J Environ Manage, 2017. **197**: p. 80-88.
161. Faber, M., Koehler, J. & Nishijima, K., Probability and Statistic in Civil Engineering: an introduction. 2011: CRC Press.
162. Dash, R., Selection Of The Best Classifier From Different Datasets Using WEKA. 2013.
163. Phyu, T.n., Survey of Classification Techniques in data Mining in Proceeding of the International multi confrence of engineers and Computer scientists. 2009, IMECS: Hong Kong. p. 1-5.
164. Uusitalo, L., Advantages and challenges of Bayesian networks in environmental modelling. Ecological Modelling, 2007. **203**(3-4): p. 312-318.
165. Yang, Y. and G.I. Webb, Discretization for naive-Bayes learning: managing discretization bias and variance. Machine Learning, 2009. **74**(1): p. 39-74.
166. P.Hart, T.C.a., Nearest neighbor pattern classification. In IEEE Transactions on Information theory, 1967. **13**(1): p. 21-27.
167. Wu, X., et al., Top 10 algorithms in data mining. Knowledge and Information Systems, 2008. **14**(1): p. 1-37.
168. Nitin Bhatia , V., Surve of nearest Neighbor techniques. (IJCSIS) International journal of Computer science and information security, 2010. **8**(2).
169. Teknomo, k. Strength and Weakness of k-Nearset neighbor. 2017 [cited 2020 06/02]; Available from: https://people.revoledu.com/kardi/tutorial/KNN/Strength%20and%20Weakness.htm.
170. Michael D. Twa, O., MS, FAAO, Srinivasan Parthasarathy, Automated Decision Tree Classification of Corneal Shape. NIH Public Access, 2005. **82**(12): p. 1038-1046.
171. J. -. R. Jang, ANFIS: adaptive-network-based fuzzy inference system,. in IEEE Transactions on Systems, Man, and Cybernetics, 1993. **23**(3): p. 665-685.
172. Olcay.T.Y, E.A., Univariate and Multivariate Decision Trees in TAINN. 2012, Department of Computer Engineering: Turkey.
173. G K, G.K. and S. Sukumaran, A study on classification techniques in data mining. 2013. 1-7.
174. Ramachandram, D.P.B.a.S., Decision Tree Induction An Approach for Data Classification Uning AVL-Tree. International Journal of Computer and Electrical Engineering, 2010. **2**(4): p. 1793-8163.
175. Sharma, S., et al., Machine learning techniques for data mining: A survey. 2013. 1-6.
176. Treceñe, J.K., Predicting Academic Performance of Information Technology Students using C4.5 Classification Algorithm: A Model Development. 2018.
177. Kalmegh, S., Analysis of WEKA Data Mining Algorithm REPTree, Simple Cart and RandomTree for Classification of Indian News. IJISET - International Journal of Innovative Science, Engineering & Technology, 2015. **2**(2): p. 438-446.
178. Novakovic, J., Using Information Gain Attribute Evaluation to Classify Sonar Targets, in 17th Telecommunications forum TELFOR 2009. 2009, Faculty of Computer Science, Megatrend University, Bulevar Umetnosti: Serbia,Belgrade.

179. Megha Aggarwal, A., Performance Analysis Of Different Feature selection methods in itrusion detection. International journal of scientific & technology research, 2013. **2**(6).

180. Howell, A.J. and H. Buxton, RBF Network Methods for Face Detection and Attentional Frames. Neural Processing Letters, 2002. **15**(3): p. 197-211.

181. Holte, R.C., Very Simple Classification Rules Perform Well on Most Commonly Used Datasets. Machine Learning, 1993. **11**(1): p. 63-90.

182. Beukelman, T. and H.I. Brunner, Chapter 6 - Trial Design, Measurement, and Analysis of Clinical Investigations, in Textbook of Pediatric Rheumatology (Seventh Edition), R.E. Petty, et al., Editors. 2016, W.B. Saunders: Philadelphia. p. 54-77.e2.

183. Kissell, R. and J. Poserina, Chapter 4 - Advanced Math and Statistics, in Optimal Sports Math, Statistics, and Fantasy, R. Kissell and J. Poserina, Editors. 2017, Academic Press. p. 103-135.

184. Hodhod, O.A. and H.I. Ahmed, Developing an artificial neural network model to evaluate chloride diffusivity in high performance concrete. HBRC Journal, 2013. **9**(1): p. 15-21.

185. Ukrainczyk, N.U.a.V., A neural network method for analysing cncrete durability. Magazine of Concrete Research, 2008. **60**(7): p. 475-486.

186. Ukrainczyk, N.B.P., Ivana ; Ukrainczyk, Velimir, Application of neural network in predicting damage of concrete structures caused by chlorides, in nternational Symposium "Durability and Maintenance of Concrete Structures, J.-Z.S.H. Durability and maintenance of concrete structures : proceedings of the International Symposium / Radić, 2004, 187-197, Editor. 2004: Cavtat, Hrvatska.

187. Marks, M., M.A. Glinicki, and K. Gibas, Prediction of the Chloride Resistance of Concrete Modified with High Calcium Fly Ash Using Machine Learning. Materials, 2015. **8**(12): p. 8714-8727.

188. Momeni, E., et al., Prediction of pile bearing capacity using a hybrid genetic algorithm-based ANN. Measurement, 2014. **57**: p. 122-131.

189. Chandwani, V., V. Agrawal, and R. Nagar, Modeling slump of ready mix concrete using genetic algorithms assisted training of Artificial Neural Networks. Expert Systems with Applications, 2015. **42**(2): p. 885-893.

190. Kirtikanta Sahoo, P.S., and Robin Davis P. , Artificial Neural Networks for Prediction of Compressive Strength of Recycled Aggregate Concrete. International Journal of Research in Chemical, Metallurgical and Civil Engineering, 2016. **3**(1).

191. Chopra, P., R.K. Sharma, and M. Kumar, Prediction of Compressive Strength of Concrete Using Artificial Neural Network and Genetic Programming. Advances in Materials Science and Engineering, 2016. **2016**: p. 1-10.

192. Güneyisi E, G.l.M., Özturan T and Özbay E, Estimation of chloride permeability of concretes by empirical modeling: considering effects of cement type,curing condition and age. Construction and Building Materials, 2009. **23**(1): p. 469-481.

193. Kong, L. and X. Chen, Influence mechanism of lightweight aggregate on concrete impermeability: prediction by ANN. Magazine of Concrete Research, 2015. **67**(1): p. 17-26.

194. Nikoo, M., Ł. Sadowski, and M. Nikoo, Prediction of the Corrosion Current Density in Reinforced Concrete Using a Self-Organizing Feature Map. Coatings, 2017. **7**(10).

195. Townes, C.H., The present Status of Microwave Spectroscopy. Annals of the New York Academy of Science, 1952. **55**(5): p. 745-751.

196. Lawson, B. Electromagnetic Radiation and Radio Waves. 2005 [cited 2020 20/08]; Available from: https://www.mpoweruk.com/radio.htm.

197. Elliott, R.S., Antenna theory & design. 2003. 1-587.

198. Frau, I., et al., Comparison of Electromagnetic Wave Sensors with Optical and Low-frequency Spectroscopy Methods for Real-time Monitoring of Lead Concentrations in Mine Water. Mine Water and the Environment, 2018. **37**(3): p. 617-624.

199. El-Mesery, H.S., H. Mao, and A.E. Abomohra, Applications of Non-destructive Technologies for Agricultural and Food Products Quality Inspection. Sensors (Basel), 2019. **19**(4).

200. A.R. CELIK , M.B.K.a.S.H., An Overview of Electromagnetic Methods for Breast Cancer Detection and A Novel Antenna Design for Microwave Imaging, in International Conference on Engineering Technologies (ICENTE'17), I. SARITAS, Editor. 2017, Selcuk University Faculty of Technology: Konya, Turkey. p. 377-383.

201. K H Joshi, A.M., A Shaw, O Korostynska, J D Cullen, A Al-Shamma'a, Online Monitoring of Milk Quality using electromagnetic waves sensors, in 2015 Ninth International Conference on Sensing Technology (ICST). 2015. p. 1-6.
202. Chiniforush, A.A., et al., Detecting the Presence of Chloride in Hardened Mortar Using Microwave Non-Destructive Testing, in High Tech Concrete: Where Technology and Engineering Meet. 2018. p. 83-90.
203. Procházka, M., et al., Microwave radiation and its application on construction materials. Engineering Structures and Technologies, 2016. **8**(4): p. 150-156.
204. Bavusi, M., et al., Electromagnetic Sensing Techniques for Non-Destructive Diagnosis of Civil Engineering Structures. 2012.
205. Wang, M.L. and G. Wang, Electromagnetic sensors for assessing and monitoring civil infrastructures. Sensor Technologies for Civil Infrastructures, 2014. **1**: p. 238-264.
206. Ahmed, H., H.M. La, and N. Gucunski, Review of Non-Destructive Civil Infrastructure Evaluation for Bridges: State-of-the-Art Robotic Platforms, Sensors and Algorithms. Sensors, 2020. **20**(14): p. 3954.
207. Teng, K.H., et al., Embedded Smart Antenna for Non-Destructive Testing and Evaluation (NDT&E) of Moisture Content and Deterioration in Concrete. Sensors (Basel), 2019. **19**(3).
208. Kot, P., et al., The application of electromagnetic waves in monitoring water infiltration on concrete flat roof: The case of Malaysia. Construction and Building Materials, 2016. **122**: p. 435-445.
209. P. Kot, M.M., A. Shaw, J. Hemingway, R. Deb, and M. Coleman, Identification of Optimal Frequencies to Determine Alpha-Cypermethrin using Machine Learning Feature Selection Techniques. in IEEE Congress on Evolutionary Computation (CEC),, 2018: p. 1-7.
210. Magomed Muradov, J.D.C., Andy Shaw, Olga Korostynska, Alex Mason ,Ahmed I. Al-Shamma'a,S. G. Bjarnadottir, and O. Alvseike,, Online non-destructive monitoring of meat drying using microwave spectroscopy, in in 2015 Ninth International Conference on Sensing Technology (ICST). 2015. p. 496-501.
211. Alex Mason, et al., Assessing Water Activity in Dry-Cured Ham using Microwave Spectroscopy. conference, 2014: p. 543-546.
212. Kwon, S. and S. Lee, Recent Advances in Microwave Imaging for Breast Cancer Detection. Int J Biomed Imaging, 2016. **2016**: p. 5054912.
213. GOH, J.H., Real time water pipes leak detection using electromagnetic waves for the water industry. Thesis, 2011: p. 178.
214. Jamil, M., et al., Concrete dielectric properties investigation using microwave nondestructive techniques. Materials and Structures, 2012. **46**(1-2): p. 77-87.
215. Jamil, M., et al., Concrete dielectric properties investigation using microwave nondestructive techniques. Materials and Structures, 2012. **46**.
216. Al-Mattarneh, H., et al., Measurement of dielectric constants and loss tangents of concrete in the frequency range 1-100 kHz. Proceedings First International Conference on Concrete and Development C and D 1, 2001: p. 539-548.
217. Shen, Y., C.L. Law, and W. Dou. Ultra-Wideband Measurement of the Dielectric Constant and Loss Tangent of Concrete Slabs. in 2008 China-Japan Joint Microwave Conference. 2008.
218. Polivka, J., An Overview of Microwave Sensor Technology. High Frequency Electronics, 2007.
219. Korostynska, O., A. Mason, and A. Al-Shamma, Microwave sensors for the non-invasive monitoring of industrial and medical applications. Sensor Review, 2014. **34**.
220. Buschmüller, C., et al., In-line monitoring of granule moisture in fluidized-bed dryers using microwave resonance technology. European Journal of Pharmaceutics and Biopharmaceutics, 2008. **69**(1): p. 380-387.
221. S. G. Bjarnadottira, K.L., O. Alvseikea, A. Masonb, A. I. Al-Shamma', Assessing Quality Parameters in Dry-1 Cured Ham using Microwave Spectroscopy. MEAT SCIENCE, 2015. **108**: p. 109-114.
222. al, W.p.D.W.e. Harmonic Electromagnetic Waves. 2019 [cited 2020 11/08]; Available from: https://phys.libretexts.org/Courses/University_of_California_Davis/UCD%3A_Physics_7C_-

_General_Physics/10%3A_Electromagnetism/10.4%3A_Electromagnetic_Waves%3A_Light/1._Harmonic_Electromagnetic_Waves.
223. D. H. Staelin, A. W. Morgenthaler, and J. A. Kong, "Electromagnetic Waves",. Prentice Hall International.
224. Kraus, J.D. and D. A. Fleisch, Electromagnetics with applications. 5th ed. 1999, McGraw-Hill,.
225. Mohammed Mejbel Salih, A.N.M.A.-h., The Effect of the Different Frequency on Skin Depth of GPR Detection. Journal of B abylon University/Engineering Sciences, 2017. **25**: p. 1-15.
226. knight, R.d., Physics for scientists and engineers, a strategic approach. 3rd ed. 2016, content technologies: James Smith. 1-1373.
227. M.Morey, R., Ground penetrating radar for evaluation subsurface conditions for transportation facilities. t. 1998, National Academy Press, Washington DC.
228. Villain, G., et al., Use of electromagnetic non-destructive techniques for monitoring water and chloride ingress into concrete. Near Surface Geophysics, 2015. **13**.
229. Al-Mattarneh, H., Determination of chloride content in concrete using near- and far-field microwave non-destructive methods. Corrosion Science, 2016. **105**: p. 133-140.
230. Savin, A.S., R.; Bruma, A.; Šturm, R., An electromagnetic sensor with a metamaterial lens for nondestructive evaluation of composite materials. Sensors (Basel), 2015. **15**(7): p. 15903-15920.
231. Yi Huang and K. Boyle, Antennas: From Theory to Practice. 2008, John Welly & Sons Ltd.
232. A. Laskarakis, S.L., In-line monitoring and quality control of flexible organic electronic materials, in Handbook of Flexible Organic Electronics,Materials, Manufacturing and Applications. 2015, Aristotle University of Thessaloniki: , Thessaloniki, Greece. p. 227-251.
233. VSWR. Antenna Theory. 2017; Available from: http://www.antenna-theory.com/definitions/vswr.php.
234. J.J.Carr, Practical Antenna Handbook. 4th Edition ed. 2001: McGraw-Hill.
235. Vijayakumar, K., et al., Non invasive rail track detection system using microwave sensor. Journal of Physics: Conference Series, 2009. **178**: p. 012033.
236. Balanis, C.A., Antenna Theory Analysis And Design. Wiley Interscience, 2005: p. 1-7.
237. Bhanarkar, M., G. Waghmare, and V. Navarkhele, Analysis of Pyramidal Horn Antenna for J-Band Application. 2016, Preprints.org.
238. Jamali, A.A. and R. Marklein, Design and optimization of ultra-wideband TEM horn antennas for GPR applications, in 2011 XXXth URSI General Assembly and Scientific Symposium. 2011. p. 1-4.
239. Balanis, C.A., Antenna. Theory. Analysis.and. Design(3rd. Edition). 2015, Canada: Hoboken, NJ:Wiley-Interscience.
240. NagarjunaTelagam, N.P.G., Nehru Kandasamy Design of substrate integrated microwave horn antenna with constant aperture distribution. IJEE, 2016. **8**: p. 5-12.
241. C.Johnson, R., Antenna Engineering handbook. Second Edition ed, ed. H. Jasik. 1984, New York; London: McGraw-Hill Inc., US.
242. Baltzis, K.B., Polynomial-Based Evaluation of the Impact of Aperture Phase Taper on the Gain of Rectangular Horns. Journal of Electromagnetic Analysis and Applications, 2010. **Vol.02No.07**: p. 7.
243. Kilby's, J. Microwave Horn Antenna Theory. The basic theory and equations or formulas behind the horn antenna provide a view of how they work and how to get the best from them. 2020 [cited 2020 08]; Available from: https://www.electronics-notes.com/articles/antennas-propagation/horn-antenna/theory-equations.php#:~:text=The%20horn%20antenna%20is%20essentially,two%20shapes%3A%20rectangular%20or%20circular.&text=Waveguide%20theory%20indicates%20that%20there,can%20occur%20within%20a%20waveguide.
244. Dick Comly, Parabolic antennas and their feeds. p. 9.
245. Wade, P. OPtimized Dual-mode Feedhorns. 2006 [cited 2020 08]; Available from: http://www.w1ghz.org/antbook/conf/optimized_dualmode_feedhorns.pdf.
246. LIAO, S.Y., microwave-devices-and-circuits. Professor of Electrical Engineering California state University, Fresno, 1990: p. 545.

247. Lanre Daniyan, N.E., Justus Chukwunonyerem, Horn antenna design: The concepts and considerations International Journal of Emerging Technology and Advanced Engineering 2014. **4**(5): p. 4.
248. James Baker-Jarvis, R.G.G., John H. Grosvenor, Jr., Michael D. Janezic, Chriss A. Jones, Bill Riddle, Claude M. Weil Dielectric Characterization of Low-loss Materials A Comparison of Techniques. IEEE Transactions on Dielectrics and Electrical Insulation, 1998. **5**(4): p. 571-577.
249. A. M. Nicolson, M., Ieee, And G. F. Ross, Measurement of the Intrinsic Properties of materilas by time-domain Techniques. IEEE Transsactions On Instrumentation And Measurement, 1970. **19**(4): p. 377-382.
250. James Baker-Jarvis, M., Eee, Eric J. Vanzura And William A. Kissick, Improved Technique for Determining Complex Permitivity with the transmission and reflection Method. IEEE Transaction on Microwave Theory and Techniques, 1990. **38**(8): p. 1096-103.
251. Aksun, M.I. Introduction to Rectangular Waveguides. 2011 [cited 2020 08]; Available from: http://kilyos.ee.bilkent.edu.tr/~microwave/programs/magnetic/rect/info.htm.
252. Swillam, M.A. and A.S. Helmy. Characteristics and applications of rectangular waveguide in sensing, slow light, and negative refraction. 2011.
253. Kot, P., et al., The Feasibility of Electromagnetic waves in determining the moisture content of the concrete. 2014: p. 5.
254. Bishop, C.M., Pattern Recognition And Machine Learning Springer, ed. t. editer. 2006, New York,NY,USA: Springer.
255. 1881-208, B.-B., Testing concrete — Part 208: Recommendations for the determination of the initial surface absorption of concrete. 1996.
256. Adámek, J. and V. Juránková, Evaluation of durability of concrete by measurement of permeability for air and water. 10th International Conference Modern Building Materials, Structures and Techniques, 2010.
257. Kucharczyková, B., P. Misák, and T. Vymazal, Determination and evaluation of the air permeability coefficient using Torrent Permeability Tester. Russian Journal of Nondestructive Testing, 2010. **46**: p. 226-233.
258. Aquino Carlos , I.M., Miura Hiroaki, Mizuta Maki, Okamoto Takahisa, The effects of limestone aggregate on concrete properties. Construction and Building Materials, 2010. **24**: p. 2363-2368.
259. Liu, H., et al., Experimental Investigation of the Mechanical and Durability Properties of Crumb Rubber Concrete. Materials, 2016. **9**(3): p. 172.
260. Baker-Jarvis, J., 'Transmission,Reflection and Short-Circuit Line Permittivity Measurmentts' National Institute ofStandards and Technology, Boulder, Colorado,1990: P. 3303-3328

261. Shah, M.A., Hasted J.B., and Moore, L, Microwave absorption by water in building materials: aerated concrete”. British Journal of Physics, 1965. **16**: p. 1747-1754.
262. Jr, D.M., The measurement of the dielectric constant of three different shapes of concrete blocks. IJRRAS, 2015. **25**(3): p. 82-102.
263. Neville, A., Chloride attack of reinforced concrete: an overview. 1995. **28**: p. 63-70.
264. Richard Sauerheber and B. Heinz, Temperature Effects on Conductivity of Seawater and Physiologic Saline, Mechanism and Significance. Chemical Sciences Journal, 2016.
265. Kot, P., et al., The Feasibility of Using Electromagnetic Waves in Determining Membrane Failure Through Concrete. International Journal of Civil Engineering, 2016. **15**(2): p. 355-362.
266. Nguyen-Truong, H.T.L., H. M, An Implementation of the Levenberg–Marquardt Algorithm Forsimultaneous-Energy-Gradient Fitting Using Two-Layer Feed Forwardneural Networks. Chemical Physics Letters, 2015. **629**: p. 40-46.
267. Yadav, A.K., H. Malik, and S.S. Chandel, Selection of most relevant input parameters using WEKA for artificial neural network based solar radiation prediction models. Renewable and Sustainable Energy Reviews, 2014. **31**: p. 509-519.
268. Deo, R.C. and M. Şahin, Application of the extreme learning machine algorithm for the prediction of monthly Effective Drought Index in eastern Australia. Atmospheric Research, 2015. **153**: p. 512-525.
269. SA, P. Permeability Tester. 2017 [cited 2021 09]; Available from: https://www.abbeyspares.co.uk/pdf/new/Torrent_Sales%20Flyer_English_high.pdf.

270. Che, X., et al. A Static Multi-hop Underwater Wireless Sensor Network Using RF Electromagnetic Communications. in 2009 29th IEEE International Conference on Distributed Computing Systems Workshops. 2009.
271. Rhodes, M. Electromagnetic Propagation in Sea Water and its value in Military Systems. 2007.
272. Singh, K., Y. Kumar, and S. Singh. A modified bow tie antenna with U-shape slot for Wireless applications. 2012.
273. Karagianni, E.A., Electromagnetic Waves under Sea: Bow-Tie Antenna Design for Wi-Fi Underwater Communications. Progress In Electromagnetics Research M, 2015. **41**: p. 189-198.
274. A.M.Neville, properties-of-concrete. 5th Edition ed. 2003. 2866.
275. Hong, K., Cyclic Wetting and Drying and its Effects on Chloride Ingress in Concrete in Department of Civil Engineering. 1998, Toronto University of Toronto p. 123.
276. Monteiro, P.K.M.a.P.J.M., Concrete: Microstructure, Properties and Materials. McGraw-Hill. 2006, University of California at Berkeley: The McGraw-Hill Companies, Inc. 684.
277. Zhang, S.P. and L. Zong, Evaluation of Relationship between Water Absorption and Durability of Concrete Materials. Advances in Materials Science and Engineering, 2014. **2014**: p. 1-8.
278. ITTC. Fresh water and Seawater properties. 2011 [cited 2019 25/02]; Available from: https://ittc.info/media/4048/75-02-01-03.pdf.
279. Wojtusiak, J., Machine Learning and Inference Laboratory, in AQ21 User's Guide., T.R.M. 04-3;, Editor. 2004: George Mason University: Fairfax, VA, USA,.
280. SALZBERG, S.L., C4.5: Programs for Machine Learning. Morgan Kaufmann Series in Machine Learning;, ed. J.R. Quinlan. 1993, San Francisco,CA,USA: Morgan Kaufmann.
281. Ian H witten, E.F.M.A.H.C.J.P., The Weka Workbench., F. Edition, Editor. 2016, Morgan Koufmann. p. 128.
282. Ukrainczyk, N. and V. Ukrainczyk, A neural network method for analysing concrete durability. Magazine of Concrete Research, 2008. **60**(7): p. 475-486.
283. Najigivi, A., et al., An Artificial Neural Networks Model for Predicting Permeability Properties of Nano Silica–Rice Husk Ash Ternary Blended Concrete. International Journal of Concrete Structures and Materials, 2013. **7**(3): p. 225-238.
284. Gang Sun, S.J.H., Brian C. Zelle,Minda A. Smith, Development and Comparison of Backpropagation and Generalized Regression Neural Network Models to Predict Diurnal and Seasonal Gas and PM 10 Concentrations and Emissions from Swine Buildings. Agricultral and Biosystems Engineering Publicatins, 2008. **51**(2): p. 685-694.
285. Shafi, I., et al., Impact of Varying Neurons and Hidden Layers in Neural Network Architecture for a Time Frequency Application. 2007. 188-193.
286. Inc, R. Total Chloride Amounts From Concrete-Making Ingredients. [cited 2019 03/10]; Available from: https://www.russtechnet.com/uploads/product-notes/chloride-ion-calculation.pdf.
287. Bertolini L., et al., Corrosion of steel in concrete-Prevention Diagnosis Repair. 2004.
288. Glass G.K. and B. N.R., The influence of chloride binding on the chloride induced corrosion risk in reinforced concrete. Corrossion Science, 2000. **42**(2): p. 329-344.
289. McDonald, H., Concrete – Complementary British Standard to BS EN 206-1. Transport Scotland, 2015. **23**: p. 1-13.
290. BSI, BS 8500-1: Concrete–Complementary British Standard to BS EN 206-1–Part 1: Method of Specifying and Guidance for the Specifier. 2006, BSI Milton Keynes, UK.
291. Glass, G.K. and N.R. Buenfeld, The presentation of the chloride threshold level for corrosion of steel in concrete. Corrosion Science, 1997. **39**(5): p. 1001-1013.
292. Manera, M., Ø. Vennesland, and L. Bertolini, Chloride threshold for rebar corrosion in concrete with addition of silica fume. Corrosion Science, 2008. **50**(2): p. 554-560.

Appendices

Appendix A: % MATLAB code was used to run the LM method for all ANN produced models, including the optimal number of hidden layers and the data division process for each sub-set.

```
.% Solve an Input-Output Fitting problem with a Neural Network
% Script generated by Neural Fitting app
% Created 08-Jul-2019 18:53:15
%
% This script assumes these variables are defined:
%
%   data - input data.
%   data_1 - target data.

x = data';
t = data_1';

% Choose a Training Function
% For a list of all training functions type: help nntrain
% 'trainlm' is usually fastest.
% 'trainbr' takes longer but may be better for challenging problems.
% 'trainscg' uses less memory. Suitable in low memory situations.
trainFcn = 'trainlm';  % Levenberg-Marquardt backpropagation.

% Create a Fitting Network
hiddenLayerSize = 10;
net = fitnet(hiddenLayerSize,trainFcn);

% Choose Input and Output Pre/Post-Processing Functions
% For a list of all processing functions type: help nnprocess
net.input.processFcns = ('removeconstantrows','mapminmax');
net.output.processFcns = ('removeconstantrows','mapminmax');

% Setup Division of Data for Training, Validation, Testing
% For a list of all data division functions type: help nndivision
net.divideFcn = 'dividerand';  % Divide data randomly
net.divideMode = 'sample';  % Divide up every sample
net.divideParam.trainRatio = 70/100;
net.divideParam.valRatio = 15/100;
net.divideParam.testRatio = 15/100;

% Choose a Performance Function
% For a list of all performance functions type: help nnperformance
net.performFcn = 'mse';  % Mean Squared Error

% Choose Plot Functions
% For a list of all plot functions type: help nnplot
net.plotFcns = {'plotperform','plottrainstate','ploterrhist', ...
```

```
    'plotregression', 'plotfit'};

% Train the Network
[net,tr] = train(net,x,t);

% Test the Network
y = net(x);
e = gsubtract(t,y);
performance = perform(net,t,y)

% Recalculate Training, Validation and Test Performance
trainTargets = t .* tr.trainMask{1};
valTargets = t .* tr.valMask{1};
testTargets = t .* tr.testMask{1};
trainPerformance = perform(net,trainTargets,y)
valPerformance = perform(net,valTargets,y)
testPerformance = perform(net,testTargets,y)

% View the Network
view(net)

% Plots
% Uncomment these lines to enable various plots.
%figure, plotperform(tr)
%figure, plottrainstate(tr)
%figure, ploterrhist(e)
%figure, plotregression(t,y)
%figure, plotfit(net,x,t)

% Deployment
% Change the (false) values to (true) to enable the following code blocks.
% See the help for each generation function for more information.
if (false)
    % Generate MATLAB function for neural network for application
    % deployment in MATLAB scripts or with MATLAB Compiler and Builder
    % tools, or simply to examine the calculations your trained neural
    % network performs.
    genFunction(net,'myNeuralNetworkFunction');
    y = myNeuralNetworkFunction(x);
end
if (false)
    % Generate a matrix-only MATLAB function for neural network code
    % generation with MATLAB Coder tools.
    genFunction(net,'myNeuralNetworkFunction','MatrixOnly','yes');
    y = myNeuralNetworkFunction(x);
end
if (false)
    % Generate a Simulink diagram for simulation or deployment with.
    % Simulink Coder tools.
    gensim(net); end
```

Appendix B: A MATLAB Neural Network Function, comprising optimum connection weights and magnitude data values for five different salt water concentrations per weight of cement model trained, validated, and tested and targeted to three different depths.

```
 % Solve an Input-Output Fitting problem with a Neural Network
% Script generated by Neural Fitting app
% Created 08-Jul-2019 22:52:49
%
% This script assumes these variables are defined:
%
%   data - input data.
%   data_2 - target data.

x = data';
t = data_2';

% Choose a Training Function
% For a list of all training functions type: help nntrain
% 'trainlm' is usually fastest.
% 'trainbr' takes longer but may be better for challenging problems.
% 'trainscg' uses less memory. Suitable in low memory situations.
trainFcn = 'trainlm';  % Levenberg-Marquardt backpropagation.

% Create a Fitting Network
hiddenLayerSize = 10;
net = fitnet(hiddenLayerSize,trainFcn);

% Choose Input and Output Pre/Post-Processing Functions
% For a list of all processing functions type: help nnprocess
net.input.processFcns = {'removeconstantrows','mapminmax'};
net.output.processFcns = {'removeconstantrows','mapminmax'};

% Setup Division of Data for Training, Validation, Testing
% For a list of all data division functions type: help nndivision
net.divideFcn = 'dividerand';  % Divide data randomly
net.divideMode = 'sample';  % Divide up every sample
net.divideParam.trainRatio = 70/100;
net.divideParam.valRatio = 15/100;
net.divideParam.testRatio = 15/100;

% Choose a Performance Function
% For a list of all performance functions type: help nnperformance
net.performFcn = 'mse';  % Mean Squared Error

% Choose Plot Functions
% For a list of all plot functions type: help nnplot
net.plotFcns = {'plotperform','plottrainstate','ploterrhist', ...
    'plotregression', 'plotfit'};
```

```matlab
% Train the Network
[net,tr] = train(net,x,t);

% Test the Network
y = net(x);
e = gsubtract(t,y);
performance = perform(net,t,y)

% Recalculate Training, Validation and Test Performance
trainTargets = t .* tr.trainMask{1};
valTargets = t .* tr.valMask{1};
testTargets = t .* tr.testMask{1};
trainPerformance = perform(net,trainTargets,y)
valPerformance = perform(net,valTargets,y)
testPerformance = perform(net,testTargets,y)

% View the Network
view(net)

% Plots
% Uncomment these lines to enable various plots.
%figure, plotperform(tr)
%figure, plottrainstate(tr)
%figure, ploterrhist(e)
%figure, plotregression(t,y)
%figure, plotfit(net,x,t)

% Deployment
% Change the (false) values to (true) to enable the following code blocks.
% See the help for each generation function for more information.
if (false)
    % Generate MATLAB function for neural network for application
    % deployment in MATLAB scripts or with MATLAB Compiler and Builder
    % tools, or simply to examine the calculations your trained neural
    % network performs.
    genFunction(net,'myNeuralNetworkFunction');
    y = myNeuralNetworkFunction(x);
end
if (false)
    % Generate a matrix-only MATLAB function for neural network code
    % generation with MATLAB Coder tools.
    genFunction(net,'myNeuralNetworkFunction','MatrixOnly','yes');
    y = myNeuralNetworkFunction(x);
end
if (false)
    % Generate a Simulink diagram for simulation or deployment with.
    % Simulink Coder tools.
    gensim(net); end
```

Appendix C: Determinate the value of mean square error statistic and Value of Coefficient of Determination statistic between the actual values and the validated values obtained from the ANN trained per weight of cement.

```
n=length(obs);
format long
B = (sum(pred - obs))/n;
NAE = (sum(abs(pred - obs)))/(sum(obs));
pbar = mean(pred)
obar = mean(obs)
stddevpbar = std(pred)
stddevobar = std(obs)
p2 = pred-pbar
obs2 = obs-obar
numPA = p2'*obs2
denoPA = (n-1)*stddevpbar*stddevobar';
PA = numPA/denoPA
numer = (pred - pbar)'*(obs - obar);
denor = stddevpbar*stddevobar';
RSQ = (numer/(n*denor))^2;
SSR = (pred - obar)'*(pred - obar)
SSE = (obs - pred)'*(obs - pred)
SST = SSR + SSE
RSQ1 = SSR/SST
RMSE1 = (pred - obs)'*(pred - obs);
RMSE2 = sum(RMSE1);
RMSE3 = RMSE2/(n-1);
RMSE = sqrt(RMSE3);
numd = (pred-obs)'*(pred-obs);
deno1d = abs(pred-obar);
deno2d = abs(obs-obar);
sumdeno3d = deno1d + deno2d;
sqsumdeno4d = sumdeno3d'*sumdeno3d;
IA = 1-(numd/sqsumdeno4d);


fprintf('Value of Normalised Absolute Error statistic is %f \n',NAE)
fprintf('Value of Root Mean Square Error statistic is %f \n',RMSE)
fprintf('Value of Index of Agreement statistic is %f\n',IA)
fprintf('Value of Prediction Accuracy statistic is %f \n',PA)
fprintf('Value of Coefficient of Determination statistic is %f \n',RSQ),
```

Appendix D:

(a) The raw data from the concrete sample experiment with single rebar.

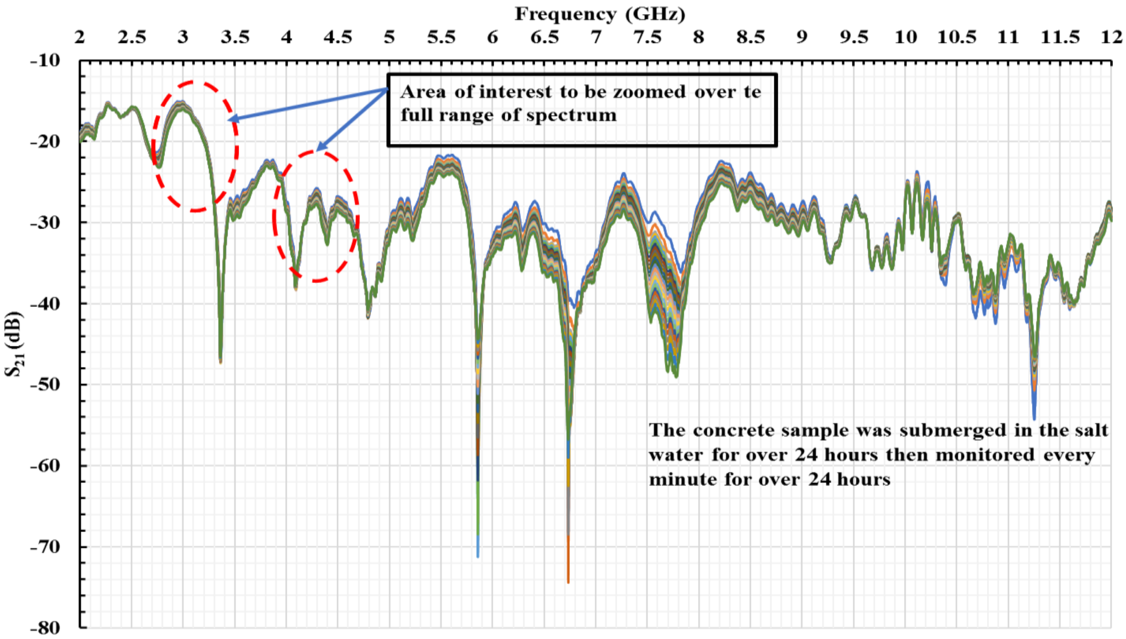

Area of interest to be zoomed over te full range of spectrum

The concrete sample was submerged in the salt water for over 24 hours then monitored every minute for over 24 hours

Figure 7.2: Transmitted power S_{21} measurements using microwave sensor were taken everyone minute in the frequency range (2-12 GHz), Saltwater

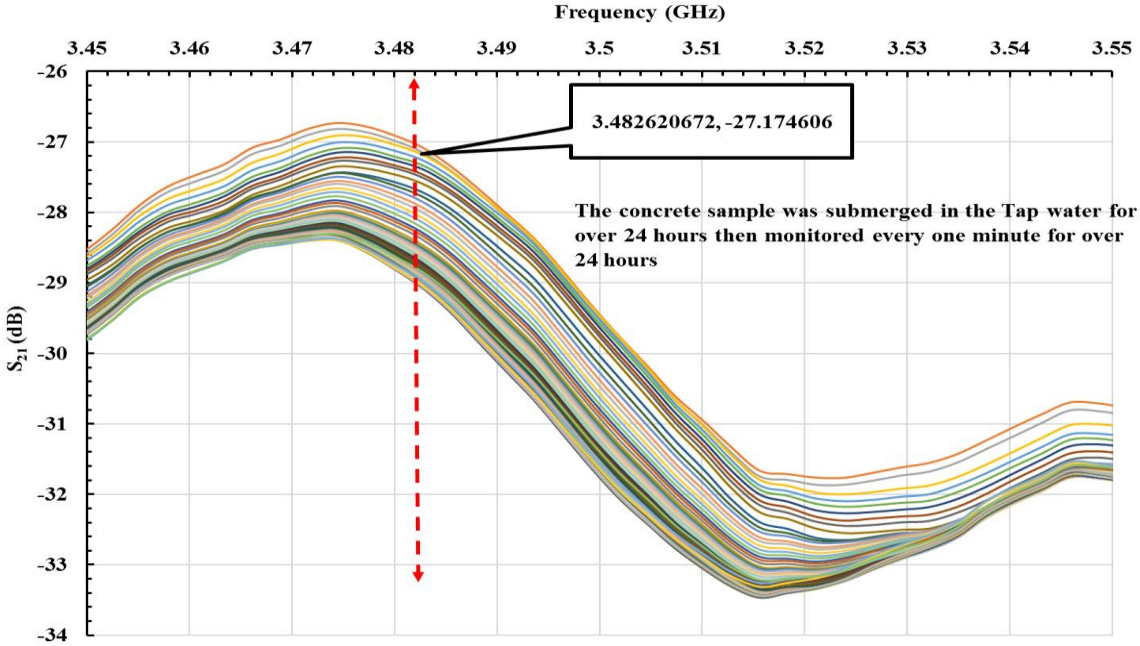

The concrete sample was submerged in the Tap water for over 24 hours then monitored every one minute for over 24 hours

Figure 7.1: Transmitted power S_{21} measurements response from the concrete using microwave sensor were taken per minute for the full range of frequencies, (2-12 GHz), but for clarity data from every hour interval and 3.45-3.55 GHz are presented (Saltwater)

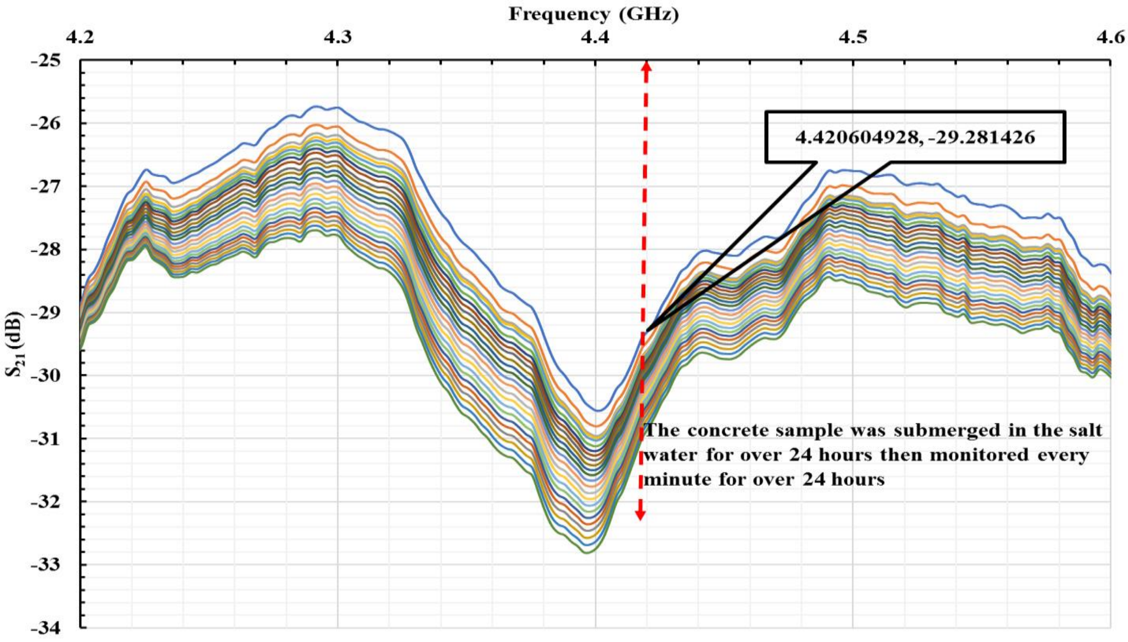

Figure 7.4: Transmitted power S_{21} measurements using microwave sensor were taken per minute for the full range of frequencies, (2-12 GHz), but for clarity data measurements from every hour intervals and 4.2-4.6 GHz are presented (Saltwater)

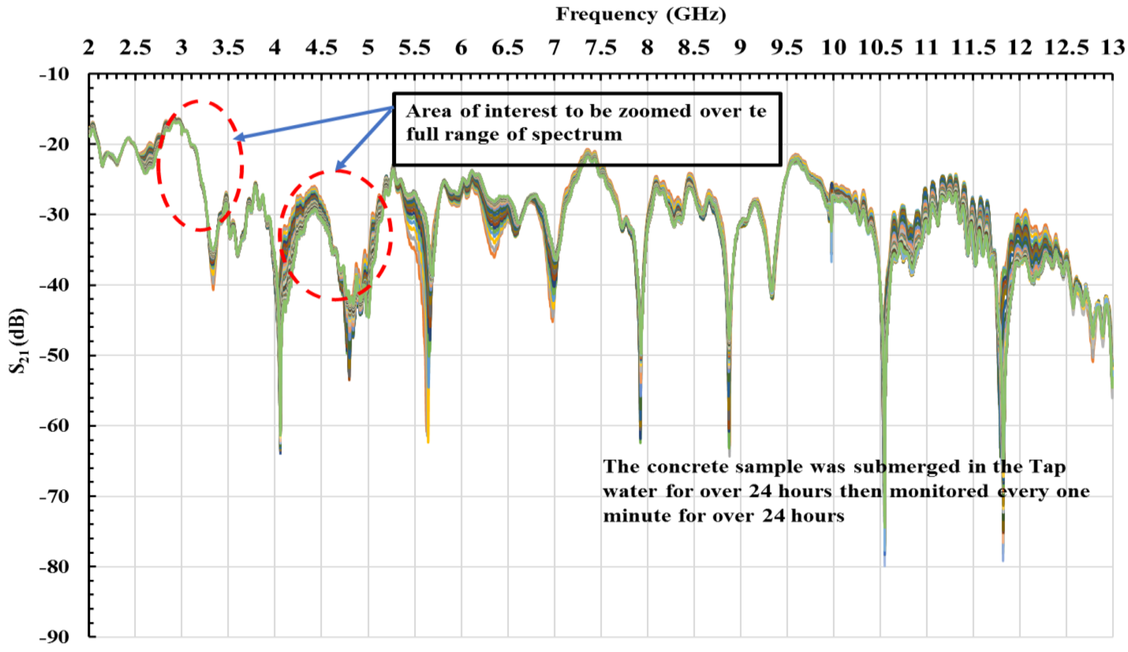

Figure 7.3*:* Microwave sensor measurements were taken every one minute in the frequency range (2-12 GHz), Tap water

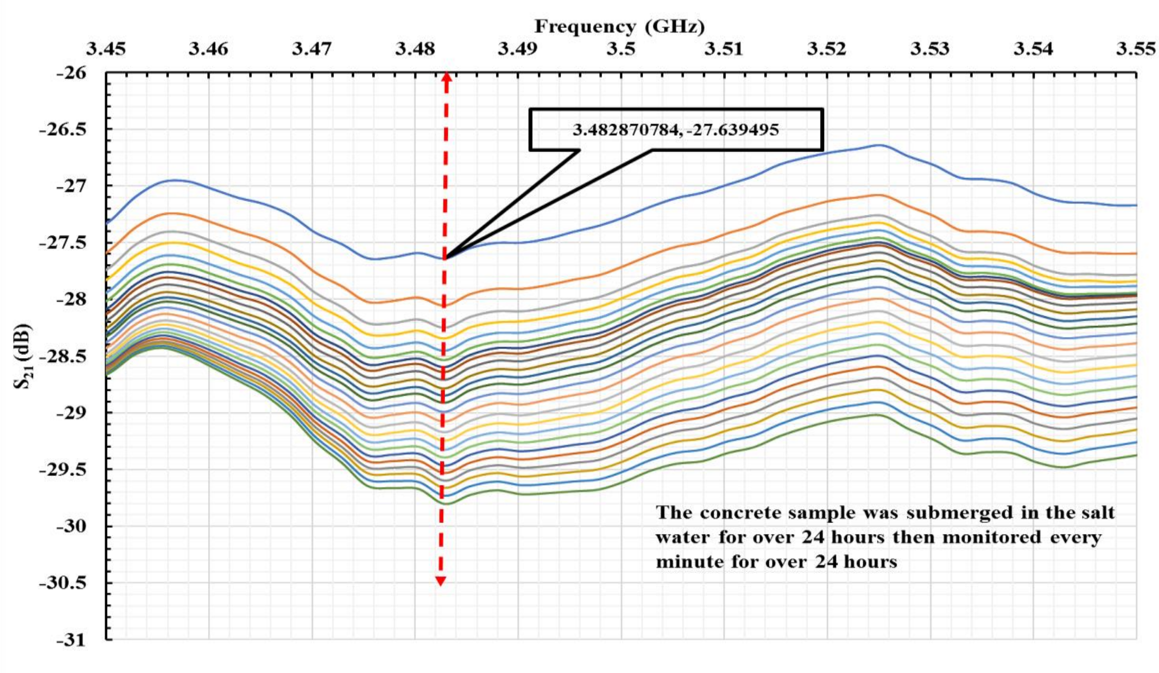

Figure 7.5: Transmitted power S_{21} measurements were taken per minute for the full range of frequencies, (2-12 GHz), but for clarity data measurements from every hour intervals and 3.45-3.55 GHz are presented (Tap water)

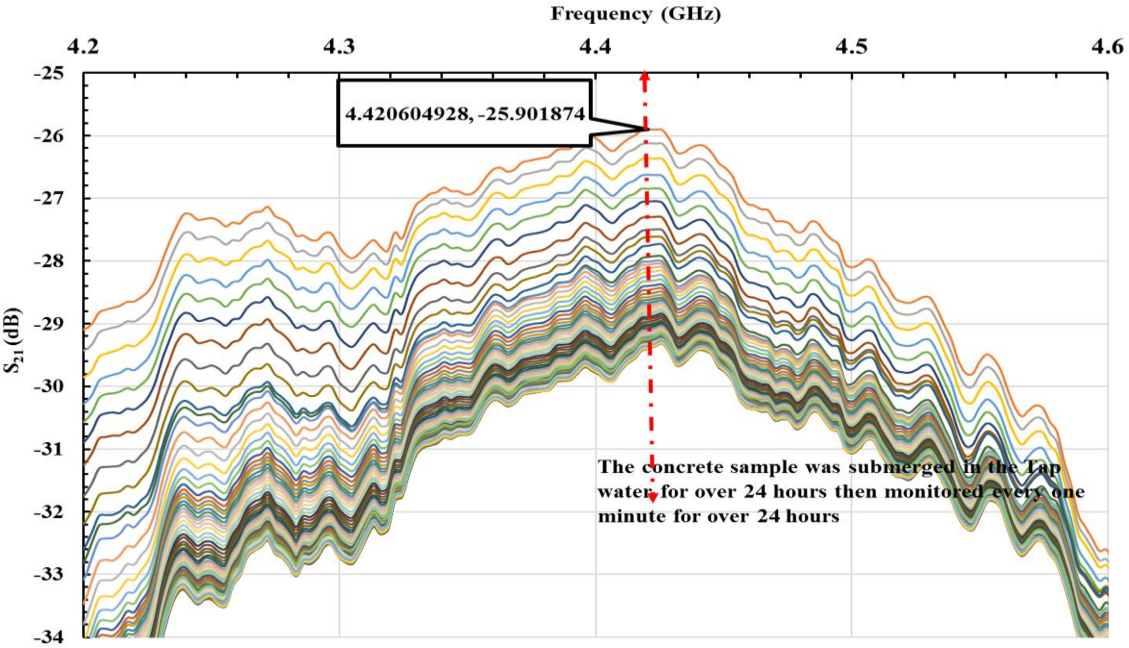

Figure 7.6: Transmitted power S_{21} measurements using microwave were taken per minute for the full range of frequencies, (2-12 GHz), but for clarity data from every hour intervals and 4.2-4.6 GHz are presented (Tap water)

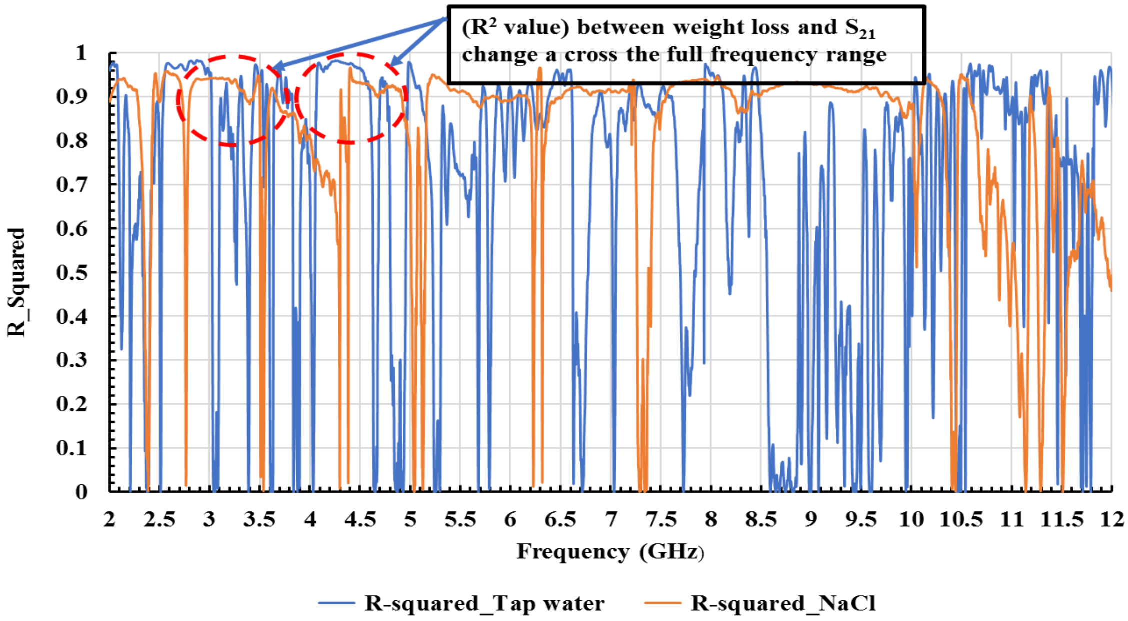

Figure 7.8: R^2 between both concrete sample weight loss and S_{21} change across the full frequency spectrum

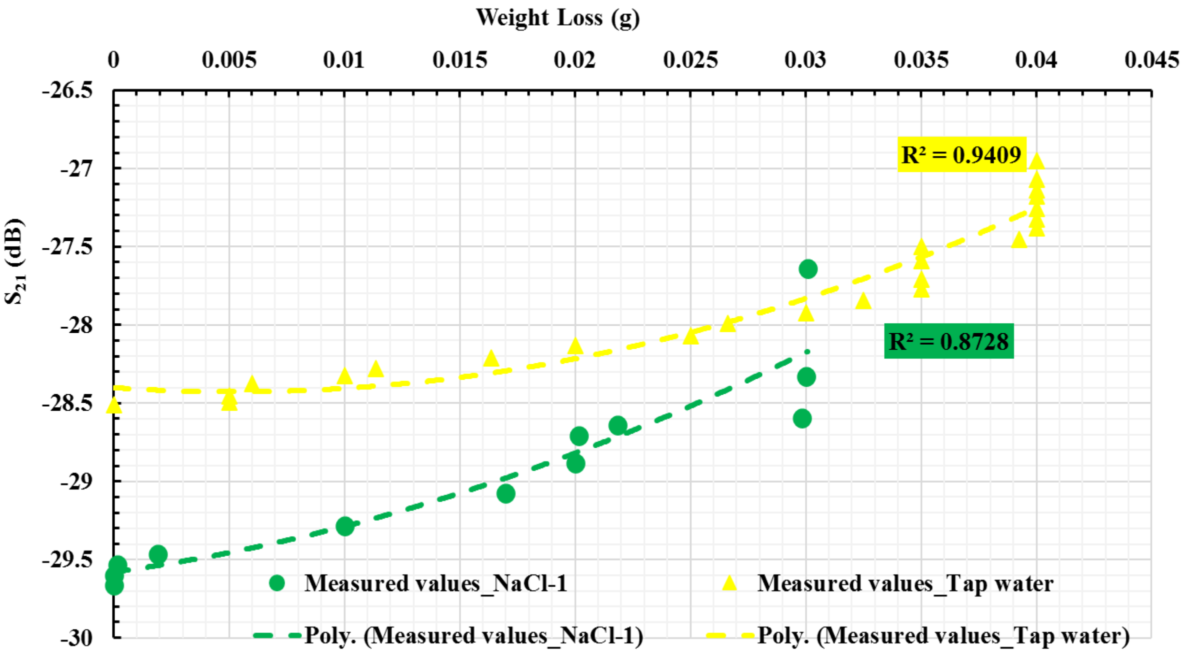

Figure 7.7: Polynomial correlation coefficient best fit between weight loss and S_{21} change at 3.482GHz, with R^2 =0.87, for saltwater sample and R^2=0.94 for tap water sample

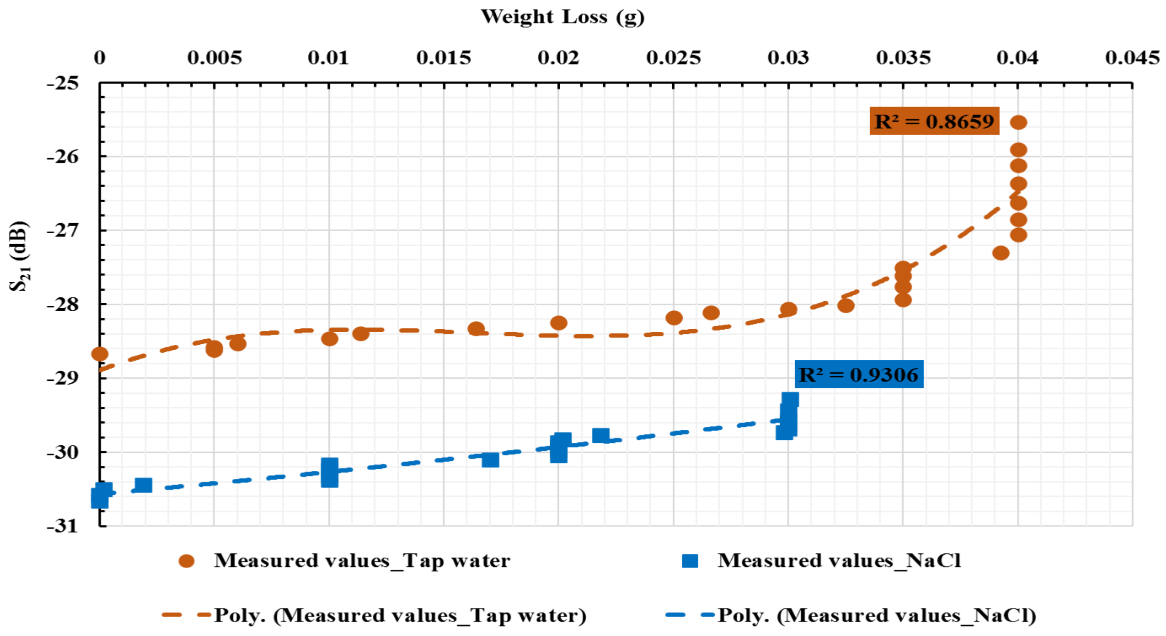

Figure 7.9: Polynomial correlation coefficient best fit between weight loss and S_{21} change at 4.42GHz, with R^2 =0.93, for salt water sample and R^2=0.86 for tap water sample

(b) The raw data from the concrete sample experiment with crossing rebars.

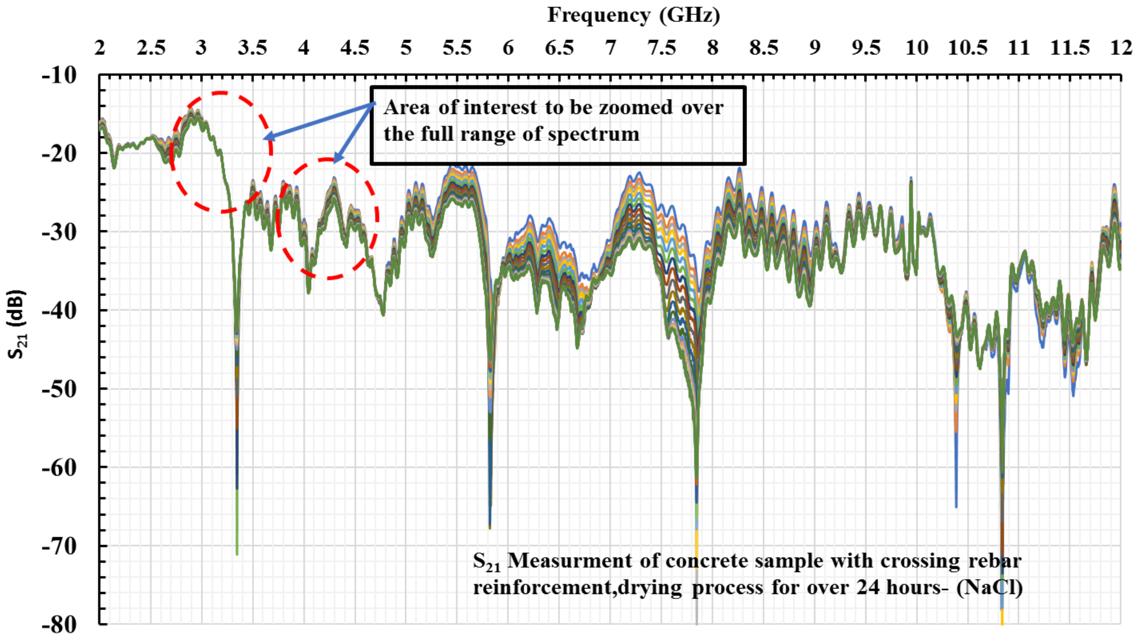

Figure 7.10: Transmitted power S_{21} using microwave sensor measurements were taken every one minute in the frequency range (2-12 GHz), Saltwater

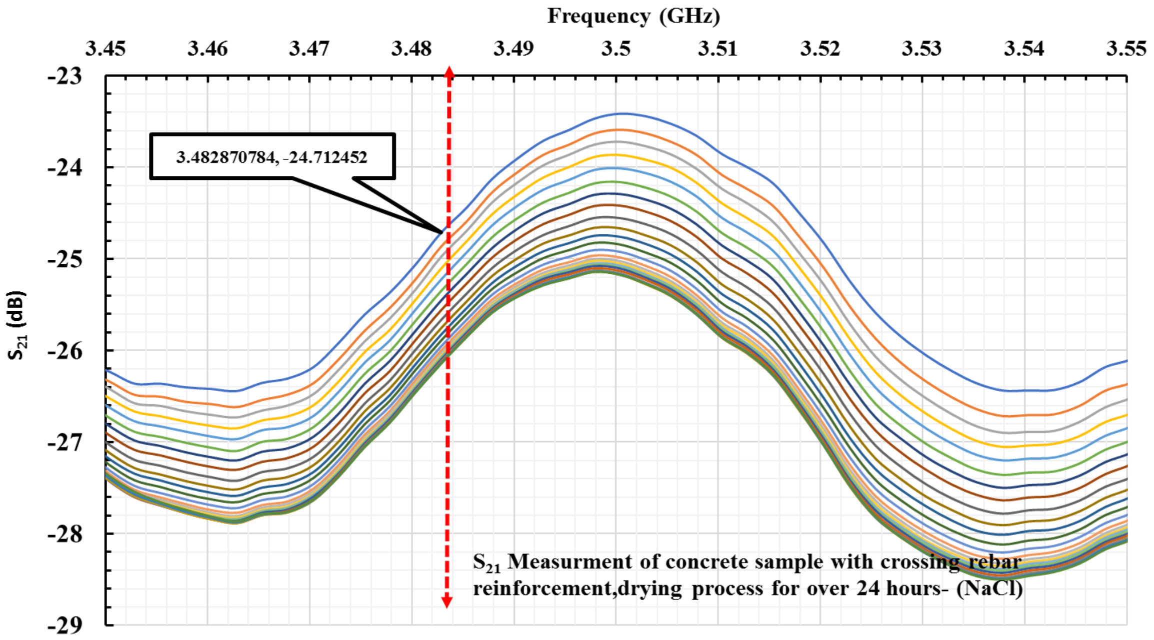

Figure 7.11: Transmitted power S_{21} measurements using microwave were taken per minute for the full range of frequencies, (2-12 GHz), but for clarity data from every hour intervals and 3.45-3.55GHz are presented (NaCl)

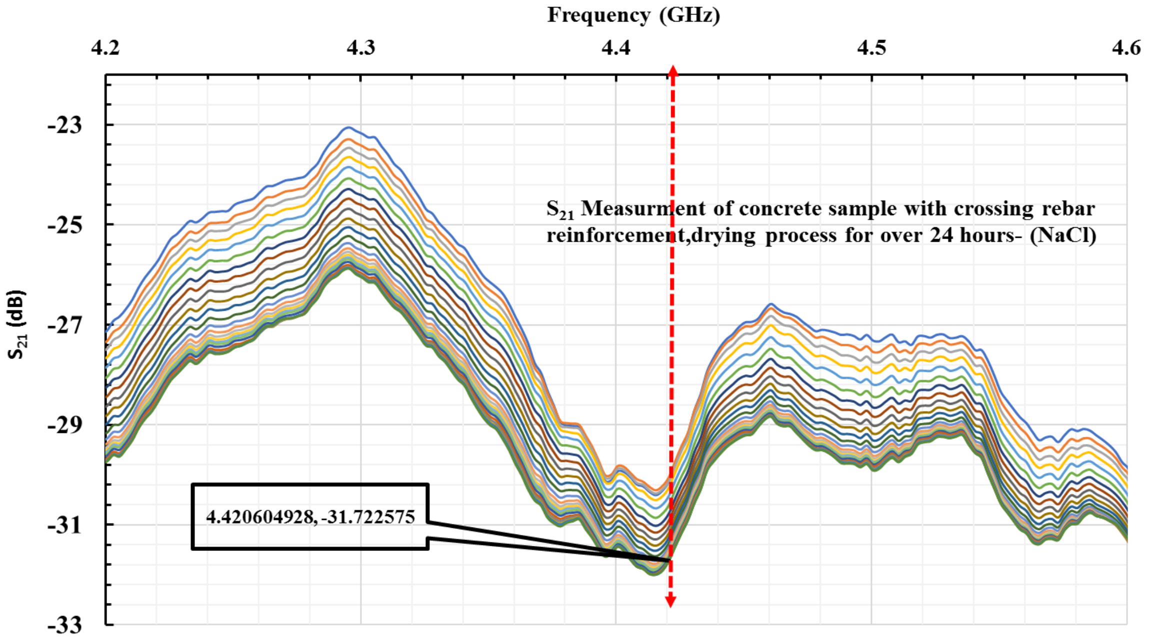

Figure 7.12: Transmitted power S_{21} measurements using microwave were taken per minute for the full range of frequencies (2-12 GHz), but for clarity, data measurements from every hour intervals and 4.2-4.6 GHz are presented (NaCl)

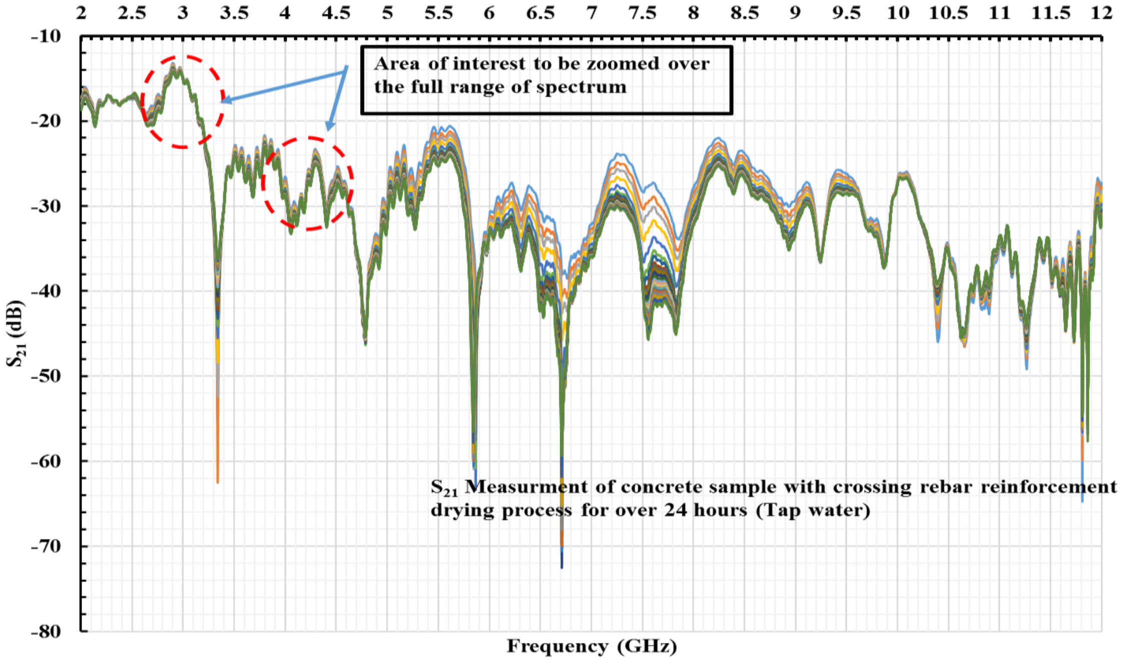

Figure 7.13: The electromagnetic wave sensor: S_{21} Measurement were taken every one minute in the frequency range (2-12 GHz), Tap water

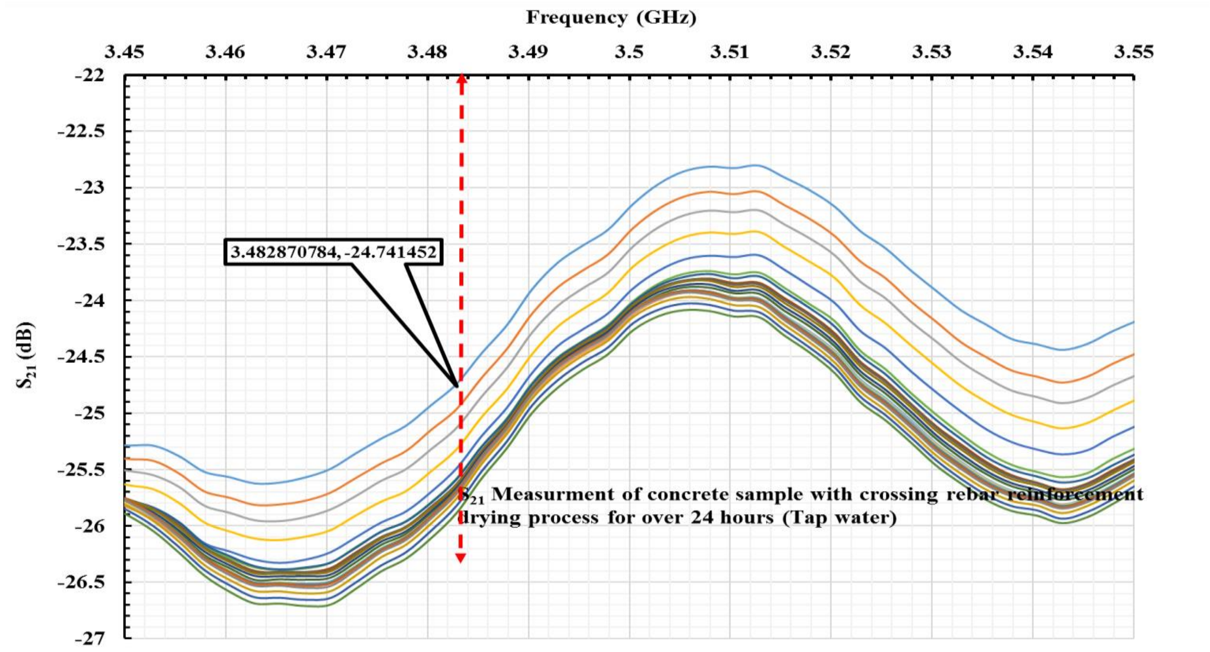

Figure 7.14: Transmitted power S_{21} measurements using microwave were taken per minute for the full range of frequencies, (2-12 GHz), but for clarity data measuments from every hour intervals and 3.45-3.55 GHz are presented (Tap water)

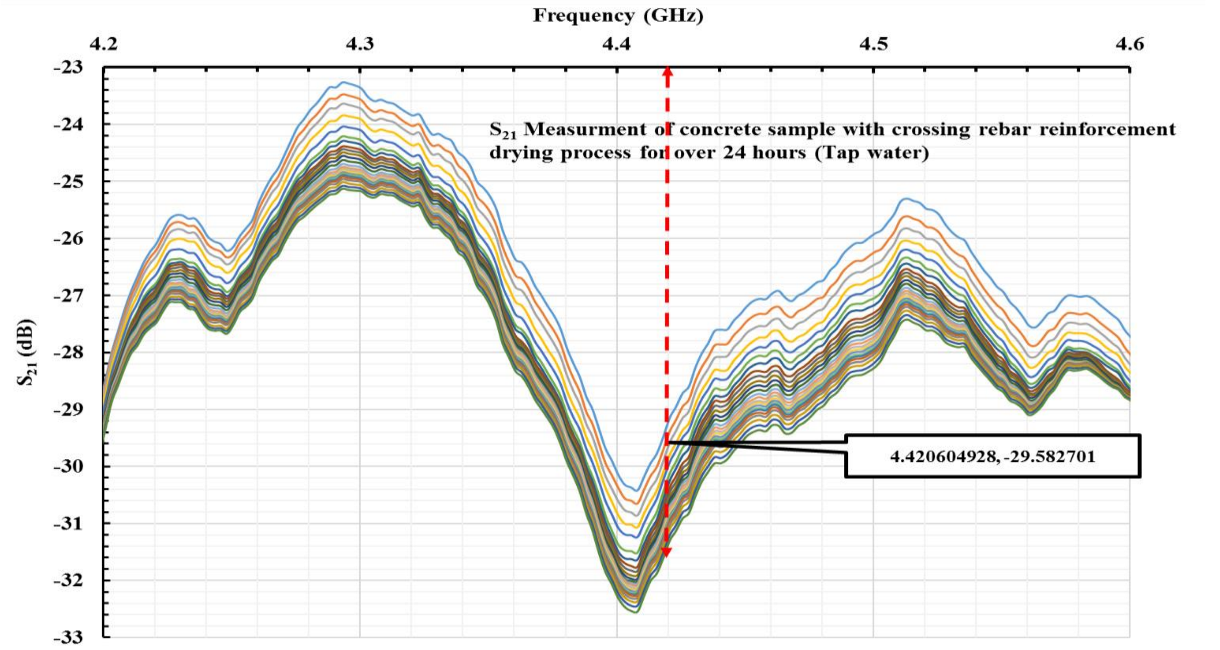

Figure 7.15: Transmitted power S_{21} measurements using microwave were taken per minute for the full range of frequencies, (2-12 GHz), but for clarity data measurements from every hour intervals and 4.2-4.6 GHz are presented (Tap water)

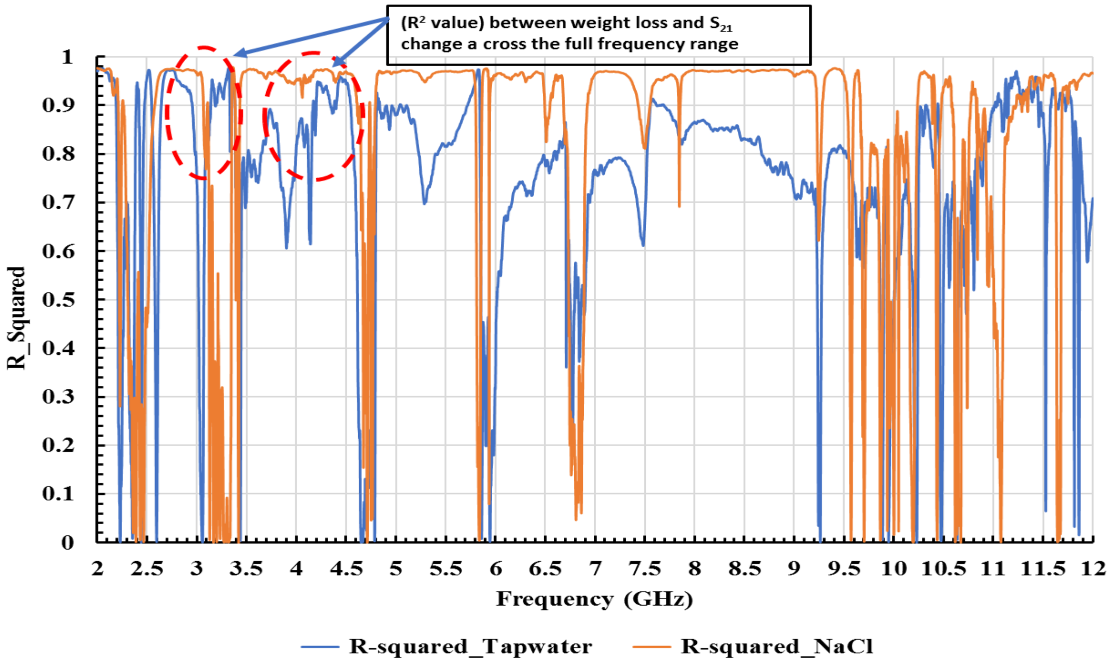

Figure 7.16: R^2 between both concrete sample weight loss and S_{21} change across the full frequency spectrum

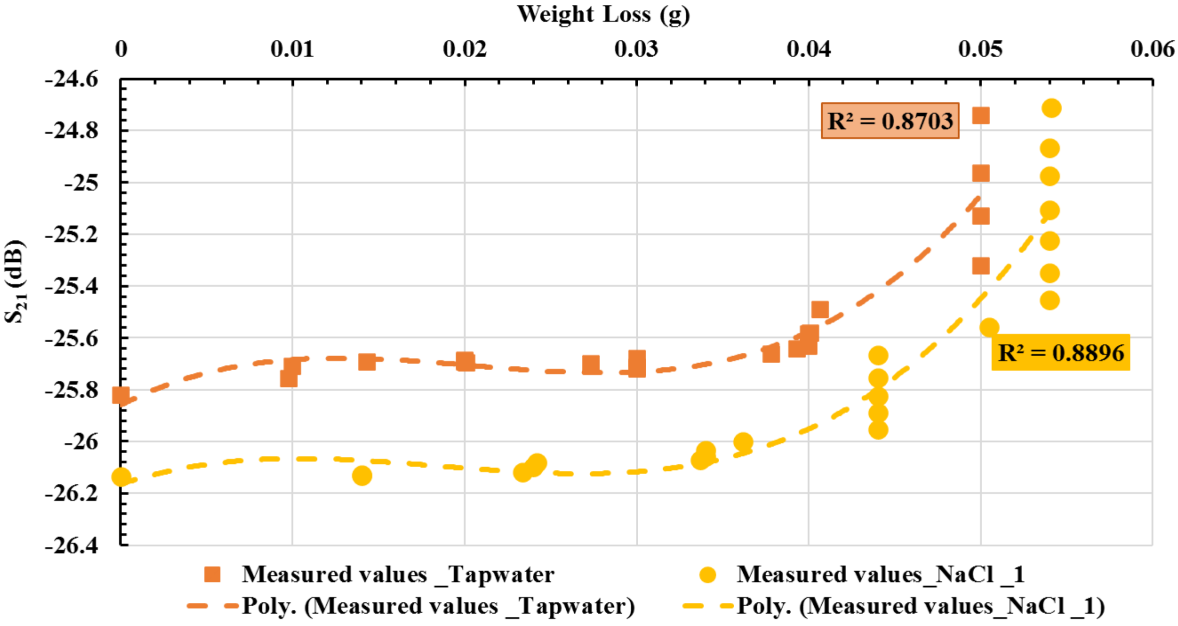

Figure 7.17: Polynomial correlation coefficient best fit between weight loss and S_{21} change at 3.482 GHz, with R^2 =0.88, for salt water sample and R^2=0.87 for tap water sample

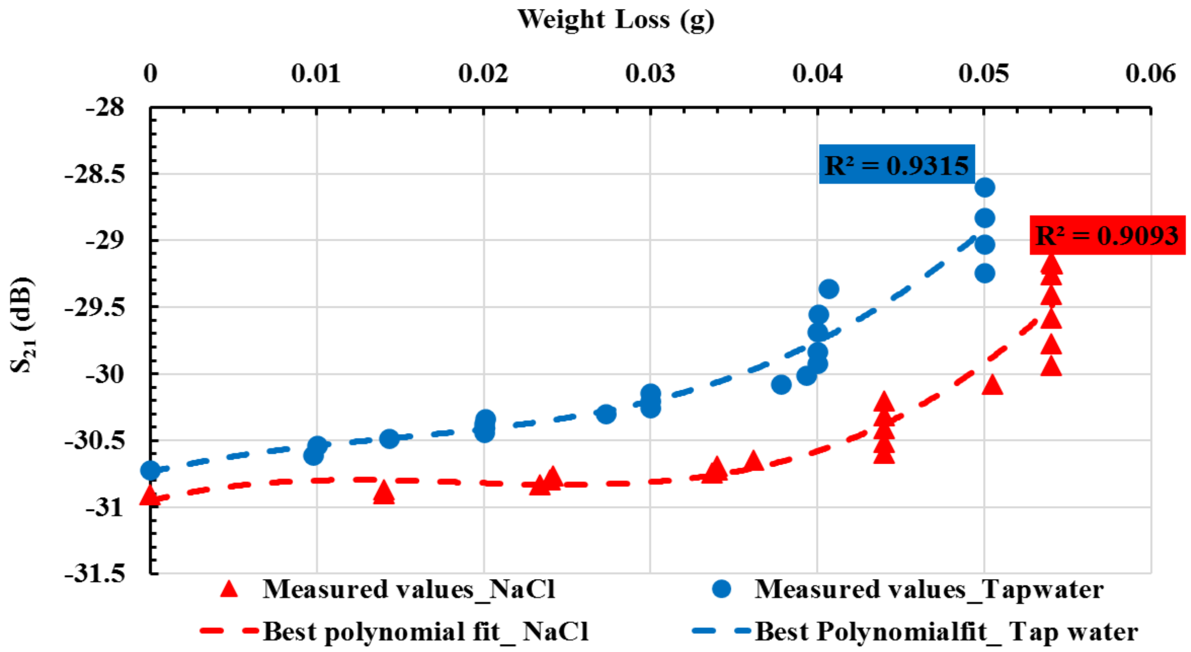

Figure 7.18: Polynomial correlation coefficient best fit between weight loss and S_{21} change at 4.428 GHz, with R^2 =0.90, for salt water sample and R^2=0.93 for tap water sample

(c) The raw data from the concrete sample experiment with mesh rebars.

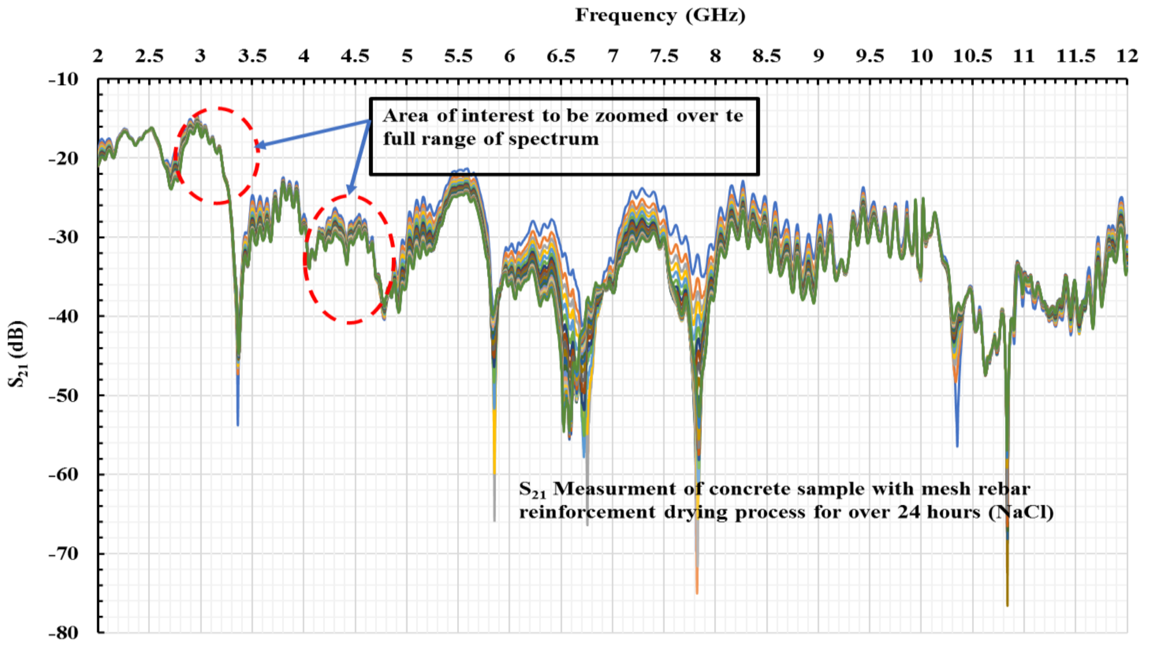

Figure 7.19: The electromagnetic wave sensor: S_{21} measurements were taken every one minute in the frequency range (2-12 GHz), NaCl.

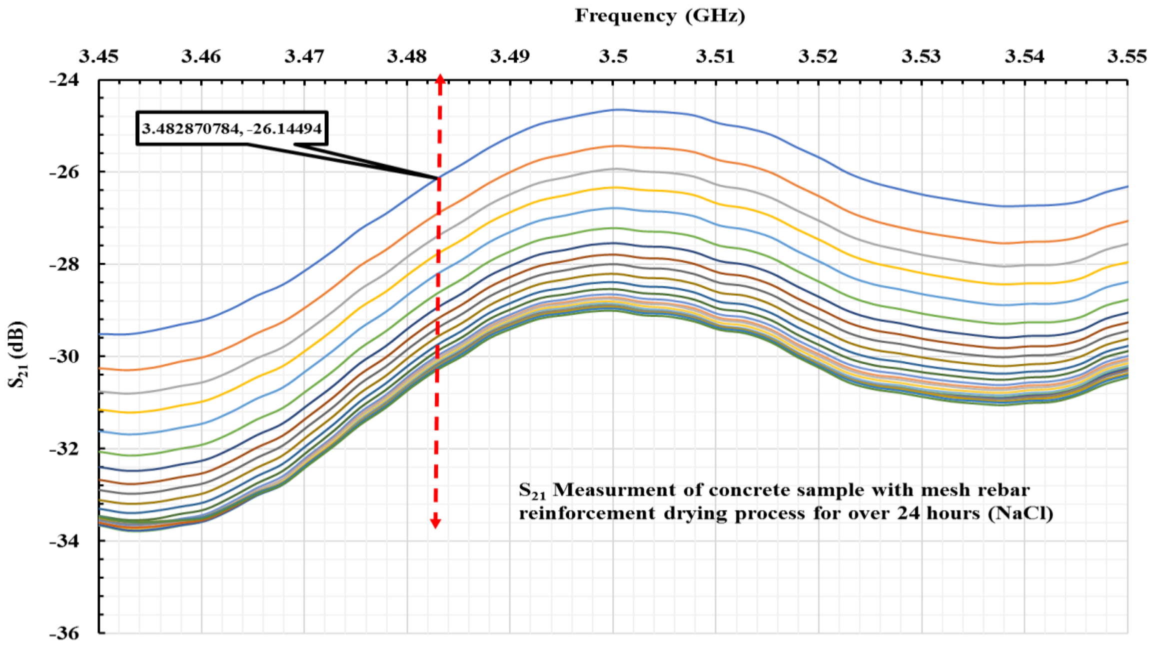

Figure 7.20: Tranmitted power S_{21} measurements using microwave sensor were taken per minute for the full range of frequencies, (2-12 GHz), but for clarity data measurements from every hour intervals and 3.45-3.55 GHz are presented (NaCl)

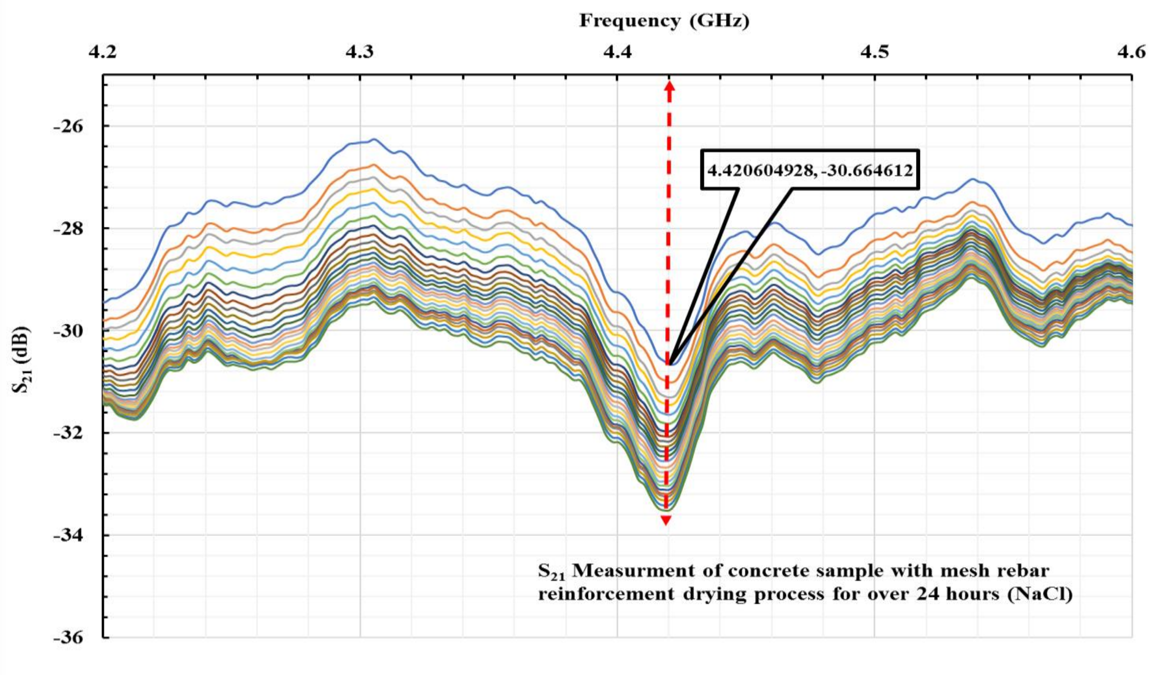

Figure 7.21: Microwave measurements of transmitted power S_{21} were taken every minute for the complete range of frequencies (2-12 GHz), although data from every hour intervals and 4.42-4.6 GHz are presented for clarity, (NaCl)

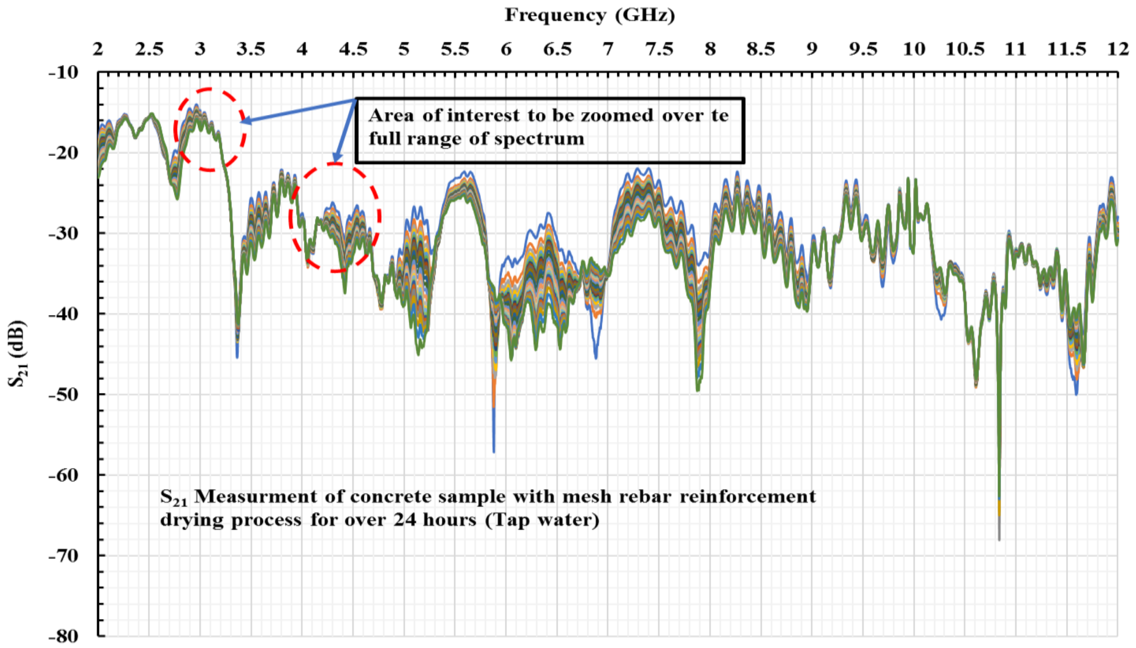

Figure 7.22: S_{21} measurement was taken every minute in the frequency range (2-12 GHz) using the electromagnetic wave sensor, Tapwater

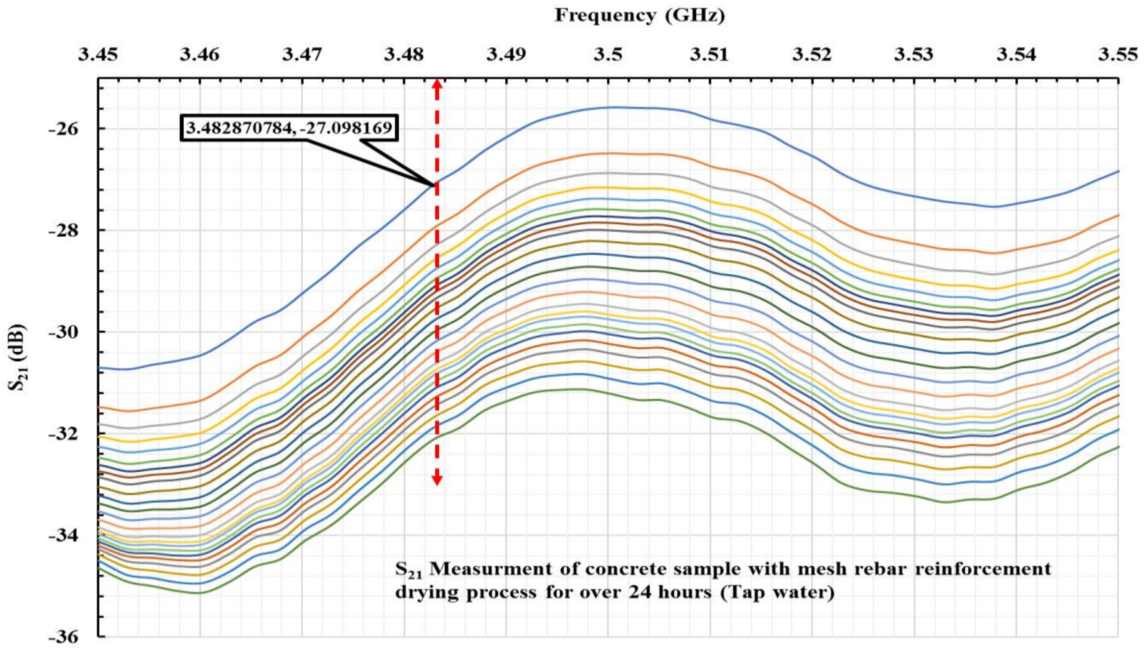

Figure 7.23: Transmitted power S_{21} measurements using microwave were taken per minute for the full range of frequencies, (2-12 GHz), but for clarity data measurements from every hour intervals and 3.45-3.55 GHz are presented (Tap water)

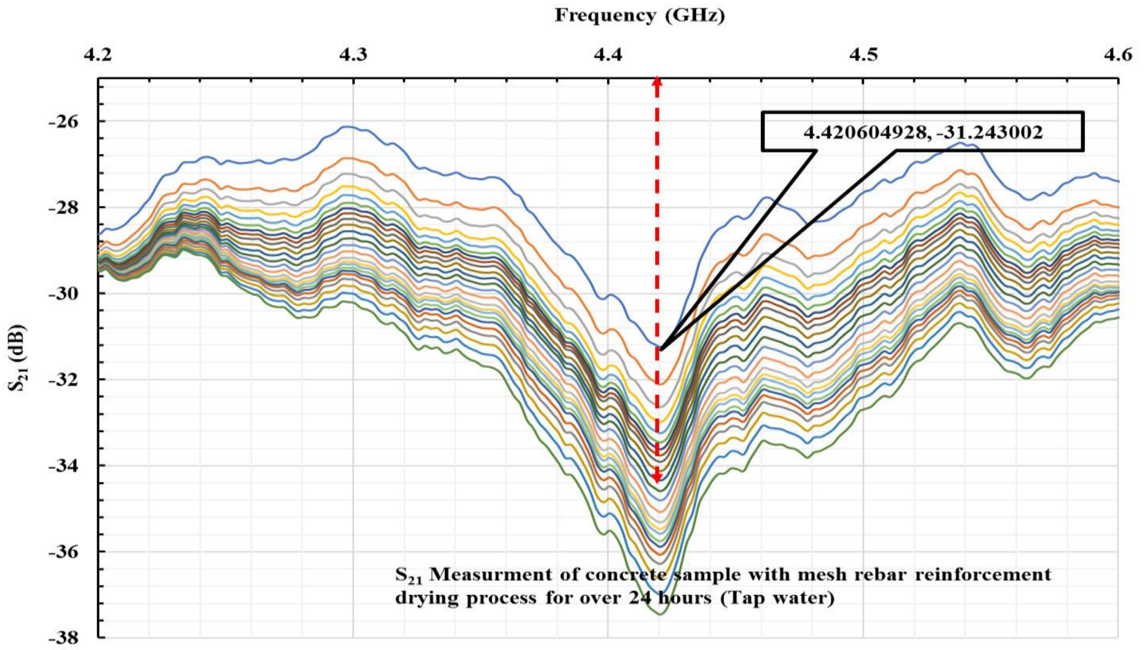

Figure 7.24: Microwave measurements of transmitted power S21 were taken every minute over the whole frequency range (2-12 GHz), but for clarity data measurements from every hour intervals and 4.2-4.6 GHz are presented (Tap water)

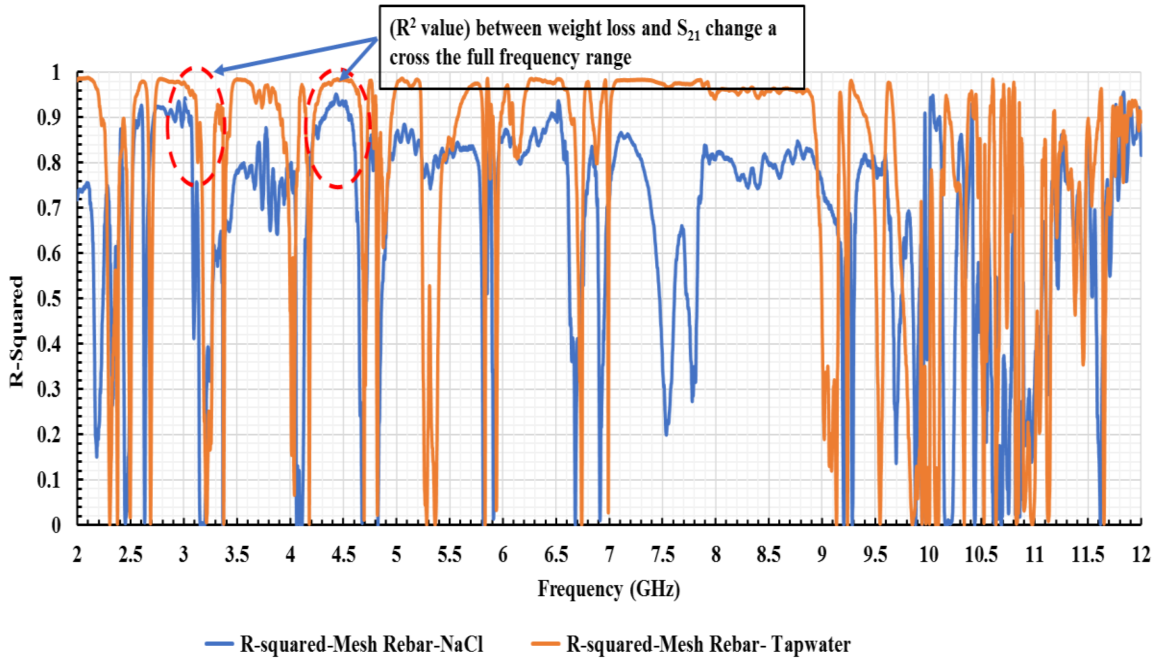

Figure 7.25: R^2 between both concrete sample weight loss and S$_{21}$ change across the full frequency spectrum

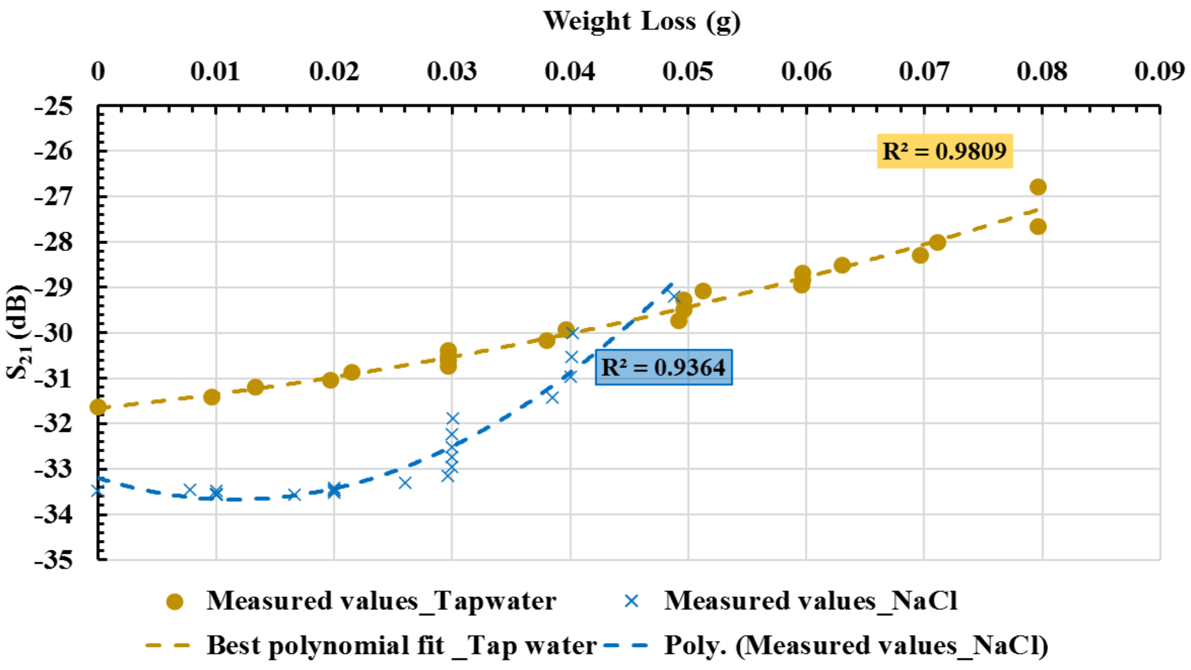

Figure 7.26: Polynomial correlation coefficient best fit between weight loss and S$_{21}$ change at 3.482 GHz, with R^2 =0.93, for salt water sample and R^2=0.98 for tap water sample

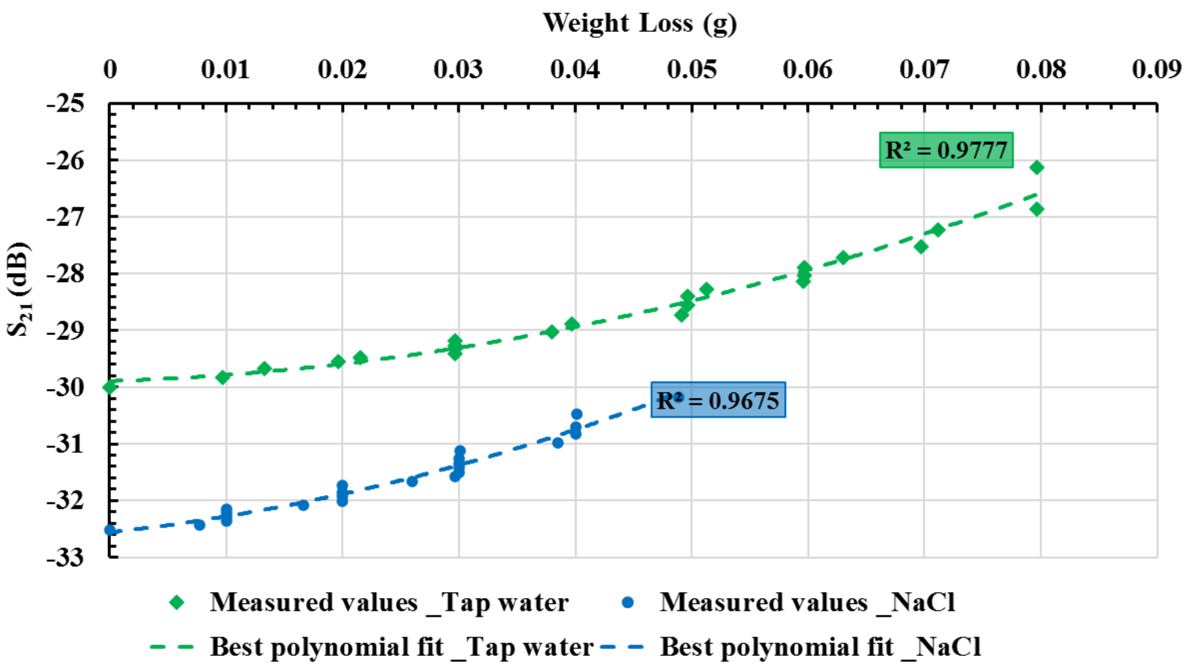

Figure 7.27: Polynomial correlation coefficient best fit between weight loss and S_{21} change at 4.428 GHz, with R^2 =0.96, for salt water sample and R^2=0.97 for tap water sample

Appendix E: Select the other frequency point based on data analysis of five concrete samples with five different saltwater concentrations.

The complete technique of this section was covered in detail in Chapter 6, Section 6.6. Furthermore, using the same classification and analysis data, the same technology was used to detect chloride ions in five different saltwater concentrations at three different depths. Fig. 7.28 illustrates the area of interest to zoom in over the range of frequency spectrums. Additionally, the complete spectrum was divided into three parts from 2.5-3 GHz, 4-4.5 GHz, and 5.4-5.6 GHz, as shown in Figure 7.29 (a and b). Other significant frequency spots were selected using the WEKA workbench classification. Chapter 6, section 6.6 shows the real outcome results for the frequency range of 5.4-5.6 and a single frequency 5.42 GHz.

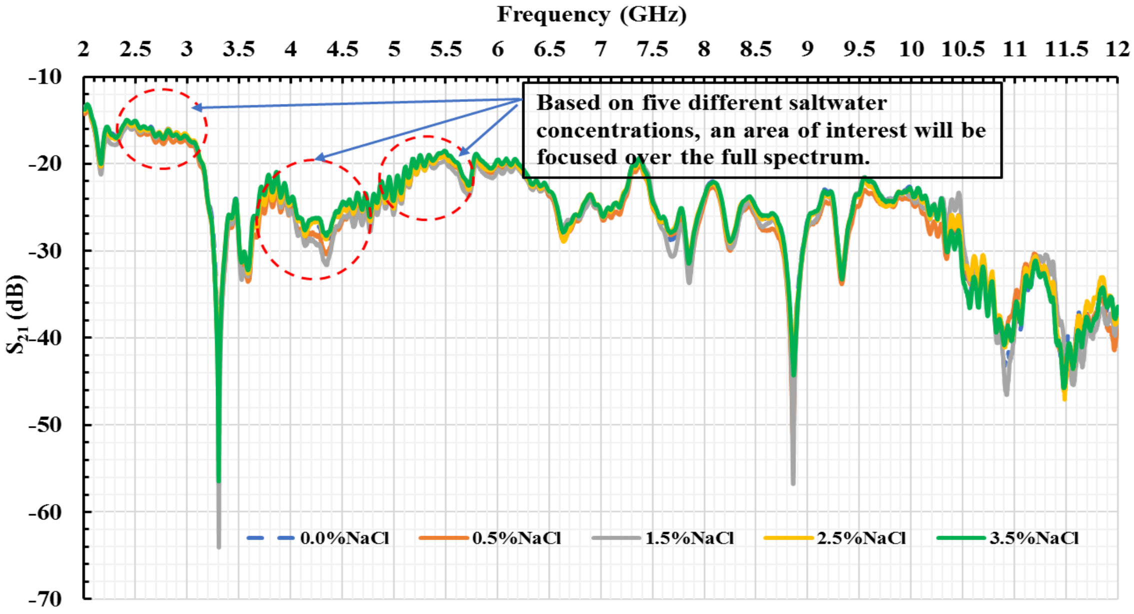

Figure 7.28: The microwave horn antenna; S_{21} measurements were taken for the frequency range 2-12 GHz.

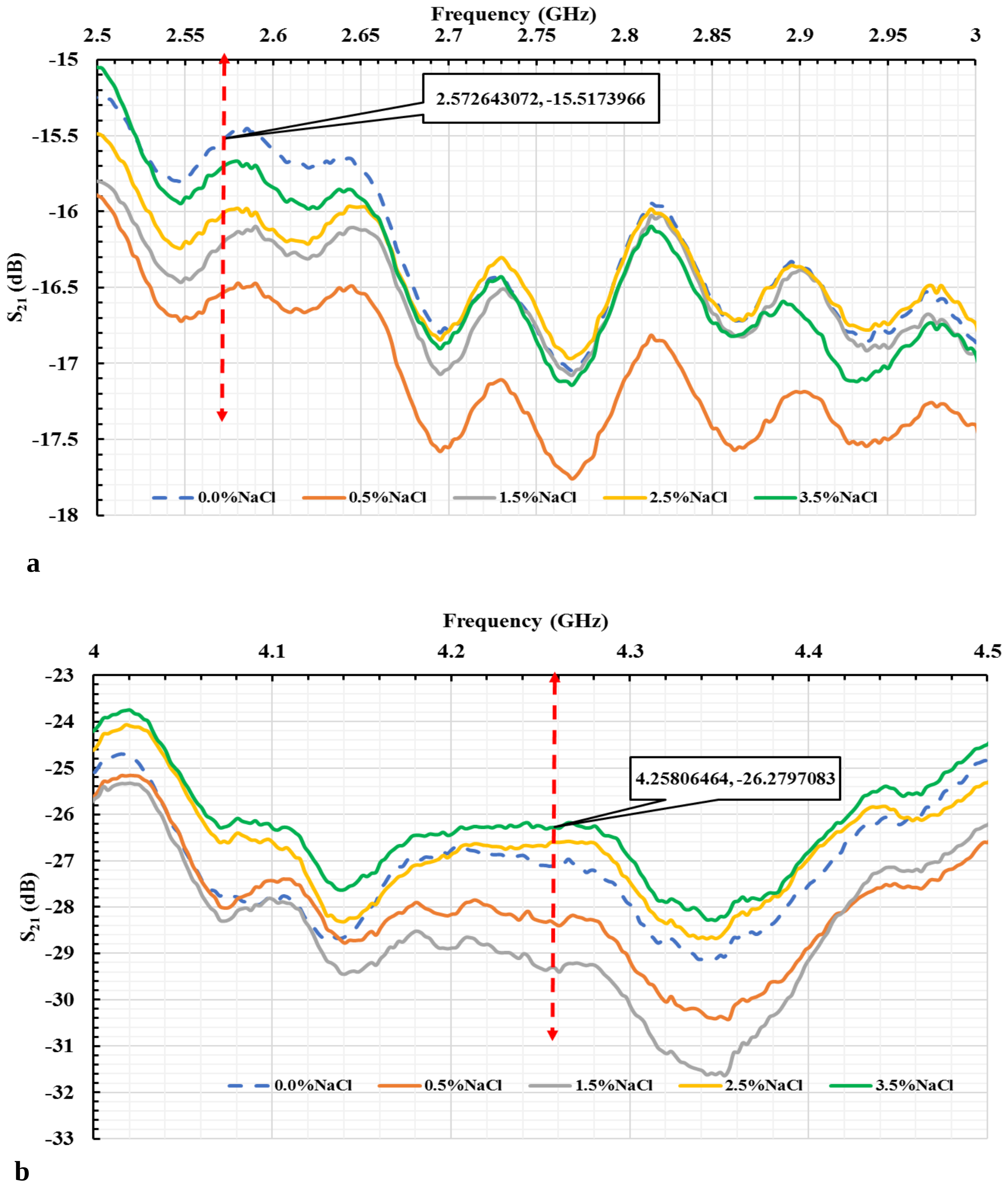

Figure 7.29: Using microwave horn antenna, S_{21} measurements were taken for the frequency range 2-12 GHz, but for clarity data (a) from the 2.5-3 GHz (b) from the 4-4.5 GHz are presented

It was found that the J48 algorithm had the best accuracy of 90 percent and 92 percent for least means absolute error and root mean square error. J48 algorithm decision tree is shown in Figure 7.30 (a and b), which illustrates the other possible significant frequency point for the different saltwater concentration levels.

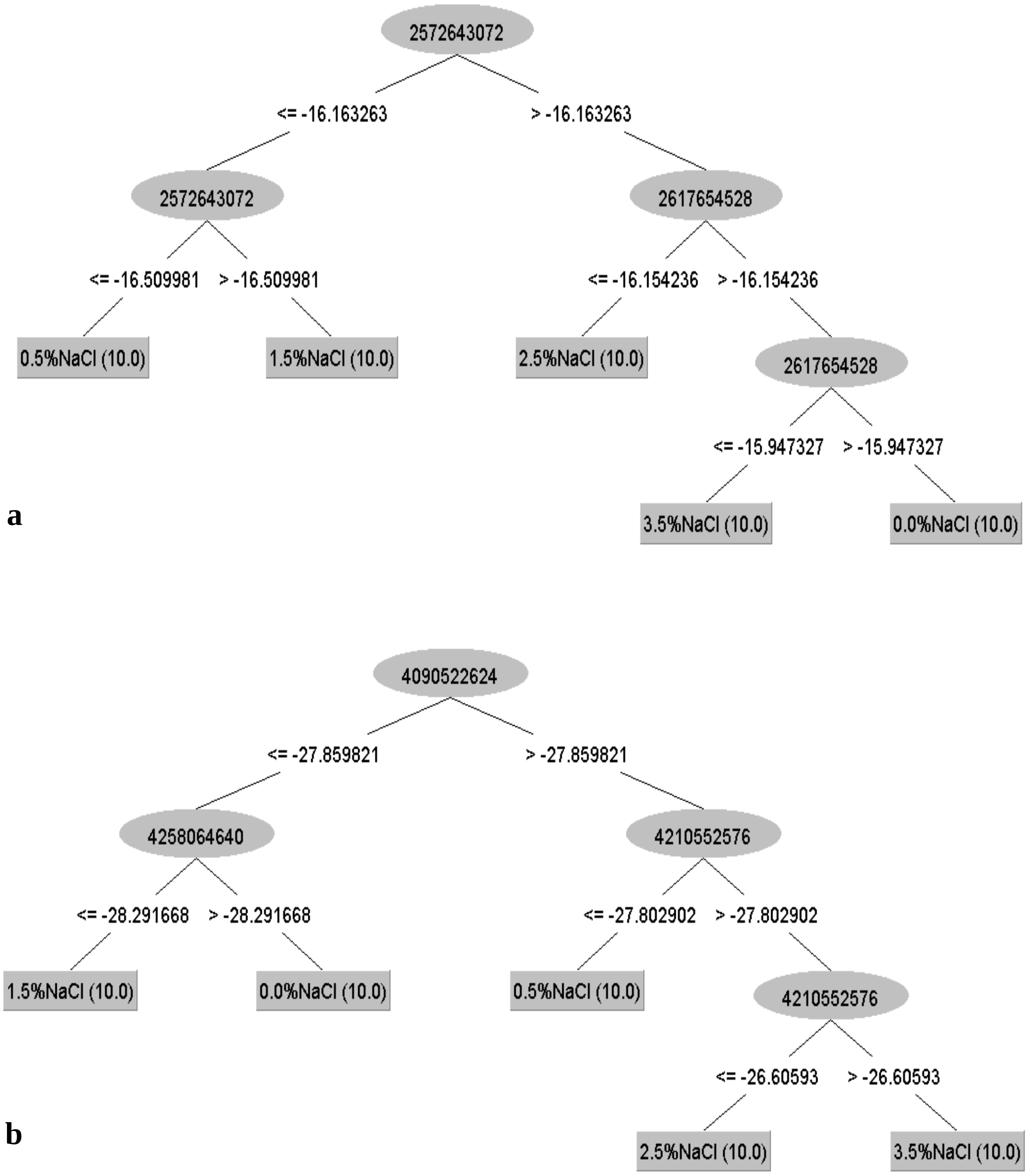

Figure 7.30: Indicates the classification of algorithm J48 decision tree graphic; selected frequency point (a) 2.5-3 GHz (b) 4-4.5GHz.

Tables 7.1 and 7.2 show the set of techniques previously described in Chapter 3 inside various classifiers with a lower mean square error and a more significant percentage of accuracy to determine the most critical possible frequency across five different saltwater concentration classes. The focus of this study was on the most popular decision tree classifier, the algorithm J48.

Table 7.1: Results obtained for different classifiers from the Weka workbench at (2.5-3 GHz)

The different classifier has been used for these algorithms	Accuracy (%),	Means Absolute error (%)	Root means square error (%)
MultiScheme	20	0.32	0.4
Bagging	20	0.33	0.4005
CVParameterSelection	20	0.32	0.4
InputMappedClassifier	20	0.32	0.4
OneR	41	0.23	0.4632
ZeroR	20	0.33	0.4
REPTree	20	0.32	0.4
RandomTree	78	0.125	0.2266
DecisionStump	56	0.154	0.2664
J48	92	0.032	0.1789

Table 7.2: Results obtained for different classifiers from the Weka workbench at (4-4.5 GHz)

The different classifier has been used for these algorithms	Accuracy (%),	Means Absolute error (%)	Root means square error (%)
MultiScheme	20	0.32	0.4
Bagging	20	0.32	0.4005
CVParameterSelection	20	0.32	0.4
InputMappedClassifier	20	0.32	0.4
OneR	20	0.32	0.5658
ZeroR	20	0.33	0.4
REPTree	20	0.32	0.4
RandomTree	78	0.125	0.2266
DecisionStump	40	0.24	0.3464
J48	90	0.04	0.2

The generated decision rules determine that other frequency points, such as 2.57 GHz and 4.25 GHz, can be used to detect chloride ions in concrete structures for the sensor used in this project. The total number of test cases is 50 (n = 50). The classification accuracy was 92% and 90%, respectively. A two-dimensional matrix containing a column and row for each class is frequently used to display the results of a test set. The number of test samples for which the actual class is the row, and the predicted class is the column is shown in each matrix element. Each row and column in the matrix represent the number of test samples for which the actual class is the row, and the projected class in the column, respectively. In addition, the classification accuracy is determined by dividing the total number of test examples by the sum of the numbers from the major diagonal of the confusion matrix with a red arrow. The confusion matrix for the solved problem is shown in Tables 7.3 and 7.4..

Table 7.3: The confusion matrix for the leave-one-out validation of classification for frequency rang (2.5-3GHz)

Classified as	**0.0% NaCl added**	**0.5% NaCl added**	**1.5% NaCl added**	**2.5% NaCl added**	**3.5% NaCl added**
0.0% NaCl	10	0	0	1	0
0.5% NaCl	0	9	0	0	2
1.5% NaCl	2	0	9	0	0
2.5% NaCl	0	2	0	9	0
3.5% NaCl	0	0	0	0	9

Table 7.4: The confusion matrix for the leave-one -out validation of classification for frequency rang (4-4.5GHz)

Classified as	**0.0% NaCl added**	**0.5% NaCl added**	**1.5% NaCl added**	**2.5% NaCl added**	**3.5% NaCl added**
0.0% NaCl	9	0	0	1	0
0.5% NaCl	0	9	0	0	2
1.5% NaCl	2	0	8	0	0
2.5% NaCl	0	2	0	9	0
3.5% NaCl	0	0	0	0	10

A Selection of Variables for the Neural Network.

To detect chloride ions in specimens, supervised applied machine learning classification methods after determining the most critical frequency using the WEKA workbench algorithm J48. In addition, the chloride ion content in concrete samples was also determined using these other frequency points from the WEKA classification. Fed the single frequency data sets into the ANN algorithm to evaluate the sensors against the gold standard approach typically used in industry. The ANN technique was constructed and tested using MATLAB programming in this research. Additional, input parameters depended on the raw data of electromagnetic waves for concrete samples in five different saltwater concentrations. An ANN model fitted using a 5x3 matrix of data that had been prepared to fit the data. The ANN inputs and outputs are listed in Table 7.5

Table 7.5: The Input and output parameters of the ANN at one single frequency (GHz)

Input Variable			**Target (output)**		
5 different percentages of salt water concentration	**Averaged (10) Number of S_{21} at (2.572 GHz), (dB)**	**Averaged (10) Number of S_{21} at (4.258 GHz), (dB)**	**% of Chloride ion per weight of cement**		
			18mm depth	**40mm depth**	**70mm depth**
0.0% NaCl added	-15.51739 (Stdev)	-27.09047 (Stdev)	0.0059	0.0047	0.0039
0.5% NaCl added	-16.52751 (Stdev)	-28.36107 (Stdev)	0.1667	0.1291	0.1222
1.5% NaCl added	-16.19105 (Stdev)	-29.31408 (Stdev)	0.1855	0.1589	0.1421
2.5% NaCl added	-16.00162 (Stdev)	-26.60306 (Stdev)	0.2316	0.1821	0.1506
3.5% NaCl added	-15.69473 (Stdev)	-26.27971 (Stdev)	0.3256	0.0952	0.0786

The ANN model was built using data from electromagnetic wave sensors

It's been shown in Table 7.6 and Table 7.7 how to optimise one single frequency for chloride prediction based on model output. A total of 50 data samples were used for ANN model training (70%), validation (15%) and testing (15%), respectively. There was a very strong correlation between the predicted and measured values when comparing the model results with those obtained using the destructive approach (chlorimeter tool).

Table 7.6: The ANN model's summary findings at one single frequency (2.57 GHz)

		Per weight of cement	
Parameter	**Samples**	**MSE**	**R^2**
Training (70%)	34	4.37485×10^{-10}	0.99994
Validation (15%)	8	1.68219×10^{-5}	0.99757
Testing (15%)	8	1.51784×10^{-5}	0.999814

Table 7.7: The ANN model's summary findings at one single frequency (4.25 GHz)

		Per weight of cement	
Parameter	**Samples**	**MSE**	**R^2**
Training (70%)	34	8.73909×10^{-7}	0.99994
Validation (15%)	8	2.66048×10^{-5}	0.99677
Testing (15%)	8	1.59637×10^{-5}	0.99916

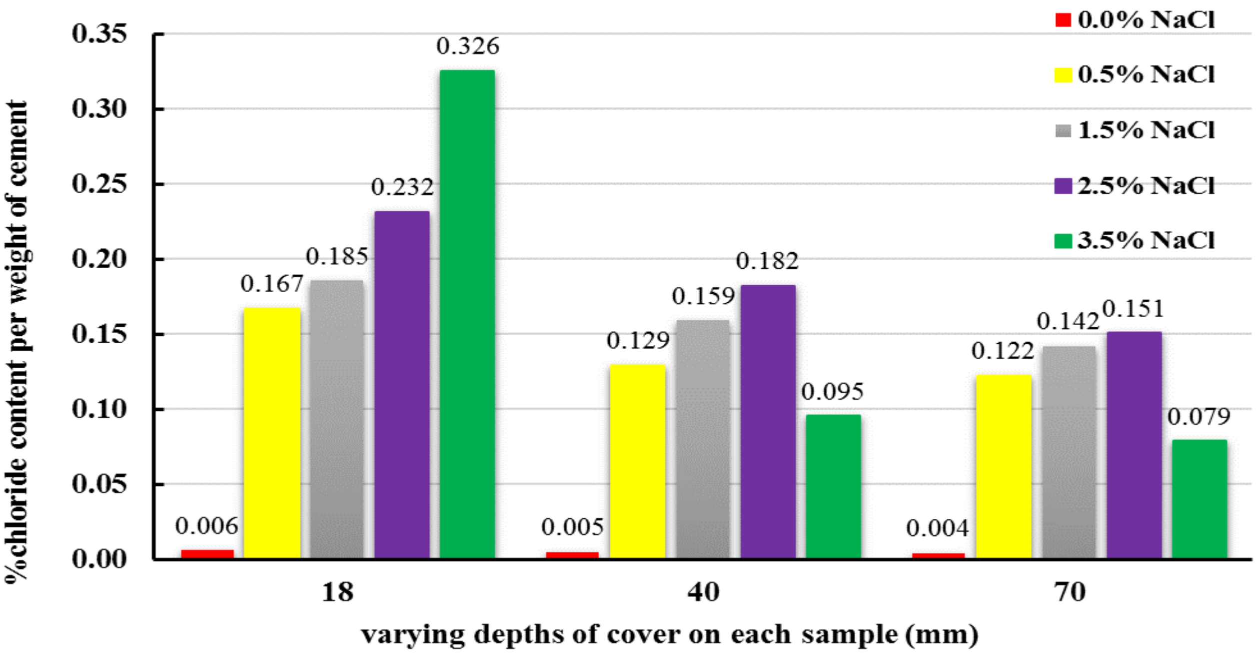

Figure 7.31: The actual of % chloride per weight of cement

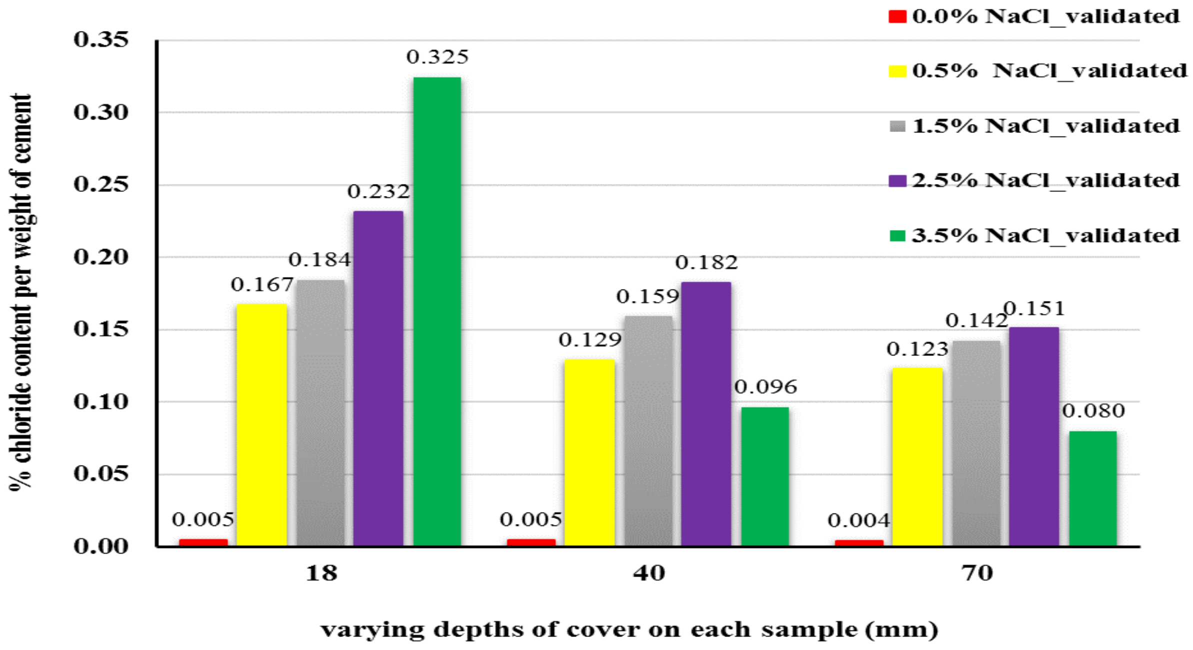

Figure 7.32: Validated percent chloride per weight of cement obtained from the ANN model for five different saltwater concentrations and three different depths using a single frequency (2.57 GHz)

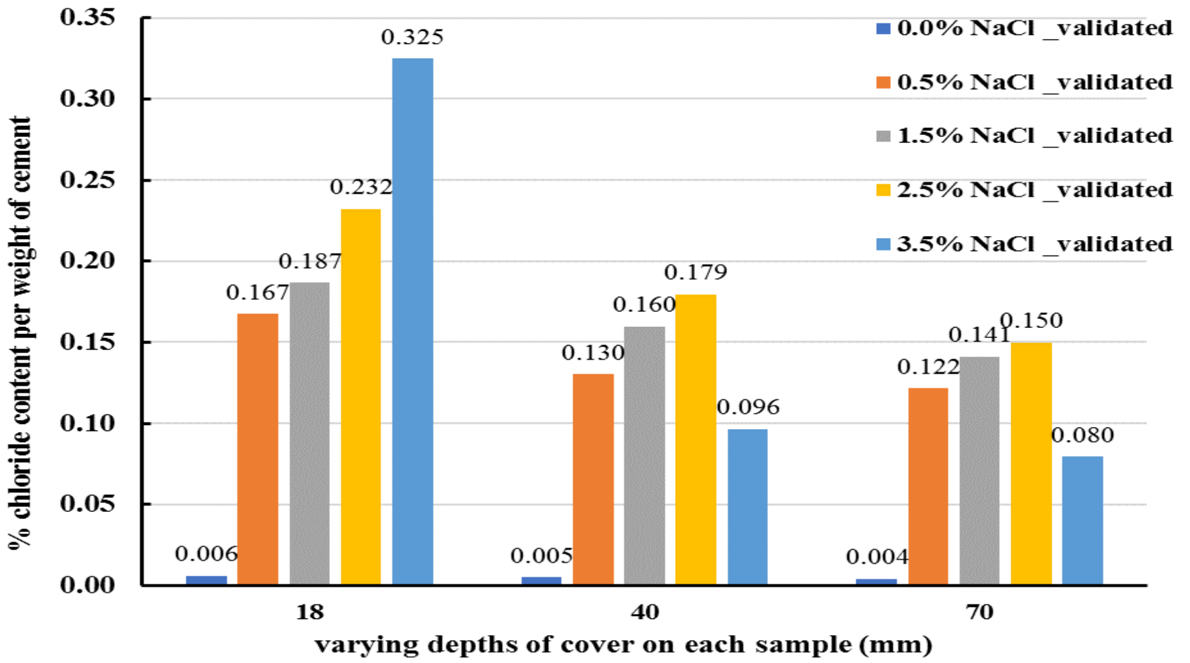

Figure 7.33: Validated percent chloride per weight of cement obtained from the ANN model for five different saltwater concentrations and three different depths using a single frequency (4.25 GHz)

Error Calculations Using the Chi-Squared Method.

Table 7.8 and Table 7.9 shows the total Chi-Squared calculation values for 5 different saltwater concentrations at three different depths for the single frequency (2.57 GHz and 4.25 GHz). The Chi-squared calculation procedure is discussed in Chapter 6.

Table 7.8: The total Chi-Squared calculation values at (2.57 GHz)

Chi-Squared					
Different depth (mm)	**0.0% added NaCl**	**0.5%NaCl**	**1.5%NaCl**	**2.5%NaCl**	**3.5%NaCl**
18	**0.0003**	**0.0034**	**0.0069**	**0.0031**	**0.0385**
40	**0.0001**	**0.0006**	**0.0026**	**0.0024**	**0.0158**
70	**0.0002**	**0.0028**	**0.0032**	**0.0005**	**0.0170**
Total	**0.097**				
P_Value	0.99999				

Table 7.9: The total Chi-Squared calculation values at (4.25 GHz)

Chi-Squared					
Different depth (mm)	**0.0% added NaCl**	**0.5%NaCl**	**1.5%NaCl**	**2.5%NaCl**	**3.5%NaCl**
18	**0.00011**	**0.00364**	**0.00634**	**0.00337**	**0.03895**
40	**0.00008**	**0.00075**	**0.00205**	**0.00271**	**0.01606**
70	**0.00002**	**0.00277**	**0.00356**	**0.00054**	**0.01757**
Total	**0.099**				
P_Value	0.99999				

The resulting chi-squared values and percentages of error for the validated percentage of chloride ions in five different saltwater concentrations specimens at three different depths on both single frequency points are shown in Table 7.10.

Table 7.10: The total Chi-Squared values and %of error

Parameter	**% of Chloride**	**Chi-Squared**	**% Error**
Chlorimeter Tool	per weight of cement	0.099000000	
Microwave spectroscopy_	per weight of cement @ 2.57 GHz	0.099136649	**0.138**
	per weight of cement @ 4.25 GHz	0.098917182	**0.083**

ANN was used to analyse and validate five different saltwater concentrations.

The performance of the trained LM algorithm is discussed and presented in this section of the project using standard performance indicators such as mean square error (MSE) and correlation coefficients (R^2). Figure 7.34 (a and b) shows the network's validation performance and mean square error from a high value to a low value.

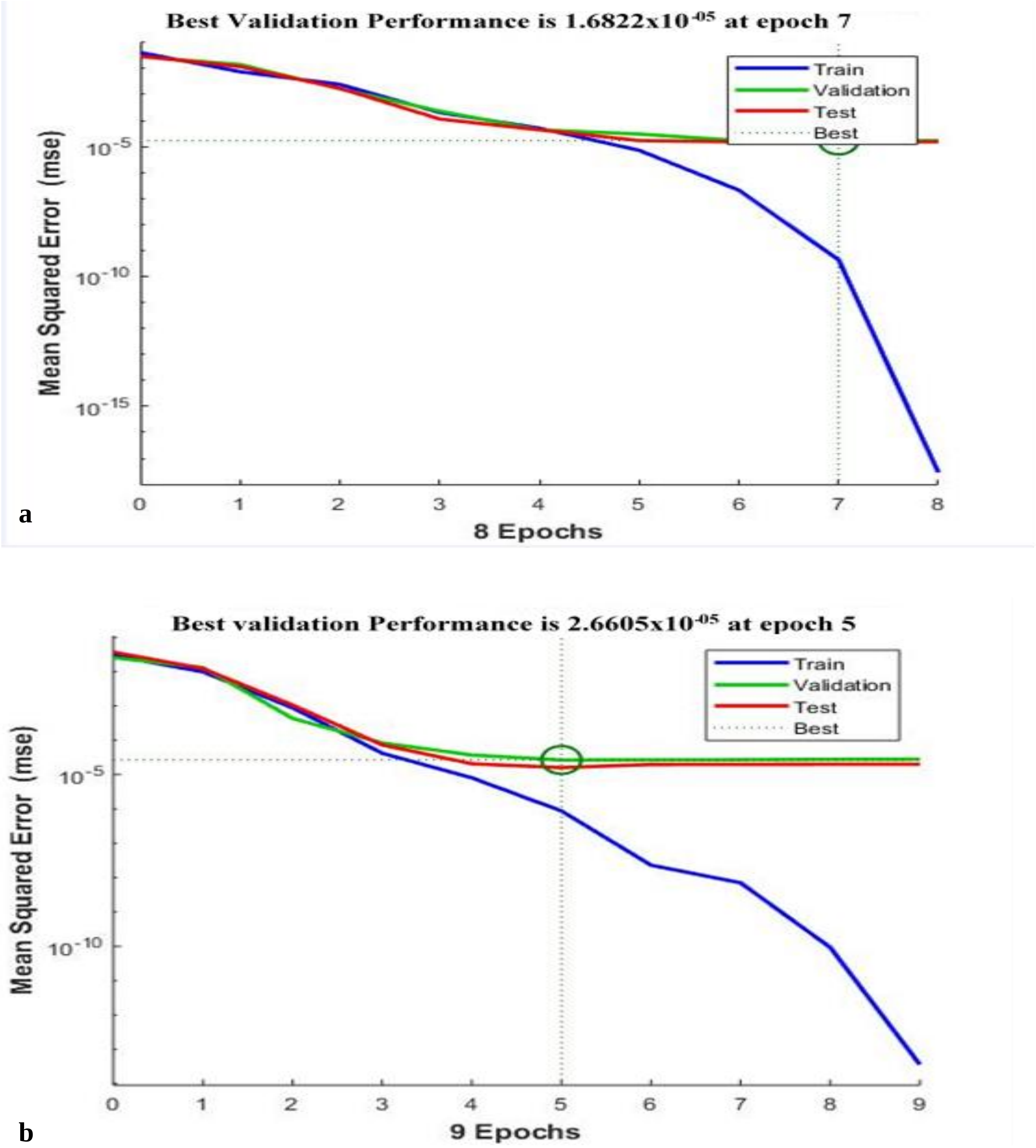

Figure 7.34: Best validation performance in Artificial Neural Network Model at one single frequency point; Per weight of cement of (a) 2.57 GHz and (b) 4.25 GHz

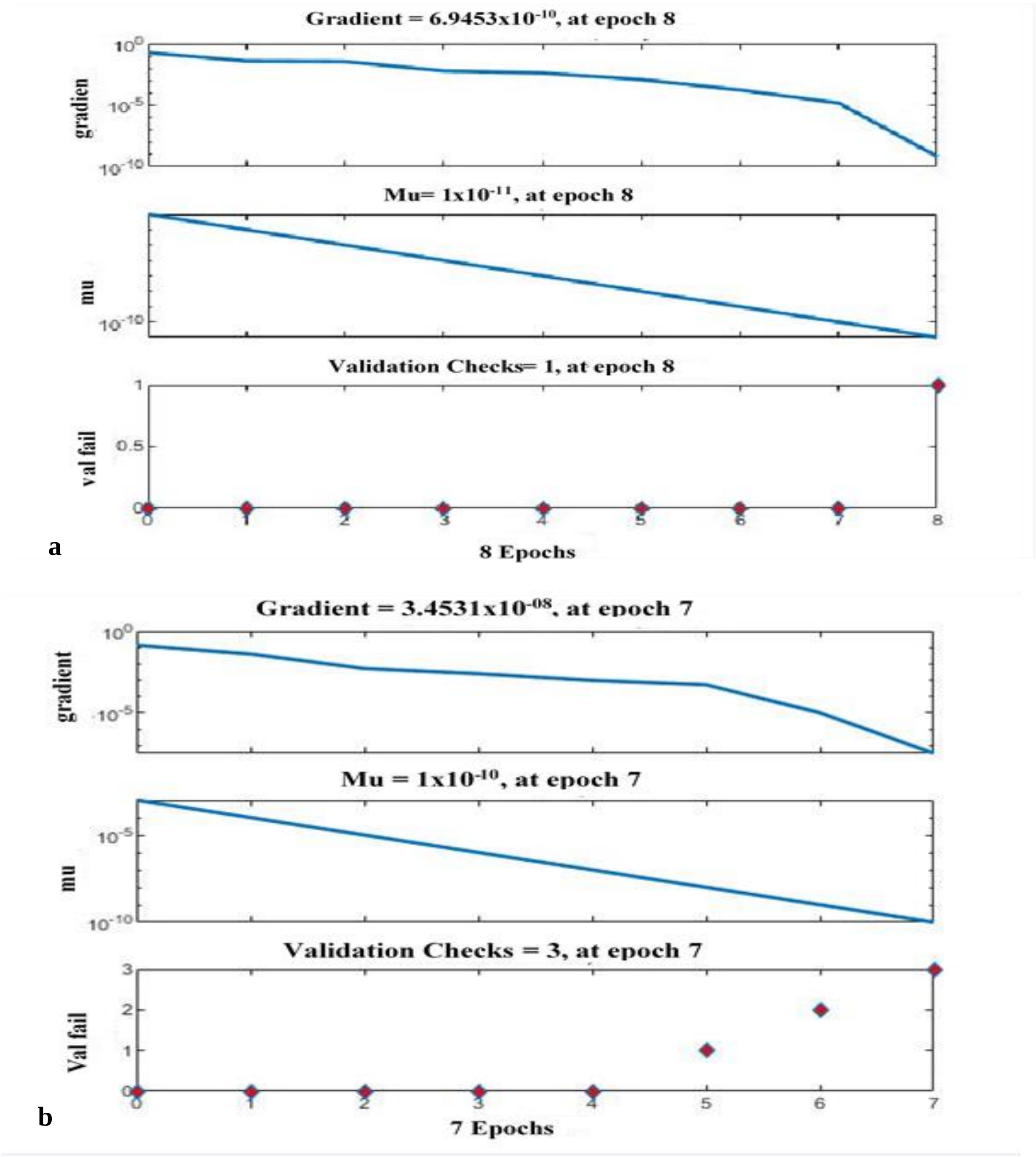

Figure 7.35: The gradient and maximum validation checks for the LM trained network for one single frequency; per weight of cement. (a0 2.57 GHz and (b) 4.25 GHz

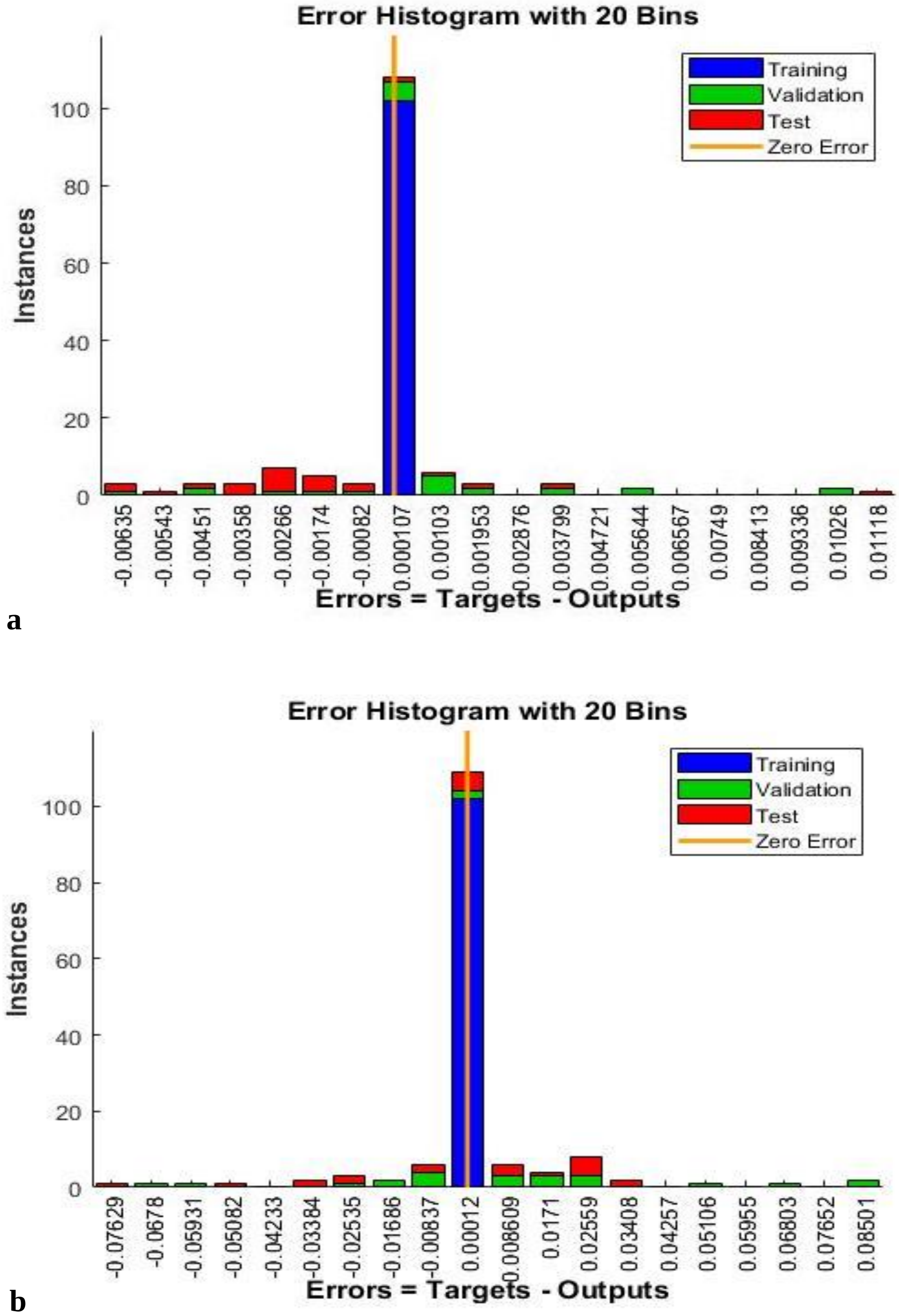

Figure 7.36: The plot of error histogram (EH) for the LM algorithm; per weight of cement. (a) 2.57 GHz and (b) 4.25 GHz

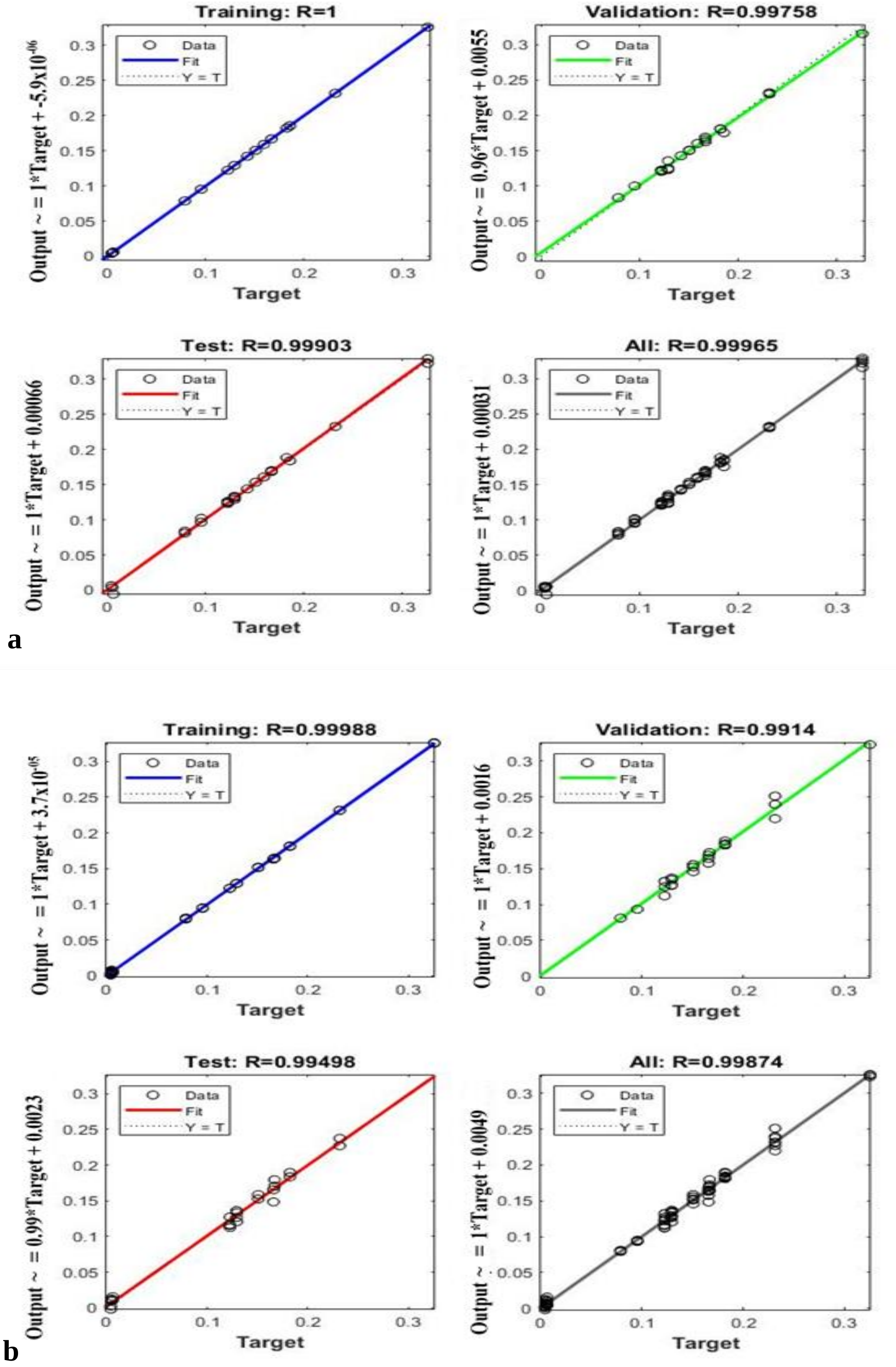

Figure 7.37: The regression graphs of the experimental results against the validated %Chloride ions per weight of cement, (a) 2.57 GHz and (b) 4.25 GHz

Table 7. 11: The results for the observed data target and output values at 2.57 GHz

%Chloride per weight of cement			
Depth (mm)	**NAEs**	**RMSE**	**R^2**
18	0.000321	0.000126	0.951387
40	0.000342	0.000156	0.960058
70	0.000274	0.000114	0.951586
Total of three depth	0.000312	0.000132	0.954343

Table 7.12: The results for the observed data target and output values at 4.25 GHz

%Chloride per weight of cement			
Depth (mm)	**NAEs**	**RMSE**	**R^2**
18	0.000245	0.000156	0.970456
40	0.000326	0.000112	0.982097
70	0.000269	0.000101	0.960298
Total of three depth	0.000266	0.000123	0.970950

There's also an additional comparison between target and validated values, as illustrated in Table 7.11 and Table 7.12. There was a significant agreement between the measured and predicted values with a Value of Normalised Absolute Error statistic (NAE), Value of Root Mean Square Error statistic (RMSE), and Value correlation coefficients (R^2), with the amount of percent chloride per weight cement at three different depths from 2.57 GHz (0.000312, 0.000132 and 0.954343) and 4.25 GHz (0.000266, 0.000123 and 0.970950). The findings show that microwave spectroscopy can be utilised to assess variable NaCl contents in concrete specimens at various depths. The other possible single frequency was discovered using classification feature selection, and it showed a frequency of 2.57 GHz and 4.25 GHz as a significant predictor of level chloride ions.

Publications:

1. Goran Omer Dr, P.K.D., William Atherton Dr, Magomed Muradov Dr, Michaela Gkantou Dr, Andy Shaw Prof, Michael Riley Prof, Khalid Hashim Dr, Ahmed Al-Shamma'a, *A Non-Destructive Electromagnetic Sensing Technique to Determine Chloride Level in Maritime Concrete* Karbala International Journal of Modern Science, 2021. **7**(1): p. 13.